X-ray scattering from magnetic metallic multilayers

Thomas Paul Anselm Hase

X-ray Scattering from Magnetic Metallic Multilayers

by

Thomas Paul Anselm Hase

A thesis submitted in partial fulfilment of the requirements for the degree of Doctor of Philosophy

The University of Durham

1998

Abstract

Study of structure and interface morphology of magnetic thin films is crucial in obtaining a better understanding of the coupling mechanisms in such systems. In this thesis various x-ray scattering techniques are applied to a series of Co/Cr trilayers, Cu/Co multilayers and spin valve structures. It is demonstrated that modifications to the distorted wave Born approximation allow the modelling of grazing incidence diffuse scatter originating from graded systems such as Co/Cr. Grazing incidence scattering techniques are also employed to investigate the out of plane correlations of lateral roughness in Cu/Co multilayers, as well as in miscible trilayer structures.

The use of soft x-rays in the investigation of *3d* transition metal multilayers is also presented. Such experiments are sensitive to the component of magnetisation aligned with the direction of the incident beam. In a series of magnetisation experiments, the dependence of the x-ray scatter sensitive to this component of magnetisation are analysed. For the first time evidenced is found for correlated magnetic roughness, which has lateral correlation lengths far greater than the structural roughness length scales. This magnetic roughness is measured in detail, and the correlation length is found to vary with applied field direction.

Grazing incidence x-ray fluorescence is applied to two spin valve structures. These experiments provide a direct measure of buried layer thicknesses which is not possible by other x-ray scattering techniques. This novel method for the determination of the copper layer thickness in spin valves shows the versatility of non-destructive x-ray methods for the characterisation of magnetic metallic multilayers.

Acknowledgements

Over the past few years there have been many people who have given me help and encouragement. If I miss anyone out in this list of acknowledgements, my apologies.

Firstly I must thank Prof. D. Bloor and Prof. B.K. Tanner who through their tenures as head of department have provided me with the excellent facilities of the Physics Department. As well as being head of department, Prof. B.K. Tanner has been an excellent supervisor, and my heartfelt thanks goes to him for putting up with all my idiosyncrasies.

I would like to thank the members of the department who have helped me over the years. Thanks to the members of the audio-visual department - Mike, Vicki and Pauline. Also to the secretarial staff for constant stationery and abuse - Nikki, Penny, Julie, Joanne, Rebecca, Clare, and the others. I would also like to thank Ian and Wayne for allowing me to borrow things from the teaching labs. The help from the members of the workshop is also gratefully acknowledged. I would also like to thank Pat for providing my breakfast of tea and chocolate everyday.

Thanks are also expressed to EPSRC for funded the project. I would also like to express my thanks to Prof. R.J. Cernik who has been my CASE supervisor at Daresbury Laboratory.

Much of the work in this thesis has been conducted within collaborations. I would like to take this opportunity to express my thanks to all those involved. Most notably, Dr. B.J. Hickey and his group at the University of Leeds which has provided many of the samples and magneto-transport results contained within this thesis. I must particularly thank Paul Ryan, Chris Marrows and Helen Laidler for all their help and advice during the course of my study. Collaborations with the University of Salford, namely Prof. P. Grundy and Dave Joyce are also acknowledged. It was also a pleasure to be part of a ECHCM project, and I would like to thank everybody

involved with it. In particular, M.J. Jackson, S.M. Thompson, E. Ho, A.K. Petford-Long, A. Daykin, J.J Freijo, F. Garnot, and its organiser J.S.S. Whiting.

The results contained in this thesis were obtained outside of the department, and I would like to thank the staff at the synchrotron sources for their time and patience. Especially C.C. Tang, S. Collins, H. Dürr, E. Dudzik, and A. Neild who have at one time or another helped me out at Daresbury, and to A. Fitch and G. Vaughan at the ESRF.

The results could not have been analysed without the simulation code written by M. Wormington of Bede Scientific. I would like to express my deepest thanks to him along with D.K. Bowen and T. Lafford of Bede Scientific.

I would also like to take this opportunity to express my thanks to other members in the group. Ian Pape, John Clarke, Brian Fulthorpe Andrea Li-Bassi, Caroline Moore, Peter Hatton, Yixi Su, Wayne Lin, C.R. Li, C.H. Du and Dirk Rose who have helped me in more ways than I care to remember. The results contained within this thesis would not have been possible without them. The other members of the greater condensed matter group also deserve a mention for making my time in the department so enjoyable. So my thanks to (in no particular order), J. Makar, T. Rogers, H. Ramsbottom, A. Horsfall, S. Ali, H. Hamidi, C. Leighton, S. Daley, J. Egglestone, M. Poli, C. Reig, I. Daniel, S. Keys, D. Read, G. Ashcroft, A. Sneary, N. Leigh, N. Cheggour, D. Hampshire, I. Terry and the eternal optimist John Dobson.

Finally, I would like to thank members of my family and friends who have encouraged me both emotionally and financially. I would like to express my deepest thanks to my father who proof read this work.

List of Publications

The work described in the chapters listed below has appeared in the following:

Chapter 6: *The Effect of Growth Temperature on the Structure of Co-Cr-Co Trilayers,* T.P.A. Hase, I. Pape, B.K. Tanner, S.M. Thompson, S.M. Jordan, J.J Freijo, *Adv. X-ray Anal.*, **40**, *CD-Rom*,(1997)

Chapter 7: *The Relation of Structure to Giant Magneto-resistance in Cu/Co multilayers,* T.P.A. Hase, I. Pape, B.K. Tanner, H. Laidler, P. Ryan, B.J. Hickey, *J. Magn. Mag. Mat.*, **177-181**, *1164-1165*, (1998)

Chapter 9: *Determination of the Copper Layer Thickness in Spin Valves by Grazing Incidence X-ray Fluorescence,* T.P.A. Hase, B.K. Tanner, P. Ryan, C. H. Marrows, B.J. Hickey, *IEEE Trans. Mag.*, **34** (Pt. 1), *831-833*, (1998)

Related material has appeared in the following:

Giant Magnetoresistance and Interface Structure in Cu/Co multilayers grown by MBE on Si(111) substrates with Copper Silicide Buffer Layers, I. Pape, T.P.A. Hase, B.K. Tanner, H. Laidler, C. Emmerson, T. Shen, B.J. Hickey, *J. Magn. Mag. Mat.*, **156**, *373-4*, (1996)

Interface Effects in Grazing Incidence X-ray Scattering from Transition Metal Multilayers, B.K. Tanner, M. Wormington, T.P.A. Hase, I. Pape, *Surface - X-ray, synchrotron and neutron investigations*, **12**, *1189-1199*, (1996); also published as, *Proc. Russian Academy of Science*, **3-4**, *10-20*, (1996)

Evidence of Grading at Polished Surfaces from Grazing Incidence X-ray Scattering, M. Wormington, I. Pape, T.P.A. Hase, B.K. Tanner, D.K. Bowen, *Phil. Mag. Lett.*, **74**, *211-216*, (1996)

Effect of Annealing on the Roughness and GMR of Fe/Cr Multilayers, H. Laidler, B.J. Hickey, T.P.A. Hase, R. Schad, Y. Bruynseraede, *J. Mag. Mag. Mat.*, **156**, *332-334,* (1996)

Magnetisation Process and Magnetic Properties of Co/Cr/Co Trilayers, H. Niedoba, B. Mirecki, M. Jackson, S. Jordan, S. Thompson, J.S.S. Whiting, P. Djemia, F. Garnot, P. Moch, T.P.A. Hase, I. Pape, B.K. Tanner, *Phys. Stat. Sol. (a)*, **158**, *259-264*, (1996)

Grazing Incidence X-ray Scattering Measurements of Interface Roughness in Sputtered Cu/Co Multilayers, B.K. Tanner, D.E. Joyce, T.P.A. Hase, I. Pape, P.J. Grundy, *Adv. X-ray Anal.*, **40**, *Cd-Rom,* (1997)

Grazing Incidence X-ray scattering for the Characterisation of InP Wafers, C.D. Moore, T.P.A. Hase, B.K. Tanner, *Adv. X-ray Anal.*, **40**, *CD-Rom,* (1997)

Crystallographic Texture and Interface Structure in Co/Cu Multilayer Films, D.E. Joyce, C.A. Faunce, P.J. Grundy, B.D. Fulthorpe, T.P.A. Hase, I. Pape, B.K. Tanner, *Phys. Rev. B.*, **58** (9), *5594-5601*, (1998)

Analysis of Grazing Incidence X-ray Diffuse Scattering from Cu/Co Multilayers, I. Pape, T.P.A. Hase, B.K. Tanner, M. Wormington, *Physica,* (1998)

Declaration

I hereby declare that the work contained in this thesis is my own and has not been submitted previously for any other degree. The work of collaborators is acknowledged at the appropriate point. In particular I would like to declare that the magnetometry results presented in chapters 8 and 9 are the work of C.H. Marrows, University of Leeds and similar measurements in chapter 7 were undertaken by P.A. Ryan and J. Xu, University of Leeds. Additionally, results pertaining to the coupling presented in chapter 6 were taken by collaborators, and their contributions are acknowledged. I would like to thank E. Ho and A.K. Petford-Long for the HR-TEM micrographs presented in this chapter.

The samples analysed in this thesis were obtained from the following sources;

Chapter 6:	S.M. Thompson, J.J. Freijo (within the framework of an ECHMC project)	*University of York*
Chapter 7:	J. Xu, M.J. Walker,	*University of Leeds*
Chapter 8 and 9:	C.H. Marrows	*University of Leeds*

Table of Contents

Chapter 1

Aim and Outline

1.1 Aim

The aim of this study was to use x-ray scattering techniques in order to study the interface morphology of magnetic multilayers. Since the late 1980s there has been much interest in the field of giant magneto-resistance (GMR) and oscillatory magnetic coupling in structures which contain magnetic layers separated by a non-magnetic spacer layer. It is now generally accepted that this giant magneto-resistance effect arises from spin dependent scattering mechanisms. The aim of this study was to attempt to isolate the roles of crystallinity and interface roughness on these scattering mechanisms, and thus relate the structure to the magneto-transport properties of the samples.

The thickness of the constituent layers within systems which exhibit GMR can range from sub-monolayer deposition to thicknesses in excess of a couple of hundred Ångstroms. The thickness of these samples makes them ideally suited to characterisation using x-ray techniques. Important structural parameters in defining the coupling and GMR within a sample are the thickness of the constituent layers, the roughnesses at the interfaces and the crystalline state of the sample. These parameters can be varied by changing the growth mode of the samples. As the crystallinity of the samples was usually well known, the relatively new technique of grazing incidence x-ray scattering was applied to the samples. The statistical nature of the surface was investigated by measuring the diffusely scattered radiation.

The samples used in this study were prepared by different techniques and were comprised of different materials. As there are no suitable growth facilities at the University of Durham, the samples were obtained from a variety of collaborations with researchers at other institutions. In the next section the origin of the samples is detailed, and the collaborators involved appropriately acknowledged.

1.2 The Samples

The data shown in chapter 6 were obtained from samples which were prepared under the auspices of a European Human Capital and Mobility Network. This network was set up to investigate the coupling in Co/Cr trilayers. Although the data obtained from only two sets of samples are presented in this thesis, many more samples were studied in the course of the research undertaken by the network. These data are not presented here because they do not contribute to a greater understanding of either x-ray scattering or magnetic coupling: these samples were studied with a view to other research aims. The samples for which the data are presented in this thesis were obtained from the ultra high vacuum facility at the University of York, and were prepared by Dr. S.M. Thompson and J.J Freijo.

The samples presented in chapter 7 et. seq. were prepared at the University of Leeds. In chapter 7, a series of samples prepared by Molecular Beam Epitaxy are studied. These samples were grown by J. Xu and M.J. Walker. In chapters 8 and 9, the samples originated from a newly commissioned magnetron sputtering source. These samples were prepared by Dr. C.H. Marrows.

1.3 Thesis Outline

In this section of chapter 1, an outline of the thesis will be presented.

Chapter 2 continues the introduction to the study of the samples by explaining the choice of grazing incidence x-ray scattering as the preferred method of characterisation. The latter half of chapter 2 introduces the reader to the history and concept of GMR.

Chapter 3 recounts the theoretical paradigms that relate to the scattering of x-rays by matter. Initially the scattering from a single, free electron is considered, and then scattering from atoms, and finally from non-ordered media. Fresnel's laws of transmission and reflection allow the simulation of specularly scattered x-rays to be calculated. Those x-rays which are not scattered into the specular condition give information about the lateral structure of the surface, and in this chapter it is shown how information about the surface can be obtained by careful modelling of this diffuse scatter.

Chapter 4 introduces the reader to synchrotron radiation, the source of all the x-rays used in this thesis. After a brief description of how synchrotron light is produced, a detailed look at the stations where the experiments were carried out is presented.

Chapter 5 continues the theoretical discussion begun in chapter 3. The need to use anomalous dispersion for x-ray scattering for samples were the electron density contrast between the layers is weak is highlighted. During the course of analysing the samples in chapter 6, it became apparent that the interfaces were interdiffused. It was clear that the existing theoretical statements required modification to allow for interdiffusion across interfaces to properly included. Such modifications to the theory were undertaken by M. Wormington (Bede Scientific Inc., USA). The resulting code has been shown to simulate the data very satisfactorily.

Chapter 6 is the first truly experimental chapter of this thesis, and details the results obtained from a full x-ray characterisation of a series of Co/Cr trilayers. The effects of the deposition temperature and applied field on the structure of the trilayers are analysed. The deduced interface structure is compared to a High Resolution Transmission Electron Microscopy (HR-TEM) study carried out at the University of Oxford by E. Ho and A.K. Petford-Long.

Chapter 7 discusses the results obtained from some Molecular Beam Epitaxy (MBE) grown Cu/Co multilayers. The effect of the deposition temperature of the multilayer as well as the buffer layer is analysed. The presence of two lateral length scales was detected in rocking curves obtained under grazing incidence and high angle diffraction conditions.

Chapter 8 describes and analyses the results from a series of sputtered Co/Cu multilayers which exhibit bi-quadratic coupling behaviour. The samples were studied with both conventional x-rays and soft x-rays. The soft x-rays are sensitive to the magnitude of the magnetic moment, and as such can be used to probe the magnetic super-structure at the same time as sampling the crystalline structure. This experiment is the first of this kind to be conducted by UK researchers and shows great potential.

The penultimate chapter, chapter 9, describes and analyses an initial study of spin valve structures using grazing incidence reflectivity and fluorescence. The fluorescence technique is used to elucidate the thickness of layers which cannot be evidenced in any other manner.

The thesis is summarised in chapter 10, which also contains an analysis of the findings, and indicates the most potentially valuable future research required in this field.

Chapter 2

Background

2.1 Introduction

This chapter continues the introduction to this thesis begun previously. In this chapter the reasons for studying the samples discussed and analysed in this thesis using grazing incidence x-ray scattering will be presented. The magneto-transport properties of magnetic multilayers are then discussed with special emphasis being placed on the effect known as giant magneto-resistance (GMR).

2.2 Review of Non-Destructive Structural Characterisation

In this section the choice of using grazing incidence x-ray scattering as the preferred method of characterisation is presented. An excellent review of structural characterisation is given by Brundle et. al. [1] and the reader is referred to this work for a detailed review of specific characterisation techniques.

There are various possible experimental techniques which can be used to study the surface and subsurface structure of materials. These can be classed as microscopy, electron scattering or scattering of neutrons, and x-rays. One of the most common methods of measuring surfaces is by the use of electrons. Electron diffraction is routinely used to monitor the nature of the surface during growth. However, it does not give a detailed statistical representation of the surface. It is further limited by its inability to measure buried interfaces. High energy electrons can be used to excite x-ray fluorescence or Auger yield, and this is the basis behind EDAX and Auger spectroscopy. These methods, although excellent at identifying constituent materials, are not sensitive to the lateral surface structure of the sample, but only to the bulk components of the materials under investigation.

Microscopy techniques are again an excellent method of imaging surfaces. However, by definition, the area of the sample that is measured by microscopy techniques is small. Atomic Force Microscopy can be used to define the fractal nature of surfaces, and image length scales from microns down to nanometres. However, this technique is highly surface sensitive and again this method cannot measure sub-surface structures. Scanning tunnelling microscopy techniques suffer for a similar reason. As will be seen in chapter 6, High Resolution Transmission Electron Microscopy (HR-TEM) can be used to image buried interfaces. HR-TEM is, however, a destructive technique which requires special sample preparation and, as such, cannot be routinely used in the characterisation of multilayer samples.

The only methods capable of studying buried interfaces, in a non destructive manner, rely on the scattering of x-rays and neutrons. Typical analysis of samples uses diffraction of the incident beams. These types of experiment are sensitive to the crystal lattice and give very accurate measures of coherent thickness and strain within samples. In order to investigate the statistical nature of the interfaces between materials in magnetic metallic multilayers, grazing incidence scattering is required. Although it is possible to conduct such experiments using neutron sources, the incident flux is extremely low when compared to synchrotron x-ray sources.

Grazing incidence experiments are thus a powerful, non-destructive tool that enable the surface and sub-surface structures of magnetic multilayers to be explored. The sample preparation is minimal, and the experiments can easily be carried out.

In the next section, the effects of oscillatory exchange coupling and GMR are presented.

2.3 Oscillatory exchange Coupling and Giant Magneto-resistance

The GMR effect is the phenomenon that describes large fractional changes to the resistance found to occur in some structures on the application of a large external field and is defined in equation 2.1:

$$GMR = \frac{\rho_0 - \rho_s}{\rho_s} \qquad [2.1]$$

In equation 2.1, ρ_o is the resistivity of the sample in zero field and ρ_s is that in a saturating applied field.

The observed changes in resistance are much larger than the normal changes in resistance found in most materials when a magnetic field is applied. There are several excellent recent review articles on the subject of GMR and oscillatory exchange coupling, and the reader is referred to these for a more detailed review of the phenomenon of GMR [2,3,4]. Only a brief over-view will be given here.

As the changes in the resistance are substantially larger than those found in normal materials, much of the driving force for the research in these new materials has come from the magnetic recording industry. Indeed, recently, new GMR read heads for hard disks have been manufactured using these new materials [5].

The original observations of an anomalous coupling effect were made in Fe/Cr systems. The first observations were made by Grunberg in 1986 [6]. In this 1986 paper, a series of Fe/Cr trilayers were investigated, and it was found that for certain thicknesses of chromium, the iron layers were coupled anti-ferromagnetically (AF). In the following couple of years it was observed that the resistivity of the AF coupled layers was reduced by a factor of approximately 2 on application of an external field large enough to saturate the samples and induce ferromagnetic (F) coupling [7]. In the same reference it was suggested for the first time that the GMR effect was caused by spin-dependent scattering.

Parkin [8] et. al. showed in 1990 that the AF alignment first observed in the Fe/Cr trilayers was not unique, and that similar alignments were found in multilayers of Co/Cr and Co/Ru, as well as, Fe/Cr. In addition it was also shown then that the resistance was oscillatory in nature, and was a function of the non-magnetic or spacer layer thickness. The AF alignment was also found in the early 1990s in Cu/Co systems as well as Fe/Ag and Fe/Al [9,10]. In a paper by Parkin [11] it was observed that the oscillatory nature of the coupling was quite general for transition metal spacer layers. A review article by Bloemen et. al. (1995) details the magnetic layer thickness dependence on the interlayer exchange coupling [12].

The experimental evidence for oscillatory coupling in transition metal multilayers outlined above was only observed in sputtered samples. It was not until 1992 that AF coupling was observed in (111) orientated Cu/Co multilayers prepared by molecular beam expitaxy (MBE) [13]. The GMR obtained in this sample was still significantly lower than that obtained on similar sputtered samples, and no evidence of oscillatory coupling as a function of spacer layer thickness was observed. However, oscillatory coupling was observed in (100) orientated Cu/Co multilayers by Egelhoff and Kief in 1992 [14].

There have been several attempts at explaining the oscillatory nature of the AF coupling from a theoretical viewpoint. Much of the theoretical work has been based on a Ruderman-Kittel-Kasuya-Yosida (RKKY) type interaction. The RKKY interaction describes the oscillatory nature of the exchange coupling between two magnetic impurities embedded in a metallic matrix [3]. When the RKKY interaction was first applied to multilayers exhibiting GMR, the predicted period of oscillation was too short. This was corrected by an "aliasing term" [15,16], and the first AF coupling peak was predicted for Cu thicknesses of 9Å. Other theories based on quantum confinement were also suggested [17]. Stiles predicts that the (100) coupling should be larger than the (111) based on a quantum well confinement model [18].

An electron travelling through a material is scattered by impurities or local lattice distortions. Such scattering results in resistance. The GMR effect is a result of the spin dependent nature of this scattering. In order to understand this effect more clearly it is useful to consider a density of states picture. As it is only electrons inhabiting states close to the Fermi energy that are scattered as they move through the material, it is only the *3d* bands of the transition metals that need to be considered. For a magnetic material a distinction must be made between electrons which have their spin aligned (spin up) and anti-aligned (spin down) to the magnetisation vector within the magnetic layer. The spin up electron band is more energetically favourable, and this band is therefore at a lower energy than the spin down band [19]. In a non-magnetic material, there is no such energy discrepancy and the density of states is equal for both spin directions. A schematic of the energy bands for a F and AF coupled system is shown in figure 2.1.

The current carrying electrons are provided by the broad, delocalised s-p hybridised conduction bands. As these electrons pass through the multilayer they experience the splitting of the *3d* bands. For electrons to move freely through a sample, there must exist free states into which they may be promoted. The spin-up electron band is below the Fermi surface of the material and as such is completely filled. However, the Fermi surface runs through the middle of the energy enhanced spin down band. In the non-magnetic spacer layer, both bands are below the Fermi surface. (figure 2.1 (a))

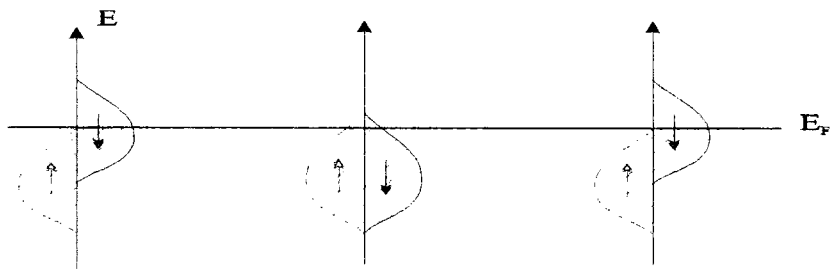

(a)

(b)

Figure 2.1: A schematic of the density of states for a ferromagnetically (a) coupled sample and an anti-ferromagnetically (b) coupled sample

In the ferromagnetic case, an electron with spin up will feel a very weak scattering potential whenever it traverses from the magnetic to the non-magnetic material. The opposite is true for the spin down electron where a large potential barrier due to the energy shift of the spin down band is present. The electron is therefore scattered at this interface. There are thus two currents present in the multilayer. The spin up electrons can travel freely through the sample, whereas the spin down electrons are scattered at each magnetic layer (figure 2.2 (a)). If the multilayer is coupled anti-ferromagnetically, however, the spin up electrons of one magnetic state become the spin down electrons for the next magnetic layer. In this way, both electron currents are scattered (figure 2.2 (b)):

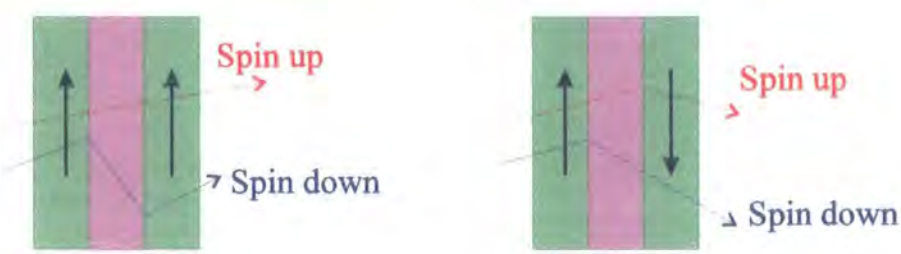

Figure 2.2: Scattering of the spin up and spin down electron currents for various coupling geometries

Using the scattering described in figure 2.2, it is possible to quantitatively model the GMR using a resistor model (figure 2.3). The scattering of an up electron is weak, and has a resistance defined as ρ_{up} and the scattering of a spin down electron is large and is defined as ρ_{down}.

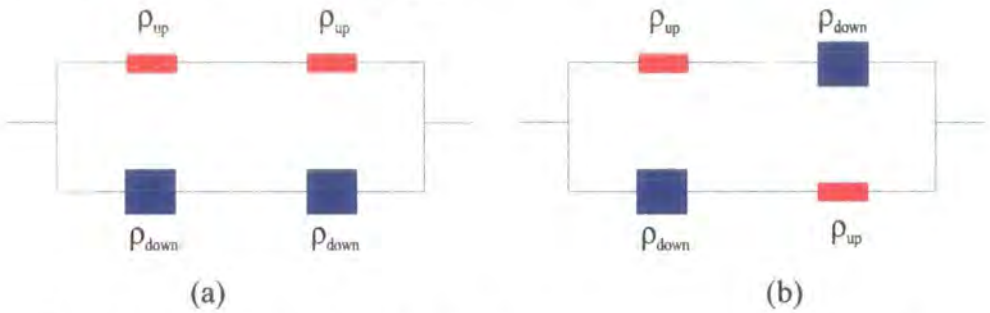

Figure 2.3: The resistor model of GMR for a ferromagnetically coupled (a) and anti-ferromagnetically coupled sample (b).

It is thus clear how the AF coupling in the multilayer induces the GMR effect. The strength of the applied field required to change the alignment from AF to F is a measure of the coupling strength, but not the magntiude of the GMR. The interface roughness generally increases the resistivity of the samples by increasing the amount of spin independent scattering. In certain circumstances it can also increase the spin dependent scattering due to localised scattering potentials.

References for Chapter 2

1 C.R. Brundle, C.A. Evans Jr., S. Wilson, *Encyclopedia of Materials Characterization: Surfaces, Interfaces and Thin Films,* **Butterworth-Heinemann**, (1992)

2 J. Mathon, *Contemporary Physics,* **32** (3), *143-156*, (1991)

3 S.S.P. Parkin in *Ultrathin Magnetic Structures II*, **Springer-Verlag,** (1994)

4 A. Fert, R. Morel, A. Barthélémy, V. Cros, J.-L. Duvail, J.-M. George, F. Parent, F. Petroff, C. Vouille, *J. Phys. IV France,* **7**, *C6-151-C6-161*, (1997)

5 *http://www.research.ibm.com/research/grm.html*

6 P. Grunberg, R. Schreiber, Y. Pang, M.B. Brodsky, H. Sowers, *Phys Rev. Lett.*, **57** (19), *2442-2445*, (1986)

7 M.N. Baibich, *Phys. Rev. Lett.* **61** (21), *2472-* (1988)

8 S.S.P. Parkin, N. More, K.P. Roche, *Phys. Rev. Lett.*, **64** (19), *2304-2307*, (1990)

9 J.J. de Miguel, A. Cebollada, J.M. Gallego, R. Miranda, C.M. Schneider, P. Schuster, J. Kirschner, *J. Magn. Mag. Mat.*, **93**, *1-9,* (1991)

10 A. Fuß, S. Demokritov, P. Grunberg, W. Zinn, *J. Magn. Mag. Mat.*, **103**, *L221-L227*, (1992)

11 S.S.P. Parkin, *Phys. Rev. Lett.* **67** (25) *3598-3601*, (1991)

12 P.J.H. Bloemen, M.T.H. van de Vorst, W.J.M. de Jonge, M.T. Johnson, R. Coehoorn, *Modern Phys. Lett. B*, **9** (1), *1-25*, (1995)

13 D. Greig, M.J. Hall, C. Hammond, B.J. Hickey, H.P. Ho, M.A. Howson, M.J. Walker, N. Wiser, D.G. Wright, *J. Magn. Mag. Mat.,* **110**, *L239-L246*, (1992)

14 W.F. Egelhoff Jr., M.T. Kief, *IEEE Trans. Mag.,* **28** (5), *2742-2744*, (1992)

15 P. Bruno, C. Chappert, *Phys. Rev. Lett.*, **67** (12), *1602-1605*, (1991)

16 P. Bruno, C. Chappert, *Phys. Rev. B.,* **46** (1), *261-270*, (1992)

17 J. Mathon, M. Villert, D.M. Edwards, R.B. Muniz, *J. Magn. Mag. Mat.,* **121**, *242-247*, (1993) and references therein

18 M.D. Stiles, *Phys. Rev. B.*, **48** (10), *7238-7258*, (1993)

19 J. Smits, *Physics World,* November 1992

Chapter 3

The Interaction of X-rays with Matter in Low Angle Regimes

3.1 Introduction

This chapter is concerned with the theoretical arguments that relate to the interaction of x-rays with matter. The most common experimental geometry for x-rays is diffraction. The general theory pertaining to this large area of experimental research will not, however, be discussed in this chapter, which is concerned only with the narrower field of the theory relating to grazing incidence scattering. The aim of the chapter is to clarify the theoretical paradigms which underpin all the experimental work which forms the basis of the other chapters of the current study.

The chapter will first introduce the reader to the scattering of x-rays from a free electron (section 3.2). This is then expanded to describe the scattering from an atom (3.2.1). The concept of reciprocal space (section 3.3) is introduced, and a clarification of the methods used in scanning reciprocal space is presented in section 3.4. A discussion of the reflection and transmission properties of x-rays as they pass through a stratified sample is shown in (section 3.5). This latter section is then developed further to allow a discussion of the effects of roughness on the reflectivity (section 3.5.1) Section 3.6 presents the theoretical background to specular reflection: a method of modelling of specular scatter based on Fresnel's Laws of reflection and transmission is then presented. As part of the discussion of diffuse scattering (section 3.7), the Born Approximation (section 3.7.1) and the Distorted Wave Born Approximation (section 3.7.2) are reviewed. An introduction to diffuse scattering from a single surface is given in section 3.8. When multiple layers are present, the effects of out of plane correlations of the roughness need to be considered. Methods of modelling such correlations are presented in section 3.9. The effects of such out of

plane correlations on the distribution of diffuse scatter in reciprocal space is demonstrated in section 3.10 by a series of simulated full reciprocal space maps. A method for calculating the roughness without recourse to detailed simulation is then introduced (section 3.11). The chapter is concluded by a summary, in section 3.12.

3.2 X-ray Scattering from a Single Electron

The scattering of a single electron can be considered in terms of dipole oscillations. The electron is forced into oscillations by the accelerating electric field of the incident radiation [1]. If the incident x-ray beam is assumed to be a spherical wave, the scattered radiation is also of the same form but with a phase shift of π occurring on scattering. The radiated electric field strength can be shown to be (in c.c.s units) [2]:

$$E_{Rad}(r,t) = -\left(\frac{e^2}{mc^2}\right)\left(\frac{1}{r}\right)E_0 \exp\left[i(k \cdot r - \omega t)\right] \qquad [3.1]$$

The first term in equation 3.1, $\left(e^2/mc^2\right)$ is the scattering power, or the scattering length of the free electron and is referred to as the Thomson scattering length. Its numerical value is 2.82 $*10^{-3}$ Å. The minus sign in equation 3.1 is due to the phase shift that occurs on scattering. For an incident x-ray beam of intensity I_0, the intensity scattered is [3]:

$$I_s = I_0\left(\frac{e^2}{mc^2}\right)^2\left(\frac{P}{R^2}\right) \qquad [3.2]$$

In equation 3.2, P is a polarisation factor and R is the distance of the observer from the particle.

3.2.1. X-ray Scattering from an Atom

In the discussion of the theoretical basis for Thomson scattering from a free electron in the previous section, the position of the electron was taken as fixed. In order to derive the total scattering from an atom, however, it is important to remember that the electrons do not, in fact, scatter with the same phase. Scattering from an atom can be interpreted as due to an atom in which the individual electrons are smeared into a continuous distribution. The number of electrons per unit volume is defined by ρ. The atomic number, Z is thus the integration of this smeared distribution over the volume of the atom:

$$Z = \int_V \rho(r)\, dV \qquad [3.3]$$

It can be shown that the atomic scattering factor is the Fourier transform of this electron density [4,5]:

$$f = \int_V \rho(r) \exp[ik \cdot r]\, dV \qquad [3.4]$$

Here $\rho(r)dV$ is the probability that an electron exists in the volume element dV.

The discussion above is restricted to atoms which are away from any absorption edges in the material. At an absorption edge, additional resonance effects cause the phase change on scattering to be slightly different from π, and the magnitude of the scattering factor is not what is given above [2]. When this is the case, the atomic scattering factor becomes modified and anomalous dispersion effects must be calculated. These effects are calculated in chapter 5.

3.3 Reciprocal Space

In the previous section, it was seen that the scattering of x-rays from atoms is proportional to the Fourier transform of the electron density. When the atoms are placed in a crystal, this electron density is periodic. As a result it makes sense to work in Fourier or reciprocal space where any periodic function will be represented by a point. Even when the samples are not crystalline it is still useful to work in reciprocal space because, as will be shown later, the x-ray scattering is also sensitive to the Fourier transform of the lateral roughness lengthscale. It therefore makes sense to consider x-ray scattering in such a reciprocal geometry

The reciprocal lattice is made up of three primitive vectors, $\boldsymbol{b_1}$, $\boldsymbol{b_2}$, $\boldsymbol{b_3}$ which are related to the three basis vectors of the real lattice, $\boldsymbol{a_1}$, $\boldsymbol{a_2}$, $\boldsymbol{a_3}$. The three reciprocal vectors are defined [6]:

$$b_1 = \frac{a_2 \times a_3}{a_1 \cdot a_2 \times a_3} \qquad b_2 = \frac{a_3 \times a_1}{a_1 \cdot a_2 \times a_3} \qquad b_3 = \frac{a_1 \times a_2}{a_1 \cdot a_2 \times a_3} \qquad [3.5]$$

Vectors in the real lattice have the dimensions of length, and in this reciprocal lattice have the dimension of inverse length. Thus spatial frequencies in real space are converted to points in the reciprocal lattice. The direction of a point in reciprocal space is the same as the direction that the frequency was propagating in real space.

The scattering vector is defined as the difference between the incident and scattered wavevectors. The use of a vectorial map enables the transforms between real and reciprocal space to be calculated. Such a vectorial map is shown in figure 3.1:

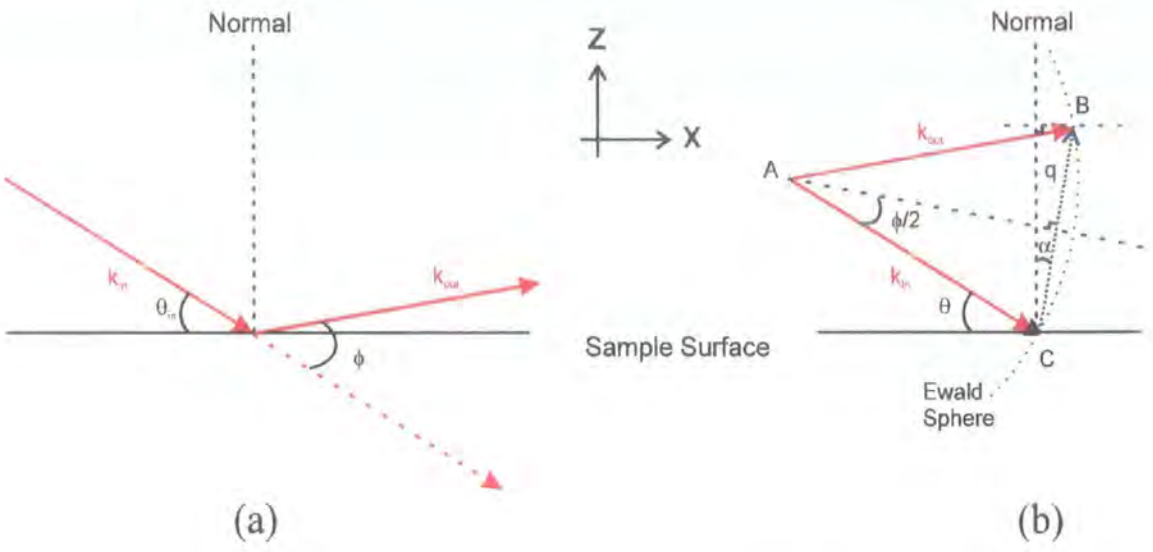

Figure 3.1: A vector map showing the relation between real (a) and reciprocal (b) space

In figure 3.1, the incident wave vector is defined by the sample angle, θ. The exit wave vector is defined by the scattering angle, ϕ. For elastic scattering the modulus of the two wavevectors is the same, thus $|k_{in}| = |k_{out}| = |k| = 1/\lambda$. The scattering vector, $\boldsymbol{q}$, is then simply $q = \frac{2}{\lambda}\sin\left(\frac{\phi}{2}\right)$. The out of plane ($z$) and in plane ($x$) components can easily be expressed in terms of the angle α. The transformations are therefore:

$$q_z = \left(\frac{2}{\lambda}\right)\sin\left(\frac{\phi}{2}\right)\cos(\alpha) \quad \text{and} \quad q_x = \left(\frac{2}{\lambda}\right)\sin\left(\frac{\phi}{2}\right)\sin(\alpha) \qquad [3.6]$$

where $\alpha = \left(\theta - \frac{\phi}{2}\right)$.

The third component of the scattering vector is also present, but an additional axis is required to sample it.

The discussions detailed thus far in this chapter are the prelude to any further development of theoretical ideas regarding the interacting of x-rays with matter. For discussions on diffraction, the ideas of periodic scattering potentials and the symmetry of the atomic unit cell could now be discussed in detail. The theory of diffraction will not be discussed here and the reader is referred to a range of texts which deal with this area specifically [4,5,7]. However the results in this study are not directly related to diffraction phenomenon and from this point onwards the theoretical ideas presented in this chapter are for those relating to the scattering of x-rays from materials under grazing incidence regimes. With the exception of grazing incidence diffraction, x-rays in this region are not sensitive to the periodic arrangement of the atoms and the scattering potential can be assumed to be constant and defined by the refractive index of the medium through which the x-rays are passing.

Prior to a review of the theory for x-ray scattering the next section details the types of scans used to probe the x-ray scattering in this grazing incidence regime.

3.4 Scanning Methods in Real and Reciprocal space

With the samples considered in this study, it is only necessary to probe reciprocal space in two dimensions. With a two circle diffractometer this is easily achieved; however, for more complex reciprocal space mapping, it is sometimes necessary to have an accurate chi/phi circle. In nearly all cases the detector is scanned out of plane, but sometimes it is advantageous to scan the detector out of the scattering plane and thereby probe the scattering as a function of q_y.

If the transforms between real and reciprocal space are recalled, (equation 3.6), it can be seen how reciprocal space can be probed in two dimensions. Both transforms have a common factor, $\left(2/\lambda\right)\sin\left(\phi/2\right)$, which is only dependent on the detector angle, and the difference between the in plane and out of plane components depends solely on δ. The component of reciprocal space normal to the surface, q_z, can

be probed if δ is 0. This occurs at the specular condition, i.e. $\theta = \phi/2$, q_x=0. A scan where the detector and sample angle are coupled in a ratio of 2:1 would therefore probe only q_z. This scan probes the specular scatter as a function of q_z and is referred to either as a specular scan or as a $\theta/2\theta$ scan.

Scanning the in-plane component of reciprocal space is similarly simple. q_x is explored by fixing the detector angle, and scanning the sample from zero to the detector angle. This type of scan is referred to as a transverse diffuse scan or a rocking curve. Although there is a slight dependence on q_z in this scan, the effect is negligible, and the scan can be considered to be probing q_x only.

It is also important to probe the diffuse scatter as a function of q_z, for fixed values of q_x. A scan similar in nature to the specular scan is required. The value of q_x is selected by off-setting the sample from the specular position by a small amount. The two axes are then scanned in a 2:1 coupled motion. In reciprocal space such a $(\theta + \Delta)/2\theta$ scan maps out as a straight line. These scans are often referred to as longitudinal diffuse scans.

The angular positions of the sample and detector during the real space scans described above were used to calculate their motion in reciprocal space. The limit of observation is due to the incident and scattered x-rays being below the sample surface. Sample scans were simulated for silicon with the detector set to angles of 2 and 4 degrees, and the offset angle for the longitudinal scan was -0.1°. The results of this calculation are shown in figure 3.2:

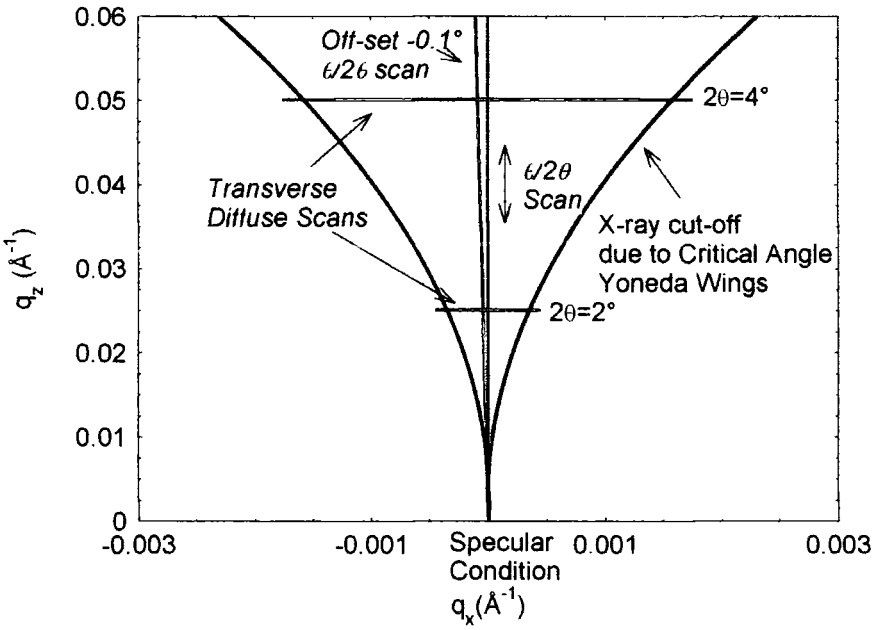

Figure 3.2: Reciprocal space representation of the experimental scans

It can be seen that by a combination of the above scans, a two dimensional reciprocal space map can be produced. In most cases, it is not necessary to go to the lengths of recording the scatter from the whole of reciprocal space. A typical data set for a given sample would include a specular scan, a longitudinal scan and at least two transverse diffuse scans for each wavelength used.

3.5 Scattering of X-rays from Surfaces and Interfaces

As x-rays are a form of electromagnetic radiation, their propagation through media is defined by Maxwell's equations. For x-rays to propagate between two media of differing refractive indices, the tangential components of their electric and magnetic fields (and their derivatives) must be continuous across the interface [8]. This is equivalent to matching their amplitude and gradient of the incident plane wave at the interface. This section starts with an introduction to x-ray scattering at grazing incidence. Snell's law and Fresnel's Law are then introduced in order to explain the effects of layers on substrates.

The refractive index for a medium is defined as a complex number [9]:

$$n = 1 - \delta - i\beta \qquad [3.7]$$

Here δ and β are small positive numbers. δ is related to the dispersion within the medium, and β is proportional to the absorption. They are defined as:

$$\delta = \frac{N_A}{2\pi} r_o \lambda^2 \sum_j \frac{\rho_j}{A_j} (Z_j + f_j') \qquad [3.8]$$

and

$$\beta = \frac{N_A}{2\pi} r_o \lambda^2 \sum_j \frac{\rho_j}{A_j} f_j'' \qquad [3.9]$$

All the units are defined in c.c.s units, and N_A is Avogadro's number, λ is the wavelength (in cm), and r_o is the classical electron radius ($2.818*10^{-13}$ cm). ρ_j, is the density of element j and A_j is its atomic mass. f' and f'' are corrections to the atomic scattering factor that are required near absorption edges. These correction terms are discussed in greater detail in chapter 5. The calculated values of δ and β for various elements for a wavelength of 1.54Å are tabulated in table 3.1:

Element	**At. Number**	**δ**	**β**
C	6	$1.12*10^{-5}$	$1.68*10^{-8}$
Cu	29	$2.43*10^{-5}$	$5.30*10^{-7}$
U	92	$4.50*10^{-5}$	$6.87*10^{-6}$

Table 3.1 Values of δ and β for three elements calculated for λ=1.54Å

As δ and β are positive, x-rays impinging onto a surface or interface are refracted away from the normal. This is shown schematically in figure 3.3:

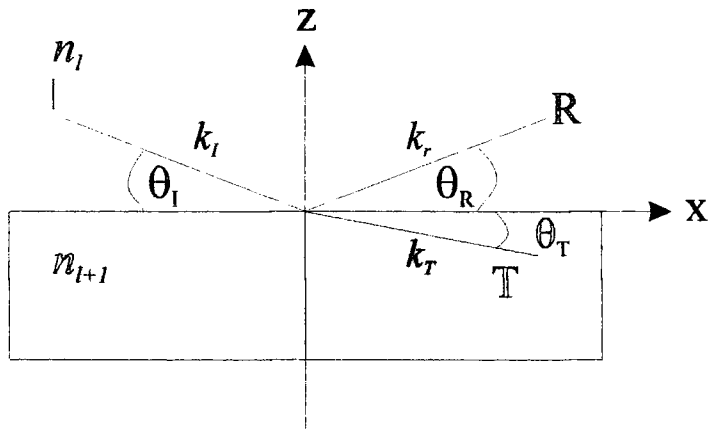

Figure 3.3: An incident plane wave, *I*, is reflected (*R*) and transmitted (*T*) at an interface between two layers, *l* and *l+1* where the refractive index changes discontinuously from n_l to n_{l+1}.

The fact that the refractive index is slightly less than unity means that there exists a critical angle, θ_c for which θ_R is zero (with n_l=1). This critical angle is the angle for total external reflection. In order to derive an expression for the critical angle in terms of δ and β, it is important to recall the definition of Snell's Law.

The three x-ray beams in figure 3.3 can be considered to be three plane waves which are all of the same form and are characterised by a phase, k_j and an amplitude C_j:

$$\psi_j = C_j \exp\left(ik_j \cdot r\right), \text{ where } j=I,\ R \text{ and } T \qquad [3.10]$$

and

$$k = \frac{|k_I|}{n_l} = \frac{|k_R|}{n_l} = \frac{|k_T|}{n_{l+1}} \qquad [3.11]$$

Where k is the wavevector in a vacuum. The coefficients, C_j, are related and can be obtained from the continuity requirements on ψ, and its derivative, $\nabla\psi$, namely;

$$C_I + C_R = C_T \qquad [3.12]$$

and $$C_I k_I + C_R k_R = C_T k_T \qquad [3.13]$$

Snell's law follows directly by expressing the surface (x) component of equation [3.13] explicitly along with equations [3.12] and [3.11]:

$$n_l \cos\theta = n_{l+1} \cos\theta_T \qquad [3.14]$$

The critical angle is now defined as:

$$\cos\theta_c = {}^{n_{l+1}}\!/_{n_l} \qquad [3.15]$$

A simple rearrangement of equation 3.15 assuming no absorption ($\beta=0$) and using equation [3.7] relates the critical angle to δ:

$$\theta_c = \sqrt{2\delta} \qquad [3.16]$$

Above this critical angle, the x-rays penetrate into the medium, and for a perfect interface the amplitude of the reflected and transmitted waves is governed by Fresnel's laws. Fresnel's equations can be derived by matching the z component of equation [3.7] and using the definition $k_{I,z} = -k_{R,z} = k_{l,z}$ and $k_{T,z} = k_{l+1,z}$. This leads to the derivation of Fresnel's laws for the reflectance, F_l^R and transmission F_l^T across the interface in terms of the normal, z, component of the wavevector:

$$F_l^R = \frac{\left(k_{l,z} - k_{l+1,z}\right)}{\left(k_{l,z} + k_{l+1,z}\right)} \qquad F_l^T = \frac{2k_{l,z}}{\left(k_{l,z} + k_{l+1,z}\right)} \qquad [3.17]$$

Fresnel's equations can be expressed in terms of the angles θ and θ_T by expressing the z component explicitly, and using Snell's law:

$$k_{l,z} = |k_l| \sin\theta = k n_l \sin\theta \qquad [3.18]$$

and similarly for $k_{l+1,z}$ giving, in the small angle limit:

$$F_l^R \approx \frac{\theta - \theta_T}{\theta + \theta_T} \qquad F_l^T \approx \frac{2\theta}{\theta + \theta_T} \qquad [3.19]$$

The polarisation dependence of the Fresnel coefficients is weak due to the fact that the refractive index differs from unity by only one part in 10^6. The transmitted amplitude is damped exponentially in the negative z direction due to absorption within the media. Above the critical angle therefore, the penetration depth of the x-rays is defined by β. Below the critical angle, θ_T is complex. Even though the x-rays are totally reflected from the surface, they still penetrate a small distance into the sample. The penetration depth of this evanescent wave is mainly dependent on the electron density of the surface material. The penetration depth of this evanescent wave is in the range of 20 to 100Å. Figure 3.4 shows the calculated penetration depth as a function of sample angle for two incident wavelengths for the element silver. The energy dependence of the critical angle (defined in equation 3.9) is also clear.

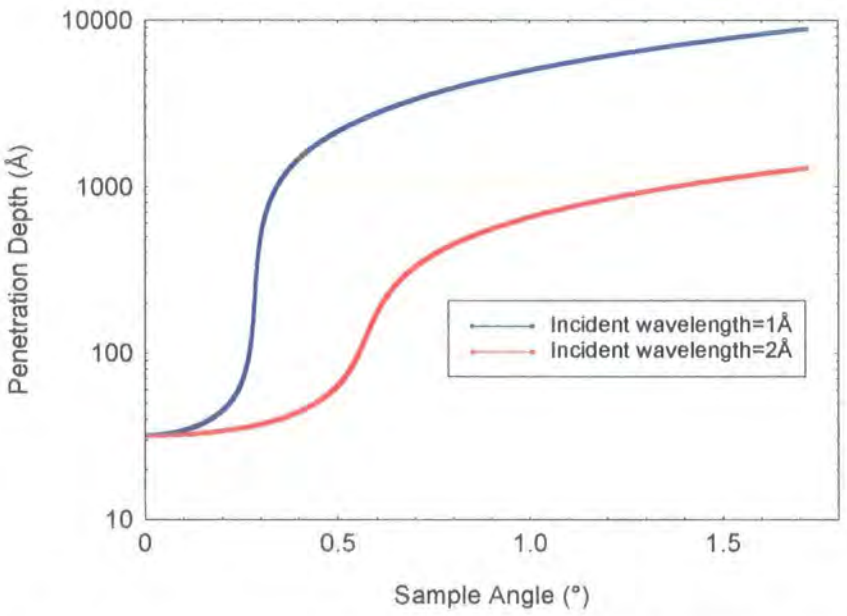

Figure 3.4: The calculated penetration depth as a function of sample angle for Ag.

The calculated depth of the evanescent wave for silver was 32Å, and this illustrates the inherent surface sensitivity of x-ray techniques for sample angles

below the critical angle. The variation of the penetration depth with sample angle shows that a degree of depth sensitivity is also possible using grazing incidence x-ray techniques. This is the basis of depth profiling using x-ray fluorescence and is discussed in greater detail in chapter 9.

Fresnel's laws not only describe the reflection and transmission from a single surface, they can be used to describe the reflections in more complex structures. Parratt [10] derived a recursive relation which describes the total reflection from a multi-planar system such as that shown schematically in figure 3.5:

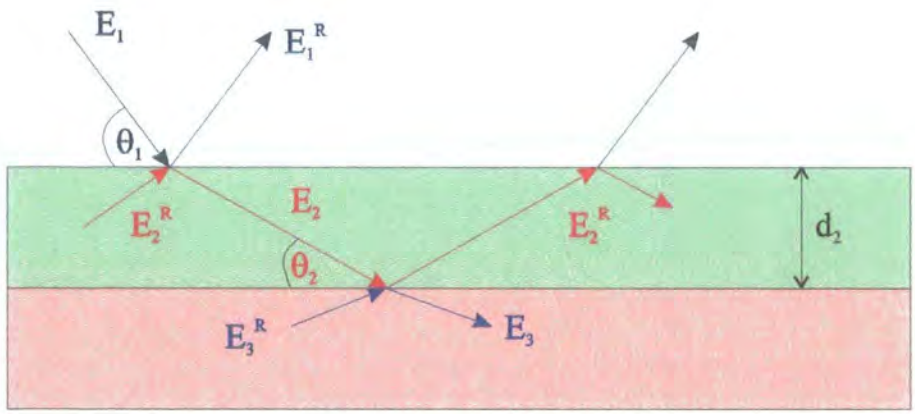

Figure 3.5: The electric field vectors of x-rays passing through a multi-planar system

Following Parratt, the matching of the tangential vectors, E, across the interface yields the continuity equation:

$$a_{l-1}E_{l-1} + \frac{E^R_{l-1}}{a_{l-1}} = \frac{E_l}{a_l} + a_l E^R_l \qquad [3.20]$$

where a_l is the phase factor for half the layer thickness, d_l, defined as:

$$a_l = \exp\left(-\frac{ikf_l d_l}{2}\right) \qquad [3.21]$$

here f_l is a function related to δ, β and the incident angle, θ.

$$f_l = \left(\theta_1^2 - 2\delta_l - 2i\beta_l\right)^{1/2} \qquad [3.22]$$

In equation 3.20, the vector amplitudes are defined in the middle of the layer. The solution to equation 3.20 and its derivative results in a recursive formulation which results in the reflection amplitude, R, for each interface:

$$R_{l-1,l} = a_{l-1}^{4}\left[\frac{R_{l,l+1} + F_{l-1,l}^{R}}{R_{l,l+1}F_{l-1,l}^{R} + 1}\right] \qquad [3.23]$$

where

$$R_{l,l+1} = a_{n}^{2}\left[\frac{E_{l}^{R}}{E_{l}}\right] \qquad [3.24]$$

and $F_{l-1,l}^{R}$ is the Fresnel reflection coefficient, here defined in terms of equation 3.22 to be:

$$F_{l-1,l}^{R} = \frac{(f_{l-1} - f_{l})}{(f_{l-1} + f_{l})} \qquad [3.25]$$

The solution of the recursive formula is achieved by starting at the bottom of the system, where the last layer is assumed to be semi-infinite. As there is no reflected wave entering this layer from below, $R_{l,l+1} = 0$. The ratio of the reflected to the incident intensity, as shown in figure 3.5, is simply defined as:

$$\frac{I_{R}}{I_{0}} = \left|\frac{E_{1}^{R}}{E_{1}}\right|^{2} = \left|R_{1,2}\right|^{2} \qquad [3.26]$$

The reflection amplitude of a surface can also be calculated using a matrix method [11].

3.5.1 The Effects of Roughness on the Reflectivity Signal

Real surfaces and interfaces contain roughness. This roughness can consist of atomic randomness, or gradients in the electron density normal to the surface. The effects of the roughness can be calculated using perturbation techniques. The simplest method to calculate roughness and its effects is to replace the rough surface by an ensemble of flat surfaces with a distribution about an average surface position. If this distribution is Gaussian in nature with a standard deviation, σ, the Fresnel coefficients for a single surface are modified by the inclusion of an exponential damping term:

$$R = F_l^R \exp\left(-q_z^2\sigma^2\right) \qquad [3.27]$$

A more general form for the modification of the Fresnel coefficients for the reflection between two media, *l* and *l-1*, was derived by Névot and Croce [12]:

$$R = F_l^R \exp\left(-\frac{k_l k_{l-1}\sigma_l^2}{2}\right) \qquad [3.28]$$

Here again, the RMS roughness of the interface is defined as σ. k_l and k_{l-1} are the wavevectors in medium *l* and *l-1* respectively. When these modified Fresnel coefficients are used in the recursive formalism of Parratt [10], equation 3.25 becomes:

$$F_{l-1,l}^R = \frac{(f_{l-1} - f_l)}{(f_{l-1} + f_l)}\exp\left(-\frac{k_l k_{l-1}\sigma_l^2}{2}\right) \qquad [3.29]$$

Equation 3.29 along with equation 3.23 are all that is required to calculate the specular reflection from a single surface or a layered structure. In the next section, some examples of specular reflectivity will be presented. The effects of roughness will be evidenced, and the nature of the interference terms resulting from layers within a multi-layered sample will be discussed.

3.6 Specular reflection

Figure 3.6 shows simulated specular scans for a silicon substrate. Three simulations with differing interface roughness are shown.

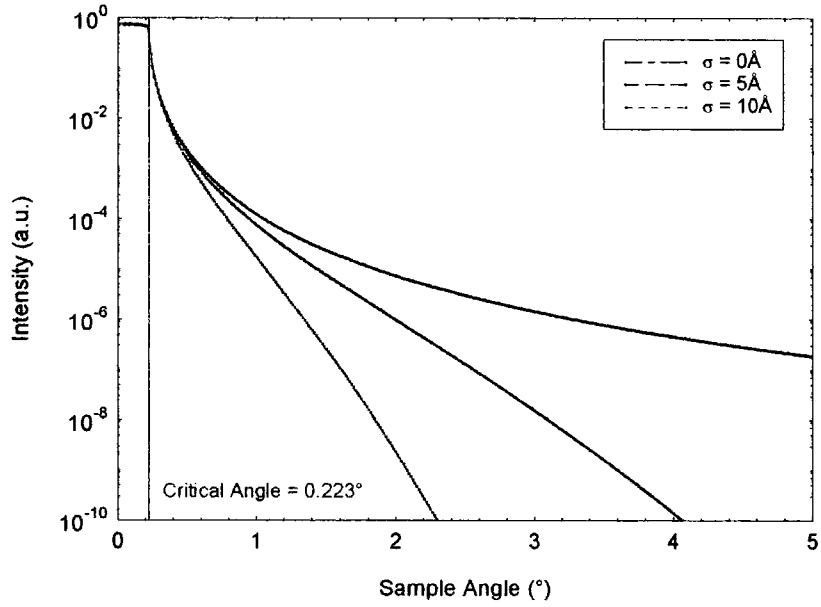

Figure 3.6: Simulated reflectivity curve for Si (λ=1.54Å) for interface roughness, σ=0, 5, 10Å

Immediately apparent in figure 3.6 is the sharp decrease in intensity of the specular scatter after the critical angle. The rate of fall-off for sample angles greater than approximately 0.5° increases as the roughness rises. However, for angles less than the critical angle, there is no difference between the simulations. In this region the incident x-rays are totally externally reflected, and the reflected intensity is constant. This is a feature of the model which essentially describes the roughness as a graded electron density normal to the surface. For real roughness, intensity would still be scattered out of the specular condition in the total reflection regime. For the simulation with zero roughness, the rate of fall-off varies as the fourth power of the sample angle. This simple relation between the sample angle and the intensity is only valid for sample angles greater than about twice the critical angle. Deviations from this power law close to the critical angle are due to refraction effects in this region. When roughness is present, the rate of fall off of the specular scatter is increased and

the intensity no longer scales as a simple power law. Figure 3.7 shows the same simulations that are represented in figure 3.6, but in this case the intensity has been multiplied by the fourth power of the sample angle.

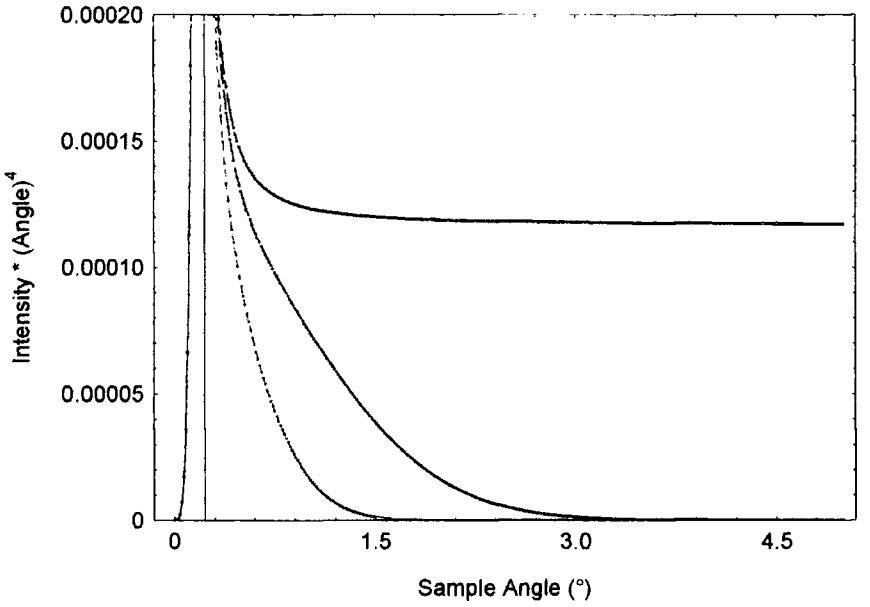

Figure 3.7: Specular simulations for a Si substrate multiplied by the forth power of the sample angle. The roughnesses are the same as those in figure 3.6

When a layer is deposited onto a substrate interference between waves reflected at the sample surface and from the substrate form a series of fringes in the observed specular scatter. These thickness fringes are commonly referred to as Kiessig fringes [13]. The period of these fringes is related to the thickness of the layer via Bragg's Law, which in the small angle approximation is:

$$d = \frac{\lambda}{2\Delta\theta} \qquad [3.30]$$

where $\Delta\theta$ is the period of the Kiessig fringes in radians. Refraction effects effect the period of the fringes, and as a consequence equation 3.30 is only valid for angles away from the critical angle. The amplitude of these Kiessig fringes is dependent on the electron density difference between the layers and the roughness on the interface between them.

Figure 3.8 shows a series of simulations of a 200Å cobalt layer deposited on a silicon substrate. The roughness of the substrate, as well as, the surface roughness are described. A comparison of figure 3.8 (a) and (b) shows that the amplitude of the Kiessig fringes is sensitive to the roughness of either interface. In addition to the reduction in Kiessig fringe amplitude, there is a subtle difference in the shape of the reflectivity curve between figures 3.8 (a) and (b). The roughening of the substrate has little effect for small sample angles, and its effects are greater at high sample angles. The opposite is true when the top surface is roughened. The effect on the shape of the specular scatter by roughening the substrate is evident in figure 3.8 (c) and (d) where a greater fall-off in intensity for high sample angles is observed as the substrate roughness increases from σ_{Si}=0Å in figure 3.8(a) to σ_{Si}=5Å for 3.13(c) and finally σ_{Si}=10Å for 3.13(d).

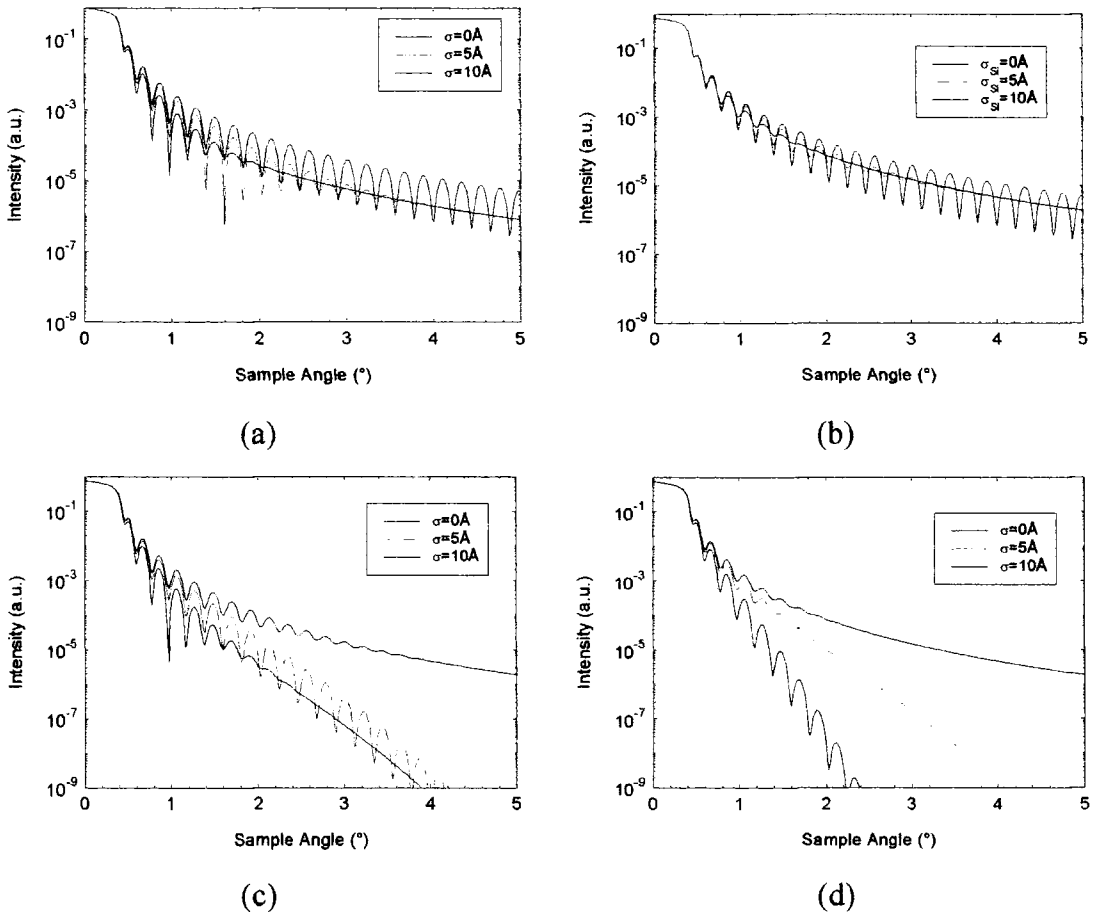

Figure 3.8: Specular simulations for a single 200Å layer of cobalt deposited on Si with σ_{Si}=0Å (a), σ_{Si}=5Å (c), σ_{Si}=10Å (d) with cobalt roughnesses as inset in legend. Example (b), σ_{Co}=0Å with silicon roughness as inset in legend.

The addition of more and more layers into the sample results in an ever more complex reflectivity signal. The final observed interference pattern is a super-position of the interference generated from all of the layers present in the sample. The addition of only a few layers can result in very complex reflectivity patterns. This complexity is evidenced in the work by Banerjee et. al. [14] and the results contained in chapters 6 and 9. Matters are somewhat simplified when a periodic multilayer is considered. For such a simple multilayer, the interference in the reflectivity signal is then made up of two components. Interference between waves scattered at the surface and substrate interfaces result in Kiessig fringes corresponding to the total sample thickness. The bi-layer repeat acts as a crystal with a large, out of plane lattice spacing, d and as such, the interference from the multilayer is defined by Bragg's Law, and constructive interference only occurs at specific sample angles which are defined according to Bragg's Law - $n\lambda = 2d\sin\left(\phi/2\right)$. The simulated reflectivity profile from a Co/Pt multilayer deposited on Si is presented in figure 3.9.

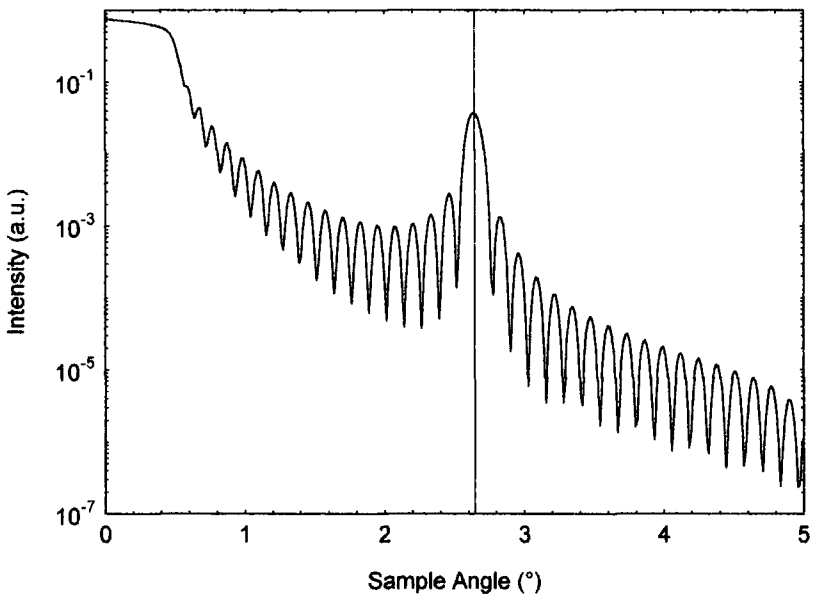

Figure 3.9: The simulated reflectivity profile from a 20 period Co/Pt multilayer deposited on Si. All roughnesses were 1Å, and the bi-layer thickness is 17Å.

3.7 Diffuse Scatter

The Debye-Waller factor that describes the roughness in the specular scatter cannot be used to model the diffuse scatter. The roughness must be modelled in a more mathematical manner. Any model of the roughness must be able to take into account the effects of both in and out of plane correlations of the roughness, as well as, accurately describing the statistical nature of the interface. Before describing such a model, it is important to discuss briefly the two approximations that are used in defining the differential cross section, $d\sigma/d\Omega$. The first is discussed in section 3.7.1 and is the Born approximation. The Born approximation is a specific use of Fermi's Golden Rule for the two wave case. A major problem with the Born wave approximation is that it fails to allow for multiple scattering events occurring in the sample. The Born wave assumes weak interactions and, as such, the reflected wave must be small and thus the Born wave approximation is invalid for angles in the vicinity of the critical angle. These problems can be overcome by using the distorted wave Born approximation (DWBA). The DWBA is discussed in greater detail in section 3.7.2.

3.7.1 Born Wave Approximation

The Born wave is a method for obtaining approximate predictions for the differential cross section that describe the way a potential *V(r)* scatters radiation into 3 dimensions. In the Born approximation, it is assumed that there are two plane waves involved. The form of the scattering potential is simply a constant within the medium defined as $V = k_0^2(1-n^2)$ where n is the refractive index, and k is the wavevector.

$$V(r) = \begin{cases} 0, & \text{r > slab dimensions} \\ \text{constant} & \text{r < slab dimensions} \end{cases} \qquad [3.31]$$

Under such a system the differential cross section can be written [15]:

$$\frac{d\sigma}{d\Omega} = N^2 b^2 \int_V dr \int_V \exp[-iq \cdot (r - r')]\,\mathrm{d}r' \qquad [3.32]$$

Here N is the number density of the particles which are scattering and b is the coherent scattering length which for x-rays is the Thomson scattering length, $b = e^2/mc^2$. The differential equation in equation 3.32 can be re-written as a surface integral by utilising Stoke's theorem. It can be shown that the differential cross section can then be written as [15]:

$$\frac{d\sigma}{d\Omega} = \frac{N^2 b^2}{q_z^2} \iint_{S_o} dxdy \iint_{S_o} \exp\left(-iq_z[z(x,y) - z(x',y')]\right) \exp\left(-i\left[q_x(x-x') + q_y(y-y')\right]\right) dx'dy' \qquad [3.33]$$

In equation 3.33, the vector $\boldsymbol{r}$ in equation 3.32 has been written in its in plane (x,y), and out of plane z(x,y) components. If the out of plane components can be described as a Gaussian random variable, it is then possible to express the out of plane component as:

$$\left\langle [z(x',y') - z(x,y)]^2 \right\rangle = g(X,Y) \qquad [3.34]$$

where $(X,Y) = (x' - x, y' - y)$. The differential cross section can now be written in terms of the illuminated area, $L_x L_y$:

$$\frac{d\sigma}{d\Omega} = \frac{N^2 b^2}{q_z^2} L_x L_y \iint_{S_o} dXdY \exp\left[-q_z^2 g(X,Y)\right] \exp\left[-i\left(q_x X + q_y Y\right)\right] \qquad [3.35]$$

It is now possible to obtain an explicit expression for the differential cross section for various models of the height difference function, $g(X,Y)$.

Sinha et. al. [15] introduced the idea of treating the surface using a Fractal description of the height difference function, namely $g(X,Y) = A(X,Y)^h$. The texture of the surface is then defined by the fractal exponent h; a highly jagged surface is obtained for $h \to 0$ whilst smooth valleys and hills are found for $h \to 1$. The roughness in such a model tends towards infinity as the distance tends to infinity. Such a model for the surface would clearly be wrong if taken to extremes and in practice, a cut off is introduced and the roughness saturates. A cut-off is automatically introduced due to finite sample size but in reality the length scale for the cut-off is much less than the sample dimensions and is determined by growth effects. A more practical form of the height difference function is given by:

$$g(X,Y) = 2\sigma^2\left[1 - \exp\left(-\left(\sqrt{(X^2+Y^2)}/\xi\right)^{2h}\right)\right] \qquad [3.36]$$

In this form of the height difference function, the relative height between the two points tends towards a value of $2\sigma^2$ as $(X,Y) \to \infty$. Thus the roughness does not exponentially increase as is the case in a purely Fractal model.

It is easier to consider, the height-height correlation function, *C(X,Y)* instead of the height difference function in scattering experiments. The height-height correlation function gives the degree of knowledge that one point on the surface has with another separated by a distance $R = (X,Y)$, and is defined as:

$$C(X,Y) = \langle z(X,Y)z(0,0)\rangle = \sigma^2 - \frac{1}{2}g(X,Y) \qquad [3.37]$$

using equation 3.36, this becomes:

$$C(X,Y) = \sigma^2 \exp\left[-\left(\sqrt{(X^2+Y^2)}/\xi\right)^{2h}\right] \qquad [3.38]$$

The functional forms of the height difference and height-height correlation function are graphically presented below in figure 3.10:

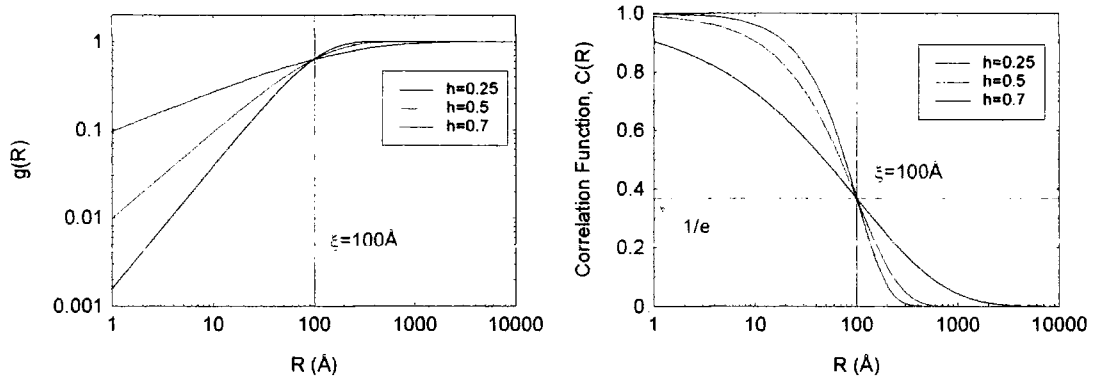

(a) (b)

Figure 3.10: The height difference (a) and height-height correlation function (b) as a function of surface vector, ***R***.

In figure 3.10 it is clear that the parameter ξ, defined as the lateral, or in plane, correlation length is the tie point between the curves with different values of the fractal parameter. It corresponds to a length scale on the surface when the correlation between the two points under consideration has reduced to a value of $1/e$. In essence it defines the area over which the surface is fractal.

The exact choice of the height-height correlation function is open to debate. That shown in equation 3.38 has the advantage that it is mathematically convenient. Other mathematical forms of the statistical form of the interface have been suggested by Palasantzas et. al. [16,17,18]. It has been observed experimentally that the height-height correlation function in Langmuir-Blodgett films can be described by either a fractal model with no cut-off [19] or by a domain model [20]. In the model that is used to study the samples contained in this thesis it is the height-height correlation function introduced by Sinha et. al. that is used. When this is the case, the differential cross section, equation 3.35 can now be re-written as:

$$\frac{d\sigma}{d\Omega} = \frac{N^2 b^2}{q_z^2} L_x L_y \exp\left[-q_z^2\sigma^2\right] \iint_{S_o} dXdY \exp\left[q_z^2 C(X,Y)\right] \exp\left[-i\left(q_x X + q_y Y\right)\right] \qquad [3.39]$$

If the differential cross section per unit surface area is defined as $S(q) \cdot N^2 b^2$, then it is possible to express the specular and diffuse components explicitly. Thus with the Born approximation:

$$S_{SPEC}(q) = F_l^R \exp\left(-q_z^2 \sigma^2\right) \qquad [3.40]$$

where F_l^R is the Fresnel reflection coefficient as defined above. The diffuse component of the cross section is now:

$$S_{DIFF}(q) = \frac{2\pi}{q_z^2} \exp\left(-q_z^2 \sigma^2\right) \int_0^\infty R \left[\exp\left(q_z^2 \sigma^2 e^{-(R/\xi)^{2h}}\right) - 1\right] J_o\left(q_{x,y} R\right) dR \qquad [3.41]$$

where $J_0(q_{x,y}R)$ is a Bessel Function of the first kind.

In summary, the Born approximation assumes that all the scatters are point like and that their interaction with the potential is weak. Thus the Born approximation is not valid for small scattering vectors, i.e. near the critical angle. In order to model the reflectivity and diffuse scatter accurately the distorted wave Born approximation is required. This will be reviewed in the next section.

3.7.2 Distorted Wave Born Approximation

In the Distorted wave Born approximation (DWBA), three wavefields exist in the zero roughness state. Instead of the surface acting as a perturbation on the Fresnel solutions as was assumed in the Born approximation, the DWBA uses perturbation theory on the exact solution of the wave equation for a smooth surface. In other words, the roughness and not the surface acts as the perturbation on the Fresnel solutions. The DWBA was applied by Sinha et. al. [15] in order to model the specular and diffuse scatter from a single layer. In this section, the format of this paper will be followed resulting in an expression for the specular and diffuse scattering cross sections. The DWBA can be realised by splitting the scattering potential into two terms:

$$V = V_1 + V_2 \qquad [3.42]$$

where V_1 represents the ideal, undisturbed system and the second potential is the disturbance to it. The solution to the ideal wave equation, $\nabla^2\phi + k_c^2\phi = V_1\phi$, can be found exactly. The form of the two scattering potentials are:

$$V_1 = \begin{cases} k_0^2(1-n^2) & -a < z < 0 \\ 0 & z > 0 \end{cases} \qquad [3.43]$$

and

$$V_2 = \begin{cases} k_0^2(1-n^2) & 0 < z < z(x,y) \quad \text{if } z(x,y) > 0 \\ -k_0^2(1-n^2) & z(x,y) < z < 0 \quad \text{if } z(x,y) < 0 \\ 0 & \text{elsewhere} \end{cases} \qquad [3.44]$$

In keeping with the derivations of the Born wave, *z(x,y)* represents the statistical average of the surface. The transition probability can be shown to be [15]:

$$\langle 2\,|T|\,1\rangle = \langle \tilde{\psi}_2\,|V_1|\,\phi_1\rangle + \langle \tilde{\psi}_2\,|V_2|\,\psi_1\rangle \qquad [3.45]$$

The incident plane wave, ϕ_1, is scattered by the potential V_1. The Fresnel theory produces the exact eigenstate, ψ_1, which is in turn a series of plane waves which have been reflected and transmitted at the interface. These waves are then perturbed by the presence of the roughness, V_2 and the scattering from waves originating within the sample, sometimes referred to as the time reversed eigenstate, $\tilde{\psi}_2$, is then considered. The time reversal of the perturbed state is required to ensure a unique final solution.

The full DWBA expression for the specular scatter is given in [15], but if the roughness is expanded assuming Gaussian statistics, the modification to the Fresnel coefficients for the specular reflectivity becomes:

$$\left|R(k)\right|^2 = F_l^R \exp(-q_z q_z^t \sigma^2) \qquad [3.46]$$

This is similar to the result obtained by the Born wave (equation 3.27) and agrees with the result obtained via a different method by Névot and Croce [12]. The pure DWBA solution for the specular reflectivity matches experiment very well for low values of scattering vector, but it diverges for high scattering vectors where it over predicts the level of the specular scatter. It is in just this angular range that the Born approximation is valid. Equation 3.46 matches the DWBA and the Born approximation in their respective regions of validity. De Boer [21] has shown by the use of second order perturbation theory that both solutions are in fact the limiting cases of a more general form of the specular component.

The DWBA for the differential cross section of the diffuse scattering can be written [15]:

$$\left[\frac{d\sigma}{d\Omega}\right]_{Diff} = L_x L_y \frac{\left|k_0^2(1-n^2)\right|^2}{16\pi^2}\left|T(k_1)\right|^2\left|T(k_2)\right|^2 S(q_t) \qquad [3.47]$$

In equation 3.47, $\left|T(k_i)\right|$ are the Fresnel transmission coefficients for the incident *(i=1)* and scattered *(i=2)* waves. L_xL_y are as defined above and $S(q_t)$ is defined:

$$S(q_t) = \frac{\exp\left(-\left[\left(q_z^t\right)^2 + \left(q_z^{t*}\right)^2\right]\sigma^2 \Big/ 2\right)}{\left|q_z^t\right|^2} \iint_{S_o}\left[\exp\left(\left|q_z^t\right|^2 C(X,Y)\right) - 1\right]\left[\exp i\left(q_x X + q_y Y\right)\right] dX dY \qquad [3.48]$$

It was subsequently shown by Weber and Lengeler [22] that it is the Fresnel coefficients for a rough surface (i.e. equation 3.29) that should be used in equation 3.47.

The Fourier transform in equation 3.48 does not, in general have an analytical solution and it must be calculated numerically. This can be very time consuming and is thus the rate determining step in computations. In order to increase the speed of computation, Wormington [23] has developed a method based on look up tables which enable the computer simulations to be carried out on standard PCs.

The major difference between the DWBA and Born approximation (a comparison of equation 3.47 and equation 3.39) is the inclusion of the Fresnel transmission coefficients in the DWBA. The inclusion of these transmission coefficients allows an accurate model of the scattering near the critical angle to be performed. It is interesting to note that the Fresnel transmission coefficients are optical in origin and are not dependent on the model of the interface.

The work highlighted to date, has demonstrated that the DWBA can be used to model specular as well as diffuse scatter originating from a statistically rough surface defined by the height-height correlation function described in equation 3.38. In a sample which contains multiple layers, out of plane correlations of roughness in adjacent layers must be considered. This is highlighted in the sections 3.9 et. seq. In the next section, the diffuse scattering from an individual layer will be discussed. The influence on the shape of the diffuse scatter by the parameters σ, h and ξ will also be examined.

3.8 Diffuse Scatter from a Single Surface

The code [24] used to simulate the data contained in this study is based on the DWBA outlined above and was written by M. Wormington [25]. The correlation function that is used is based on that introduced by Sinha et. al.

As we have seen in section 3.4 there are a variety of methods of measuring the diffusely scattered radiation. In this section, the diffuse scatter from a single surface will be presented. The features observed in simulated transverse diffuse scans will be explained.

The transverse diffuse scan maps out the diffuse scatter horizontally in q_x. It is symmetrically centred about q_x=0, and the range it scans is determined by the detector angle, i.e. q_z. Several features are to be found in all transverse diffuse scans. The coherently scattered (specular) intensity is seen as a sharp, instrument defined peak centred at q_x=0. This is shown in figure 3.11(b). The rises in intensity at scattering vectors corresponding to the critical angles (figure 3.11 and 3.12) arise from the transmission coefficients being present in the DWBA. These peaks are referred to as Yoneda wings. Their origin can be explained by considering the position of the transmitted beam. At the critical angle, the transmitted beam lies along the surface and thus the electric field at the surface is doubled, and the intensity of the diffuse scatter is increased.

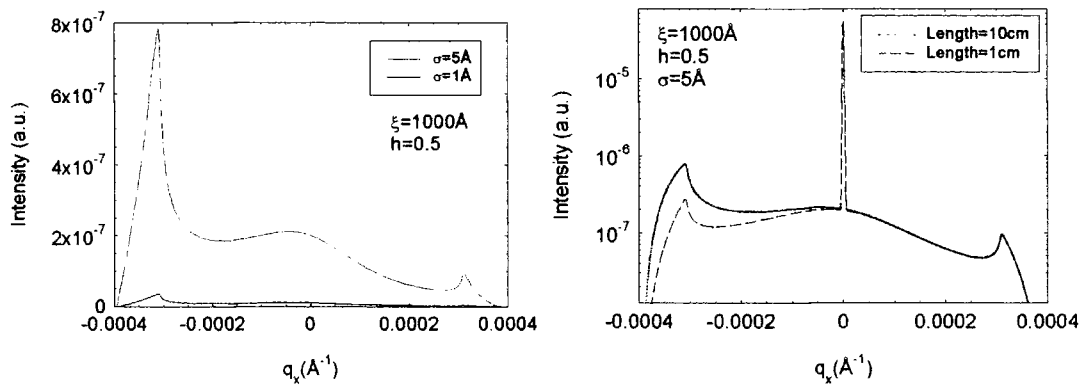

(a) (b)

Figure 3.11: The effects of roughness (a) and sample size (b) on the diffuse scatter

Figure 3.11 shows the effects of roughness and sample size on the observed diffuse scatter. We have already seen that an increase in the roughness at the interface reduces the specular scatter. As a result of conservation of energy, this results in an increase in the diffuse scatter. The effects of sample size are due to conservation of flux arguments. The intensity of the diffuse scatter is proportional to the area of the sample that the x-rays are impinging onto, and the incident flux. At extremely low sample angles, some of the incident beam passes over the sample, and the number of photons incident onto it are reduced. The angle at which all the beam is incident onto the sample is proportional to the beam and sample sizes. A conservation of flux argument is also used to explain why the intensity of the diffuse scatter is seen to reduce as the sample angle is increased. Here the projected footprint of the beam is changing as the sine of the incident angle and thus the area of the sample from which the x-rays are scattering from is reducing.

Figure 3.12 shows the effects of changing the lateral correlation length, ξ, and fractal parameter, h on the shape of the diffuse scatter.

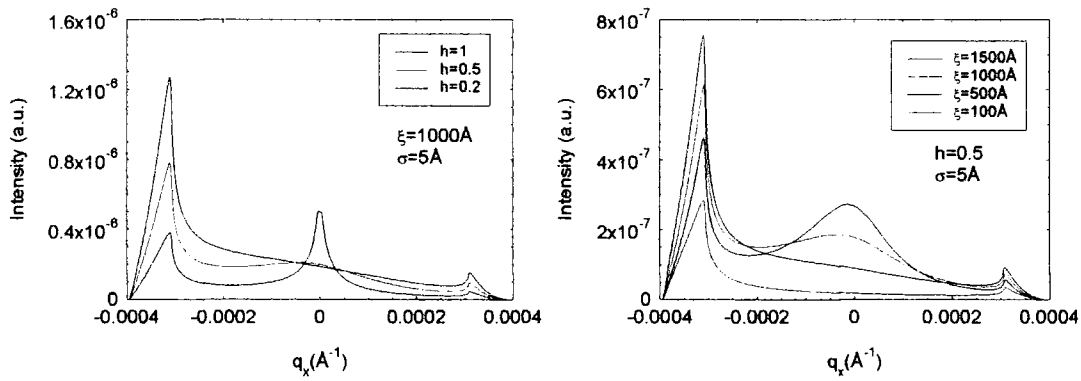

(a) (b)

Figure 3.12: The effects of the fractal parameter and lateral correlation length on the shape of the diffuse scatter.

The effect of the fractal parameter on the shape of the diffuse scatter is to cause the central region to become more peaked. The shape and intensity of the diffuse scatter is much more sensitive to the lateral correlation length. From figure 3.12(b) it is clear

that, as the correlation length rises, so the intensity of the diffuse scatter at small values of q_x increases.

As the diffuse scatter is proportional to the Fourier transform of this roughness length scale (equation 3.38) it is not surprising that the shape of the diffuse scan is sensitive to the correlation length. The nature of reciprocal space is such that a lateral periodicity on the surface is directly transformed to a single point in q_x. Thus the periodicites of the roughness will effect the distribution of diffuse scatter along q_x. The intensity at small q_x will be greatest for long frequency roughness. As the correlation length is an indication of this long frequency roughness, the larger the correlation length the greater the intensity of the diffuse scatter at low q_x. For short correlation lengths the diffuse scatter is confined to large q_x values which are commonly not observable due to the cut-off introduced by the sample surface.

In order to measure the scatter from short correlation length samples, a high scattering vector (q_z) must be employed to maximise the range of q_x that can be sampled. This introduces problems because the amplitude of the diffuse scatter falls as approximately q_z^{-2}. It has also been shown that high scattering vectors must be probed in order for the diffuse scatter to become sensitive to the fractal nature of the surface, namely h. A method proposed by Metzger and Salditt [26,27,28,29,30,31] overcomes this problem by moving the detector out of the plane of scattering. This type of scan is then dependent on q_y. In this geometry, there is no cut off introduced and q_y can be probed over a large range. By defining a low value of q_z, the flux is high. This geometry was not used in the course of this thesis, and the reader is referred to the references above for more details.

3.9 Roughness and its Effects in Reciprocal Space

In this section the exact nature of the roughness in a multilayered structure will be considered. When one or more layers are deposited onto a substrate, the effects of out of plane correlations must be considered [32,33,34]. Figure 3.13 (a-d) shows the possible out of plane correlations of the roughness that can exist in a multilayered sample. In the schematic diagram shown in figure 3.13(a) there is no interface roughness and the resulting diffuse scatter is zero. Figure 3.13(b) shows what is termed totally correlated or conformal roughness. In this case, the roughness profile of layer *l* is replicated exactly on all other layers. Figure 3.13(c) shows totally uncorrelated roughness. In this instance, the roughness on each layer is statistically independent of the roughness on other layers. Figure 3.13(d) represents a mixture of the two kinds of roughness, i.e. partially correlated roughness, and is the most commonly observed kind of roughness.

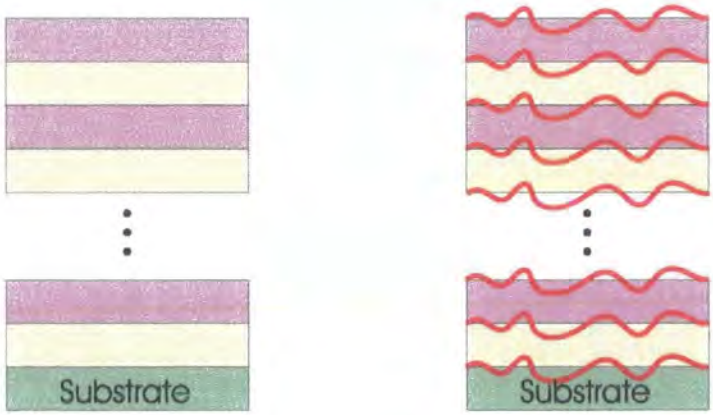

(a) (b)

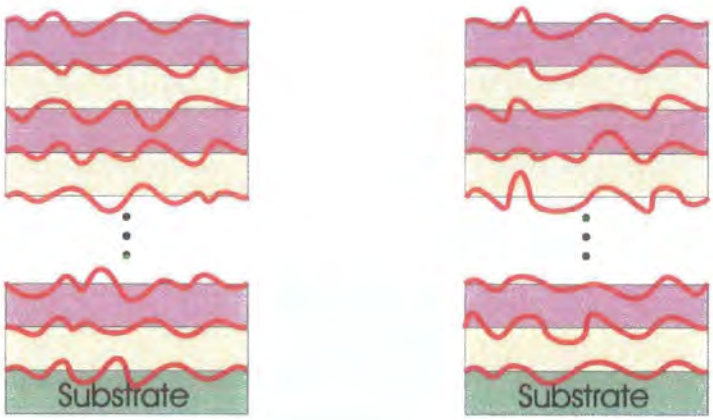

(c) (d)

Figure 3.13: Roughness in a multilayer: Zero roughness (a), roughness which is totally correlated (b), roughness which is totally uncorrelated (c) and partially correlated (d)

The model of diffuse scattering introduced by Sinha et. al. in their seminal paper has been extended by a variety of groups, most notably that of Holý, to include the effects of multiple layers deposited onto a substrate [35,36,37,38].

Out of plane correlations can be modelled mathematically by use of the covariance function [39]:

$$C_{j,k}(R) = \left\langle \delta z_j(0) \delta z_k(R) \right\rangle \qquad [3.49]$$

Here δz_j and δz_k represent the local centres of the roughness profile at the j-th and k-th interfaces. If out of plane correlations exist, then equation 3.49 will be non zero. In the model that is used throughout this study there are two possible covariance functions based on the height-height correlation function introduced by Sinha, namely equation 3.38.

One method of calculating the effects of correlated roughness is to introduce a second, out of plane correlation length, ζ which describes the length scale over which the substrate roughness is correlated vertically. It is defined as the distance over which the correlations between fluctuations at the j-th and k-th interfaces are damped

by a factor of $1/e$. The roughness is perfectly correlated if ζ is much greater than the sample thickness. There are no correlations if $\zeta = 0$. The covariance function for this model is written:

$$C_{j,k}(R) = \sigma_{j,k}^2 \exp\left[-\left(R/\xi_{j,k}\right)^{2h}\right] \exp\left[-|z_j - z_k|/\zeta\right] \qquad [3.50]$$

In equation 3.50, the roughness and lateral correlation length are defined for each of the interfaces: $\sigma_{j,k}^2 = \sigma_j^2 + \sigma_k^2$ and $\xi_{j,k}^{2h} = \left(\xi_j^{2h} + \xi_k^{2h}\right)/2$. This form of the covariance function is extremely useful as it enables the effects of out of plane correlation length and lateral frequency variations to be investigated. However, the computation time scales as the number of interfaces squared.

The second covariance that can be used has the advantage that the computation time scales linearly with the number of interfaces. Such a covariance function can be written:

$$C_{j,k}(R) = \left(\sigma_{u,j}\sigma_{u,k}\delta_{j,k} + \sigma_{c,j}\sigma_{c,k}\right) \exp\left[-\left(R/\xi\right)^{2h}\right] \qquad [3.51]$$

In this model the roughness of any layer is written in terms of a random component, $\sigma_{u,j}$ and a component of the roughness that replicates the substrate roughness perfectly, $\sigma_{c,j}$. The relation of the two to the total interface roughness is $\sigma_j^2 = \sigma_{u,j}^2 + \sigma_{c,j}^2$. The lateral correlation length and the fractal parameter, *h* is the same for all the interfaces. The amount of correlated roughness is thus independently set for each of the layers. Due to the much increased computation speed it is this second model that has been used throughout this study. A simulation of a 20 period multilayer on a Pentium 200 computer takes approximately 1min using this second covariance function.

3.10 Diffuse Scatter from a Multilayer

In this section the two covariance functions defined in equations 3.50 and 3.51 will be used to demonstrate the effects of out of plane correlations on the diffuse scatter. Four full reciprocal space maps (FRSM) will be presented. The first three have been calculated using the second covariance function and show the intensity as a function of q_x and q_z. The FRSMs have been calculated for a twenty period Co(18Å)/Pt(10Å) multilayer deposited on silicon. The roughness of the interfaces within the multilayer structure were 4Å, and the substrate roughness was 2Å. Figure 3.14 shows the simulated specular scatter from such a sample.

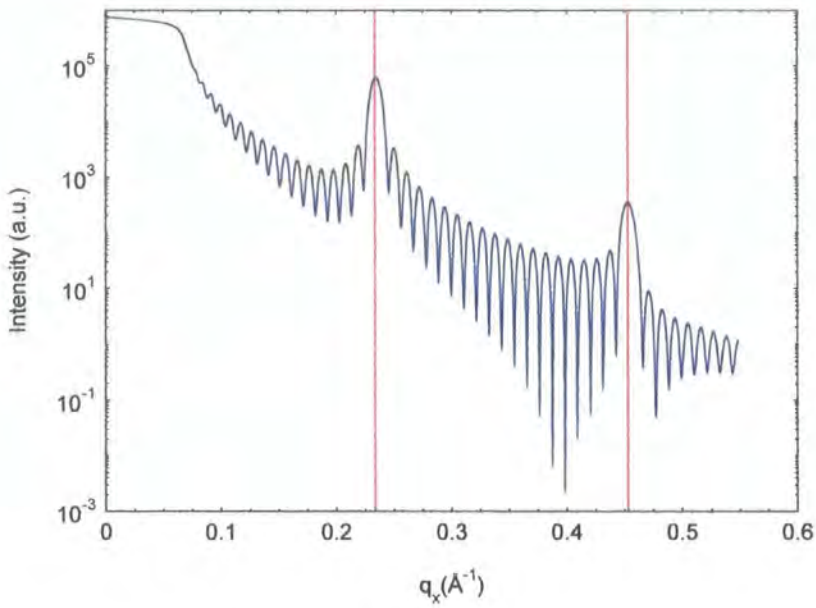

Figure 3.14: The specular simulation for the model sample

There are two Bragg peaks which are clearly defined at q_z=0.234Å^{-1} and q_z=0.453Å^{-1}. The Kiessig fringes originating from the total stack thickness are also clearly evident in figure 3.14.

For the simulation of the diffuse scatter the correlation length was set to 500Å and the fractal parameter was 0.3. In all the simulations, the specular component at $q_x=0$ was not included in the simulation. The asymmetry of the diffuse scattering in

the FRSMs is due to the inclusion in the simulation of beam footprint effects. The first FRSM is shown in figure 3.15. Here the roughness was completely uncorrelated.

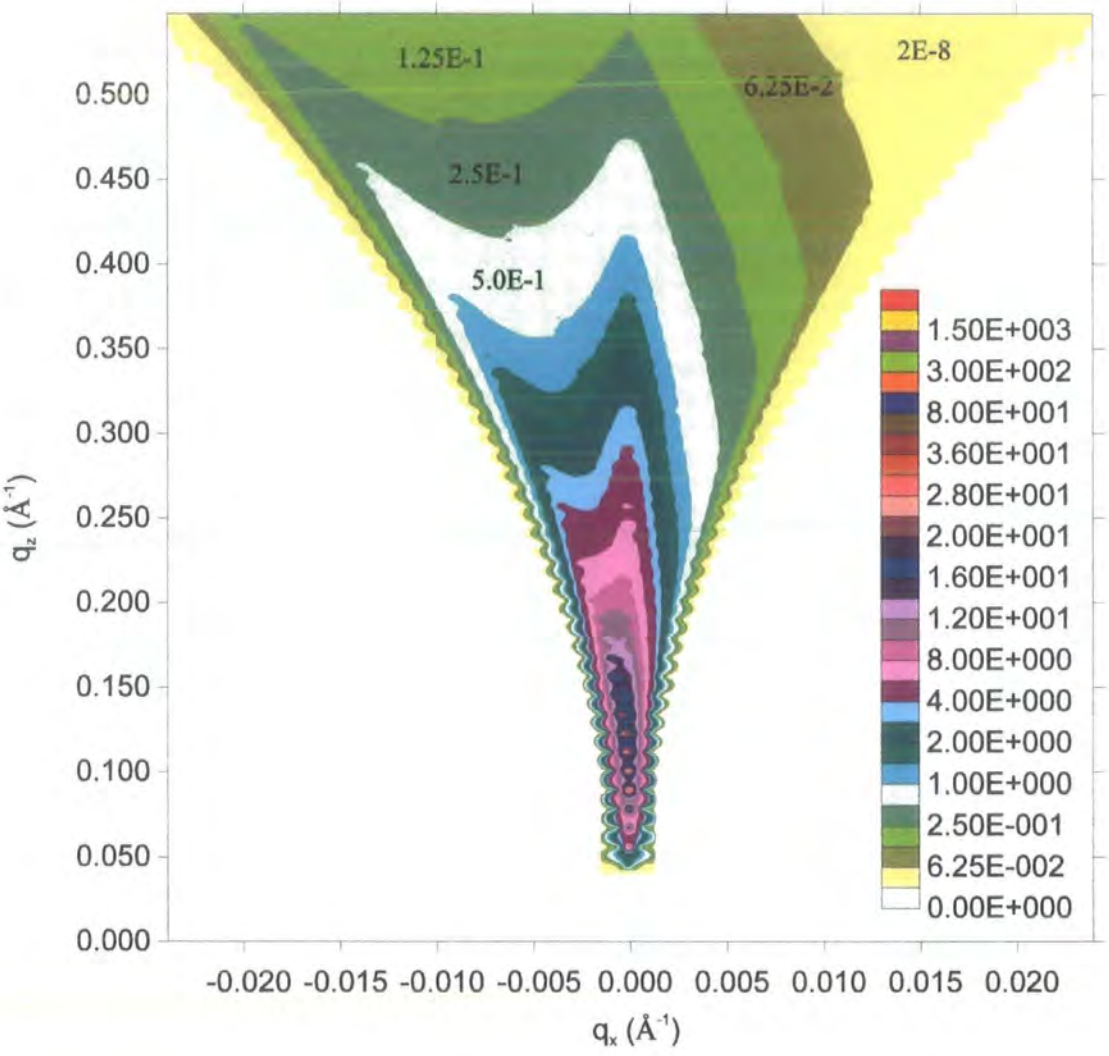

Figure 3.15: FRSM of the diffuse scatter from a Co/Pt multilayer where the roughness was totally uncorrelated. Asymmetry due to inclusion of beam footprint.

A steady, featureless reduction in the intensity in the diffuse scatter is observed in figure 3.15. Indeed, it is identical to a FRSM that would be obtained from a single surface. For totally uncorrelated systems, the addition of more layers simply scales the diffuse scattering by the number of additional layers. This is certainly not the case when the roughness is correlated. This is demonstrated in figure 3.16 where the same structure as above has been simulated with all the layers

exhibiting perfect correlations. The data is displayed with the same contour increments as above.

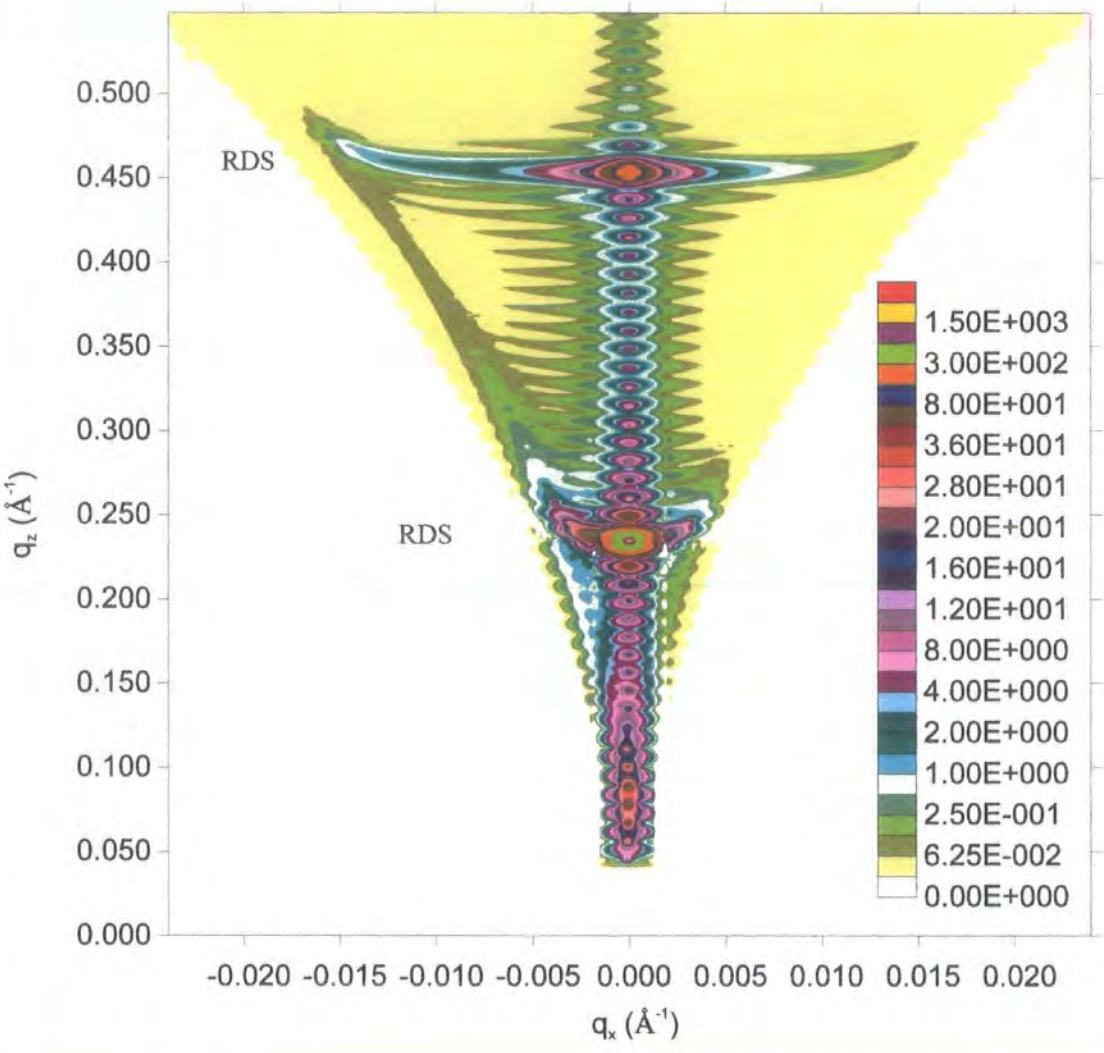

Figure 3.16: FRSM of the diffuse scatter from a Co/Pt multilayer where the roughness was totally correlated. Asymmetry due to inclusion of beam footprint.

In sharp contrast to the uncorrelated FRSM, there are many features present in this FRSM. Instead of the diffuse intensity being evenly distributed in reciprocal space as was the case in figure 3.15, the diffuse scatter is confined to specific areas, most notably, into sheets, at the positions of the Bragg peak in the specular simulation. These are called, resonant diffuse sheets and have been labelled RDS in figure 3.16. If refraction effects are ignored, these diffuse sheets extend straight and parallel to q_x. If refraction is taken into account, these resonant sheets are seen to

curve slightly at the critical angles. These have been named Holý Bananas after Vaclav Holý who first explained their existence [36]. The presence of diffuse scatter at specific q_z values, corresponding to the Bragg position, which extend into q_x are a measure of lateral frequencies (q_x) which have been replicated through the multilayer repeat distance. The extension of the enhancement into q_x is a direct measure on the frequencies of the roughness that are being correlated. In has been shown that it is the lowest frequencies that are the most easily replicated [40], and as such these resonant diffuse sheets are sometimes seen to reduce in intensity for high q_x.

The diffuse scatter is also seen to oscillate with a period exactly the same as that obeyed by the Kiessig fringes in the reflectivity scan. These occur for similar reasons that give rise to the resonant diffuse Bragg sheets. The out of plane correlations now extend over a much larger distances. As the Kiessig fringes are proportional to the total stack thickness, oscillations in the diffuse scatter with the same period imply roughness correlations over the entire sample thickness.

Figure 3.17 shows the effects of partial correlation using the second covariance function. The ratio of the correlated to uncorrelated roughness was 50:50. The contours are again set the same as those in the previous FRSMs.

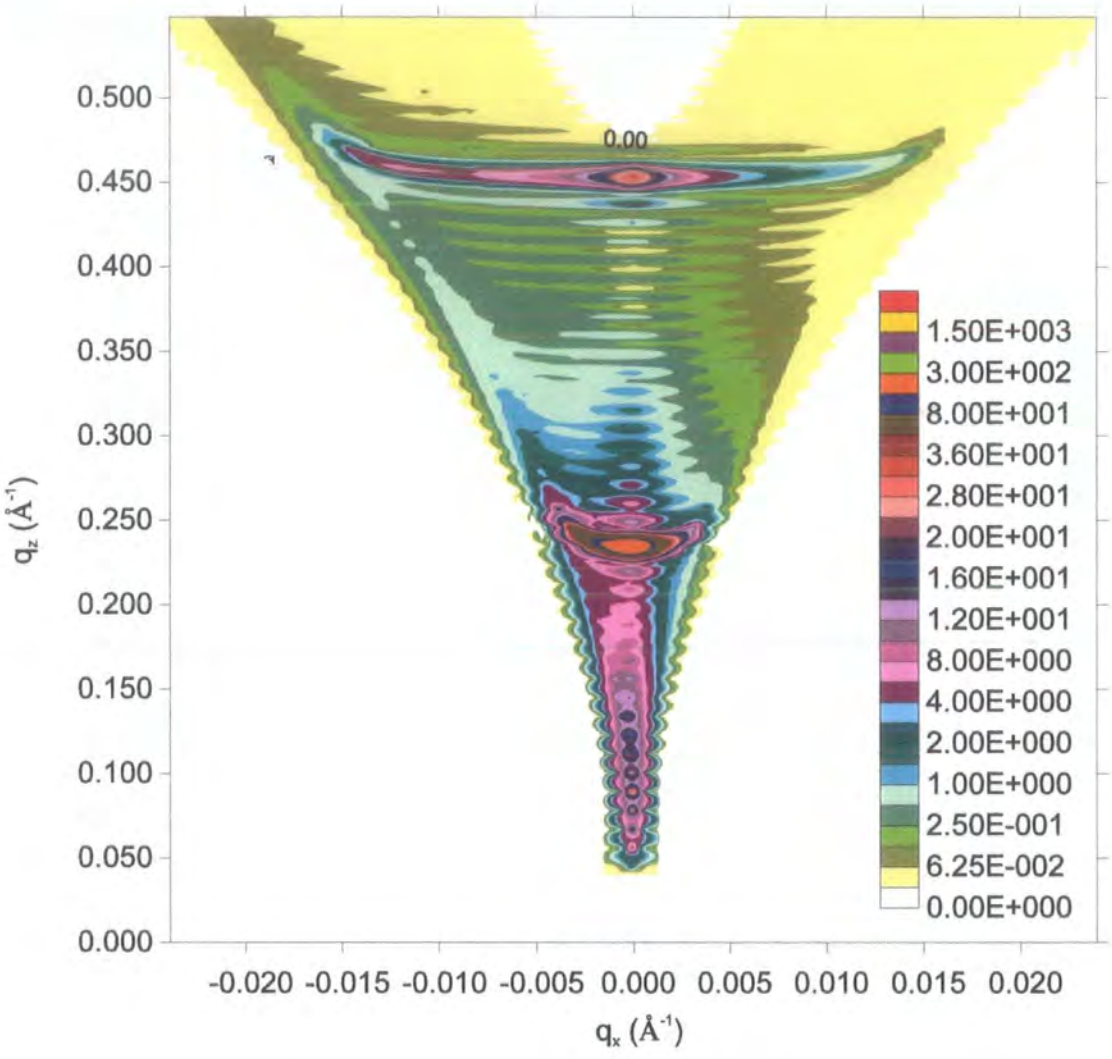

Figure 3.17: FRSM of the diffuse scatter from a Co/Pt multilayer where the roughness was partially uncorrelated. The second covariance function was used, and the ratio of correlated to uncorrelated roughness was 50:50. Asymmetry due to inclusion of beam footprint effects.

The distribution of the diffuse scatter in figure 3.17 still shows the resonant Bragg sheets that were observed when the roughness was totally correlated. However, the inclusion of a random component has increased the diffuse intensity away from the resonance conditions, and as a consequence the resonant sheets have reduced in intensity. As the model assumes that the correlated component replicates the roughness perfectly, there are still correlations that extend from the substrate to

the surface and diffuse Kiessig fringes result. However, these are not as clearly defined as in figure 3.16.

A FRSM has been calculated using the first covariance function, and this is shown in figure 3.18.

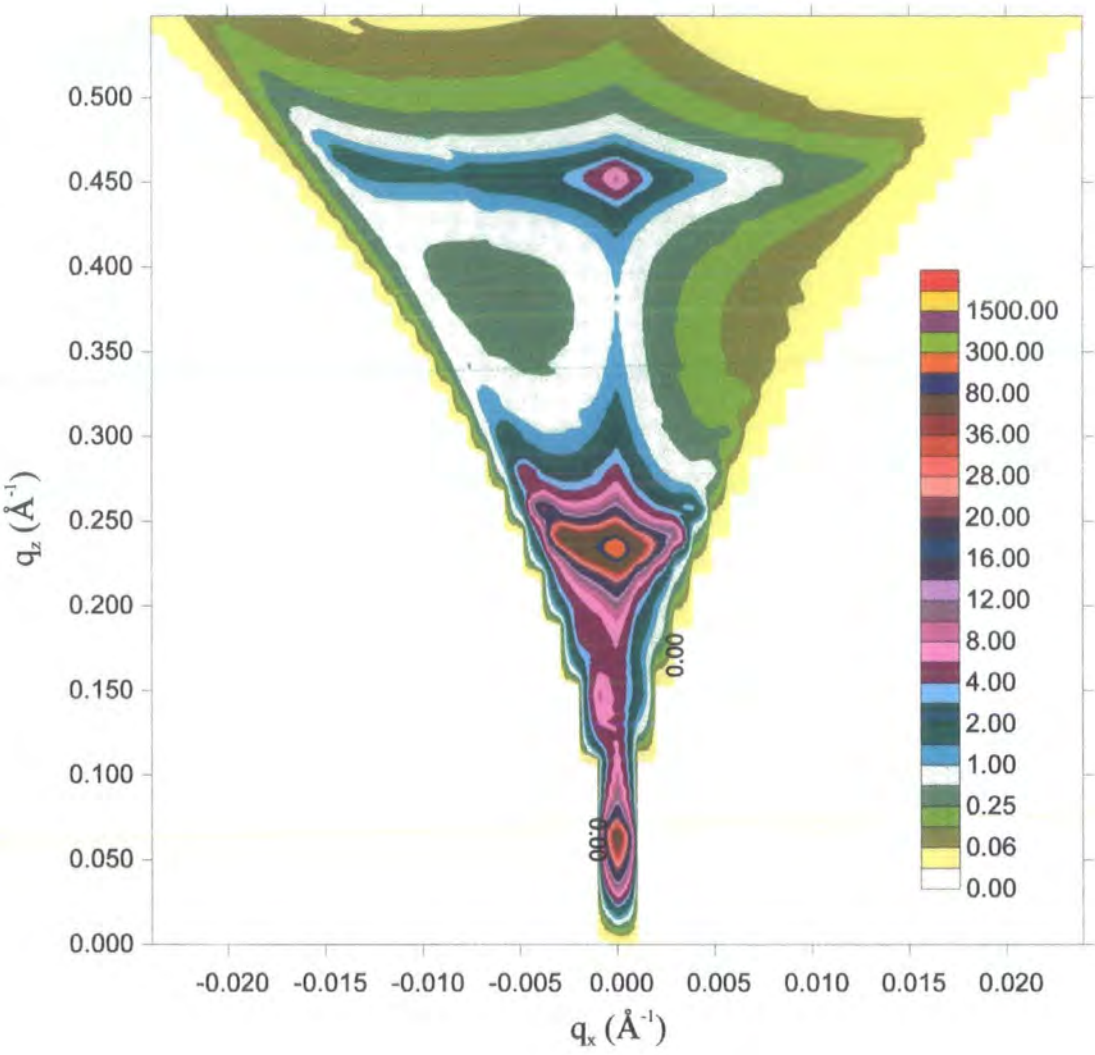

Figure 3.18: FRSM of the diffuse scatter from a Co/Pt multilayer where the roughness was partially uncorrelated. The first covariance function was used, and the out of plane correlation length, $\zeta = 180$Å.

The FRSM in figure 3.18 closely resembles that shown in figure 3.17. However, there are two important differences between them. As the out of plane correlation length was substantially less than the sample thickness (ζ=180Å), there

are no out of plane correlations which extend through the sample thickness. This effect removes any Kiessig fringes in the diffuse scatter. The width of the resonant Bragg sheets is also seen to be broader when this first covaraiance function is used. The variation of the width of the Bragg peak with out of plane correlation length is shown in figure 3.19 below:

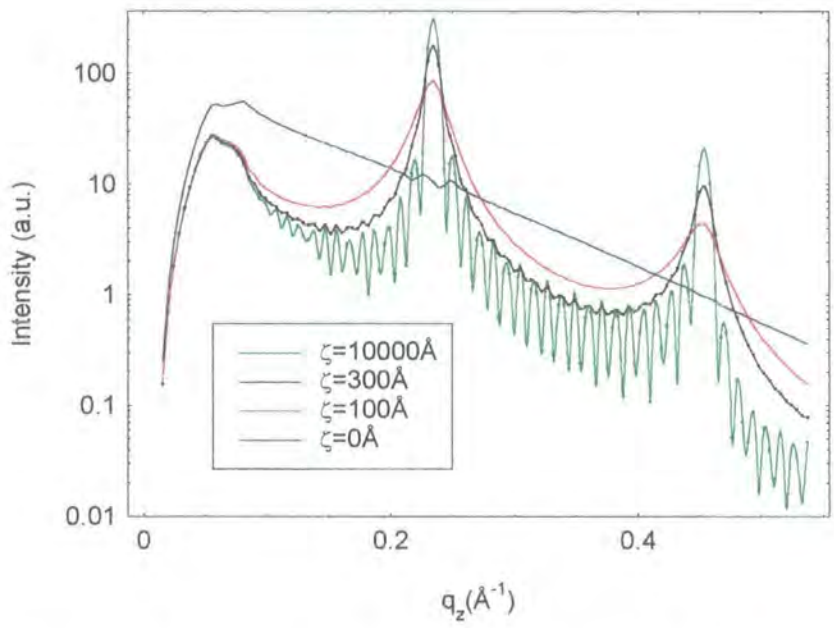

Figure 3.19: A series of Off-specular scans with different out of plane correlation lengths for the same structure as simulated above.

Figure 3.19 shows a series of simulated longitudinal diffuse scans with varying out of plane correlation length. The width of the Bragg peak is seen to reduce as the out of plane correlation length increases. This is because, the width of the Bragg peak is proportional to the number of correlated interfaces. For the simulation where the out of plane correlation length is much greater than the sample thickness, presence of Kiessig fringes are seen and the scattering is the same as that shown in figure 3.16.

3.10.1 Dynamical Effects Observed in FRSM

Additional features are sometimes observed both in FRSM and transverse diffuse scans. Fringes are occasionally observed in the transverse diffuse scan, and additional stripes of intensity are occasionally observed in FRSM originating from multilayer samples. An example of these fringes in a transverse diffuse scan is illustrated in figure 3.20 where the diffuse scatter from a gold film has been simulated.

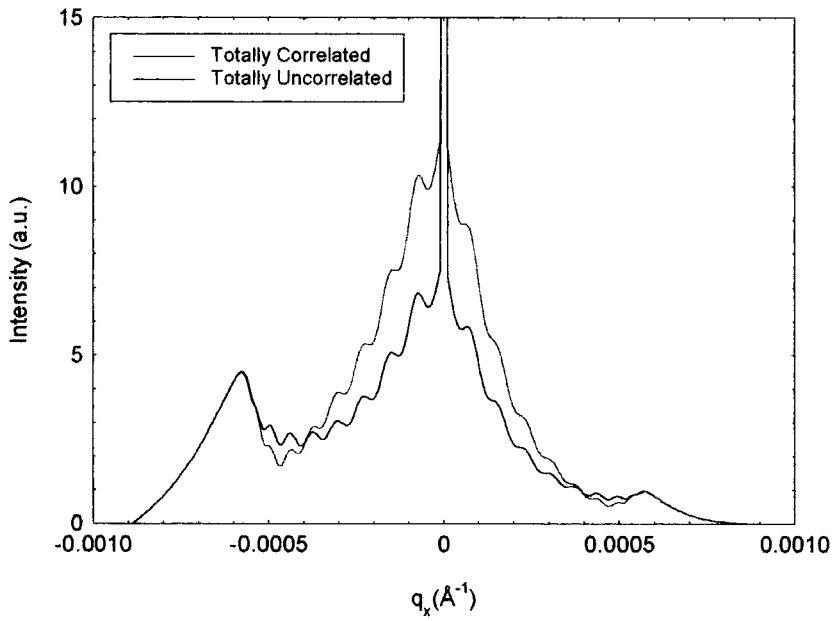

Figure 3.20: Transverse diffuse scan at $2\theta=3°$ for a 300Å Au film deposited on Si. ξ=1000Å and h=0.5.

The fringes in figure 3.20 do not arise due to correlations in the roughness. They are the result of a dynamical interaction between the standing wave created by the coherent wavefields associated with the wave transmitted at the surface and that reflected from the substrate. As the sample angle is varied, this standing wave moves through the sample and an increase in diffuse intensity is observed whenever the maxima of the standing wave is coincident on an interface.

Dynamical effects and resonant diffuse scattering have been observed by several groups. The reader is referred to a bibliography comprised of a selected series of papers which discuss these effects in more detail [41,42,43,44,45,46,47].

3.11 Analysis of Diffuse Scatter without Simulation

The time consuming nature of simulating diffuse scatter makes analysis without recourse to detailed simulation very attractive. Work by Savage et. al. [40] has shown how by simple conservation of energy arguments, the roughness of an interface can be estimated without simulation. We have already seen that the Born wave models the attenuation of the specular scatter caused by the presence of roughness at the interface by the inclusion of a Debye-Waller factor - $I_{Spec} = I_0 \exp\left(-q_z^2\sigma^2\right)$. From conservation of energy, the diffuse intensity can now be expressed as:

$$I_{Diff} = I_0 - I_{Spec} = I_0\left(1-\exp\left[-q_z^2\sigma^2\right]\right) \qquad [3.52]$$

A ratio of the integrated diffuse intensity to the integrated specular intensity will therefore only depend on the scattering vector and the roughness of the interface:

$$\frac{I_{Diff}}{I_{Spec}} = \exp\left(q_z^2\sigma^2\right)-1 \qquad [3.53]$$

Thus by measuring the integrated intensity of the diffuse and specular scatter in a transverse scan, the roughness of the surface can be deduced. This method of calculating the roughness assumes that all the diffuse scatter is accessible. As we have seen, the sample surfaces restrict the range of q_x that can be probed, and as a result some of the diffuse scatter is not observed and equation 3.53 is an underestimation of the true roughness. By simulating a series of transverse diffuse scans calculated using the DWBA, Pape [48] has been able to demonstrate the effects

of correlation length, fractal parameter and scattering vector on the underestimation of the surface roughness calculated using equation 3.53. Such an analysis shows that the deduced roughness is unaffected by the fractal parameter and is only weakly dependent on the scattering vector (for q_z>0.015). The largest effects are observed for the changing correlation length. This is because for small correlation lengths, much of the diffuse scatter cannot be observed in the transverse scan.

The extension of the work by Savage et. al. to include multiple surfaces was undertaken by the same authors as in reference 47 [49,50,51]. In keeping with the covariance function described in equation 3.51 the roughness of the interface is described in terms of a correlated and an uncorrelated component, i.e. $\sigma_j^2 = \sigma_{u,j}^2 + \sigma_{c,j}^2$. The simple analysis is complicated by the presence of the two terms, but for highly correlated or highly uncorrelated systems, it is still possible to obtain estimates of the roughness using the Born wave.

The correlated component of the roughness gives rise to the resonant Bragg sheets seen in figures 3.16, 3.17 and 3.18. Transverse scans taken through these Bragg peaks will therefore be primarily sensitive to the correlated roughness component, and the ratio of the diffuse to the specular intensity then reveals the correlated component of the roughness. Transverse scans taken away from the Bragg peak are sensitive to the uncorrelated roughness component only and so will give an indication of this parameter.

3.12 Conclusion

This chapter has introduced the reader to the theoretical ideas required to understand the scattering of x-rays under grazing incidence conditions. There are two good review papers to which the reader is referred to which summarise the results of this chapter very well [52,53].

References from Chapter 3

1 The Crystalline State Vol. 2: The optical principles of the diffraction of X-rays, *R.W. James,* **G. Bell & Sons**, (1948)

2 Neutron and Synchrotron Radiation for Condensed Matter Studies Vol. 1, *Eds. J. Baruchel, J.L. Hodeau, M.S. Lehmann, J.R. Regnard, C. Schlenker*, **Springer-Verlag**, (1993)

3 I. Hamley, Introduction to Condensed Matter - *Lecture course notes*

4 X-Ray Diffraction in Crystals, Imperfect Crystals and Amorphous Bodies, *A. Guinier*, **Dover Pub.,** (1994)

5 Theory of X-Ray Diffraction in Crystals, *W.H. Zachariasen*, **Dover Pub.**, (1994)

6 Introduction to Solid State Physics - Sixth Edition, *C. Kittel*, **John Wiley & Sons**, (1991)

7 X-ray Diffraction, *B.E. Warren,* **Dover Publications**, (1990)

8 Optics second Edition, *E. Hecht,* **Addison-Wesley**, (1990)

9 B. Lengeler in Photoemission and Absorption Spectroscopy in Solids and Interfaces with Synchrotron Radiation, *Eds. M. Campagna, R. Rosei,* **North Holland**, (1990)

10 L.G. Parratt, *Phys. Rev.*, **95** (2), *359-369*, (1954)

11 M. Manciu, L. Dudas, C. Sürgers, R. Mãnãilã, *J. Appl. Cryst.*, **28**, *160-167*, (1995) and references therein

12 L. Névot, P. Croce, *Revue Phys. Appl.*, **15**, *761-779*, (1980)

13 H. Kiessig, *Ann. Phys. (Leipzig)* **10**, *769* (1931)

14 S. Banerjee, M.K. Sanyal, A. Datta, S. Kanakaraju, S. Mohan, *Phys. Rev. B.*, **54** (23), *1-4*, (1996)

15 S.K. Sinha. E.B. Sirota, S. Garoff, H.B. Stanley, *Phys. Rev. B.* **38** (4), *2297-2311*, (1988)

16 G. Palasantzas, J. Krim, *Phys. Rev. B.*, **48** (5), *2873-2877*, (1993)

17 G. Palasantzas, *Phys. Rev. B.*, **48** (19), 14472-14478, (1993)

18 G. Palasantzas, *Phys. Rev. B.*, **49** (15), 10544-10547, (1994)

19 A. Gibaud, N. Cowlam, G. Vignaud, T. Richardson, *Phys. Rev. Lett.*, **74** (16), *3205-3208, (1995)*

20 R. Stömmer, J. Grenzer, J. Fischer, U. Pietsch, *J. Phys. D: Appl. Phys.*, **28**, *A216-A219*, (1995)

21 D.K.G. de Boer, *Phys. Rev. B.*, **49** (9), *5817-5820*, (1994)

22 W. Weber, B. Lengeler, *Phys. Rev. B.*, **46** (12), *7953-7956*, (1992)

23 M. Worminton, *Ph. D. Thesis,* University of Warwick

24 GIXA, courtesy of Bede Scientific

25 I. Pape, T.P.A. Hase, B.K. Tanner, M. Wormington, *Physica*, In press (1998)

26 T. Salditt, T.H. Metzger, J. Peisl, *Phys. Rev. Lett,* **73** (16), *2228-2231*, (1994)

27 T. Salditt, T.H. Metzger, J. Peisl, C.H. Morawe, H. Zabel, *Mat. Res. Soc. Symp. Proc.*, **355**, *269-274*, (1995)

28 R. Paniago, H. Homma, P.C. Chow, S.C. moss, Z. Barnea, S.S.P. Parkin, D. Cookson, *Phys. Rev. B.*, **52** (24), *R17052-R17055*, (1995)

29 T. Salditt, T.H. Metzger, J. Peisl, G. Goerigk, *J. Phys. D: Appl. Phys.*, **28**, *A236-A240*, (1995)

30 T. Salditt, T.H. Metzger, Ch. Brandt, U. Klemradt, J. Peisl, *Phys. Rev. B.*, **51** (9), *5617-5627,* (1995)

31 T. Salditt, D. Lott, T.H. Metzger, J. Piesl, G. Vignaud, P. Høghøj, O. Schärpf, P. Hinze, R. Lauer, *Phys. Rev. B.*, **54** (8), *5860-5872*, (1996)

32 Y.H.-Phang, D.E. Savage, T.F. Kuech, M.G. Legally, J.S. Park, K.L. Wang, *Appl. Phys. Lett.*, **60** (24), *2986-2988*, (1992)

33 E.E. Fullerton, J. Pearson, C.H. Sowers, S.D. Bader, X.Z. Wu, S.K. Sinha, *Phys. Rev. B.*, **48** (12), *17432-17444,* (1993)

34 A.P. Payne, B.M. Clemens, *Phys. Rev. B.*, **47** (4), *2289-2300*, (1993)

35 V. Holý, J. Kub•na, I. Ohlídal, K. Lischka, W. Plotz, *Phys. Rev. B.*, **47** (23), *15896-15903*, (1993)

36 V. Holý, T. Baumbach, *Phys. Rev. B.*, **49** (15), *10668-10676*, (1994)

37 V. Holý, T. Baumbach, M. Bessière, *J. Phys. D: Appl. Phys.*, **28**, *A220-A226*, (1995)

38 J.-P. Schlomka, M. Tolan, L. Schwalowsky, O.H. Seeck, J. Settner, W. Press, *Phys. Rev. B.*, **51** (4), *2311-2321*, (1995)

39 I.Pape, T.P.A. Hase, B.K. Tanner, M. Wormington, *Accepted for publication in Physica C*

40 D.E. Savage, J. Kleiner, N. Schimke, Y.-H. Phang, T. Jankowski, J. Jacobs, R. Kariotis, M.G. Legally, *J. Appl. Phys.*, **69** (3), *1411-1424*, (1991)

41 J.B. Kortright, *J. Appl. Phys.*, **70** (7), *3620-3625*, (1991)

42 X. Jiang, T.H. Metzger, J. Peisl, *Appl. Phys. Lett.*, **61** (8), *904-907*, (1992)

43 G.T. Baumbach, V. Holý, U. Pietsch, M. Gailhanou, *Physica B*, **198**, *249-252*, (1994)

44 M. Kopecký, *J. Appl. Phys.*, **77** (6), *2380-2387*, (1994)

45 M. Jergel, V. Holý, E. Majková, Ò. Luby, R. Senderák, *J. Phys. D: Appl. Phys.*, **28**, *A241-A245*, (1995)

46 D.K.G. de Boer, A.J.G. Leenaers, R.M. Wolf, *J. Phys. D: Appl. Phys.*, **27**, *A227-A230*, (1995)

47 V.M. Kaganer, S.A. Stepanov, R. Köhler, *Phys. Rev. B*, **52** (23), *16369-16372*, (1995)

48 I. Pape, Ph. D. Thesis, University of Durham (1997)

49 D.E. Savage, N. Schimke, Y.-H. Phang, M.G. Legally, *J. Appl. Phys.*, **71** (7), *3283-3293*, (1992)

50 Y.-H. Phang, D.E. Savage, R. Kariotis, M.G. Legally, *J. Appl. Phys.*, **74** (5), *3181-3188*, (1993)

51 D.E. Savage, Y.-H. Phang, J.J. Rownd, J.F. MacKay, M.G. Legally, *J. Appl. Phys.*, **74** (10), *6158-6164*, (1993)

52 D.K.G. de Boer, A.J.G. Leenaers, W.W. van den Hoogenhof, *X-ray Spectroscopy*, **24**, *91-102*, (1995)

53 S.K. Sinha, *Acta Physica Polonica A*, **89**, *219-234*, (1996)

Chapter 4

Experimental Considerations for X-ray Scattering

The data used in this study were all obtained from synchrotron sources. This chapter consists of a theoretical discussion of synchrotron radiation, leading into a discussion of the characteristics of the synchrotron beamlines used.

As all the x-ray results contained within this study were obtained from synchrotron sources, a detailed description of electron impact sources such as sealed tubes and rotating anodes will not be given here. For a more detailed description of these sources, the reader is referred to the work of Michette and Buckley [1], and Lin [2].

4.1 An Introduction to Synchrotron Radiation

Synchrotron radiation is the radiation emitted from a relativistically accelerated charged particle. It occurs not only in man-made particle accelerators and storage rings, but also in the furthest reaches of the Universe. Cosmological synchrotron radiation is found in active galactic nuclei where there are strong magnetic fields, such as the Crab nebula.

All purpose built particle accelerators share the same basic structure. There is a linear accelerator used to produce the charged particles and accelerate them. The charged particles are then injected into a booster ring where they are further accelerated, prior to final injection into, and acceleration within, the main storage ring. The easiest way to steer a beam of charged particle is to use a static magnetic field, and use the Lorentz force, as in the following equation:

$$F = ev \times B \qquad [4.1]$$

where v is the velocity of the charged particle and $\boldsymbol{B}$ is the magnetic field. In order to confine the charged particles to move in a circular orbit, magnetic fields perpendicular to the horizontal orbital plane are used. The radius of curvature for the magnets used can be expressed as:

$$\rho = \frac{m_o \gamma \, c}{eB} \qquad [4.2]$$

where m_o is the rest mass of the electron and $\gamma = \left(1 - \left(v/c\right)^2\right)^{-1/2}$ [3]. Another important parameter is the power radiated by a bending magnet. This can be shown to be proportional to the fourth power of the electron energy, and inversely proportional to the radius of curvature:

$$P = 88.5\frac{E^4}{\rho} = 26.5E^3B \qquad [4.3]$$

where E is in GeV, ρ is in meters and the magnetic field is expressed in Tesla [1,4].

For storage rings designed for the production of x-rays, the size of the ring is determined by the bending magnet field strength and the energy of the electrons. As an example, the energy of the Daresbury SRS is 2 GeV, and the dipole magnetic fields are 1.2T. The radius of curvature of the magnets is 5.56m and the overall radius of the storage ring is 15.28m [1]. As the electrons move through the storage ring, they loose energy at each of the bending magnets. The lost energy is replaced by a radio frequency cavity whose frequency is a harmonic of the revolution frequency of the particles. The radio frequency is of the order of a few hundred megahertz and the power is approximately 2 MW [2].

Although synchrotron sources can produce a large number of energetic photons it is the collimation and the frequency spectrum that make them so appealing to the user. In the laboratory frame, the emission of the photons from the relativistic electrons is Lorentz contracted, and is no longer emitted into a large solid angle. The

opening angle of the emission cone can be approximated to $1/\gamma$ [4]. The value of gamma for Daresbury is 3913, and so the total synchrotron emission is confined into a vertical opening angle of only 65". This represents a huge increase in the efficiency of the machine over electron impact sources, as all the emitted radiation can be utilised in the experiment. In the horizontal plane, the collimation is less good, and depends on the time that the electron is within the magnetic field [4].

The frequency spectrum of a synchrotron can be explained by considering the time structure of the synchrotron pulse. The time of the pulse is simply the difference between the time it takes the electron to travel along an arc of $2/\gamma$, and the photon to travel along a chord corresponding to this arc. This is given by:

$$\Delta t \approx \frac{4\rho}{3c\gamma^3} \qquad [4.4]$$

A time pulse of Δt will contain Fourier components up to a frequency of the order of $\omega_c = 2\pi/\Delta t = 3\pi c\gamma^3/2\rho$. This frequency is referred to as the critical frequency, and it refers to that point which exactly divides the total emitted radiation, with half being irradiated at frequencies lower than the critical frequency, and half above it. The continuum of the emission spectrum results from a smearing out of the multiple harmonics.

The power of synchrotrons are normally compared in terms of three parameters. The first is the *flux* which is defined as the number of photons emitted per second per horizontal milliradian and into 0.1% bandwidth. The *brightness* is the flux per vertical milliradian, and the *brilliance* is the brightness divided by the area of the optical source. The brilliance is typically used as the comparator when there are focusing optics such as mirrors or monochromators which can introduce additional aberrations which effect the size of the source.

The results obtained in this study were acquired either on Station 2.3 at the Daresbury SRS or on beamline BM16 at the ESRF. In the next section, a description of Station 2.3 is given along, with some important experimental parameters that apply to the station.

4.2 Station 2.3 at the Daresbury SRS

Station 2.3 is situated 15 meters, tangentially, from a pair of 1.2T dipole magnets, from which wavelengths in the range 0.5-2.5Å are available. The white x-ray beam, with a vertical divergence of approximately 200" [5] was incident upon a water cooled Si(111) monochromator. The temperature of the monochromator was maintained at 303± 0.1K to give a wavelength dispersion, $\left(\Delta\lambda/\lambda\right)$, of $1.5*10^{-4}$ at a wavelength of 1.4Å. [6]. Due to the inherently high degree of vertical collimation, the beam emerging from the monochromator had an angular divergence of approximately 7". The Si monochromator was not offset for harmonic suppression, so the resulting x-ray beam was contaminated. The strongest of these resulted from the Si(333) reflection. However, as the lowest available wavelength is 0.5Å, this contamination was limited to incident wavelengths above 1.5Å. The beam defining slits (up to 10*10mm) were situated after the monochromator, thereby ensuring that wavelength changes did not effect the position of the beam at the sample.

The incident beam was monitored by scatter from a Kapton® foil placed in the beam, prior to the sample. This allows the data to be corrected for beam decay. Typical values for the beam current were 250mA just after a fill which decayed to 120mA, 24 hours later. Figure 4.1 shows the measured intensity distribution on the station. The intensity of the beam was monitored as the monochromator angle was varied. The peak flux of the station occurs at a wavelength of approximately 1.3Å.

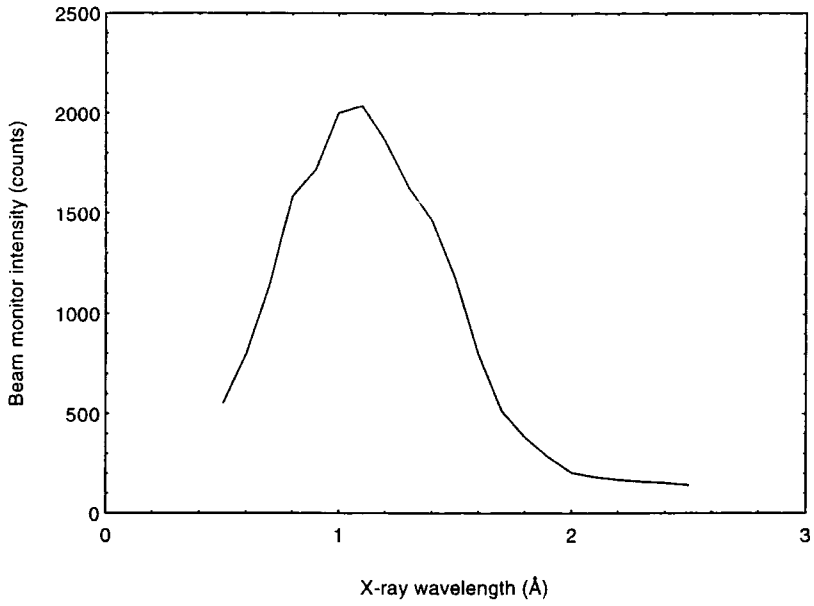

Figure 4.1: The intensity distribution from the station

The monochromatic x-ray beam is incident onto the sample which is placed on a flat plate at the centre of the diffractometer. Station 2.3 was originally designed for powder diffractometry studies, and so has two encoded circles. The sample or omega circle has a resolution of 0.72" and the detector axis has a resolution of 0.36". Both axes are controlled independently by a servo-drive system. The sample plate has motors which are capable of translating the sample vertically and a basic chi rotation is also available. Both of the vertical translation and chi rotation are controlled by motors which have a high degree of backlash. These motors are not encoded, but they are only required for the initial sample alignment.

The resolution of the instrument is not only defined by the incident slits, but also by the detector geometry. Analyser slits immediately in front of the detector were set to the same height as the incident slits. The height of the slits are here defined to mean out of the plane of the beam. An additional slit was placed on the detector arm, closer to the sample. This additional slit was kept to 1mm in height and reduced extraneous scatter. Both slits on the detector axis were set to a width of 10mm, which resulted in very poor resolution in the q_y direction. The distance between the two slits and their relative heights gave a calculated angular acceptance

for the detector of 613". The path between the two detector slits was evacuated with an aluminium can fitted with Kapton® windows in order to reduce the air scatter. With the slits in this arrangement, a count rate of typically 10^8 c.p.s. was observed in the detector for the main beam. Figure 4.2 shows a scan across an attenuated beam when the two sets of slits were set to 100μm and the incident wavelength was 1.38Å. In this alignment, the instrument resolution was very good, and the beam profile could be fitted to a Gaussian with a FWHM of 43±1" [7].

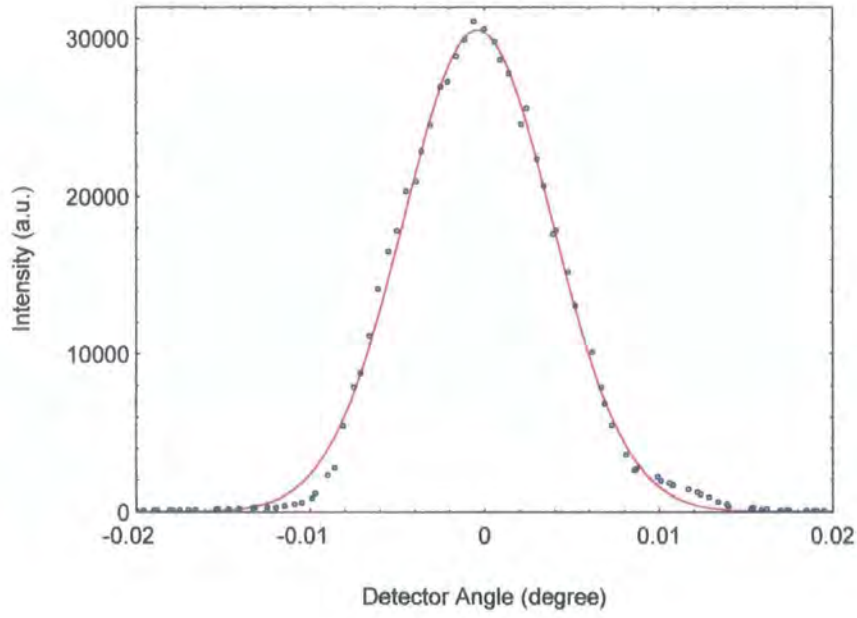

Figure 4.2 Scan of the detector across the incident beam at λ=1.38 fitted to a Gaussian (line). The FWHM of the fitted peak is 43 ± 1".

A schematic of the station set up for reflectometry studies is shown in figure 4.3. It is relatively easy to change the set-up in order to conduct diffraction or fluorescence experiments. For detailed, energy dispersive, fluorescence experiments, a Si(Li) detector is situated 20cm, vertically above the sample. For high angle diffraction experiments, it is sometimes advantageous to reduce the resolution of the instrument. This can be achieved by either increasing the height of the post-monochromator or analyser slits. The resolution can also be reduced by replacing the

two slits defining the acceptance angle of the detector by a pair of Soller slits (parallel foils).

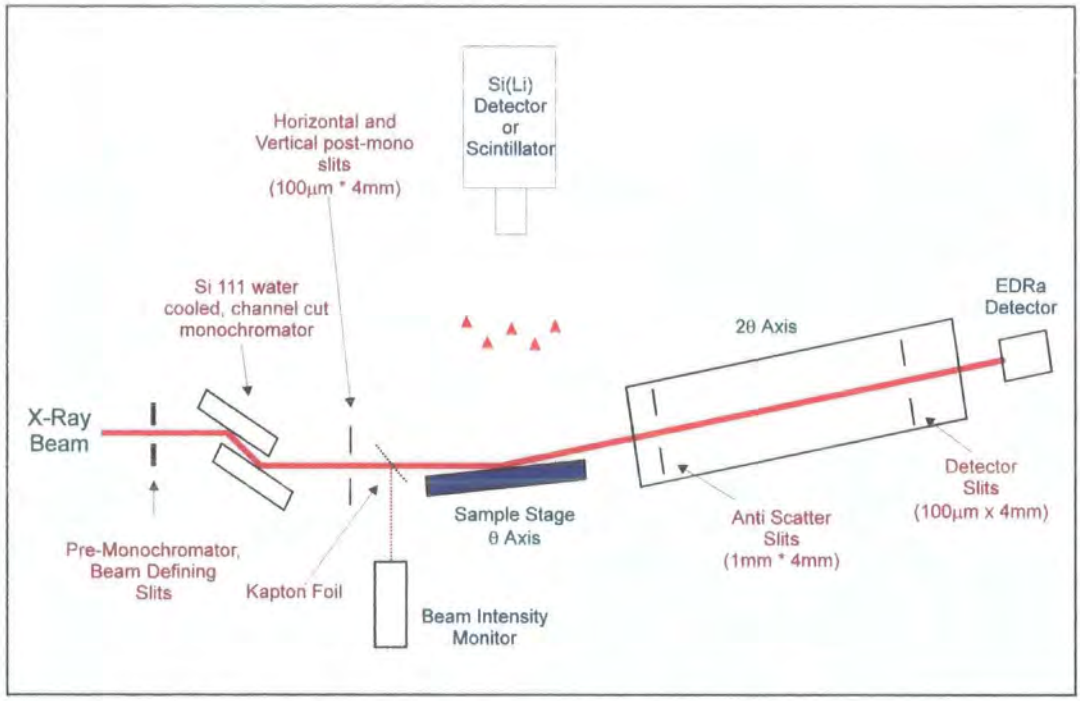

Figure 4.3: A schematic of Station 2.3

Plate 4.1 shows a close up photograph [5] of the diffractometer when it is set up for reflectometry studies. Clearly visible are the two encoded axes (*A* shows the 2θ axis, and *B* marks the sample axis). The sample is placed on the vertical goniometer, marked by *C*. The evacuated detector assembly is shown by *D*. As the count rates are so high, it is sometimes necessary to attenuate the beam, and *E* shows a remote controlled attenuation system.

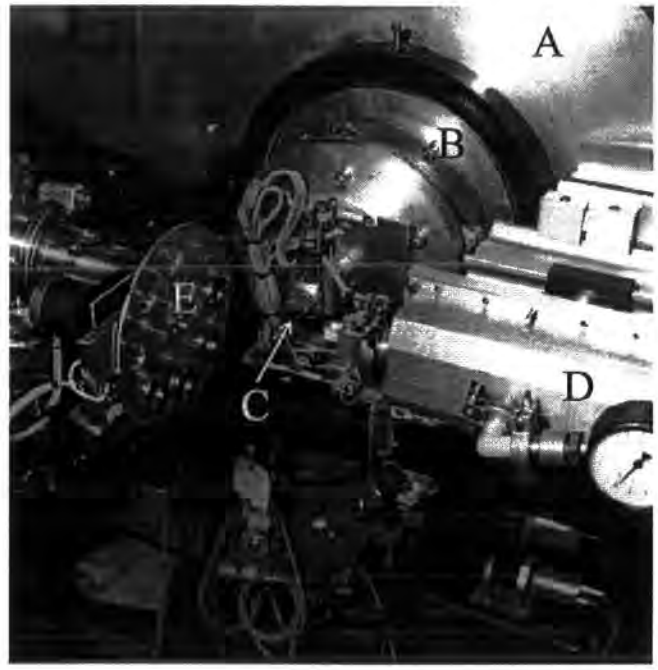

Plate 4.1: A close in of the diffractometer when set up for reflectivity.

An important part of any experimental synchrotron set-up is the detector. With the high flux inherent in synchrotron sources, detectors with a high dynamic range are advantageous. Typical detectors used for counting x-rays are based on scintillation materials, commonly NaI(Tl). These materials produce a pulse of light for each x-ray absorbed by the material, which is then amplified by complex electronics. The intrinsic decay time for NaI(Tl) is 230ns, but aluminium yttrium oxide, which can be used for this purpose, has an intrinsically lower decay time of 27ns [8] which is advantageous in some circumstances. The dead time for a paralysable detector can be calculated using the equation [9]:

$$R_{meas} = R_{real} \exp(-R_{real}\tau) \qquad [4.5]$$

where τ is the dead time of the system. The detector used for all x-ray scattering studies conducted using hard x-rays was a Bede Scientific EDRa with a dead time calculated to be approximately 350ns. The minimum count rate was 0.15 counts per second. and the detector was non-linear for count rates greater than $4*10^5$ c.p.s. A program based on a Newton-Raphson routine was written to correct the data sets for

the detector dead time. A copy of the printed code is attached to this thesis in appendix *A*. This program worked extremely well for real counts up to $1.8*10^6$, and was particularly useful in correcting data taken on a laboratory source. Although the detector has an extremely large dynamic range, attenuation was still required to monitor the main beam. When the range exceeded that observable by the detector, the beam was attenuated using aluminium and the data scaled accordingly. All such scaling was seen to overlap effectively with no glitches in the data sets.

4.3 Beamline 16, ESRF

Beamline BM16 at the ESRF [10] is very similar to Station 2.3 at the Daresbury SRS. Both beamlines were designed for powder diffraction studies and as such both use an encoded two circle diffractometer. The only difference in the design of the experimental end of the beamline, is that there is an additional analyser system on the detector axis of the diffractometer at BM16. This analyser system comprises nine germanium (111) crystals separated by 2 degrees. The presence of an analyser stage enables triple axis diffraction studies to be undertaken, as well as the conventional powder scans. As the storage ring at the ESRF operates at 6 GeV, the critical wavelength is shorter, and there is therefore more intensity at the higher energy end of the incident spectrum on BM 16.

The major difference between BM 16 and station 2.3 is in the design of the optical elements placed in the beam. The monochromator is comprised of two Si(111) crystals. The first crystal is flat and water cooled, whilst the second can be bent to focus sagittally the beam. A horizontal focusing system is adopted with the source to crystal distance being equal to the crystal to sample distance. This sagittal focusing does not effect the vertical collimation of the beam at all and therefore the angular divergence is unaffected. An increase in flux can be achieved by focusing the beam vertically by the use of a mirror placed directly down-stream of the monochromator, but this reduces the angular resolution.

The background in this arrangement is also considerably reduced. Much of the background radiation comes from scatter from the monochromator and slits which are here in a separate room, twenty meters away from the experiment. The horizontal arrangement of the beamline is shown in figure 4.4:

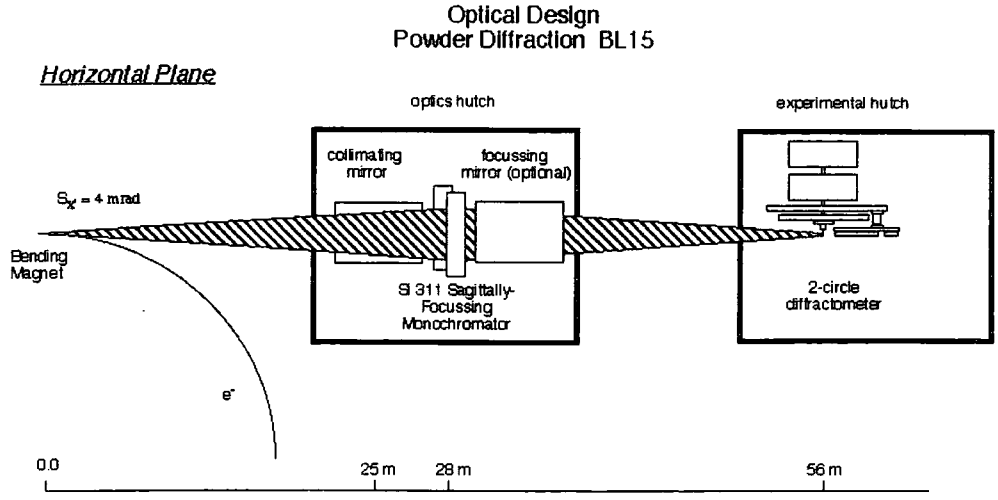

Figure 4.4: The horizontal alignment of BM 16 showing the sagittally focusing monochromator and mirrors [11]

In previous sections details on BM 16 and Station 2.3 have been presented. Although there are considerable differences between the two, both stations use a two circle diffractometer. In the following sections considerations for the alignment of both the diffractometer and subsequently samples will be discussed.

4.4 Alignment of a Two Circle Diffractometer Station

The most important criteria in aligning the diffractometer is to ensure that the sample holder, and consequently the sample itself, is at the centre of rotation of the diffractometer. This is achieved by rotating the omega axis by 180 degrees and ensuring that the surface of the sample holder does not move, laterally or vertically. An iterative process is used, by using small corrections to the goniometer. A travelling microscope ensures that this alignment is accurate to within 25μm, in both directions. The height of the diffractometer is then adjusted such that the sample

holder half cuts the incident 100μm beam. Once this has been achieved, the position of the diffractometer is not changed, and the height of the sample is adjusted by the motor on the goniometer until the sample surface half cuts the beam.

For experiments exploiting the tunability of synchrotron radiation to enhance the scattering from the interfaces by the use of anomalous dispersion (chapter 5), it was found impossible to rely on the absolute accuracy of the monochromator calibration. As the variation in the anomalous dispersion correction to the scattering factor changes very rapidly, it was essential to locate reproducibly the wavelength with respect to an absorption edge such as copper. This was achieved by recording a near edge X-ray absorption fluorescence (NEXAFS) spectrum from a standard sample in the vicinity of the copper absorption edge. As the energy dispersive nature of the signal was not important, a scintillator situated 20cm vertically above the sample was used. It was found that the first peak of the NEXAFS spectrum of copper in brass (Figure 4.5) was clearly visible in the fluorescence detector and this proved a very convenient reference point.

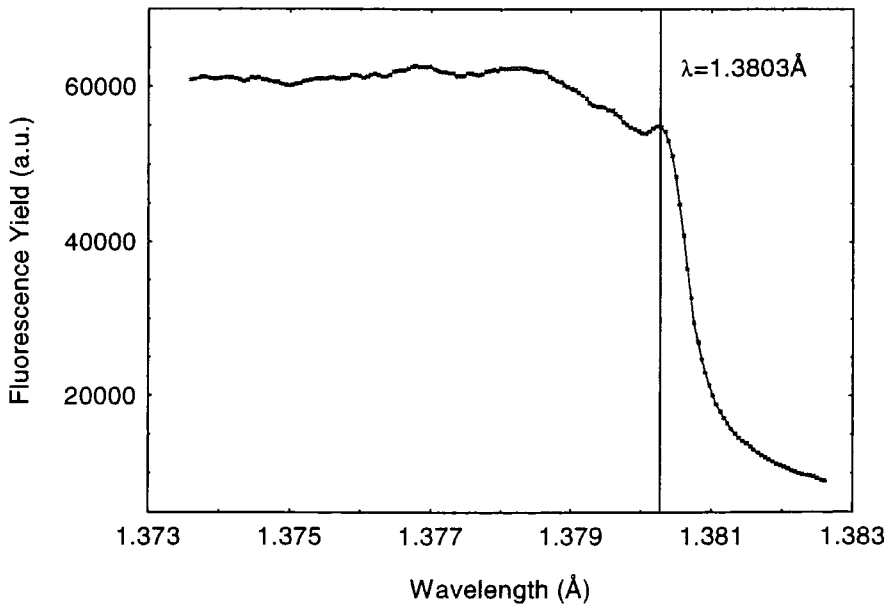

Figure 4.5: Measured fluorescence yield from Cu in brass as a function of wavelength. The marked line is at λ=1.3803Å

4.5 Sample Alignment

The alignment of the sample is reasonably straight forward once the diffractometer has been properly aligned. Initially an absorber was placed into the beam (E in plate 4.1), and then the detector arm was scanned through the attenuated beam to ensure that the maximum intensity occurred at zero angle. It was found that over the wavelength range available on the station, the position of the beam changed by 20". The sample was then mounted on the vertical goniometer and raised until the beam's intensity had halved. To ensure that the sample was flat, the sample angle was rocked until a maximum signal was measured. This value of omega was then set to zero, and the height of the sample was again adjusted until the beam had been half cut. The attenuator was then removed and the detector moved to 2°. The sample was rocked in 1.8" steps until a maximum was found. This value of sample angle was set to half the detector value. This process was repeated at higher scattering angles to ensure correct alignment. The sample was now aligned to the specular condition and was at the centre of rotation of the diffractometer.

4.6 Conclusions

This chapter has introduced the reader to synchrotron radiation. The high flux from such sources has been observed to be caused by Lorentz transform of the radiated x-rays into a very narrow cone. The stations where experiments analysed in this study were carried out were then introduced. With the high flux of synchrotron sources a detector with a high dynamic range is required. Although such a detector was used, it was still found necessary to correct the data for the dead time and a computer programme developed from a Newton-Raphson technique was used. The wavelength calibration of the station was conducted by studying the NEXAFS signal from copper. The chapter was rounded off by a brief discussion on the alignment of the samples.

References from Chapter 4

1 X-ray Science and Technology, *Eds. A G. Michette and C.J. Buckley*, IOP Publishing, (1993)

2 Wen-Jih Lin, Ph. D. Thesis, University of Edinburgh

3 Neutron and Synchrotron Radiation for Condensed Matter Studies Vol 1., *Eds. J. Baruchel, J.-L. Hodeau, M.S. Lehmann, J.R. Regnard and C. Schlenker*, Springer-Verlag, (1993)

4 G. Margaritondo, *J. Synchrotron Rad.*, 2, *148-154*, (1995)

5 C.C. Tang, M. Miller, D. Laundy, *Station 2.3 Manual*, CCLRC Daresbury Laboratory: *http://www.dl.ac.uk/SRS/XRD/2.3.dir/stn23.html*

6 R.J. Cernik, P.K. Murray, P.Pattison, A.N. Fitch, *J. Appl. Cryst.*, 23, *292-296*, (1990) AND S.P. Collins, R.J. Cernik, P. Pattison A.M.T. Bell, A.N. Fitch, *Rev. Sci. Instrum.*, 63 (1), *1013-1014*, (1992)

7 B.K. Tanner, D.E. Joyce, T.P.A. Hase, I. Pape, P.J. Grundy, *Adv. X-ray Analysis*, **41**, *CD-Rom Edition,* (1997)

8 S. Cockerton, B.K. Tanner, *Adv. in X-ray Anal.*, 38, *371-376*, (1995)

9 D.R. Beaman, J.A. Isasi, H.K. Birnbaum, R. Lewis, *J. Phys. E: Sci. Inst 1*, 5, *767-776* (1972)

10 A.N. Fitch, *Materials Science Forum,* **228** (1&2), *219-221*, (1996)

11 Reproduced from *http://www.esrf.fr/exp_facilities/bl15/handbook/handbook.html*

Chapter 5

Anomalous Dispersion and Graded Interfaces

This chapter aims to introduce the reader to some important extensions to the theoretical ideas given in chapter 3. It falls into two main sections; in the first, changes to the atomic scattering factor when the incident energy is close to an absorption edge are discussed. The latter part of the chapter deals with the idea of a graded interface, or an interface where there is heavy interdiffusion between the two materials.

Section 5.1 contains an overview of the theoretical advances in our understanding of anomalous dispersion. Section 5.1.1 gives a more detailed theoretical description of anomalous dispersion following the work of James [1]. The methods used to calculate the correction terms, as well as experimental verification of them is detailed in section 5.1.2. A more general overview of experimental studies undertaken using anomalous dispersion is given in section 5.2, and section 5.3 discusses in greater detail experimental results using anomalous dispersion from Cu/Co multilayers. Finally in the last section details on how the theory in chapter 3 was extended to include a graded electron density profile across an interface .

5.1 Anomalous Dispersion

It is the goal of this section to introduce the reader to the theory of anomalous dispersion, and the problems involved in calculating its effects. In this section an overview of the classical formulation of dispersion will be given, and the basic equations required to calculate the effects of anomalous dispersion will be derived (equations 5.17 and 5.18). Following on from this, a brief overview of the methods used to calculate these equations is presented.

It has already been shown that the cross section for elastic scattering of x-rays (known as Thomson scattering) is the Fourier transform of the electron density function, $\rho(r)$. In the previous derivations in chapter 3 it was assumed that the incident x-ray frequency, ω, was away from any absorption edge. When this is the case, the absorption of the x-rays can be excluded, and the scattering can be described by the normal atomic scattering coefficient, f_o.

Anomalous dispersion arises when the incident energy is high enough such that the photons can be scattered normally, or they can be absorbed. When this is the case, the atomic scattering factor is modified and becomes complex:

$$f = f_o + f' + if'' \qquad [5.1]$$

It is the additional term f' which give rise to the effect known as anomalous dispersion. The two factors, f' and f'' vary with energy, and show large changes in the vicinity of the absorption edges. With the ability to change wavelengths using synchrotron light it is particularly important to be able to calculate these correction terms accurately.

In order to arrive at a series of equations whereby these correction terms can be calculated, it is useful to follow the classical work of James [1]. This is done in more detail in section 5.1.1. The electron is initially considered to be an electric dipole oscillator. Starting from this position, James derived the radiative field produced from such an oscillator (eqn. 5.6). The atomic scattering factor is defined as the ratio of the scatter produced from this dipole to the scatter arising from a free, isolated electron (eqn 5.7). In order to account for the large number of possible excited states that the electron can be scattered into, the idea of a continuum of oscillators with associated oscillator coupling strengths is then introduced. The final equations for calculating the anomalous dispersion correction terms is accomplished by relating these oscillator densities to the photoelectric absorption coefficient.

5.1.1 The Classical Formulation of Anomalous Dispersion

The classical theory of dispersion assumes that the electrons can be considered as electric dipole oscillators. These oscillators exhibit damped, simple harmonic oscillations under a force exerted by the exciting electric field, introduced by the photon. This oscillator can be considered to be a mass m, moving about a massive, stationary positive charge. This model is due to the nature of the bound electronic state. Impinging on this state is the x-ray photon of frequency, ω. Associated with this photon is an electric field, at the position of the dipole defined as $\vec{E} = \vec{E}_o \exp(i\omega t)$. If the polarisation factor is assumed to be unity, then all the scatter is confined to a plane perpendicular to the plane of the incident electric vector. The dipole is thus forced into oscillations whose displacement $\vec{x}$, perpendicular to the direction of the field, has the equation of motion [1]:

$$\ddot{\vec{x}} + \gamma\dot{\vec{x}} + \omega_s^2\vec{x} = \frac{e\vec{E}_o}{m}\exp(i\omega t) \qquad [5.2]$$

where ω_s is the natural frequency of the oscillator and γ is a damping constant associated with the velocity of the displaced charge.

In the steady state, the dipole executes forced oscillations with a frequency ω, and its displacement will be of the form $\vec{x} = A\vec{E}_o \exp(i\omega t)$. It can be shown that this displacement is in fact:

$$\vec{x} = \frac{e}{m}\,\frac{\vec{E}_o \exp(i\omega t)}{\omega_s^2 - \omega^2 + i\gamma\omega} \qquad [5.3]$$

The moment of this oscillating dipole is defined as:

$$\vec{M} = e\vec{x} \qquad [5.4]$$

The radiated electric field produced, in the forward direction, from this oscillating dipole can be expressed in terms of this moment (in the far-field approximation) [2]:

$$\vec{E}_{Rad} = \frac{\left[\ddot{\vec{M}}\right]}{|\vec{r}|c^2} \qquad [5.5]$$

The instantaneous electric field at time, t, is a function of the retarded time, $t - |\vec{r}|/c$, and so by using this and equations 5.3 and 5.4, the radiative electric field from the dipole can be written as:

$$\vec{E}_{rad} = \frac{e^2\omega^2\vec{E}_o \exp\left(i\omega\left(t - |\vec{r}|/c\right)\right)}{mc^2\,|\vec{r}|\left(\omega_s^2 - \omega^2 + i\gamma\omega\right)} \qquad [5.6]$$

The dipole scattering factor is defined as the ratio of the scatter arising from this oscillating dipole to the scatter produced by a classical, free electron under identical conditions. The scatter from a free electron is calculated by setting $\gamma=\omega_s=0$. Thus the scattering factor of the dipole is:

$$f = \frac{\omega^2}{(\omega^2 - \omega_s^2 - i\gamma\omega)} \qquad [5.7]$$

A simple rearrangement enables equation 5.7 to be re-written in a form comparable to equation 5.1:

$$f = \left[\frac{\omega^2\left(\omega^2 - \omega_s^2\right)}{\left(\left(\omega^2 - \omega_s^2\right)^2 + \gamma^2\omega^2\right)}\right] + i\left[\frac{\gamma\omega^3}{\left(\left(\omega^2 - \omega_s^2\right)^2 + \gamma^2\omega^2\right)}\right] \qquad [5.8]$$

The real part of the atomic scattering factor also includes the Thompson scatter, f_o, and if $\gamma=\omega_s=0$, then the dipole scattering factor for the free electron, $f=f_o=1$ is obtained. If the damping constant, γ in equation 5.7, is small such that the incident wavelength is sufficiently far from an absorption edge that it does not couple strongly to the atomic frequencies, then the real part of the scattering factor becomes:

$$\Re(f) = \frac{\omega^2}{\omega^2 - \omega_s^2} \qquad [5.9]$$

Even in the most simple single electron atom, the hydrogen atom, there is (in the classical derivation) a continuum of negative energy states into which the electron can be excited. So instead of a single oscillator, a range of oscillators, *g(1)....g(s),* with associated frequencies $\omega(1)....\omega(s)$ must be considered. Equation 5.9 will then become a summation over all these excited states, *s* [1]:

$$\Re(f) = \sum_s \frac{g(s)\omega^2}{\omega^2 - \omega_s^2} = \sum_s \left[g(s) - \frac{g(s)\omega_s^2}{\omega_s^2 - \omega^2} \right] \qquad [5.10]$$

Quantization of the excited states leads to fewer oscillators, but with well defined frequencies, those given by the Bohr model. The oscillator coupling strengths for these 'quantum' oscillators is now defined by the function, *g(k,n).* So for each of the oscillator strengths, *g(s)* there exists the equivalent quantum mechanical coefficient *g(k,n).* These *g(k,n)* coefficients describe the spontaneous transition probabilities between the states *k* and *n* with a frequency ω_{kn}. In the case of hydrogen, as there is only one electron, there is an additional requirement on *g(k,n)* and therefore on *g(s)* such that the sum of the coefficients must equal the total number of electrons in the system:

$$\sum_k g(k,n) = 1 \qquad [5.11]$$

This is the well known Thomas-Reiche-Kuhn summation rule.

Before this single-electron model can be extended to a multi-electron atom, several assumptions are required. These are that the electrons are independent, or isolated, and that it is only the core electrons that contribute to the anomalous scattering. This in practice limits the validity of the calculations to energies in the range 4 to 100keV (3Å<λ<0.1Å). To ensure that there is no angular dependence on the scatter from the anomalous terms, the size of the charge distribution must be small in relation to the incident wavelength. This assumption

was tested by Suortti et al. [3] who found that the angular variation of f' was less than 0.2 electron units.

The most significant difference between the single electron model and a normal atom is in the electron configuration. In the single electron atom, all the excited states are available but in the multi-electron system a high number of these states are already occupied. By the Pauli exclusion principle all transitions, and hence oscillator strengths, relating to excitations between occupied states must be zero. There will, however, be some negative energy states into which the electron can be scattered. As the wavefunction overlap between these negative energy states is small, the corresponding transition probability tends towards zero. The only significant transitions are thus into this positive energy continuum.

The number of virtual oscillators in the range $\omega + \delta\omega$ is defined as $\left(dg/d\omega\right)d\omega$. $\left(dg/d\omega\right)$ is the oscillator density at frequency ω. By only considering the positive states, this distribution has a lower limit set to the absorption edge of type k, ω_k. This enables the total oscillator coupling strength associated with the k electrons to be expressed as:

$$g_k = \int_{\omega_k}^{\infty} \left(\frac{dg}{d\omega}\right)_k d\omega \qquad [5.12]$$

For a multi-electron atom, the Thomas-Reiche-Kuhn summation rule is now extended to include all the electrons, such that $\sum_k g_k = Z$, where Z is the atomic number. Equation 5.10 now therefore becomes:

$$\Re(f) = Z - \sum_k \int_{\omega_k}^{\infty} \frac{\omega^2 \left(dg/d\omega\right)_k d\omega}{\omega^2 - \omega_i^2} \qquad [5.13]$$

The exciting photon has a frequency now defined as ω_i. The summation in equation 5.13 is now taken over all the electron groups, K, L ,M ... In general the integral in equation 5.13 will not be equal to the number of electrons in each group, but to a

smaller number [1]. A comparison between equations 5.13 and 5.1 shows that the Thompson scattering component is equal to the atomic number, Z, the limit in the low angle or forward scattering limit, and f' becomes:

$$f' = \sum_k \int_{\omega_k}^{\infty} \frac{\omega^2 \left(dg/d\omega \right)_k d\omega}{\omega_i^2 - \omega^2} \qquad [5.14]$$

This oscillator density can be determined exactly if the atomic wavefunctions are known and all the transitions calculated. However, the oscillator density can also be defined in terms of the atomic photoelectric absorption coefficient, $\tau(\omega)$ [4]

$$\left(dg/d\omega \right)_k = \frac{mc}{2\pi^2 e^2} \tau(\omega)_k \qquad [5.15]$$

where $\tau(\omega)_k$ is the photoelectric absorption coefficient for k type electrons for a frequency ω. The photoelectric absorption coefficient is related to the linear absorption coefficient, $\mu(\omega)$, by $\mu(\omega) = \tau(\omega) + \sigma(\omega)$ where $\sigma(\omega)$ is the linear scattering coefficient [5]. $\tau(\omega)$ is also known as the fluorescence absorption coefficient.

To enable the integral in equation 5.13 to be calculated in a closed form, the absorption coefficient can be approximated by [1,4]:

$$\tau(\omega)_k = \begin{cases} \left(\omega_k / \omega \right)^n \tau(\omega_k) & \text{for} \quad \omega > \omega_k \\ 0 & \omega < \omega_k \end{cases} \qquad [5.16]$$

where $\tau(\omega_k)$ is the absorption coefficient at the absorption edge and n depends on the specific electron orbital considered. Substitution of equations 5.15 and 5.16 into equation 5.14 results in an expression for the real part of the anomalous scattering [6,7]:

$$f' = \sum_k \left[\frac{mc}{2\pi^2 e^2} \tau(\omega_k) \omega_k^n \int_{\omega_k}^{\infty} \frac{\omega^2 d\omega}{(\omega_i^2 - \omega^2)\omega^n} \right] \qquad [5.17]$$

It is also possible to describe the imaginary component of the anomalous scattering in terms of the photoelectric absorption coefficient [8]:

$$f'' = \sum_k \left[\frac{mc}{4\pi e^2} \omega_i \left(\omega_k / \omega \right)^n \tau(\omega_k) \right] \qquad [5.18]$$

Equations 5.17 and 5.18 contain all the information required to calculate the anomalous dispersion terms. In the following section, 5.1.2, the various methods used to calculate these anomalous dispersion terms corrections are discussed. The problems in experimentally confirming the calculations are also presented.

5.1.2: Calculation and Experimental verification of the Anomalous Dispersion Corrections

In order to justify neglecting the damping term from equation 5.9 onwards, the integral in equation 5.17 was calculated by Parratt and Hempstead [4] both with and without the damping term, γ included in the calculations. It was shown by the authors that neglecting the damping term in the derivation was justified so long as ω/ω_k differed from unity by 10^{-4}.

Initial attempts to calculate the anomalous dispersion corrections were undertaken by Dauben and Templeton [9] who used experimental values for the absorption coefficient. Cromer [6] improved the accuracy of Dauben and Templeton's calculations by calculating the oscillator strengths calculated from Dirac-Slater wavefunctions. In both cases the authors followed both James [1] and Parrat and Hempstead's [4] work (equation 5.17 and equation 5.16) and summed over the different absorption edges. The values of n (equation 5.16) used in these calculations were taken from the same work [4] and were assumed to be 11/4 for the

$1s_{½}$, 7/3 for the $2s_{½}$ and 5/2 for all other edges. The limiting accuracy of this method is in the approximation of the photoelectric absorption. To remove this approximation Cromer and Liberman [10,11] used relativistic calculations of the absorption cross-section and performed the integral in equation 5.14 (after substituting equation 5.15) numerically. These calculations introduced an additional correction to the real part of the anomalous scattering which is proportional to the total energy of the atom, E_{Tot}, such that:

$$f'_{True} = f'_{James} + \frac{5E_{Tot}}{3} \qquad [5.19]$$

The values of f' and f'' were tabulated for all the elements for specific incident wavelengths. Interpolation routines are used to calculate the anomalous dispersion terms for any wavelength in-between these tabulated values. A version of this interpolation code was written by M. Wormington [12], and this interpolation routine is the basis of all the anomalous scattering work contained in this study.

Experimental verification of these theoretical values is complicated by the binding and chemical effects in real samples. However methods do exist to determine either f' or f''. As f' and f'' are the real and imaginary response to a linear, passive system they must obey the Kramers-Kronig relations. These relations enable the real part of the response to the system to be calculated, if the imaginary part of the response is known over a wide frequency range, and vice-versa [13]. As f'' is directly related to the absorption coefficient, much of the experimental verification of anomalous dispersion correction terms comes via absorption studies. If the absorption data is taken over a sufficiently large energy range, f' can be calculated via the Kramers-Kronig relations. Absorption studies as a function of energy are complicated by interference effects coming from the local binding of the atoms under investigation (extended x-ray absorption fine structure - EXAFS). It is also possible to measure f' and f'' via x-ray interferometry techniques [14], as well as by direct measurements on the shape of crystal rocking curves [15,16]. In all cases, the theoretical values have been shown to be accurate to within 0.3 electrons.

Figure 5.1 shows the variation of f' and f'' as a function of wavelength for lanthanum [17]. It is clear that changes in f' and f'' are greatest at the absorption edges. The absorption edges, calculated from tabulated electron binding energies [18], are also shown in figure 5.1:

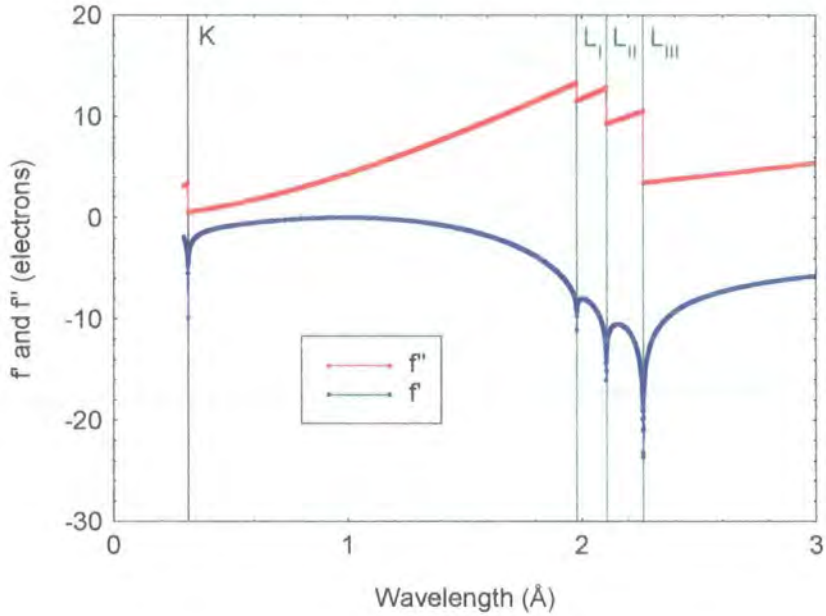

Figure 5.1: f' and f'' as a function of wavelength for La.

Figure 5.2 shows the calculated [17] mass attenuation coefficient for lanthanum. A comparison between figures 5.1 and 5.2 clearly show the relation between f'' and the absorption coefficient as described in equation 5.18.

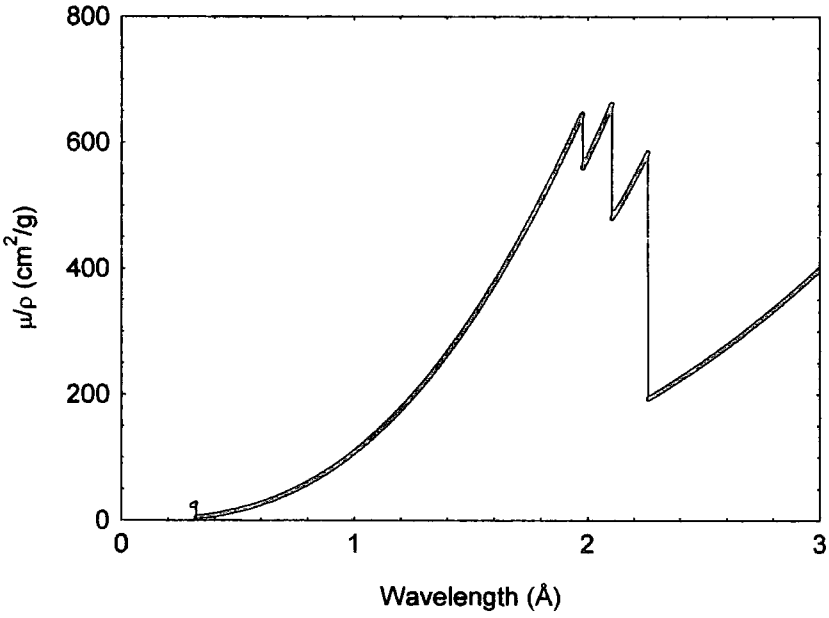

Figure 5.2: The mass absorption coefficient as a function of wavelength for La

The corrections to the atomic scattering factor that are detailed above show the importance of the anomalous dispersion terms. Although the effect is greatest at the absorption edges themselves, there are still corrections to be made away from the absorption edges. Anomalous dispersion is particularly important for scattering experiments undertaken at synchrotron sources where, due to the continuous emission spectrum of a synchrotron source, the incident wavelength can be deliberately tuned close to an absorption edge of the material under investigation.

5.2 Using Anomalous Dispersion

The deeper understanding of the nature of anomalous dispersion detailed in the previous section has allowed the phenomenon to be used in various experimental environments since the advent of synchrotron radiation. Anomalous dispersion is now commonly used in protein crystallography where it can be used to give a degree of phase information on the diffracted scatter [8]. It is also commonly used in powder diffraction studies, where, in conjunction with Rietveld analysis, it can be used to increase the sensitivity to atomic positions within the unit cell. This site selectivity is achieved by conducting two experiments, one with the wavelength

tuned close to the absorption edge of the particular element of interest [19], and one with the incident wavelength far from any absorption edges in the material.

In this study, anomalous dispersion has been used to increase the contrast between layers composed of elements close to each other in the Periodic Table. Work undertaken by Nakayama et al. [20] showed that the intensity of the zero order diffraction peak of a Fe/Mn multilayer increased sharply at the absorption edge of the manganese. Nakayama et. al. showed that the Bragg peak intensity was proportional to $\left|f_{Mn}n_{Mn} - f_{Fe}n_{Fe}\right|^2$ where f_X is the complex scattering factor and n_X is the atomic number density for element x. For multilayers where the number density of the two materials is equal, as is close to the case for the multilayers contained in this study, the intensity of the Bragg peak is simply proportional to the difference between the two atomic scattering factors.

Much of the experimental work undertaken in this study centred on Cu/Co interfaces. These interfaces occurred both within Cu/Co multilayers (chapters 7 and 8) or in spin valve structures (chapter 9). Anomalous dispersion was also used in chapter 6 where the interface under investigation was Co/Cr in trilayer structures. Figure 5.3 shows the variations of f' and f'' as a function of wavelength for copper and cobalt. For both elements, large changes to the scattering factor corrections occur as the wavelength is tuned through the *K* absorption edge.

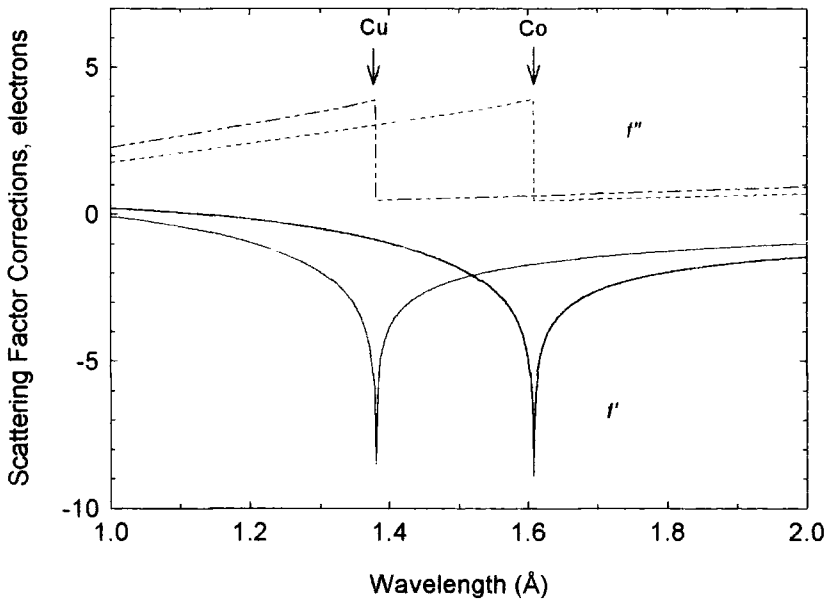

Figure 5.3: The variation of f' and f'' as a function of wavelength

Following the work of Nakayama et. al. [20], the scattering factor difference for an equal atomic density of Cu/Co was calculated. Figure 5.4 shows the modulus squared of the difference between the complex scattering factors of copper and cobalt. Near the absorption edges, the difference in the x-ray scattering factors is significantly enhanced, mainly by f' terms. An example is shown below for an incident wavelength of 1.381Å, which is just above the copper absorption edge:

$$\left|f_{Cu} - f_{Co}\right|^2 = \left|(Z_{Cu} - Z_{Co}) + \left(f'_{Cu} - f'_{Co}\right) + i(f''_{Cu} - f''_{Co})\right|^2 =$$
$$\left|(29-27) + (-8.49 + 0.87) + i(0.4831 - 3.04)\right|^2 = 38.1e^2$$

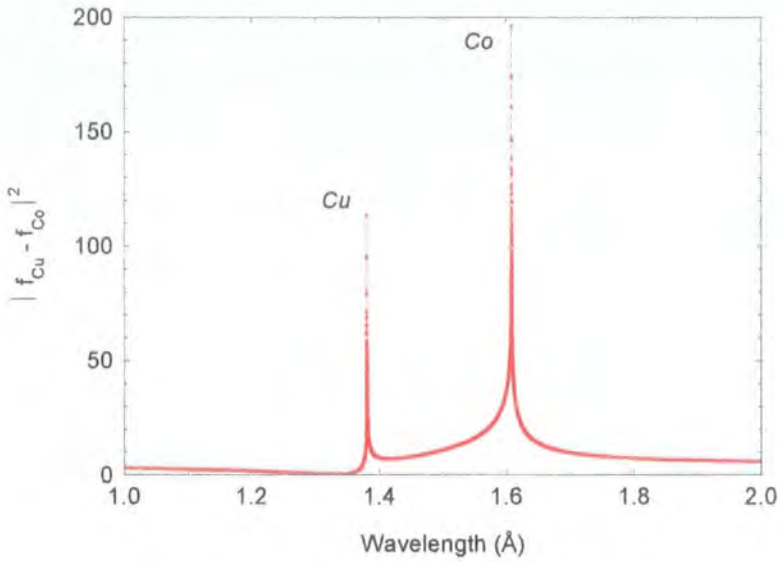

Figure 5.4: The scattering factor difference for equal atomic numbers of copper and cobalt

The large increase in the scattering factor difference observed at the copper edge is repeated at the cobalt edge (λ=1.608Å). The difference of approximately $80e^2$ between the two absorption edges is directly related to the absorption coefficient. Figure 5.5 shows the calculated absorption coefficients for copper and cobalt.

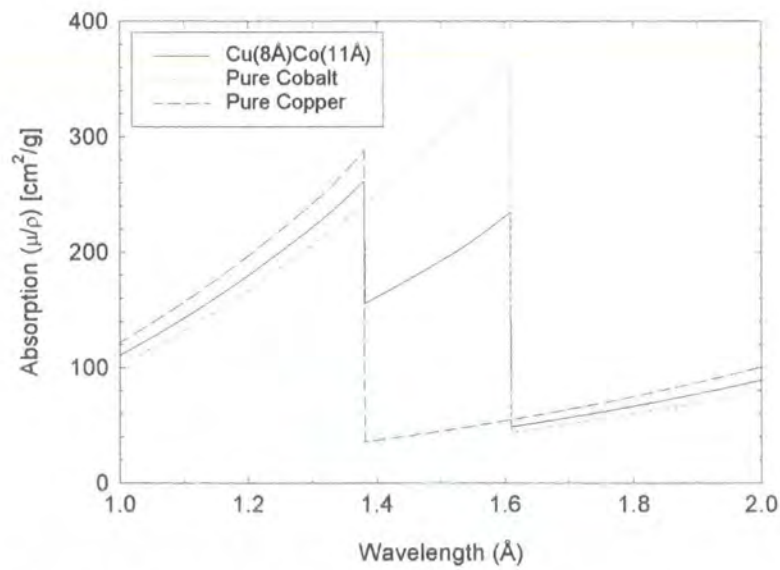

Figure 5.5: The mass absorption coefficient for copper, cobalt and a Cu(8Å)/Co(11Å) bi-layer.

The mass absorption coefficient for the Cu/Co bi-layer shown in figure 5.5 was calculated using

$$\mu_{Cu/Co} = \frac{\left(D_{Cu}\mu_{Cu} + D_{co}\mu_{Co}\right)}{\Lambda} \qquad [5.20]$$

where D_{Cu} and D_{Co} are the individual thickness of the copper and cobalt layers, and Λ is the total bilayer thickness. Although the scattering factor difference is enhanced at the copper edge, the absorption of cobalt atoms is, at these wavelengths rather high. It is for this reason that the anomalous enhancement is always greatest at a wavelength just above the absorption edge of the lightest element, in this case cobalt.

The factors determining the exact wavelength to be used in any experimental situation depend on a variety of parameters; the wavelength reproducibility, and the incident flux. For grazing incidence studies the sample structure is also important. The dependence of the sample structure can be explained in terms of the inherent surface sensitivity of the technique. For multilayer structures where anomalous dispersion can be used on either constituent element, it is often advantageous not to excite the surface material which may be oxidisied or contaminated in other ways. The background fluorescence signal is also reduced by not exciting the surface layer.

5.3 Anomalous Dispersion in Cu/Co Multilayers

All the anomalous dispersion experiments in this study were undertaken on Station 2.3 at the Daresbury SRS, details of which are given in chapter 4. The peak flux on this station was found to occur for wavelengths of approximately 1.3Å (figure 4.1) which was conveniently close to the copper *K* absorption edge of λ=1.3803Å. The high flux at this wavelength more than compensated for the higher scattering factor difference at the cobalt absorption edge. In order to separate the scatter originating from the multilayer itself, as opposed to the buffer and capping layers, the experiments were repeated at a wavelength far from any absorption peaks in the sample, namely, λ=1.48Å.

In this section the findings from a series of experiments demonstrating the anomalous dispersion effect will be presented. The results will show that although the enhancement is less than figure 5.4 might suggest, a significant enhancement of the copper and cobalt interfaces is still possible when the wavelength is tuned close to the copper absorption edge.

Figure 5.6 shows the specular reflectivity from a Cu/Co multilayer deposited on a GaAs substrate by MBE [21]. The experiment was undertaken at and away from the copper absorption edge so as to highlight the effects of the anomalous dispersion. The anomalous dispersion effect increases the scattering power of the copper, and thereby enhances the scattering originating from the Cu/Co interfaces. As the scatter from these interfaces is confined to the Bragg Peak, the effect of the anomalous dispersion corrections should also be confined to this region only. This is clearly demonstrated in figure 5.6. The critical angle, and the Kiessig fringes, are exactly matched in both phase and amplitude for both wavelengths. At the Bragg Peak, however, there is an increase in the intensity when the incident wavelength is tuned close to the copper edge.

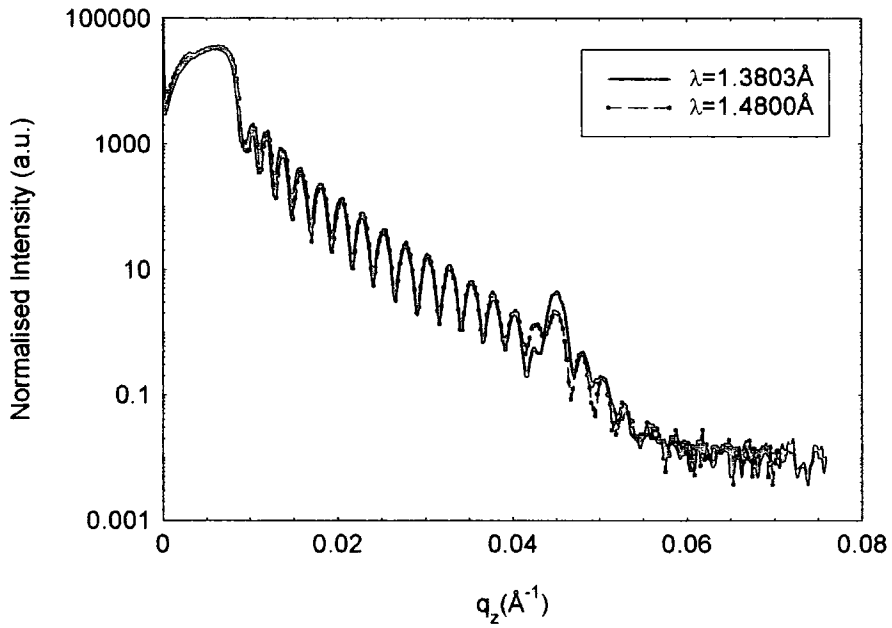

Figure 5.6: Specular Reflectivity at (λ=1.3803Å) and away from (λ=1.48Å) the Cu absorption edge from a sample with nominal structure-
GaAs/Ge(500Å)/Co(15Å)/Au(10Å)/{Co(15Å)/Cu(7Å)}*15/Au(15Å)

It follows from equation (3.53) that the integrated diffuse intensity must scale with the specular intensity. Therefore, the anomalous dispersion technique can also be illustrated by considering the integrated diffuse intensity at a Bragg Peak. Figure 5.7 shows the integrated diffuse intensity measured as a function of wavelength, ratioed with the same scan taken at λ=1.48Å, from a Cu/Co multilayer grown on Silicon. The nominal structure for the sample was Si/Co_3Si/Au(18Å)/{Co(15)/Cu(7)}x20/Au(10Å).

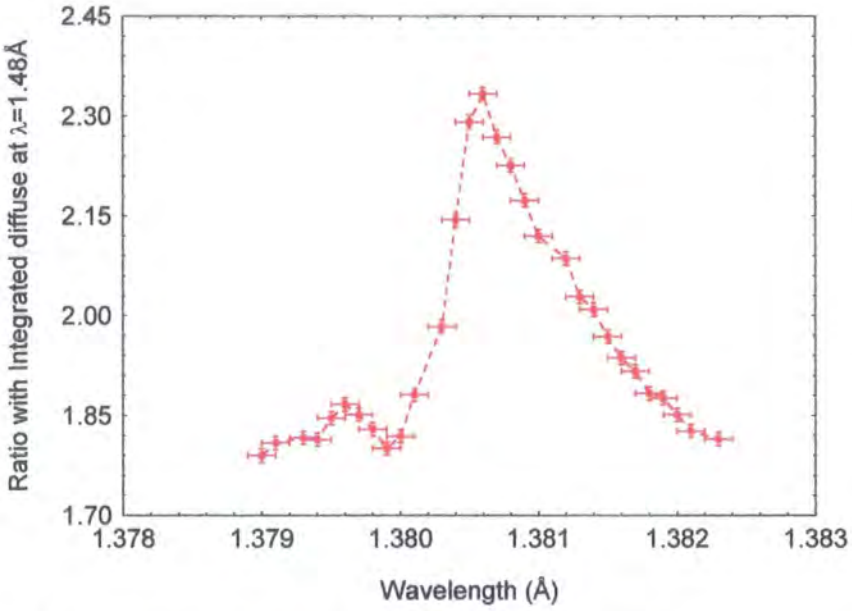

Figure 5.7: The integrated intensity of the diffuse scatter from an MBE grown Cu/Co multilayer deposited on silicon as a function of wavelength, scaled with the same measurement taken at λ=1.48Å

Although the enhancement at the copper edge is not as sharp, or as large as that suggested in figure 5.4, there is still a considerable enhancement (approximately double) of the diffuse scatter as the wavelength is tuned through the copper edge. This large enhancement confirms that much of the diffuse scatter is coming from correlated roughness from the copper interfaces. A more detailed analysis of the data in figure 5.7 is not possible due to the effects of partially correlated and uncorrelated roughness originating from the buffer and capping layers. These data do however, clearly demonstrate the usefulness of the technique of anomalous dispersion when studying diffuse scatter in materials which are close in the Periodic Table.

In the previous sections, the equations required to calculate the anomalous dispersion terms have been derived. The experimental verifications have shown that these calculations are accurate to within 0.3 electrons. Experiments utilising anomalous dispersion are becoming more wide spread with the increase in synchrotron radiation availability and the relative ease of calculating the anomalous terms accurately. In particular the use of anomalous dispersion in Cu/Co multilayers has been demonstrated. A clear enhancement in the x-ray scattering from the Cu/Co interfaces was observed for wavelengths tuned close to the copper absorption edge. For multilayer samples where the materials are close in the Periodic Table, enhancement of the Bragg peak scatter occurs when the wavelength is tuned to the lighter of the two materials due to absorption effects. This study uses anomalous dispersion in Cu/Co multilayers, as well as spin valve structures and Co/Cr multilayers.

This chapter now moves away from studying anomalous dispersion and concentrates on the extension of the theory outlined in chapter 3 that enables grading at an interface to be considered.

5.4 Interdiffusion or Grading Across an Interface

The theory of x-ray scattering described in Chapter 3, was specifically for interfaces which contained real roughness. In this section the effects of grading across an interface will be discussed in greater detail.

In chapter 3, the interface was assumed to be a purely rough interface, like that depicted in figure 5.8:

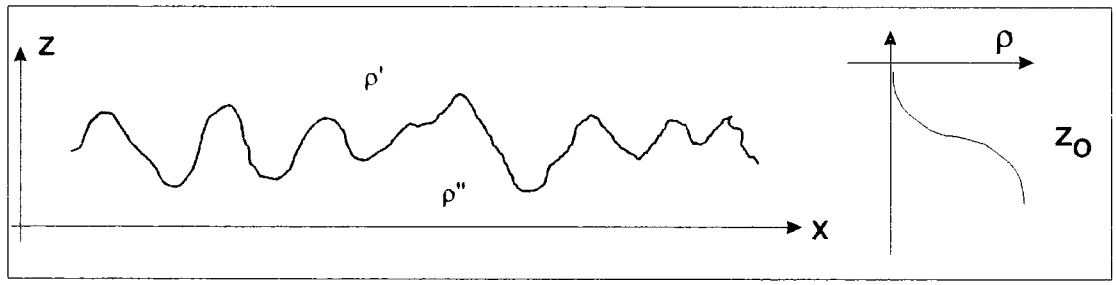

Figure 5.8: A schematic of a rough interface between two media ρ' and ρ''

When this is the case, the x-rays scattered at this interface are naturally split into their specular and diffuse components that have been discussed in more detail in chapter 3. In calculating the roughness in a specular scan the rough surface is replaced by an equivalent, graded interface (the profile shown on the right of figure 5.8). As an example, a surface defined by a Gaussian height distribution would be replaced by an effective grading profile, defined by an error function. The width of this error function, defines the roughness of the interface.

It is also possible to have an interface which is purely graded. In this case the graduated profile shown in figure 5.8 would be the correct representation of the electron density change across the interface. Such a surface is shown schematically in figure 5.9:

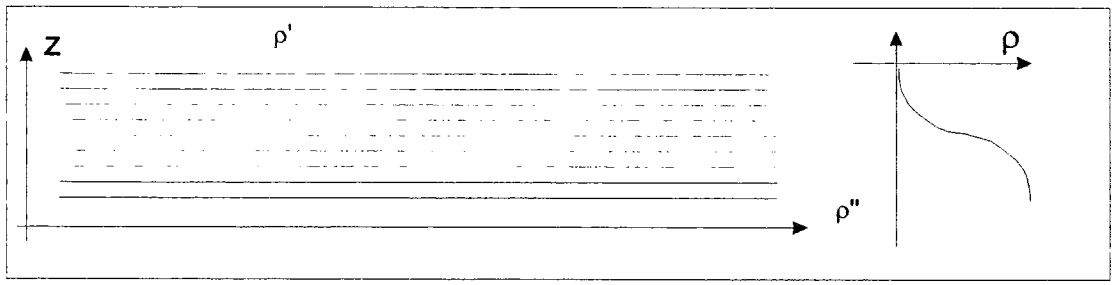

Figure 5.9: A schematic of a purely graded interface between two media ρ' and ρ''

The purely graded interface shown above would have the same interface width as that in figure 5.8, and so could be said to have the same interfacial 'roughness'. However, in the interface above, there is no mechanism whereby incident radiation can be scattered out of the specular condition and hence no diffuse scatter results. The specular scatter is, however, reduced to the same extent as that at a rough interface because destructive interference between waves scattered from different points across the interface builds up as the wave traverses the entire interface region.

Specular scans can therefore only deduce the total interface width between two media. In order to determine the exact interface type, the diffuse scatter must be investigated. In the two extreme cases outline above, the difference is immediately obvious - in the case of a graded roughness there is no diffuse scatter.

During the course of this study, it became clear that in real systems, the interface structure is likely to be a combination of the two interface types - figure 5.10. This type of structure is most often found in surfaces which have been allowed to oxidise or have been polished, as well as in multilayers made from miscible elements.

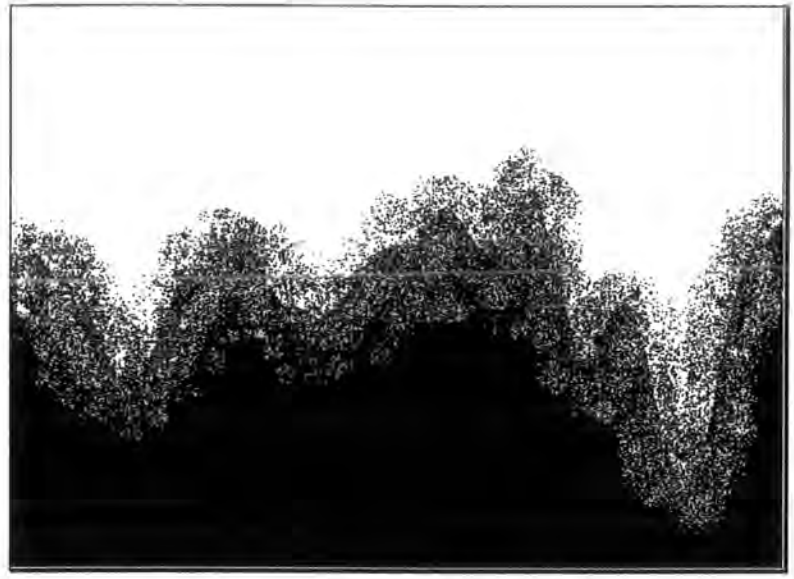

Figure 5.10: A schematic of an interface exhibiting both roughness and grading

The extensions to theory outlined in chapter 3 have only recently been attempted. Caticha [22] developed a theory for calculating reflection and transmission coefficients for an arbitrary interface profile, but this theory was not tested experimentally. Experiments conducted on polished Zerodur® [23,24] during the course of this study, have for the first time enabled the theory developed by Sinha et. al. [25] to be extended to include grading at an interface. By extending the distorted wave Born approximation to include grading it was possible to fit all the experimental data to a single set of parameters. These experiments have shown that, so long as the interface width is not too large, the Fresnel reflection coefficient contained in equation 3.23 can be re-written:

$$\left\langle F_l^R \right\rangle \approx F_l^R \exp\left(-q_{z,l} q_{z,l+1}\, \sigma_{r,l+1}^2\right) \int_{-\infty}^{\infty} g_l(z) \exp\left(i q_{z,l} q_{z,l+1}\, z\right) dz \qquad [5.21]$$

The exponential term following the ideal Fresnel reflection coefficient for interface l, r_l, accounts for the real interface roughness, σ_r, which in this case is assumed to follow a Gaussian height-height distribution. The Fourier integral takes into account the effects of grading, where $g_l(z)$ is the normalised first derivative of the electric susceptibility across the interface [24]. For a truly rough interface, this second term reduces to unity. If however there is a grading profile across the interface which can

be approximated by an error function of width, $\sigma_{g,l+1}$, the second correction term is equal to $\exp\left(-q_{z,l}q_{z,l+1}\sigma^2_{g,l+1}\right)$, which is identical in form to the roughness term. If the interdiffusion across the interface is accurately described by an error function, equation 5.21 reduces to:

$$\left\langle F_l^R \right\rangle \approx F_l^R \exp\left(-q_{z,l}q_{z,l+1}\sigma^2_{t,l+1}\right) \qquad [5.22]$$

where $\sigma_t^2 = \sigma_r^2 + \sigma_g^2$. This is an important result as it highlights again the inability to distinguish roughness from grading at an interface from specular scatter alone.

It has already been shown that there is no process by which a vertically graded interface can produce diffusely scattered radiation, however grading must still be taken into account when considering the diffuse scatter. Real roughness at an interface, *l*, will produce diffuse scatter as defined in chapter 3. However, this diffusely scattered radiation must traverse through the interface, *l+1*, which may have a graded profile. The destructive interference which reduces the specular scatter, causes a similar reduction to the observed diffuse scatter as it crosses the interface.

If the scattering conditions are such that the Born wave approximation holds, it is possible to deduce the roughness, without recourse to detailed simulation. Savage et al [26] have shown that the roughness of an interface can be calculated by ratioing the diffuse to the specular scatter:

$$\frac{I_{Diff}}{I_{Spec}} = \exp(q_z^2\sigma^2) - 1 \qquad [5.23]$$

This simple model may now be generalised [27]. Assuming the Gaussian height-height distributions that enable the roughness to be defined by error functions, the effective roughness caused by grading σ_g and the real roughness σ_r can be added in quadrature to give the total effective roughness σ_t. As we have already seen, this is

the roughness that is measured by the specular reflectivity curve. The effect of the grading is to moderate the Fresnel amplitudes by an additional Debye-Waller factor. The specular and diffuse intensities are now given by:

$$I_{Spec} = \int I_s(\theta)d\theta = I_o \exp(-q_z^2\Sigma_G^2)\exp(-q_z^2\sigma_R^2) \qquad [5.24]$$

and

$$I_{Diff} = \int I_d(\theta)d\theta = I_o \exp(-q_z^2\Sigma_G^2)\left[1-\exp(-q_z^2\sigma_R^2)\right] \qquad [5.25]$$

where I_o is the Fresnel amplitude of the interface.

It is therefore possible to calculate the roughness from the ratio of the integrated diffuse scatter to the integrated specular scatter, and equation (5.23) remains valid. An estimate of the grading parameter, can then be made by comparing the roughness deduced here to that observed in the specular scan. This method allows the amount of grading to be approximated without undertaking a detailed simulation. However, in order to obtain a more detailed measure of the surface and interface structure, it is necessary to model the scatter in a simulation, and test the model experimentally.

The changes to the theory that are highlighted above, are covered in more detail in reference 24. In reference 23 a new code [28] for simulating diffuse scatter which contains the modifications to include grading was tested on a single surface of polished Zerodur®. This was then extended to more interfaces by investigating the effects of polishing InP wafers [29]. The new theory has been tested extensively in this study, with all the results in Chapter 6 requiring it due to the highly miscibility between the metals cobalt and chromium. Recently a study by Lee et. al. [30] have studied graded interfaces within a 30 period Mo/Si multilayer. They have also assumed Gaussian height-height correlation functions and treat the graded roughness in exactly the same way is described above.

5.5 Conclusions

This chapter has attempted to expand the theoretical ideas contained in chapter 3. Anomalous dispersion has been discussed in detail and its applications described. The use of anomalous dispersion in grazing incidence experiments where the materials are close in the Periodic Table has been demonstrated. In the latter part of the chapter, the original theory described in chapter 3 was extended to include grading at an interface. This extension of the theory was found to be necessary in order to obtain consistent fits to the x-ray scatter for a single set of parameters. The samples studied covered a wide range of materials ranging from single surfaces to samples with a large number of interfaces.

References from Chapter 5

1 The Crystalline State Vol 2: The optical principles of the diffraction of X-rays, *R.W. James,* **G. Bell & Sons**, (1948)

2 Electricity and Magnetism 4th edition, *W.J. Duffin,* **McGraw-Hill Book Company (UK) Ltd.,** (1990)

3 P. Suortti, J.B. Hastings, D.E. Cox, *Acta. Cryst.*, **A41**, *417-420,* (1985)

4 L.G. Parrat, C.F. Hempstead, *Phys. Rev.*, **94,** *1593-1600,* (1954)

5 International Tables for X-ray Crystallography Vol III, *Gen. Ed. K. Lonsdale,* **D. Reidel Publishing Company,** (1985)

6 T.D. Cromer, *Acta Cryst.*, **18**, *17-23,* (1965)

7 J.L. Hodeau, *HERCULES Course Notes*, (1997)

8 I.U.C.R. Teaching Commission

http://www.fos.su.se/iucr-top/comm/cteach/pamphlets/8/node6.html

9 C.H. Dauben, D.H. Templeton *Acta Cryst.*, **8**, *841-842,* (1955)

10 T.D. Cromer, D.A. Liberman, *J. Chem. Phys.*, **47,** *1891-1898,* (1970)

11 T.D. Cromer, D.A. Liberman, *Acta. Cryst.*, **A37**, *267-268,* (1981)

12 M. Wormington, *X-ray Anomalous Scattering Factors ver 1.00*, Bede Scientific

13 Introduction to Solid State Physics (6th Edition), *C. Kittel*, **John Wiley & Sons**, (1991)

14 R. Begum, M. Hart, K.R. Lea, P.D. Siddons, *Acta Cryst.*, **A42**, *456-464* (1986)

15 T. Kanamaru, M. Kuribayashi, K. Ishida, *J. Jap. Phys. Soc.*, **64** (9), *3529-3536*, (1995)

16 M. Kuribayashi, K. Takumi, T. Kanamaru, H. Katoh, K. Ishida, *J. Jap. Phys. Soc.*, **66** (3), *859-863*, (1997)

17 Calculated using, *X-rays ver. 1.0* (Contained in *GIXS ver 2.0*) by M. Wormington

18 Tabulated at: *http://xray.uu.se/hypertext/EBindEnergies.html*

19 R.H. Jones, P. Lightfoot, R.M. Ormerod, *J. Chem. Soc. - Chem. Commun.*, **7**, *783-784,* (1995)

20 N. Nakayama, I. Moritani, T. Shinjo, Y. Fujii, S. Sasaki, *J. Phys. F.*, **18**, *429-442,* (1988)

21 Sample courtesy of H. Laidler, T. Shen - *University of Leeds*

22 A. Caticha, *Phys. Rev. B*, **52** (13), *9214-9223*, (1995)

23 M. Wormington, I. Pape, T.P.A. Hase, B.K. Tanner, D.K. Bowen, *Phil. Mag. Letts.*, **74**, *211-216*, (1996)

24 I. Pape, T.P.A. Hase, B.K. Tanner, M. Wormington, *Physica B,* **in press** (1998)

25 S.K. Sinha, E.B. Sirota, S. Garoff, H.B. Stanley, *Phys. Rev. B.*, **38** (4), *2297-2311*, (1988)

26 D.E. Savage, J. Kleiner, N. Schimke, Y.-H. Phang, T. Jankowski, J. Jacobs, R. Kariotis, M.G. Lagally, *J. Appl. Phys.* **69**, *1411-* (1991)

27 T.P.A. Hase, I. Pape, B.K. Tanner, S.M. Thompson, S.M. Jordan, J.-K. Freijo, *Adv. X-ray Anal.*, **41**, *CD-Rom edition,* (1997)

28 M. Wormington, *GIXS ver 2.5*, (Bede Scientific Ltd.)

29 C.D. Moore, T.P.A. Hase, B.K. Tanner, *Adv. X-ray Anal.*, **41**, *CD-Rom edition*, (1997)

30 D.R. Lee, Y.J. Park, D. Kim, Y.H. Jeong, K.-B. Lee, *Phys. Rev. B*, **57** (15), *8786-8789*, (1998)

Chapter 6

Miscible Systems - Coupling and Structure in Co/Cr/Co Trilayers

6.1 Introduction

6.1.1 Background

This chapter initiates the discussion of experiments using x-rays to characterise the structure of metallic layered systems. It is, of course, important to understand the role that structure plays on magnetic coupling mechanisms in these types of systems. In this chapter particular focus is placed on the miscible Co/Cr system.

As Co/Cr is not among the forefront of systems suited for sensor device technology, there are relatively few experimental results in the literature. Most examples deal exclusively with epitaxial (100) [1,2], (001) [3,4,5], or (110) [6] Co/Cr multilayers. These samples are prepared on either MgO or sapphire with various buffer layers. Due to the lack of information with regard to the coupling between cobalt layers through a chromium spacer layer in polycrystalline materials a European Community funded Human, Capital and Mobility network was established under the grant CHRX-CT93-0320 to investigate the coupling in Co/Cr/Co trilayer structures. The role of the project was to measure the differences between samples prepared by Molecular Beam Expitaxy (MBE), High Vacuum Electron Beam Evaporation, and RF sputtering. Particular emphasis was placed on elucidating the anisotropy and the character of the coupling between the two cobalt layers. As the coupling is weak in these systems it was anticipated that small changes to the structure and interfaces could lead to large observed differences in the coupling, and that difficulties might arise when comparing nominally identical samples prepared

by different techniques. The research discussed in this chapter was accordingly conducted within the framework of this EC network.

6.1.2 Introduction to the Experiment

In order to simplify the analysis of the magnetic coupling it was decided to investigate metallically symmetric trilayers. The thickness of the cobalt layer was large to facilitate Ferromagnetic Resonance (FMR) measurements. X-ray reflectivity measurements on cobalt calibration samples showed that the cobalt had oxidised to CoO to a thickness of approximately 12Å. The structures that were to be investigated were therefore of the form: Si/Co(200Å)/Cr(x)/Co(212Å).

The structural work on these samples was conducted using grazing incidence x-ray techniques, as well as high resolution cross-sectional transmission electron microscopy performed at Oxford. The results of these experiments on particular series of samples will be discussed in sections 6.4 et seq.

All samples were subjected to magnetometry studies to varying degrees. In the next section (section 6.2), the various magnetometry techniques used to obtain information on the coupling will be discussed. A general overview of the experimental results relating to coupling and anisotropy in Co/Cr systems will be presented at the end of section 6.3, prior to a detailed analysis of the structural experiments undertaken.

6.2 Magnetometry techniques used to Investigate the Samples

All the magnetometry results presented in this chapter were measured by colleagues at various institutions and the results are only reproduced here to give a more complete insight into the system under investigation. Information on the coupling was supplemented by experiments which investigated the coercivity and anisotropies of these materials. In some cases, magnetometry was conducted within

the growth chamber so that information could be obtained about the sample after deposition of individual layers.

In the following sections, a very brief description of the types of magnetometry experiments that were performed on the samples is presented along with a brief summary of the information which could be obtained from them.

6.2.1 Magneto-Optical Kerr Effect (MOKE)

MOKE relies upon the fact that the polarisation state of light reflected from a magnetised surface depends on the magnitude and direction of the magnetisation within the penetration depth of the incident light (typically 200Å). The typical change in polarisation angle is extremely small, typically a few milli-radians. MOKE can be used to image magnetic domains [7] or to measure magnetisation versus field loops.

Typical experimental MOKE apparatus, consist of a polarised He/Ne laser which is incident upon the sample. The reflected light is passed through an analyser polaroid set to be crossed with the polariser defining the incident beam. The change in rotation of the polarisation caused by the magnetic state of the sample is then recorded as a change in the intensity of the transmitted light incident onto a photodiode. The MOKE system at the University of York allows the use of vector magnetometry whilst recording the magnetisation loops. Two directions of magnetisation can be measured; longitudinal (the magnetisation is parallel to both the external field and the optical plane) and transverse (the optical plane is perpendicular to the applied field). For incident light aligned to the applied magnetic field, the MOKE scan is sensitive to the longitudinal magnetisation only whereas for an incident laser beam where the optical plane is orientated at 45° to the magnetisation direction, the MOKE scan is much more sensitive to the transverse component of the sample's magnetisation vector. With this vector magnetometry, it is possible to use the system as a torque magnetometer to measure the anisotropy of the sample [8].

6.2.2 Lorentz Force Microscopy

This is a technique which can be used to study the spatial variation of the magnetisation configuration across and through the sample. Samples to be investigated by this technique must be prepared on carbon grids, suitable for use in a transmission electron microscope (TEM) - section 6.4.1. The samples to be studied are subjected to a high energy electron beam (400kV). A highly magnified electron diffraction pattern, figure 6.1, can be viewed by careful alignment of the objective lens [9].

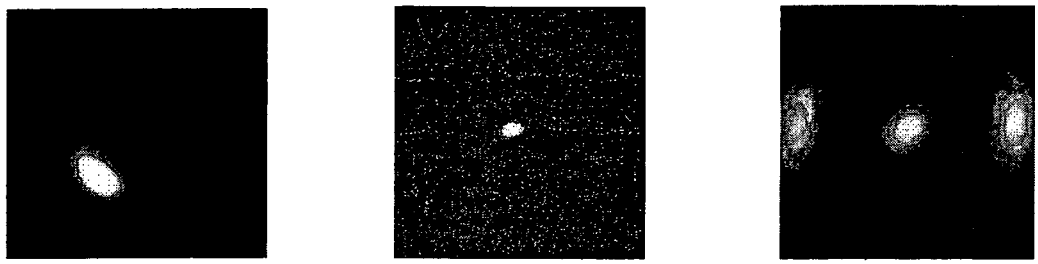

(a) (b) (c)

Figure 6.1: High magnification of the electron diffraction pattern of a ferromagnetically coupled sample (a), anti-ferromagnetically coupled trilayer (b), and a sample exhibiting both types of coupling (c). [10]

For layers of equal thickness, anti-parallel alignment of the metallic layers will result in there being no net Lorentz force on the electrons, and thus no deflection of the diffraction peak will occur - figure 6.1(b). When the coupling is ferromagnetic, the electrons are subject to the same Lorentz force in both layers and the diffraction peak is shifted from the centre of the pattern as in figure 6.1(a). By examining these diffraction patterns it is possible to deduce the ratio of the two types of coupling. It has been shown [3], that the coupling in Co/Cr trilayers is non-uniform across the sample and some areas of the sample show both types of coupling. Although this method can only probe the sample over approximately 10μm, it is possible to define unambiguously the coupling type in the trilayer.

6.2.3 Ferromagnetic Resonance

In the classical ground state of a ferromagnet, the spins are all parallel. The first excited state would occur when one of the spins becomes aligned anti-parallel. This is however, a highly energetic state and it is possible to form a lower energy excited state by allowing all the spins to share this reversal and form a spin wave [11]. Spin waves, or magnons, are simply oscillations in the relative orientations of the spins, analogous to phonons which are oscillations of the crystal lattice. If a ferromagnetic system is excited by an electromagnetic field of the same polarisation and frequency as one of the spin wave modes, a sharp increase in the absorption of the radiation is observed. Resonance occurs for electromagnetic radiation in the microwave region of the spectrum and for general spin wave resonance, the resonance frequency, ν, is given by [2,12]:

$$h\nu = g\mu_B\left(B_o - \mu_o M\right) + Dk^2 \qquad [6.1]$$

where g is the gyromagnetic ratio, which describes the splitting of the spin-orbit state on the application of a field, B_o is an external field applied normal to the sample and M is its magnetisation. D is a constant proportional to the exchange integral and is a measure of the strength of the interaction between the spins in the material, and k is the wavevector of the spin wave. Ferromagnetic resonance is defined as the resonance of spin waves with zero wavevector. In typical FMR experiments, the external field B_o is varied and the incident microwave frequency kept constant. The resonance is observed by a sharp reduction in the microwave power reflected from the sample surface.

The FMR results contained in this chapter relate to trilayer systems, and not to a single ferromagnetic layer. A detailed description of FMR in these systems is given by Jackson [13] who produced the results discussed within this chapter. In

trilayer systems which contain two ferromagnetic materials coupled through a non-magnetic spacer layer, two resonance peaks are observed corresponding to each of the layers. By fitting the position and intensity of each of the peaks the nature of the coupling, as well as the in-plane anisotropy of each of the layers can be calculated.

6.2.4 Brillouin Light Scattering

Brillouin light scattering (BLS) [14] is a complementary technique to FMR, and can be considered to be analogous to seismology, but using light instead of sound. The main information that can be obtained by BLS in the investigation of the structure of metallic multilayers is both the intra and interlayer exchange coupling as well as the anisotropy field, H. The anisotropy can be measured separately for each of the cobalt layers. However, the BLS spectra are highly sensitive to the magnetisation in the sample and the value of the gyromagnetic factor, g. Not only are the spectra sensitive to these factors, they are especially sensitive to the exact thickness of the layers. In order to deduce the exchange coupling and anisotropy fields, the samples are normally placed in an external magnetic field which is strong enough to saturate the sample. The value of the gyromagnetic ratio, is typically taken to be 2.16, but this value can be adjusted to values fitted from the FMR spectra. All the BLS spectra, and subsequent analysis discussed in this chapter were experimentally deduced by F. Garnot at Université Paris-Nord.

6.3 Summary of Magnetometry results relating to Coupling in Co/Cr/Co Trilayers

As stated above, the majority of the literature deals with epitaxial Co/Cr multilayers. For epitaxial (001) multilayers of the form $[Co_{11}/Cr_x]$ grown on a niobium buffered sapphire substrate at 300°C [3-5], it was found that the cobalt layers were anti-ferromagnetically coupled for chromium thicknesses between 6Å and 13Å. A similar value for chromium thickness is found for epitaxial $[Co_{10}/Cr_x]_{20}$ systems deposited on MgO(100) and MgO(110) substrates with annealed chromium buffer layers [6]. Here an anti-ferromagnetic coupling strength of -0.15 erg/cm^2 was

found for a chromium thickness of 13Å for the MgO(110) and 10Å for the MgO(100) with a coupling strength of -0.55 erg/cm^2. This is in contradiction to the results found by Liou et al [1] who showed that antiferromagnetic coupling in (100) multilayers was only possible for chromium thicknesses less than 5Å. In all cases, there was no indication of oscillations in the sign of coupling as a function of chromium thickness.

The coupling between the two cobalt layers studied within the network was found to be generally weak, and in some cases very difficult to detect. For samples where the chromium layer was less than 10Å, however, the two cobalt layers were always strongly coupled ferromagnetically. A further exception to this general rule occurred in all the samples prepared by electron beam evaporation at CNRS, Paris, which showed ferromagnetic coupling for all thicknesses of chromium. This may be attributed to the fact that a small external field was present during growth. The only samples to show systematic anti-ferromagnetic coupling were samples prepared by MBE, at the University of York. The cobalt films were found to be anti-ferromagnetically coupled for chromium thicknesses of 12.5Å, but no oscillations in the sign of the coupling was observed as a function of chromium thickness.

Obviously it was important to investigate the structure of the samples. In the next section, the two methods used to elucidate the structure are reviewed.

6.4 Structural Characterisations

As many samples as possible were subjected to structural analysis. Two possible methods were available to the network, grazing incidence x-ray scattering studies and Transmission Electron Microscopy (TEM). Both methods have their advantages and disadvantages. The x-ray analysis was complicated both by the proximity of Co and Cr in the periodic table, resulting in the need to use anomalous dispersion, and by the time needed to fit the data accurately. TEM is a destructive technique and is only sensitive to small, localised regions of the sample and typically information is obtained over hundreds of Angstroms only.

Where x-ray and TEM results are available for both samples, the TEM measurements were always undertaken after the results from the x-rays were known. In all cases both experiments were undertaken separately.

6.4.1 High Resolution Transmission Electron Microscopy (HR-TEM)

In a conventional transmission electron microscope, a very thin sample is illuminated by an electron beam. The electrons, emitted from a heated cathode, are focused into a small, thin, coherent beam by two condenser lenses. As the interaction between electrons and mater is strong, the thickness of the sample must be of the order of 1 μm. Various techniques, reviewed by Horiuchi [15], exist to produce the thin samples required for the TEM. As the electron beam interacts with the sample some of the incident electrons are diffracted out of the main beam. Following Abbe [16], the resulting diffraction pattern caused by the sample can be focused onto a transform plane by the use of an objective lens (figure 6.2). In a conventional transmission electron microscope, only one of the diffraction orders is selected by the use of a small aperture (10-25 mrad) [17]. Electrons accepted by the aperture can continue and are imaged on a fluorescent screen or film.

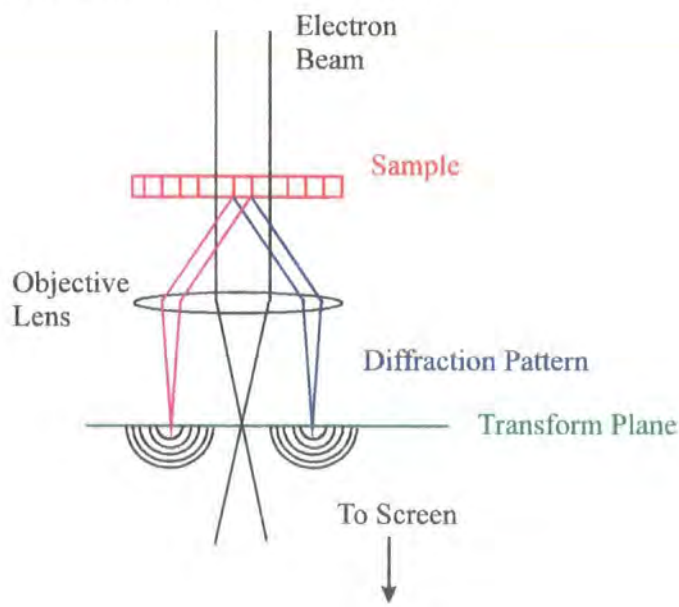

Figure 6.2: A schematic of a transmission electron microscope

High resolution transmission electron microscopy is a phase contrast image caused by allowing many of the diffraction orders to interfere between the transform plane and the phosphor screen. The focused electron diffraction pattern can be considered to be a series of point emitters producing Huygen wavelets. These wavelets interfere and increase the sensitivity of the final image. A HR-TEM can therefore be considered as an image formed from a double diffraction process. The aberrations caused by the lenses and fluctuations in the electron gun energy limit the resolution of a HR-TEM micrograph to a few angstroms.

6.4.2 Grazing Incidence X-ray Scattering from Co/Cr Trilayers

As the scattering factor of x-rays varies monotonically across the Periodic Table, there is very little scattering factor difference between the cobalt and chromium in these samples. This necessitated the use of anomalous dispersion (chapter 5), and hence all the x-ray experiments on these samples were undertaken at Station 2.3, at the Daresbury SRS. In order to increase the scatter from the layer that was of most interest - the chromium layer - it was necessary to tune to the chromium edge, λ=2.0703Å [18]. Figure 6.3 shows the experimental fluorescence signal from a chromium calibration sample as the wavelength is tuned through the chromium edge:

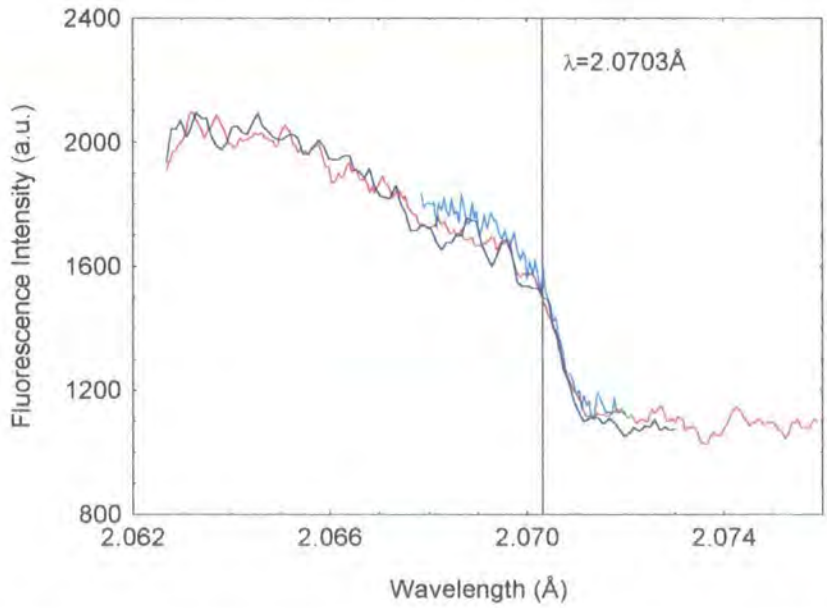

Figure 6.3: Experimental fluorescence signal from a chromium calibration source as a function of wavelength

Unlike the copper absorption edge where there is clear near edge structure, the chromium edge is broad and poorly defined. The value for the absorption edge was taken from the International Tables and is shown in figure 6.3. The incident flux on the station for this wavelength is substantially lower than at its peak flux which was found by experiment to be in the vicinity of 1.3Å (figure 4.1).

Figure 6.4 shows the calculated scattering factor difference from monolayers of cobalt and chromium as a function of wavelength.

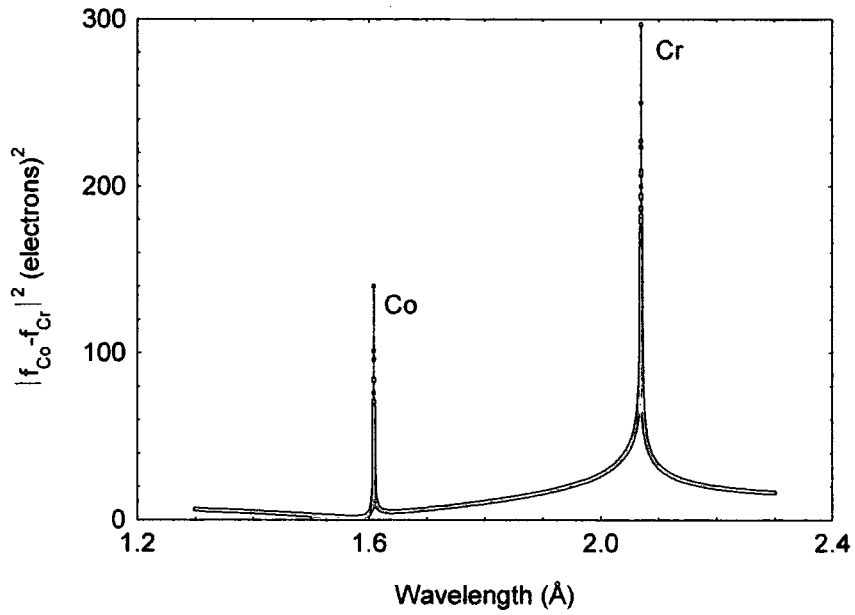

Figure 6.4: Scattering factor difference for Co and Cr as a function of wavelength through the Co and Cr K Absorption edges

The effect of the anomalous dispersion is clear; at the normal laboratory wavelength of Cu Kα, λ=1.54Å, the scattering factor difference between cobalt and chromium squared is only $1.998e^2$, whilst at the chromium edge this has dramatically increased to $297e^2$. Thus for x-ray scattering experiments to be sensitive to the chromium layer, and thereby the trilayer structure, the x-ray wavelength must be tuned to the chromium absorption edge. In order to ensure that simulation parameters were accurate, the experiment was also repeated away from the absorption edge at a wavelength of λ=1.7075Å. Although the scattering factor difference at this wavelength is low, $6.81e^2$, there is sufficient contrast still to detect the chromium layer.

It was hoped that by tuning into the chromium absorption edge it would be possible to identify the chromium layer unambiguously and extract details of the chromium thickness and roughness. However, this proved to be impossible. The reflectivity profile from Co/Cr layers is dominated by two periods, the total thickness of the sample and an additional period which is evident at higher sample angles. This is demonstrated below in figure 6.5, where a Co/Cr trilayer has been simulated at the chromium edge. The two cobalt layers were fixed at the same thickness, 200Å, and the chromium layer was 15Å.

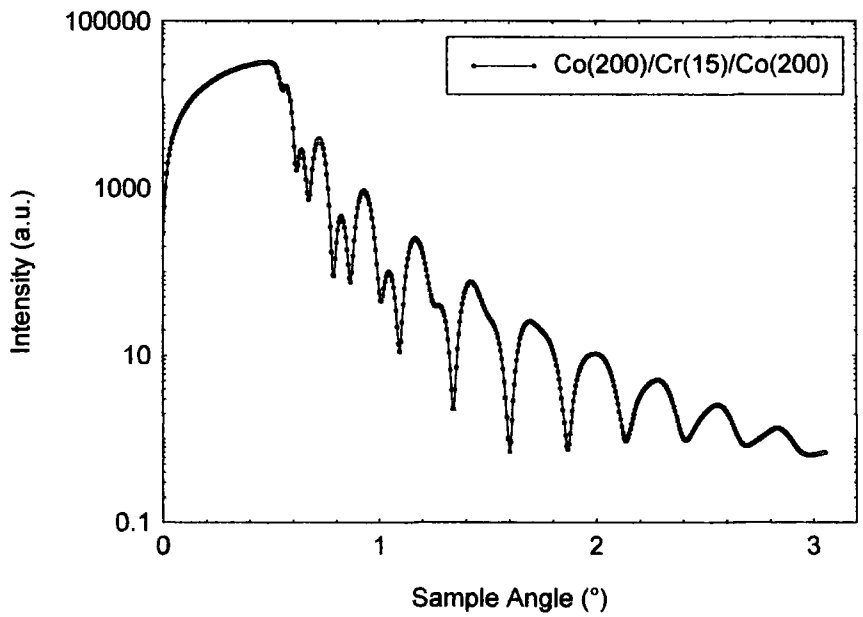

Figure 6.5: A simulation of a Co/Cr/Co trilayer. For parameters see text.

A clear period is evident at higher sample angles. The average period of this fringe corresponds to a thickness of 217 ± 5Å. This obviously corresponds to the thickness of the sum of the bottom two layers. The phase of these high angle fringes is very sensitive to the ratio between the two cobalt layers, and it is in this way that the chromium thickness, and hence the trilayer structure, can be extracted.

In the following sections, the techniques outlined above are applied to two series of trilayer samples. In the first series, the deposition temperature of the layers was varied, and in the second three nominally identical samples exhibiting

anomalous coupling were investigated. The structures of the trilayers were investigated using HR-TEM and grazing incidence x-ray scattering.

6.5 The effect of temperature on trilayers produced by MBE

Four polycrystalline trilayers of Co(200Å)-Cr(10Å)-Co(212Å) were grown on (111) oriented silicon wafers by ultra-high vacuum evaporation at the University of York. The base pressure of the MBE system was $2*10^{-10}$, and the growth was monitored by insitu RHEED analysis and quartz rate meters [19]. The samples were grown such that various layers were deposited either at room temperature or at 150°C. This study was primarily designed to investigate the influence of interdiffusion on the magnetisation of the samples. As cobalt and chromium are highly miscible, it was expected that growing some layers at elevated temperatures would induce more diffuse interfaces.

The growth temperatures for each of the layers in the series - designated series *N*, is tabulated in table 6.1:

Sample	*Si*	*Co*	*Cr*	*Co*
YNA	-	150	150	150
YNB	-	150	25	25
YNC	-	150	150	25
YND	-	25	25	25

Table 6.1: The growth temperatures (°C) for the *YN* series

The magnetometry of the samples was investigated by the complementary techniques of FMR and BLS along with in-situ MOKE.

In-situ MOKE [20] was carried out with an incident angle to the sample of 30°. The MOKE data showed that growing the first layer at an elevated temperature results in significantly different magnetisation loops from those in which the first layer was grown at room temperature. Growing the first cobalt layer at 150°C results in a larger coercivity of 30 Oe (approximately double) and less anisotropy than when the first layer was deposited at room temperature. None of the curves from the completed trilayers showed a significant transverse component of magnetisation, and for samples *YNC* and *YND* the MOKE curve for the completed trilayer, sensitive to the longitudinal component of magnetisation, was similar to that obtained from the first cobalt layer. The coercivity of samples *YNA* and *YNB* increased upon completion of the trilayer.

FMR [21] and BLS [22] measurements were also carried out on these samples, and the coupling between the two layers calculated. In all cases, the samples were found to be ferromagnetically coupled and the coupling strength increased as more of the layers were grown at an elevated temperature. The lowest coupling strength (FMR: 0.33 and BLS: 0.15 erg cm^{-2}) was for the sample with all the layers grown at room temperature, *YND*, and this value steadily increased (>1.8erg cm^{-2} [from BLS] for *YNA* and *YNC*) as more layers were deposited at elevated temperatures. This can easily be understood if the effective thickness of the chromium layer was reducing as more of the chromium layer was being incorporated into the cobalt layer when the latter was deposited at 150°C. The anisotropy of sample *YNA* 500 ± 50 Oe is lower than the other samples which were all 800 ± 50 Oe (values calculated from BLS spectra). The reduction in the anisotropy of sample *YNA* is also suggested in the ex-situ MOKE results, however, these require a more detailed analysis which has yet to be undertaken.

The magnetometry results show that layer deposition temperature can effect the magnetic properties of Co/Cr trilayers. Although no change was observed in the sign of the coupling, the coupling strength increases considerably as more layers are deposited at 150°C. The relation of coupling to growth temperature and the reduction in anisotropy can be explained in terms of structural models with

extremely diffused interfaces [23]. The samples were then subjected to a detailed x-ray scattering study at station 2.3 at the SRS to investigate the level of inter-diffusion at the interfaces. As described above, this required grazing incidence experiments to be undertaken at and away from the chromium absorption edge (λ=2.0703Å).

Figure 6.6 shows the specular reflectivity for the wavelength far from the chromium absorption edge (λ=1.7075), from *YND*. In the low angle region short period fringes corresponding to the whole trilayer thickness dominate the profile, but in the high angle region, a longer period modulation is observed. When the wavelength is tuned close to the absorption edge, as in figure 6.7, this longer period structure becomes more pronounced. This confirms the results that were described in figure 6.5, namely that the period of the high angle fringes comes from the total thickness of the bottom cobalt and chromium layers. It can be seen that both the chromium and cobalt thickness correspond well with the intended structure. Nevertheless, in order to obtain such a good fit, there is a tight tolerance on the fit parameters, including the effective interface roughness. Not surprisingly the effective roughness of the Co/Cr, Co/CoO and CoO/air interfaces is substantially higher than that of the silicon substrate.

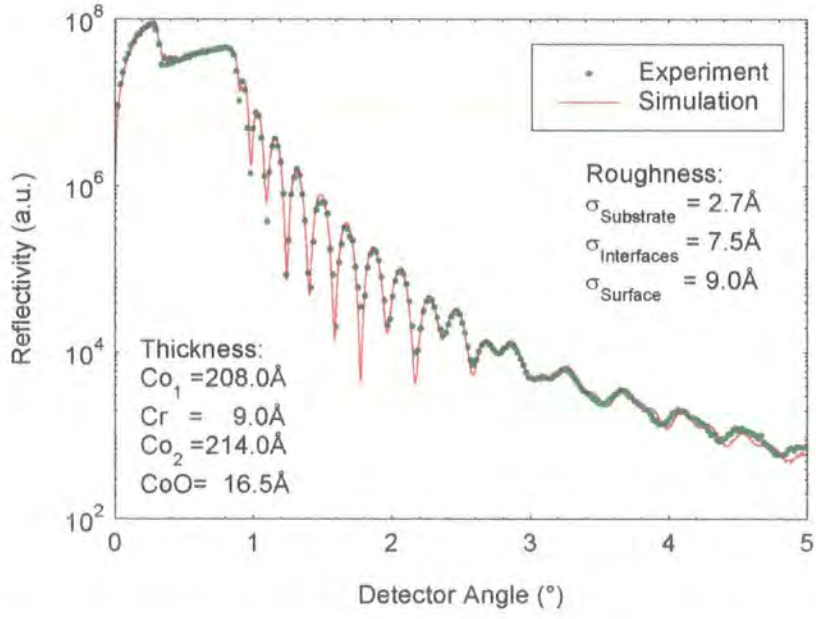

Figure 6.6: Specular $\theta/2\theta$ scan for *YND* (points) taken at λ=1.7075A and the simulation (line) with parameters as shown inset.

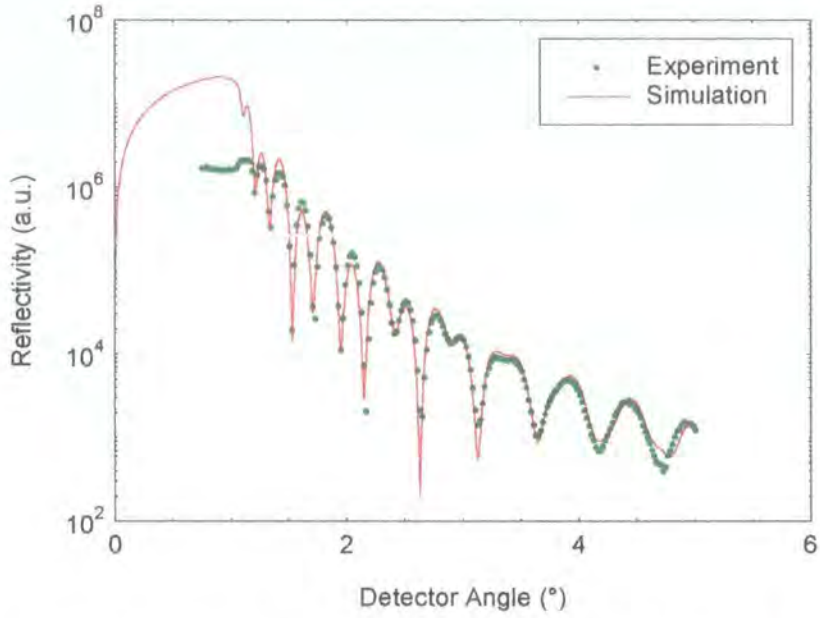

Figure 6.7: Specular $\theta/2\theta$ scan for *YND* taken at λ=2.0703A and the simulation with the parameters shown in Figure 6.6.

A comparison of the specular reflectivity profiles from all four samples is shown in figure 6.8. From this figure it is possible to draw a number of qualitative conclusions. The first arises from the loss of the long period fringes between sample *YND* and *YNC*, the latter having both the bottom cobalt and the chromium layers grown at 150°C. Somewhat surprising is the observation that sample *YNB*, in which only the bottom cobalt layer was grown at elevated temperature, shows lower Kiessig fringe amplitude than sample *YNC*. The reduction of the interference fringes in the reflectivity at high sample angle again suggests that growth of the cobalt layer on silicon at 150°C results in significant changes to the structure of the trilayer, due to increases in inter-diffusion across the Co/Cr interface. Sample *YNA*, for which all layers were grown at 150°C shows almost no Kiessig fringes suggesting very substantial alloying and no clear interfaces between the layers. All samples where the bottom cobalt layer was grown at 150°C show substantial roughness at the Si/Co interface. This high level of roughness may suggest the formation of a cobalt silicide layer at this interface which would in turn increase the coercivity of the rest of the cobalt layer.

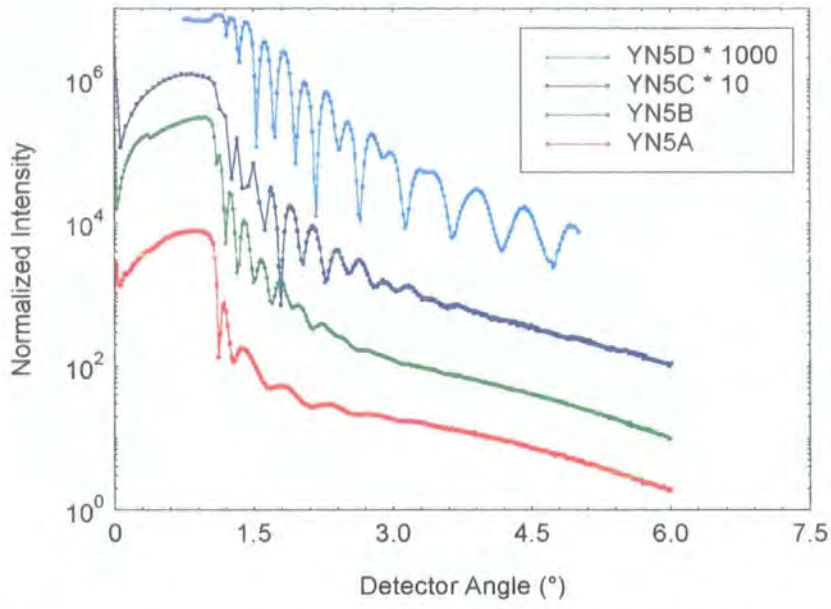

Figure 6.8: Specular scans for the four samples taken at the Cr absorption edge

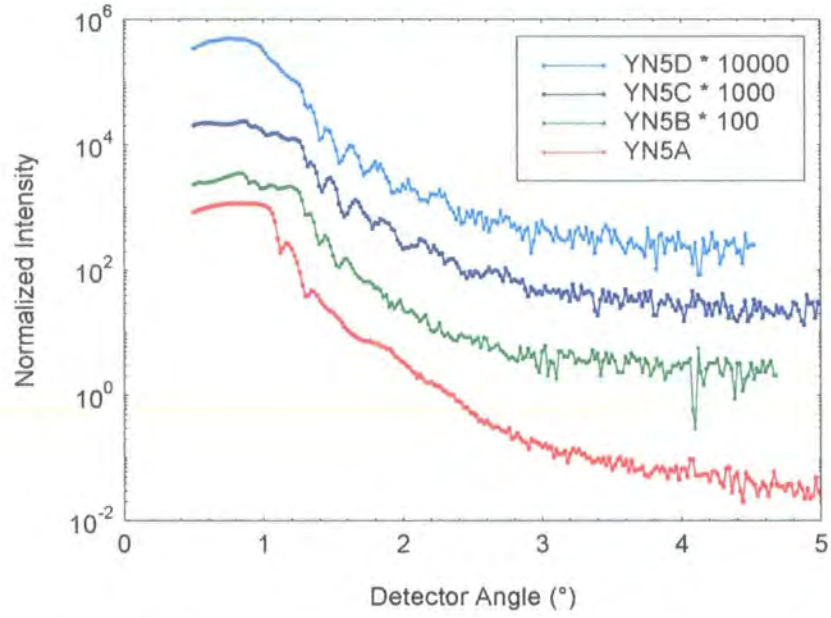

Figure 6.9: Off-set (-0.1°) specular scans of the four samples taken at the Cr absorption edge

Analysis of the off-specular *6-26* scans showed that there was significant correlated roughness through the sample. This shows up as interference fringes (Figure 6.9) in the off-specular scans. The preservation of fringes in the diffuse scatter when the bottom cobalt and chromium layers were grown at 150°C suggests

that even when interdiffusion occurs, the real roughness is still replicated from the substrate to the surface of the sample.

In order to quantify the fraction of the roughness which was conformal to that which was uncorrelated through the layers, an attempt was made to simulate the diffuse scatter detected using specimen-only scans. These simulations would also provide a measure of the real roughness at each of the interfaces, and thereby determine the interdiffusion profile across the interfaces. Thus far it has only been possible to fit the data for the sample for which all layers were grown at room temperature, as this is the only sample for which we obtained a good fit to the specular reflectivity. A fit to the other samples was attempted, but the reflectivity profile could not be simulated by assuming a simple trilayer structure. As discussed previously, small amounts of inter-diffusion are observed as an increase in the effective interface roughness in reflectivity measurements. As the amount of interdiffusion increases, the interface profile deviates from the error function that is assumed in the theory, it becomes impossible to fit the reflectivity data without changing the model of the interface profile. In trying to fit the remaining samples in series *N*, it was found that the data could not be fitted to a simple error function type interface.

Figure 6.10 shows specimen scans taken at two different values of scattering angle for sample *YND*, one corresponding to a maximum (Figure 6.10(a)) and one to a minimum (Figure 6.10(b)) in the specular Kiessig fringe pattern. Due to the low number of interfaces and the low incident flux, the intensity of the diffuse scatter is low, and long count times were required to produce the data. However, good agreement is obtained between the simulation and the experimental data, except for sample angles close to the specular ridge. Figure 6.10(a) is shown on a log scale to demonstrate the matching of the simulation at the peak of the specular ridge.

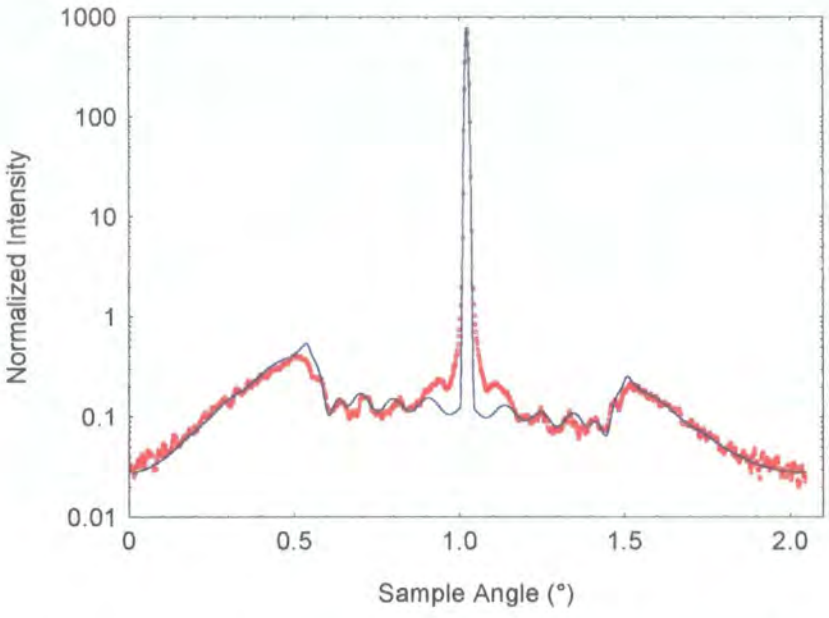

Figure 6.10(a): Specimen scan at 2.0703Å through a Kiessig fringe maximum.
Points experimental-data, solid line-simulation

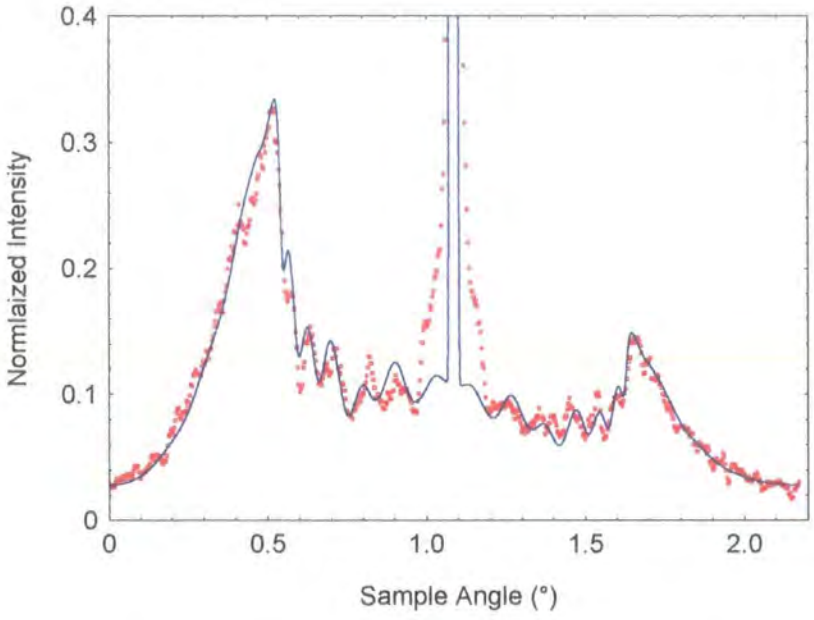

Figure 6.10(b): Specimen scan through a Kiessig fringe minimum
Points experimental-data, solid line-simulation

Table 6.2 shows the parameters used for the simulations of Figure 6.10 and it is important to note that the layer thickness and interface roughness parameters deduced from the specular fits are used in the simulation of the transverse diffuse

data. The lateral correlation length, ξ was found to be 110 ± 10Å, and the fractal parameter, h was 0.25 ± 0.02.

Layer	Thickness (Å)	Uncorrelated roughness (Å)	Correlated roughness (Å)	Interdiffusion parameter (Å)
Si	∞	0.0	1.5	2.3
Co	208	2.8	3.0	6.2
Cr	9	2.9	1.2	6.8
Co	214	0.0	4.0	6.3
CoO	16.5	1.7	3.7	8.6

Table 6.2: Parameters used for the diffuse scatter simulations in Figure 6.10

The deviation of the simulation from the experimental data around the base of the specular ridge indicates the presence of long lateral scale roughness, or alternatively, roughness beyond the coherence length of the x-rays. However, the fit close to the specular ridge could be improved by lowering the fractal parameter, but it is unclear whether the fractal model could be justified with such a low value. In a highly diffused system, as is the case here, it is difficult to rationalise how a sharp, highly jagged surface, typified by a low fractal parameter, could exist.

As the fits to both the specular and diffuse scatter are very good, it can be concluded that the structural model is well defined for this sample. It is interesting to note that for room temperature deposition the amount of interdiffusion across all interfaces is still extremely high, and that much of the roughness is correlated. The high degree of interdiffusion, at low growth temperatures, suggests that when interdiffusion is encouraged by deposition at high temperature the interface profile will not be Gaussian in nature, confirming the difficulties faced when attempting fits to the other samples in the *N* series.

This sample was also investigated using high resolution transmission electron microscopy as described above. As this is a destructive technique, this was the last experiment that was performed on the sample. The TEM work was undertaken at the University of Oxford by E. Ho and A.K. Petford-Long.

A cross sectional TEM micrograph of *YND* is shown in figure 6.11 [24]. The phase image produced by the silicon atoms from the substrate are clearly visible and their spacing was used to calibrate the system for thickness measurements. A SiO_2 layer is clearly visible, which is smooth and flat. The chromium layer is reasonably clear, but very thin and in some places discontinuous. Whereas the SiO_2/Co interface is flat, the Co/Cr and Cr/Co interfaces are rough and wavy. This wavy nature of the interface is replicated to the surface, by which time it has become more pronounced. Large columnar grains which are incoherent across the chromium layer and measure 150 to 200Å are visible, with strong texturing (predominantly $(11\bar{2}0)$ and $(10\bar{1}0)$[25]). The thickness of the layers that was deduced from the micrograph, are compared to the layer thicknesses that were found from the x-ray measurements in Table 6.3:

	SiO_2	**1st Co**	**Cr**	**2nd Co**	**CoO**
HR-TEM	6Å - 13Å	189Å-203Å	7Å-14Å	178Å-208Å	---
X-rays	---	*208Å*	*9Å*	*214Å*	*16.5Å*
Roughness	*2.7Å*	*7.5Å*	*7.5Å*	*7.5Å*	*9.5Å*

Table 6.3: A comparison between the structural parameters independently obtained from x-ray and HR-TEM experiments

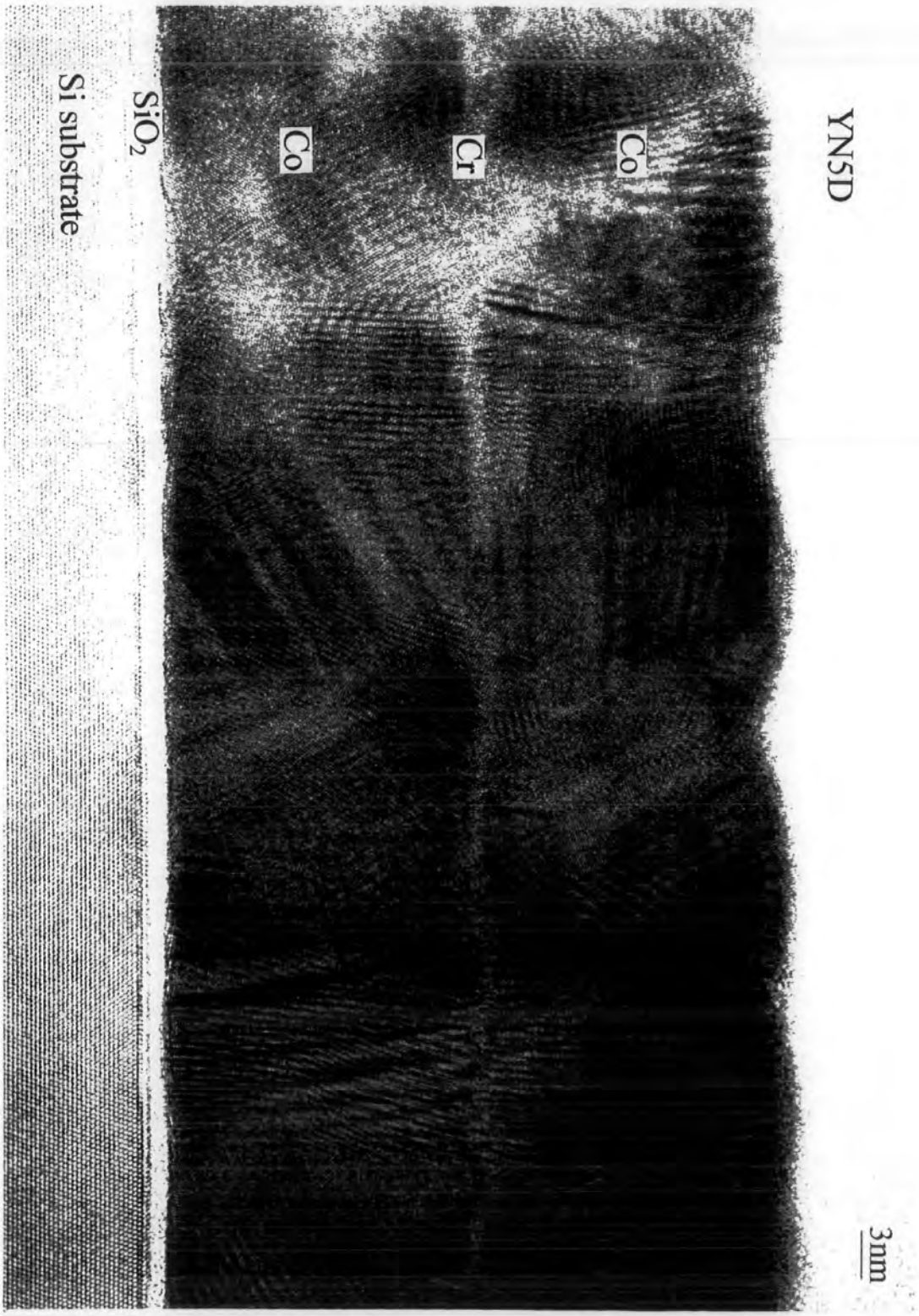

Figure 6.11: High Resolution TEM Micrograph of *YND* [24]

When comparing the thickness obtained from the two methods, it should be remembered that the x-ray technique measures the thickness from the centre of the roughness error function whilst the HR-TEM measures it from the edge of this profile. This is shown graphically in figure 6.12 where a 90Å layer is shown, deposited between materials of different electron density. The role of roughness is also incorporated into the diagram assuming a Gaussian model.

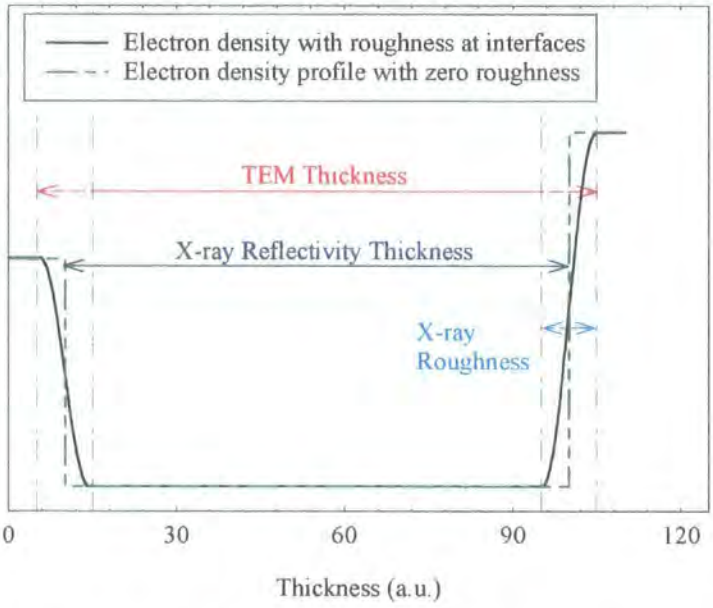

Figure 6.12: A 90Å layer as seen by GIXR and HR-TEM

It is impossible to measure the thickness of the SiO_2 layer in the x-ray reflectivity curve because of the extremely close electron density between silicon and its oxide. The oxide layer is detected in the reflectivity profile as a rougher silicon substrate. The HR-TEM cannot distinguish the CoO layer due to the technique of preparation which can confuse the amorphous oxide layer with the glue used to prepare the samples. Although ambiguity may exist between the two techniques when comparing the thickness of the layers, both methods clearly show the high level of inter-diffusion that is found in this sample.

The excellent agreement between the two techniques in terms of the thickness of the constituent layers is hardly surprising considering the inherent accuracy of the two techniques to length scales in the Ångstrom range. More

important is the close relation between the measured grain size and the lateral correlation length that is measured from the diffuse scatter. From the TEM micrograph, a very clear wavy 'roughness' is observed on the top layer which is of the order of 150Å. This length scale is also reproduced at the chromium interfaces, although it is harder to visualise. The lateral correlation length as measured by the x-rays is 110 ± 10Å. This is lower than the wavy roughness observed in the HR-TEM because it is calculated from the average correlation function which is applied to all the interfaces, including the SiO_2/Co layer which, according to the TEM micrograph, has a substantially less wavy nature than the other interfaces.

It has been shown that Co/Cr trilayer structures are highly sensitive to the deposition temperature [26]. Recent work by Scheurer et al. [27] shows that the growth mode of chromium deposited on epitaxial Co(0001) changes abruptly at 410K. If this were to be the case in the samples studied here, it would be expected that there would be a greater difference between the reflectivity curves from samples *YNB* and *YNC*. Nevertheless, the results in this chapter pertaining to the amount of diffusion at the interfaces are confirmed in NMR studies of semi-epitaxial $[Co_x/Cr_8]_{10}$ multilayers deposited on a mica substrate with a ruthenium buffer layer [23]. These results show that for multilayers deposited at 100°C the amount of Co alloyed with Cr at the interface is equivalent to a cobalt thickness of 11Å. This interface width compares favourably with the results from *YND*, where the roughness was measured to be 7.5Å.

The structure of a Co/Cr trilayer, deposited at room temperature, has successfully been determined. The results from grazing incidence x-ray scattering and HR-TEM compare favourably. Both the thickness and the correlation length/grain size are found to be in excellent agreement between the two techniques. It was found that even for room temperature growth, a large amount of interdiffusion had occurred at each interface. In the following section, these structural techniques will be tested again on three nominally identical trilayers exhibiting anomalous coupling behaviour.

6.6 Samples Deposited in Zero Field

A series of samples, designated series *L*, were prepared at room temperature by all growers in the network ensuring that no external field was present during deposition. The chromium thickness were nominally 5, 10, 15, 20 and 25Å. The samples were prepared both on Si(111) and on carbon coated TEM grids. Samples were deposited on carbon grids such that Lorentz microscopy could be carried out. The magnetisation loops of the samples deposited on silicon were investigated by in-situ MOKE. The coupling and anisotropy was also investigated by FMR and BLS.

All samples showed clear ferromagnetic coupling, typified by square hysteresis loops, with chromium spacer layer thickness, except for the sample prepared by MBE with 15Å of chromium at the University of York. Three nominally identical samples with this thickness of chromium were prepared at the University of York. Two of these samples showed definite indications of anti-ferromagnetic coupling between the cobalt layers which was strong enough to produce a stepped hysteresis loop. However, Lorentz force microscopy on these samples showed that some areas of the sample still retained a degree of ferromagnetic alignment at remenance, although most of the sample showed anti-ferromagnetic alignment. This could be due to oscillations or fluctuations in the thickness of the chromium layer, or that over small areas the spacer layer was discontinuous.

However, one of the three samples, sample *B*, showed a very complicated FMR spectra with eight peaks, and straight hysteresis loops which indicated that this particular sample was strongly ferromagnetically coupled. All samples were studied by in-situ MOKE which showed that the hysteresis loop from the first deposited cobalt layer in sample *B* was significantly different than that observed in the other two samples. It was expected that this difference could be explained in terms of structural differences between sample *B* and samples *A* and *C*.

In the same way that the magnetometry results from series *N* could be explained by structural models that included interdiffusion, it was hoped that structural changes could explain the anomalous coupling found in sample *B*. As it was predominantly the coupling that had changed, it was expected that the thickness of the chromium layer may be different between sample *B* and the other two. The MOKE curves from sample *B* suggested that some structural changes may have occurred to the bottom cobalt layer. The structure of the samples was investigated by grazing incidence x-ray analysis as well as HR-TEM.

The samples deposited on Si(111) were investigated at Daresbury in a similar way to the *N* series, which is described in detail in the previous section. Figure 6.13 shows the specular data with the corresponding best fit simulation. Also included in figure 6.13 is the offset (-0.1°) longitudinal diffuse scan. Figure 6.14 shows the same fit at the chromium absorption edge with the best fit parameters that were obtained from the specular fit inset.

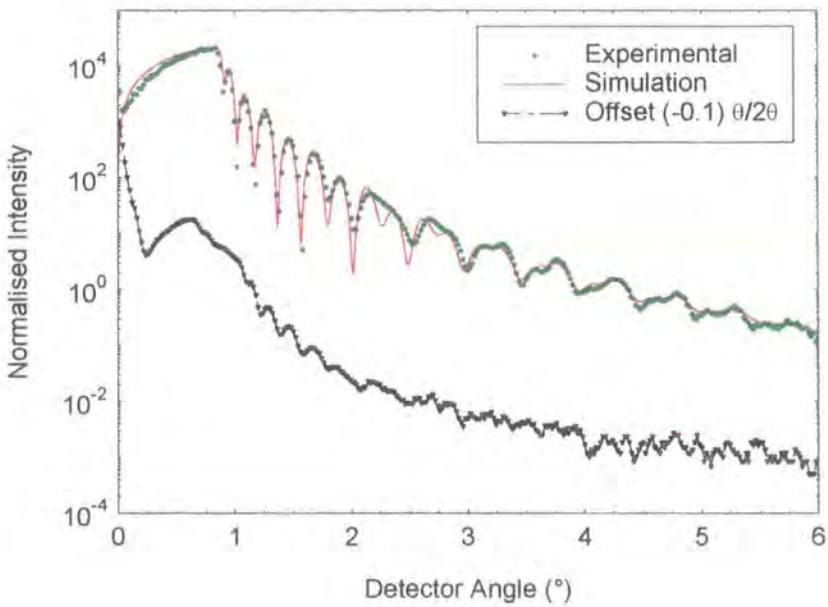

Figure 6.13: Specular and Offset (-0.1) scans from sample A with experimental (points) and simulation (lines)

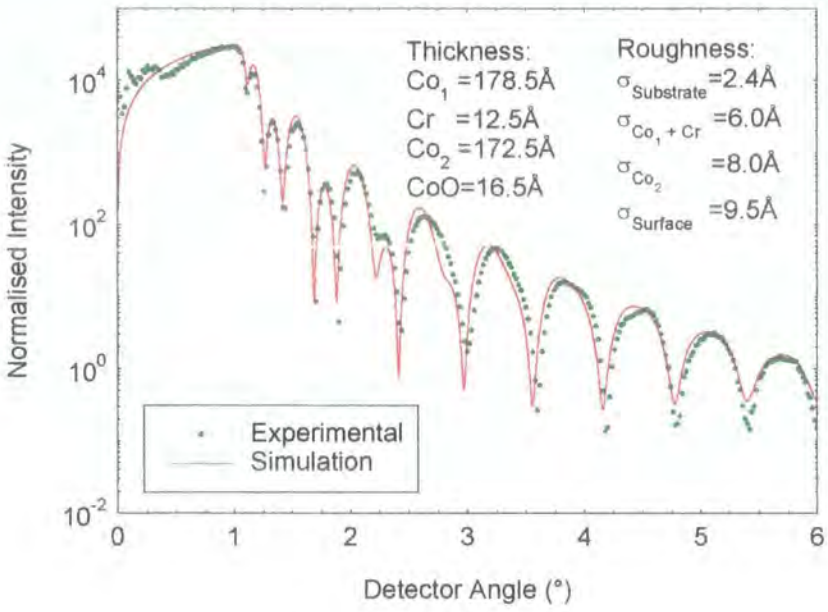

Figure 6.14: Best fit simulation to sample *A* at the chromium absorption edge, with parameters inset.

Both figures 6.13 and 6.14 show that the fit to the specular reflectivity from sample *A*, is extremely good. From the fits to the specular scatter, it can be seen (Figure 6.14) that the interfaces are quite rough, but of the same order as those found in *YND*. The offset longitudinal diffuse scan in figure 6.13 shows that the roughness within the sample is correlated, again in keeping with the results obtained from *YND*. However, the low level of the diffuse scatter indicates that much of this apparent roughness is again interdiffusion. This implies that the interface profile of this sample is similar to that found for *YND*. Figure 6.15 shows the best fit that was possible for sample *C*. Both wavelengths are presented in the same figure along with the best fit parameters.

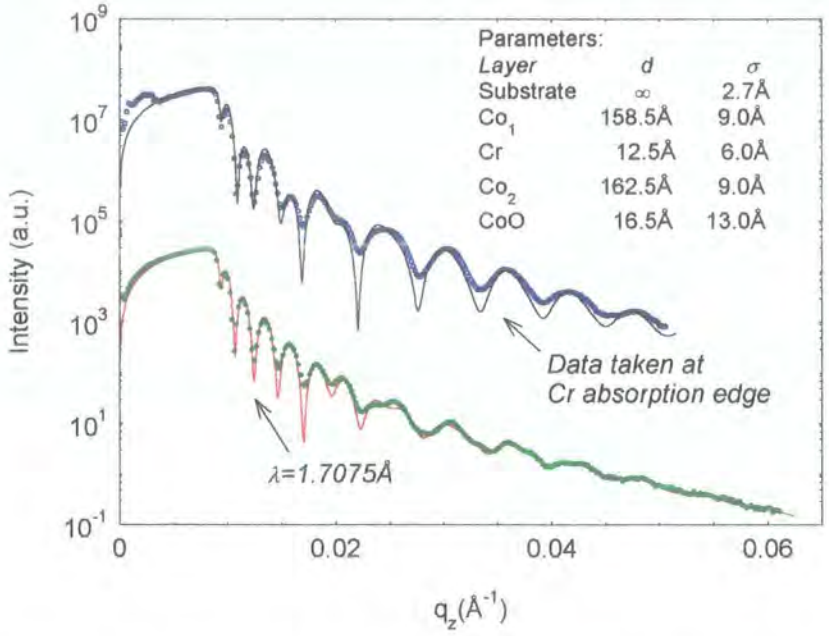

Figure 6.15: Data (points) and best fit (line) of sample *C*.

The best fits from both samples shows that although the samples were nominally identical, the thickness of the cobalt layers were different in the two samples. The thickness of the two cobalt layers in sample *C* was approximately 11% less than those in sample *A*. However, even though the two samples differ from the nominal structure (more so for sample *C*), the chromium thickness is the same in both samples, i.e. 12.5 ± 1Å, which may account for the similar coupling found in the two samples. The similarities between sample *A* and *YND* suggested that it would be possible to fit the diffuse scatter generated from sample *A* using the parameters from *YND* as the initial model. The results of these simulations is shown in figure 6.16 a-d:

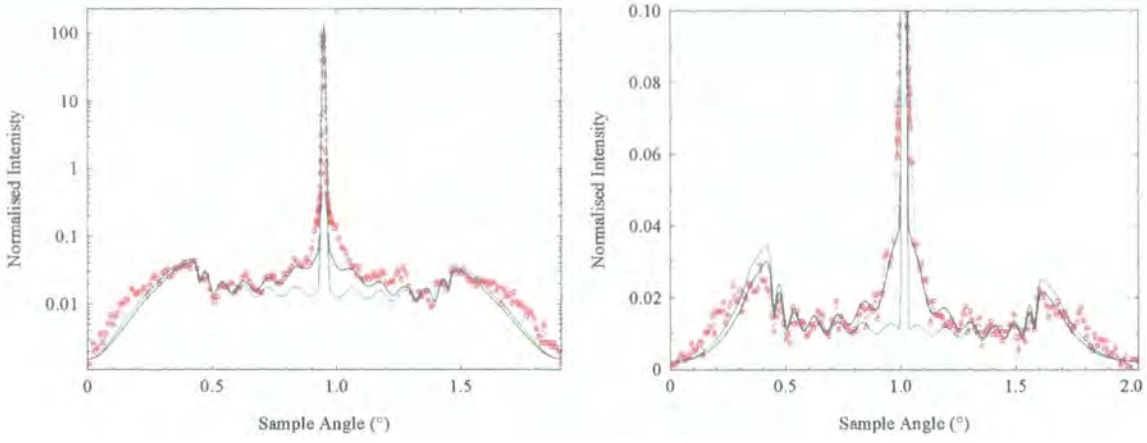

Figure 6.16: Transverse diffuse scatter from *YLA* through a Kiessig Maximum (a) and (c), and a Kiessig minimum (b) and (d). Data taken through the same Kiessig fringes at chromium edge (c) and (d). Model with ξ=150, h=0.15 shown in blue and ξ=110, h=0.25 shown in green.

From figure 6.16, it is clear that extremely good fits to sample *A* have been achieved at all wavelengths and scattering vectors probed, for the same set of input parameters. As discussed in the previous section, which deals with the results from *YND*, the fit to the diffuse scatter is consistently better, in the low q_x region, for a correlation function with low values of *h*. This effect can clearly be seen in figure 6.16 where two correlation functions are plotted; firstly the best fit using a low fractal parameter (h=0.15, ξ=150Å), plotted in blue, and secondly in green the best fit using the fractal parameter used in the simulation of *YND* (h=0.25, ξ=110Å).

Although it has been shown, from the fits, that a low fractal parameter model is possible for all angles and wavelengths in this sample, the validity of the fractal model with such a short fractal parameter is still not confirmed, especially with the extremely high degree of interdiffusion that is encountered in these samples. The values of the various roughness parameters that can be deduced from the fits to sample *A* are tabulated below (table 6.4):

Layer	**Thickness (Å)**	**Uncorrelated roughness (Å)**	**Correlated roughness (Å)**	**Interdiffusion parameter (Å)**
Si	∞	0.5	0.2	2.4
Co	178.5	0.7	0.2	6.4
Cr	12.5	2.2	0.4	6.1
Co	172.5	1.0	4.4	6.6
CoO	16.5	4.0	2.3	8.3

Table 6.4: The roughness parameters corresponding to the fits shown in figure 6.16

It is interesting to note that the interdiffusion parameter for each of the interfaces in this sample is very similar to those found in *YND*. There is slightly less correlated roughness in the lower layers in this sample when compared with *YND*. However the overall structure is very similar to *YND*, even though the chromium thickness has increased to 12.5Å from 9Å.

All the *L* series samples were investigated by TEM where it was again seen that samples *A* and *C* were very similar, and that the structure of both samples was similar to that observed in *YND*. However, the samples had slightly smaller grain sizes; ranging from only 90Å to 140Å, as opposed to 150 Å to 200Å in *YND*. These grain sizes are again in agreement with the correlation length deduced from the fit to the diffuse scatter originating from sample *A*. The TEM micrograph from sample *A* is shown in figure 6.17.

Figure 6.17: HR-TEM micrograph from sample *A* [24]

The thickness of the layers that were deduced from the TEM micrograph are tabulated in table 6.5, and compared to the x-ray reflectivity results:

Sample	SiO2	1st Co	Cr	2nd Co	CoO
Sample A	**4Å - 7Å**	**169Å - 173Å**	**8Å - 4Å**	**137Å - 160Å**	---
X-rays	---	178.5Å	12.5Å	172.5Å	16.5Å
roughness	*2.4Å*	*6.0Å*	*6.0Å*	*8.0Å*	*9.5Å*
Sample C	**12Å - 14Å**	**156Å - 165Å**	**5Å - 7Å**	**144Å - 149Å**	---
X-rays	---	158.5Å	12.5Å	162.5Å	16.5Å
roughness	*2.7Å*	*9.0Å*	*6.0Å*	*9.0Å*	*13.0Å*

Table 6.5: Layer thickness deduced from the TEM micrographs (bold) and x-ray reflectivity from samples *A* and *C*.

Samples *A* and *C* can be used to show the importance of a detailed knowledge of the structure when calculating coupling and anisotropies from BLS and FMR spectra. Using the nominal structures for samples *A* and *C*, the interlayer coupling K_c, was deduced to be -0.09 erg cm^{-2}, and -0.05erg cm^{-2} respectively. However, when the true thicknesses were used, taking into account the reduction of the cobalt layers, both samples had the same anti-ferromagnetic coupling strength of -0.10 erg cm^{-2} [28].

Sample *B*, which showed ferromagnetic alignment, was also studied by both TEM and grazing incidence x-rays to investigate whether the observed ferromagnetic coupling was caused by structural changes in the sample or whether it was due to a change in the chromium thickness. It was hoped that the anomalous in-situ MOKE curve from the first Co layer could be explained by a structural model that was different to the other samples. Figure 6.18 shows the specular reflectivity from sample *B*, taken at the chromium absorption edge:

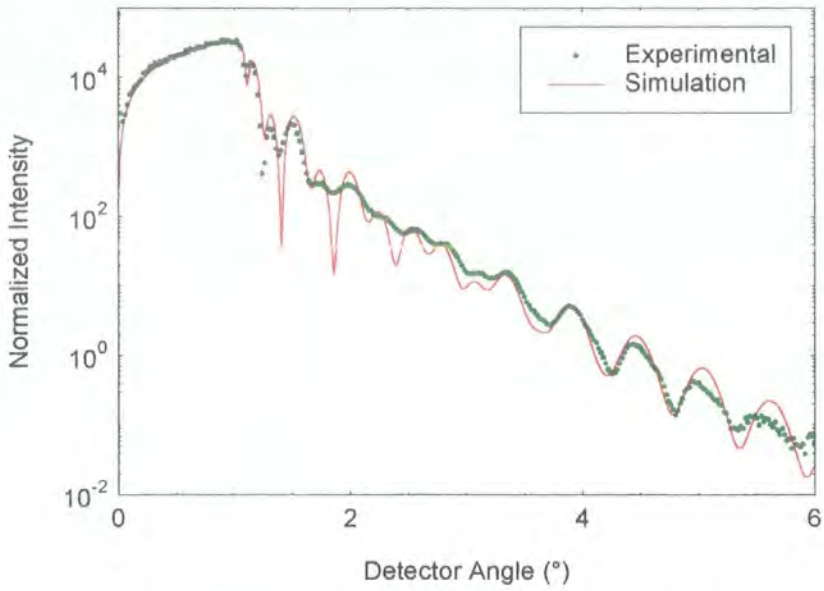

Figure 6.18: Specular reflectivity from sample *B* taken at the chromium absorption edge

The significantly different shape of the reflectivity curve between detector angles of 2 and 4 degrees is immediately obvious. The best fit to the data is also shown in figure 6.18. However, it was found that a more complicated model was needed to fit sample *B* than any of the other trilayers studied. A deduced schematic of the structure of sample *B*, deduced from the current best fit, fitted is shown in figure 6.19

Figure 6.19 Schematic of the model used to fit sample *B*.

Initially the sample was fitted with a simple Si/Co interface, in the same way as for all other samples. This method required an extremely large interface roughness at this interface which clearly implied that interdiffusion had occurred across this interface. The fit was considerably improved with the addition of a thin cobalt silicide layer, which took into account the large amount of interdiffusion that was thought to have occurred. The formation of a silicide layer could well explain the anomalous MOKE curve because the subsequent growth of the cobalt layer would have been affected. It was extremely difficult to find an accurate thickness of the chromium layer in this sample, and an alloyed interface layer was added to the model. Thickness measurements based on EDAX [29] suggested that the chromium layer was 23Å thick. However, no fit was possible using a discrete chromium layer of this thickness. Moreover, this technique was known to be highly inaccurate as it gave incorrect thickness measurements for sample *A* for which the thickness of the layers was well known.

HR-TEM studies (figure 6.20) showed that there was a large fluctuation of layer thickness for both the bottom cobalt and chromium layers, even over the small area of sample studied. The chromium layer was more distinct in this sample showing that it was thicker and more continuous than samples *A* and *C*. Table 6.6 shows the thickness of the layers that were deduced from the micrograph:

Sample	**SiO_2**	**1st Co**	**Cr**	**2nd Co**
Sample B	15Å - 24Å	150Å - 163Å	10Å - 24Å	139Å - 156Å

Table 6.6: Layer thickness calculated for sample *B* from HR-TEM

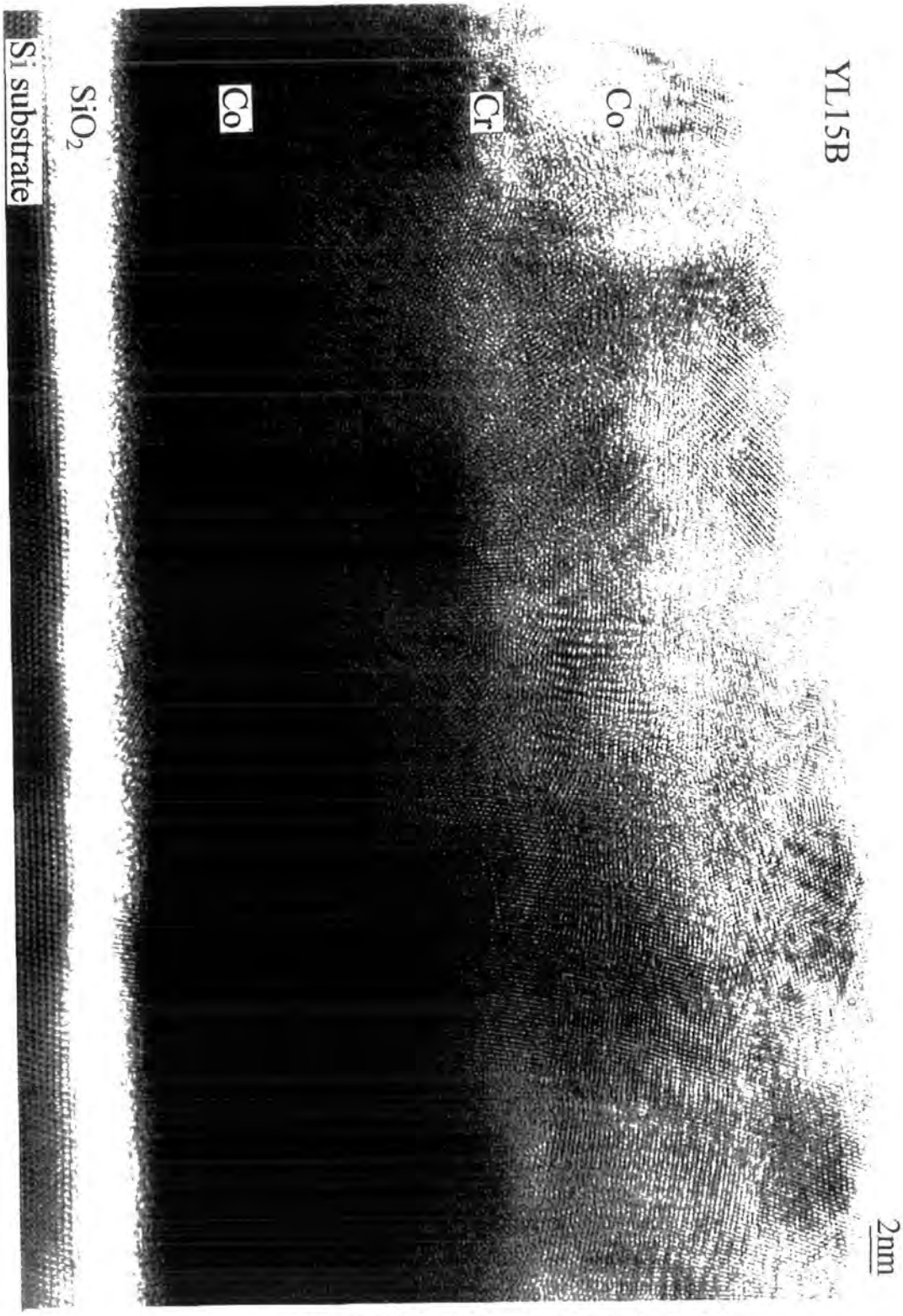

Figure 6.20: HR-TEM of sample *B* [24]

The most striking difference between this TEM micrograph and the ones presented previously is the structure of the Si/Co interface. The silicon oxide layer is much thicker for this sample, but more importantly there is an interdiffused layer of material approximately 16 ± 5Å thick between the oxide layer and the deposited cobalt. This is the layer that was simulated independently in the reflectivity by assuming the formation of a cobalt silicide. As silicon oxide is extremely stable, it seems unlikely that a silicide layer should have formed for room temperature deposition. However a definite layer is present which may have resulted from the preparation technique of the substrate or may indeed be a silicide layer. From neither structural technique, HR-TEM or x-rays, has it been possible to identify categorically this layer; however its effects may have caused considerable change to the structure of the sample.

6.6.1 Concluding remarks about samples deposited in zero field

Although it has not been possible to characterise structurally sample *B* using GIXS as fully as the other samples in this chapter, it has been shown that there is a significant difference in terms of structure between sample *B* and the other two. A model of the sample is proposed which includes a cobalt silicide and an alloyed Co/Cr layer. These structural changes are confirmed in the TEM micrograph where a thicker chromium layer was seen. In both techniques a thin layer of an unknown material is present on the substrate/cobalt interface. This layer may well have effected the subsequent growth of the cobalt layer resulting in the anomalous MOKE curve observed.

For the two samples which showed anti-ferromagnetic coupling, the value of the chromium thickness found agrees well with values found in the literature. In both cases the specular reflectivity was fitted accurately, and for sample *A*, the diffuse scatter was also fitted. The fits to the diffuse scatter show that this sample is indeed similar in structure to sample *YND*, with similar levels of interdiffusion at the interfaces.

6.7 Conclusions

In this chapter the structure of Co/Cr trilayers have been investigated. The grazing incidence x-ray technique has been successfully applied to system with a high degree of interdiffusion. Independent structural work on the same samples carried out by HR-TEM has confirmed many of the results found by the x-rays.

The GIXS results show that it is possible to fit systems which exhibit a high level of interdiffusion. It has been shown that even though much of the roughness deduced from the specular scans is in fact due to interdiffusion, much of the remaining roughness is correlated through the system. In fitting the diffuse scatter, it was shown that the fits could be improved by fitting to a very low fractal parameter. The validity of the fractal model for such a low value of h has yet to be confirmed.

The most important result obtained in this chapter is the close relation between the HR-TEM micrographs and the grazing incidence diffuse scatter. It is interesting to note that the results from the two methods agree, even though they sample the system over very different length scales:- 100Å for TEM, 1cm for GIXS. The TEM micrographs show conclusively that the correlation length determined from fits to the transverse diffuse scatter is a measure of the lateral grain size. Although, it is possible to fit the x-ray data with a correlation length defined for each interface, the computations are extremely time consuming. However, it has been shown that fitting to an average correlation function gives results which are comparable to the HR-TEM results.

This chapter has continued the investigation of graded systems and tested the GIXS code on samples for which TEM is available. The close matching of the two techniques gives an added confidence level in both the GIXS technique and the fractal model in investigating metallic multilayered systems.

References from Chapter 6

1 Y. Liou, C.-R. Chang, C.K. Lo, C.P. Chang, Y.D. Yao, I. Klik, *IEEE Trans Mag,* **33** (5), *3652-3654,* (1997)

2 Y.Liou, C.A. Huang, Y.D. Yao, S.F. Lee, W.T. Yang, S.Y. Liao, C.P. Chang, *IEEE Trans Mag*, **31** (6), *3927-3929* (1995)

3 Th. Zeidler, F. Schreiber, H. Zabel, *J. Appl. Phys.*, **79** (8), *4793-4795*, (1996)

4 Th. Zeidler, W. Donner, N. Metoki, F. Schreiber, A. Schreyer, J.F. Ankner, C.F. Majkrzak, H. Zabel, *J. Magn. Mag. Mat.*, **148**, *211-212* (1995)

5 N. Metoki, W. Donner, H. Zabel, *Phys. Rev. B.*, **49** (24), *17351-17359*, (1994)

6 J. Picconatto, M.J. Pechan, E.E. Fullerton, *J. Appl. Phys.*, **81** (8), *5058-5060*, (1997)

7 H. Niedoba, B. Mirecki, M. Jackson, S. Jordan, S. Thompson, J.S.S. Whiting, P. Djemia, F. Garnot, P. Moch, T.P.A. Hase, I. Pape, B.K. Tanner, *Phys. Stat. Sol. A,* **158** (1), *259-264* (1996)

8 S.M. Jordan, C. Prados, *J. Mag. Magn. Mat.,* **172** (1-2), *69-73* (1997)

9 A.C. Daykin, J.P. Jakubovics, A.K. Petford-Long, *J. Appl. Phys,* **82** (5), *2447-2452* (1997)

10 Reproduced from Reference 3 (a and c), and data collected within the network (Sample A section 6.6) , courtesy of A.C. Daykin

11 Introduction to Solid State Physics Sixth Edition, *C. Kittel*, **John Wiley & Sons**, (1991)

12 Solid State Magnetism, *J. Crangle*, **Hodder & Stoughton**, (1991)

13 M. Jackson, Ph.D. Thesis, University of York, (1997)

14 P. Mutti, C.E. Bottani, G. Ghislotti, M. Beghi, G.A.D. Briggs, J.R. Sandercock, *Advances in Acoustic Microscopy, Vol 1., Chapt. 7*, **Plenum Press** (1995)

15 Fundamentals of High-Resolution Transmission Electron Microscopy, *S. Horiuchi*, **North-Holland** (1994)

16 Optics 2nd Ed., *E. Hecht*, **Addison-Wesley** (1990)

17 Transmission electron microscopy, *L. Reimer*, **Springer-Verlag** (1984)

18 International Tables for X-ray Crystallography Vol. III, *Gen. Ed. K. Lonsdale*, **D. Reidel Publishing Company,** (1995)

19 Samples prepared by *S.M. Thompson*, University of York, and *J.-J. Freijo*, Universidad Computense, Madrid

20 Courtesy, *S.M. Jordan and S.M. Thompson*, University of York

21 Courtesy, *M. Jackson*, University of York, ECHMC Network bi-anual reports, Sept. 1996

22 Courtesy, *F. Garnot*, Université Paris-Nord, ECHCM Network bi-anual reports, April 1997

23 Y. Henry, C. Mény, A. Dinia, P. Panissod, *Phys. Rev. B*, **47** (22), *15037-15045* (1993)

24 Courtesy, *E. Ho and A.K. Petford-Long*, University of Oxford

25 Calculated from the selected area diffraction pattern

26 T.P.A. Hase, I.Pape, B.K. Tanner, S.M. Thompson, S.M. Jordan, J.-J. Freijo, *Adv. X-ray Analysis*, **40**, (1997)

27 F. Scheurer, P. Ohresser, H. Bulou, J.P. Deville, B. Carrière, A. Dobriou, *Phys. Rev. B,* **56** (20), *13490-13495,* (1997)

28 Courtesy, *F. Garnot*, ECHCM Network bi-anual reports, October 1996

29 Measured by H. Nieodba, ECHMC Network bi-anual reports, October 1996

Chapter 7

X-Ray scattering from Molecular Beam Epitaxy (MBE) grown Cu/Co (111) Multilayers

7.1 Introduction

The results presented in this chapter are taken from a series of experiments undertaken by the author together with, in particular, P.A. Ryan of the University of Leeds. These experiments were designed to investigate the effects of growth temperature on the magneto-transport properties of Cu/Co multilayers. The background to these experiments is presented to the reader in section 7.2. Section 7.3 consists of a description of the growth conditions of the samples studied. The magneto-transport results relating to the samples under investigation are then discussed in section 7.4. An analysis of the x-ray characterisation of these samples is begun in section 7.5, where the specular scatter from the samples is reviewed. Following this, and prior to a brief look at the diffuse scatter (section 7.5.1), the current best fits of the specular scatter are presented. In order to model the diffuse scatter, the results of high-angle diffraction experiments are important. The results from double and triple axis diffraction experiments are thus presented in section 7.6. The diffuse scattering from the grazing incidence measurements is analysed in the light of the results obtained in section 7.6 in section 7.7. The results obtained from all the x-ray scattering experiments are then summarised in section 7.8.

7.2 Background

As has already been discussed in chapter 2, the giant magneto-resistance (GMR) effect was first discovered in 1988. It was quickly found that this effect was observable in Cu/Co multilayers. Oscillatory exchange and magneto-resistance was observed up to the fourth anti-ferromagnetic maximum for sputtered materials.

However, when the same experiment was repeated on multilayers deposited using molecular beam epitaxy, the resulting strongly textured samples exhibited very weak oscillatory behaviour. The first antiferromagnetic (AF) peak is predicted to occur for a copper spacer layer thickness of 9Å [1]. There are several reports in the literature that AF coupling does indeed occur for copper thickness of this value, however, in contrast to the sputtered samples the second order AF peak is rarely seen [2]. In the work of Schreyer et. al. [2] the second AF coupling peak in Cu/Co (111) multilayers has been observed using spin polarised neutron reflectivity.

The major difference between MBE and sputtering is in the crystallographic structure and interface morphology of the films. Despite the existence of differing models which describe the GMR effect in transition metal systems (chapter 2) in relation to either surface roughness or Fermi surface effects associated with crystallographic texture, definitive experiments which can separate the two are rare. The experiments which gave the results described in this chapter originated from a desire to create an experiment whereby it would be possible to separate unambiguously the effects on the GMR by the Fermi surface and effects from interfacial roughness.

An initial experiment was carried out by Xu et. al. who showed that the GMR was proportional to the width of the high angle rocking curve [3]. With the correlation between structure and GMR being observed it was decided to conduct a more in-depth analysis.

7.3 Sample Preparation

The samples were all grown in a VG80 Semicon MBE machine at the University of Leeds [4]. Four sets of samples were prepared covering the first anti-ferromagnetic coupling peak, which in this case occurred for copper thicknesses in the range of 7-8Å [3]. The buffer, seed and capping layers, as well as the cobalt layers, were deposited with a constant thickness. The thickness of the copper spacer

layer was varied across the sample by the use of a shutter to produce a wedged multilayer.

The samples were deposited onto a $(11\bar{2}0)$ sapphire substrate which had been cleaned in acetone and ethanol and mounted onto a molybdenum block. The substrate was then heated to a temperature of 950°C. At this temperature a nominally 30Å thick niobium seed layer was deposited at a speed of 1Å/s. Due to the reactivity of niobium it is not possible to deposit cobalt directly onto a niobium layer [5] and so the sample was allowed to cool to 375°, and a copper buffer layer of the same nominal thickness as the niobium was deposited at a slower rate of 0.2Å/s. The multilayer was then deposited when the substrate had reduced to the correct temperature. Finally a thin gold capping layer of approximately 15Å was deposited to prevent oxidation of the top few bi-layers. The sample was cut with a diamond saw to produce a set of samples with different copper thicknesses. This method of sample preparation is similar to that used by Bröhl et. al. [5] where Co/Cu multilayers were also deposited onto sapphire substrate with niobium seed layers.

Two series of samples will be considered in this chapter. In the first, designated series *A*, the copper thickness was nominally 7Å, and series *B* corresponds to that part of the wedge where the copper thickness was 8Å. The multilayer was prepared at three different substrate temperatures; room temperature, 100°C and finally at 150°C. Table 7.1 summarises the growth temperatures for the constituent layers within the samples:

	Nb Seed (°C)	Cu Buffer (°C)	Multilayer (°C)
Sample 1	950	375	23
Sample 2	950	375	100
Sample 3	950	375	150

Table 7.1: The sample temperature during deposition of the layers for both series of samples

As a comparison, an additional wedged sample was prepared with the copper buffer layer deposited at 250°C, with all the other parameters the same as for sample 1. These control samples have been designated *CA* for the sample which corresponds to sample 1 in series *A* (Cu = 7Å), and *CB* for the corresponding sample in series *B* (Cu=8Å). The deposited layer quality in all samples was monitored during growth by the use of an in-situ reflection high energy electron diffraction (RHEED) system.

After deposition, the samples were subjected to a magneto-transport investigation at the University of Leeds. The resistivity as a function of applied field was recorded at 4.2K using a standard 4-probe d.c. system. The contacts were spring loaded and were spaced at an interval of 2.5mm, and the resistance measured whilst the field was applied in the plane of the layers. The resistivity was then calculated from the resistance when corrected for shape effects [6]. The magnetisation versus field data was recorded by making use of the optical Kerr effect. In the next section, the magneto-transport results from the two series of samples will be presented.

7.4 Magneto-transport Measurements

The magnetometry results contained in this section were carried out by P.A. Ryan and J. Xu at the University of Leeds, who were working throughout the collaboration with the author in the work described and analysed in this chapter. The magneto-resistance and the coupling were measured for all the samples. The giant magneto-resistance (GMR) versus field, for all the samples in series *A* is presented in figure 7.1.

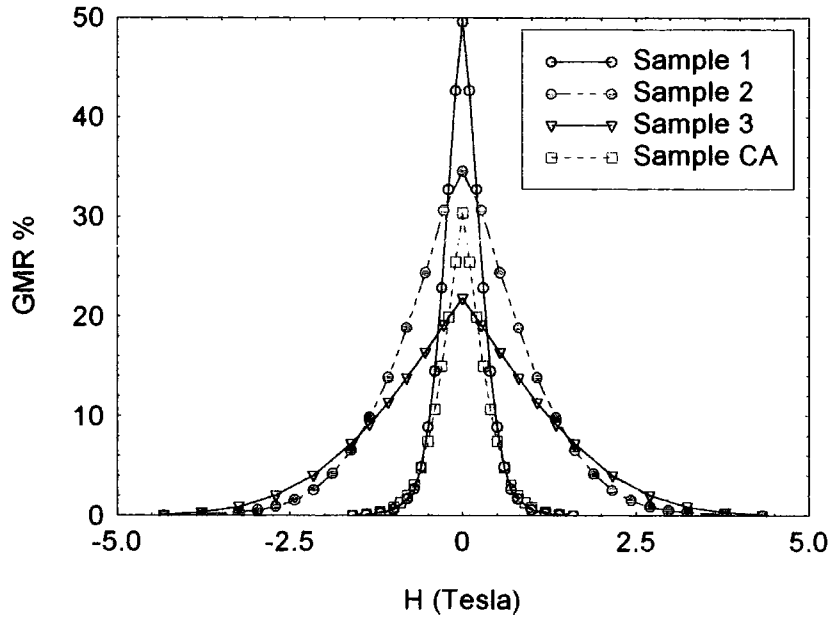

Figure 7.1: The GMR loops at 4.2K for series *A*.

The GMR loop for sample *CA* is also shown in figure 7.1. The shape and size of the GMR is seen to be different for all the samples, but as well as the GMR changing, the saturation field is also seen to depend on the deposition temperature. The saturation field for the two samples where the multilayers were deposited at room temperature are identical, even though their GMR is very different. On the other hand, the saturation field is clearly seen to follow the multilayer deposition temperature. The magnitude of the GMR does not follow such a clear trend.

The magneto-resistance decreases steadily from 50% for sample *A1* down to 22% for sample *A3*, as the multilayer deposition temperature increases. These results are in contradiction to the results obtained by Harp et. al. who observed that a significant enhancement (25%) of the GMR occurred for multilayers deposited at 150°C [7]. It is interesting to note that the two samples with the same multilayer deposition temperature and saturation field have different GMRs, (50% for sample *A1*, compared with 31% for sample *CA*). The resistivity of the samples across a series was also seen to change with deposition temperature. The changes in the resistivity for the samples in series *A* are tabulated in table 7.2:

Sample	GMR (%)	Resistivity (μΩcm)
A1	50	9.7
A2	35	11.1
A3	22	12.3
CA	31	11.7

Table 7.2: The GMR and resistivity of series *A*, at 4.2K

The resistivity of the samples in series *A* is seen to fluctuate over a couple of μΩcm. Although changes in the resistivity of samples clearly occur with multilayer deposition temperature, these changes are not sufficient to explain the changes in the observed GMR. An earlier study by Laidler et. al. on the effects of annealing Cu/Co multilayers found that the changes in GMR could be attributed to changes in the resistivity of the samples resulting from a change in the structure of the capping layer [8].

It is well known, (see chapter 2) that the GMR is strongly dependent on the amount of AF coupling between the magnetic layers, which in turn varies with the spacer layer thickness. The volume fraction of AF coupling can be inferred from the remanent magnetisation. To confirm that the changes observed in the GMR could not be attributed to a difference in the AF coupling strength between the samples, room temperature MOKE loops were undertaken. The MOKE curve for sample *A3*, is shown in figure 7.2. Also included in figure 7.2 are the remanent magnetisation values for all the samples in series *A*.

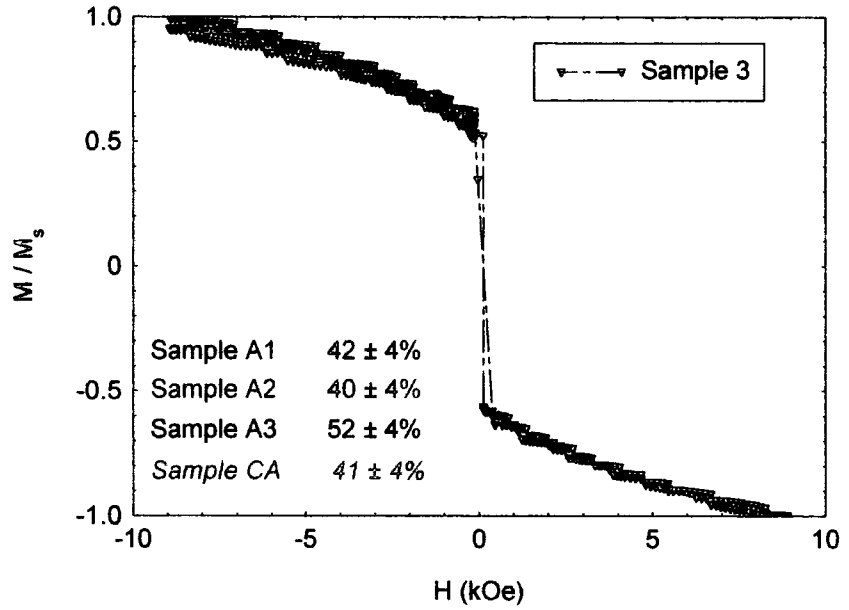

Figure 7.2: The room temperature MOKE loop from sample A3, and inset the tabulated values of the remanence from the other samples in series *A*.

As can be seen from figure 7.2 there is no trend in the remanence with GMR. The fact that the remanence is similar for all the samples indicates that the volume fraction of anti-ferromagnetic coupling in each sample was similar. The room temperature MOKE curves suggest that the GMR changes cannot be attributed to changes in the magnetic coupling; however the changes observed in the saturation field of the GMR suggest otherwise. Such a discrepancy has been observed previously by Clarke et. al. [9]. The observed changes in the magnitude of the GMR are thus likely to be caused by changes in the structure of the samples.

The data presented above has all been from series *A*. The data from Series *B* exhibits similar behaviour. The difference in the magneto-resistance between series *B*, and series *A* can be explained in terms of the thickness of the copper layer. Changes to the thickness of the copper layer result in changes to the coupling, and hence the GMR. The GMR values for both series of samples are tabulated below in table 7.3:

Series A		Series B	
Sample	*GMR*	*Sample*	*GMR*
A1	50	B1	47
A2	35	B2	29
A3	22	B3	18
CA	*31*	*CB*	*28*

Table 7.3: The GMR for the samples in series *A*,*B* and *C*

As can be seen in table 7.3, the changes in the magneto-resistance between series *A* and *B* were typically only a few percent.

The magneto-resistance loops in figure 7.1 are affected by two mechanisms: The saturation field is dependent on the growth temperature of the multilayer, whilst the GMR and resistivity are affected by both the buffer and multilayer growth temperatures. As evident from the MOKE curves, the large changes in the magneto-transport properties of the multilayers cannot be explained in terms of changes in the coupling.

In order to understand the dependence of the GMR on growth temperature, an in-depth x-ray characterisation of the samples was then carried out. Both grazing incidence scattering as well as high angle diffraction experiments were undertaken in order to identify structural changes in the samples which could then be correlated to the known changes in the magnetic properties of the samples.

7.5 Grazing Incidence Characterisations

Both series of samples were subjected to a full x-ray characterisation on station 2.3 at the Daresbury SRS by the author. Specular, (-0.1°) off-specular and transverse diffuse scans were recorded on all samples. Due to the low contrast between the materials, anomalous dispersion (chapter 5) techniques were required.

The scans were recorded at (λ=1.38Å) and away (λ=1.48Å) from the copper absorption edge.

Due to the time consuming nature of quantitative analysis, fits to the specular and diffuse scatter were only undertaken on series *A*. However, qualitative information on the structural changes induced by the changing temperature of deposition can readily be obtained by direct comparison of similar data sets. Figure 7.3 shows the specular scatter from series *B*, taken at the copper absorption edge.

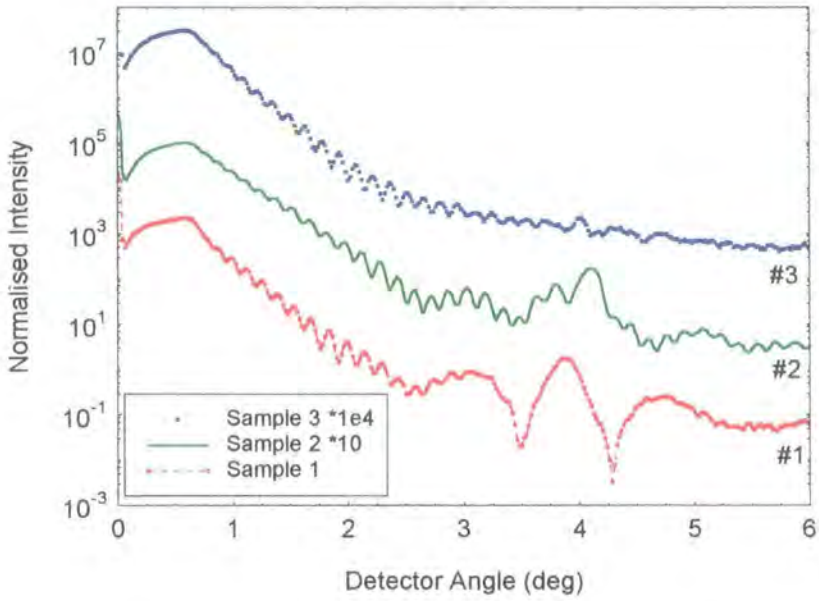

Figure 7.3: Specular $\theta/2\theta$ scans for series *B*, recorded at the copper absorption edge.

As expected, the specular scans from series *A* were identical, but with the Bragg peak at a slightly different position due to the different bi-layer repeat thickness caused by the thinner copper layer. The specular scans for series *A* are shown below, with their corresponding best fits. All the specular scans show clear Kiessig fringes, but there are significant differences between the samples. The specular scans from both series of samples show differences in the vicinity of the Bragg peak. There is an additional fringe which becomes more pronounced as the GMR rises. These fringes were subsequently found to be due to the effects of the capping and buffer layers. The Bragg peak intensity, which is proportional to the roughness at the interfaces

within the multilayer, is seen to reduce as the deposition temperature of the multilayer was increased.

These results suggest that the GMR is proportional to the interface roughness. The variation of GMR with interface roughness has been studied by several authors, for example see Ueda et. al. [10] and references therein. The results obtained above, namely that the MR decreases as the surface roughness increases has been observed in sputtered Cu/Co multilayers by a number of investigators at different institutions [10,11]. On the other hand, epitaxial Cu/Co multilayers investigated by Kingetsu et. al. [12] and Fe/Cr layers studied by Fullerton et. al. [13] show the opposite behaviour. Studies where the interface has purposely been damaged by the inclusion of Zr [14] or Au [15] suggest that the GMR is proportional to the interfacial roughness and that this underlies all the results obtained above.

The conclusions drawn above, as well as those in references 9-14, (which relate the structure to GMR, result from reflectivity studies alone) suggest that roughness plays an important role in defining the GMR, but that there are other mechanisms which can also effect the magnitude of the GMR. It has been shown in a series of theoretical papers by Barnas et. al. that the statistical nature of the surface can also effect the GMR [16,17,18]. The variation of the GMR with the statistical nature of the interfaces may explain why the GMR of sputtered systems ($0.6 \leq h \leq 1$) and MBE epitaxial samples ($0.1 \leq h \leq 0.4$) is so different. In order to study the statistical nature of the surface the diffuse scatter should be investigated. This will be undertaken in sections 7.5.1. and 7.7. Prior to the discussion of the diffuse scatter, the results obtained from fitting the specular scatter from series *A* is here presented.

The specular scatter from the samples was fitted using the code described in previous chapters. The fitting of the reflectivity data was undertaken in conjunction with Paul Ryan of the University of Leeds. The samples were fitted at both wavelengths, and the final best fits apply equally to both wavelengths. When the fitting was attempted it was found that only if the top copper layer had alloyed with the gold cap could the samples be fitted. This assumption was required before the

near surface electron density and the phases of the Kiessig fringes could be fitted. This phenomenon had been observed before in an annealing study of Cu/Co multilayers by Laidler et. al. [8] and in other studies [e.g. 19].

In the case of samples *A1* and *A2* it was not possible to fit the rise in specular scatter for scattering angles just greater than the Bragg peak (figure 7.3) by varying any of the parameters. The best fit to sample *A1*, assuming the nominal structure, is shown in figure 7.4.

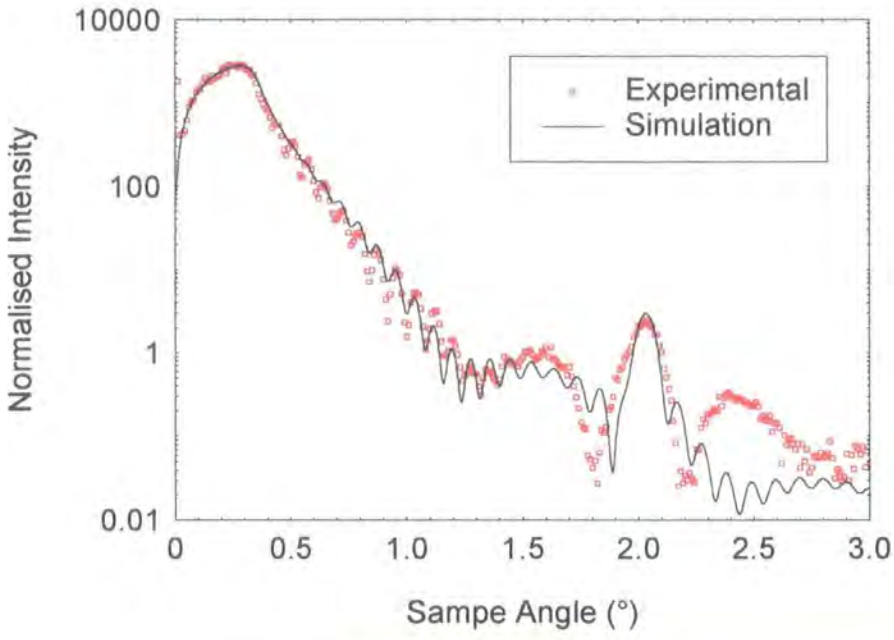

Figure 7.4: The best fit to Sample *A1*

The enhancement of the specular scatter could only be fitted by assuming an additional periodicity in the structure [20]. The fitting of the multilayer position and roughness was difficult for sample *A3*, where there is not a clearly defined Bragg peak. The specular scans for series *A* recorded at the copper absorption edge are shown in figure 7.5 along with the their current best fits.

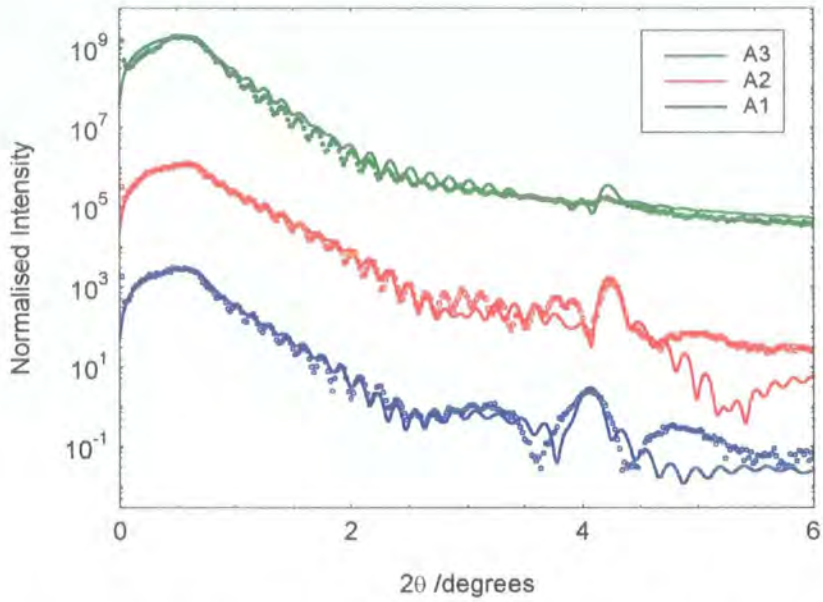

Figure 7.5: The specular scatter recorded at the absorption edge for series *A* with their corresponding best fit structures [21]

The best parameters obtained from the best fit curves in figure 7.5 are tabulated below in table 7.4:

	Seed	**Buffer**	**Bi-layer**		**Cap**		
	t /Å ± 3	t /Å ± 3	t /Å ± 0.5	$\sigma_{total} \pm 1$	t /Å ± 1	$\sigma_{total} \pm 1$	*Alloy*
A1	20	22	19.9	7	33	5	$Cu_{66}Au_{34}$
A2	22	46	18.8	7	30	4	$Cu_{37}Au_{63}$
A3	35	45	19.2	11	27	10	$Cu_{42}Au_{58}$

Table 7.4: Fit parameters from series *A*.

The fits to the specular scatter confirm the quantitative trends observed from series *B*. The roughness of the multilayer increases as the deposition temperature rises. It has proved difficult to isolate the thickness of the buffer and seed layers. The total thickness of these two layers can be estimated from the Kiessig fringe period. The alloy composition is also shown to vary across the range of samples.

The fitting of the specular scatter was further complicated by the fact that the samples are highly figured, and therefore the specular ridge is not smooth. This is an artefact of using sapphire as a substrate. However, figuring does not effect the diffuse scatter, and in the next section, the diffuse scatter originating from the samples will be investigated.

7.5.1 Diffuse Measurements

Figure 7.6 shows the off set (-0.1°) specular $\theta/2\theta$ scans for the samples in series *B*.

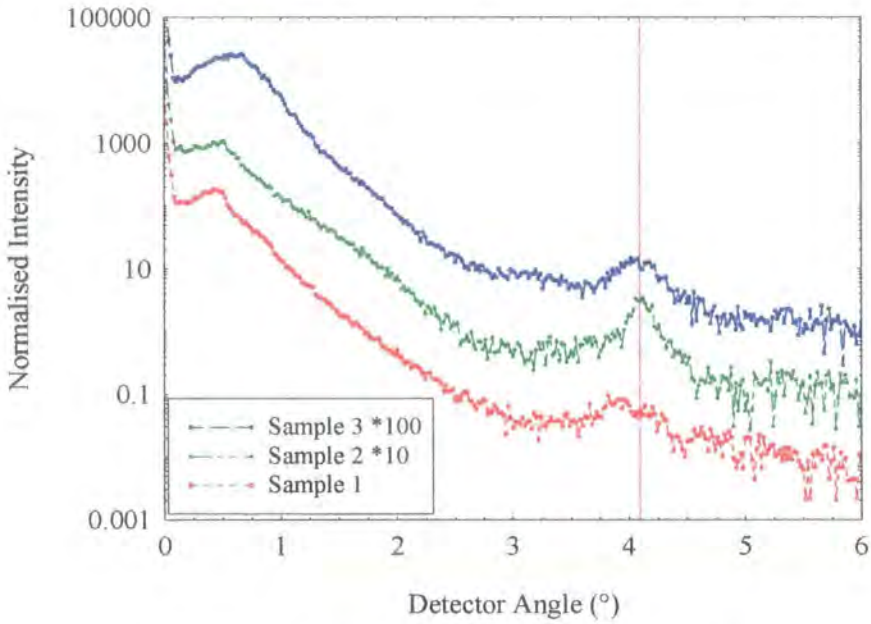

Figure 7.6: The off-specular scans for series *B*

All the off-specular scans show a clear off-specular Bragg peak. Again, the scans for series *A* were the same. The presence of an off-specular Bragg peak is indicative of correlated roughness through the multilayer. However, as there are no other modulations in the off-specular scans, the vertical correlation length is deduced to be less than the total thickness of the sample. The width of this off-specular Bragg peak is significantly narrower for sample *B2*. This is probably due to there being less variation in the bi-layer thickness in this sample, although it could also be indicative of a larger out of plane correlation length.

Figure 7.7 shows a full reciprocal space map (FRSM) of the diffuse scatter recorded from sample *A2*. By comparing this FRSM to those calculated in chapter 3, the partially correlated nature of the roughness is emphasised.

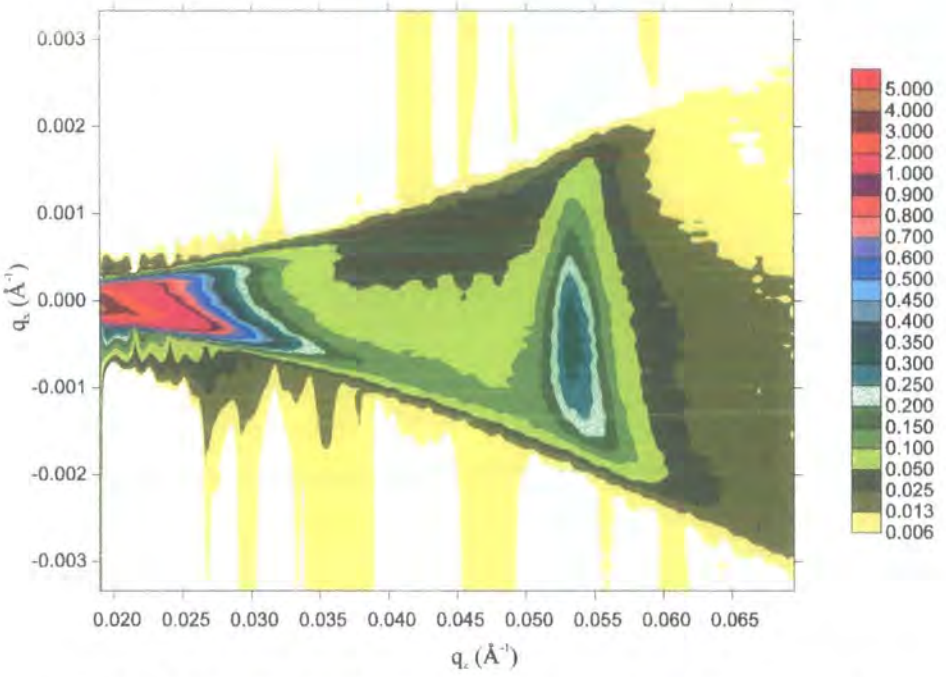

Figure 7.7: FRSM of the diffuse scatter originating from sample *A2*.

Unlike the specular scans, it is possible to identify the Bragg peak position clearly for all the samples in the off-specular scans shown in figure 7.6. The line marked in figure 7.6 shows that the bi-layer thickness is similar for all samples within each series. For series *B* the bi-layer thickness was calculated to be 19.3 ± 0.2Å and the same analysis on series *A* results in a bi-layer for the multilayer of 18.4 ± 0.2Å. These changes are consistent with the copper layer changing by 1Å.

The correlated roughness was investigated more fully by undertaking the analysis developed by Savage et. al. [22] which is discussed in more detail in chapter 3 above, in section 3.11. The amount of correlated roughness is plotted as a function of GMR in figure 7.8:

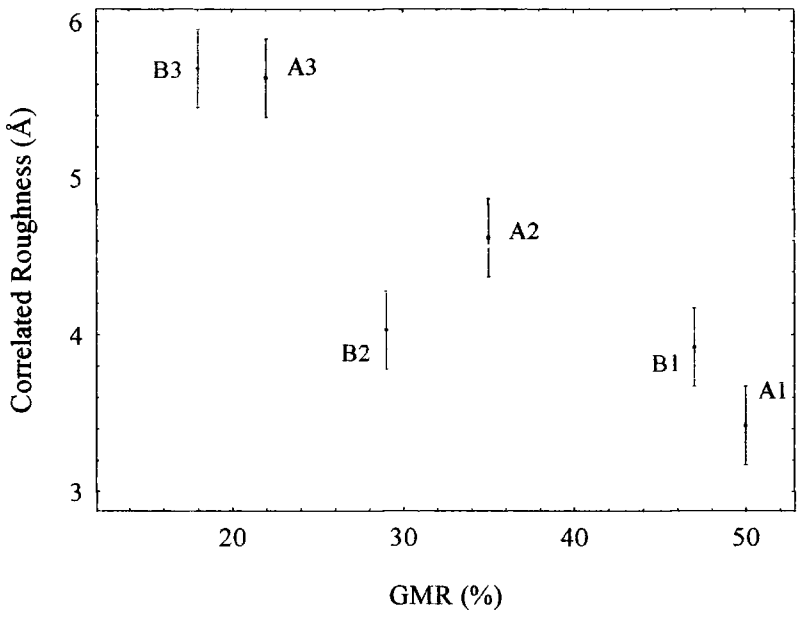

Figure 7.8: The correlated roughness as a function of GMR as deduced using the method developed by Savage et. al.

The uncorrelated roughness was also estimated using the same technique. This uncorrelated component of the roughness was found to be 4.5 ± 1Å, and there was little variation between the samples.

All the data to this point points implies that the GMR is proportional to the interface roughness and more importantly to the amount of correlated roughness. The specular scatter clearly shows that as the roughness decreases, the GMR increases. The analysis of the diffuse scatter also shows that GMR increases as the roughness decreases. The analysis of the diffuse scatter at the Bragg peaks shows that it is the correlated component of the roughness that is decreasing.

However, it has already been shown that the Born analysis of the diffuse scatter only yields correct results when (a) the sample is either highly correlated or highly uncorrelated and (b) that the lateral correlation length is large. The second criterion is, however, clearly not so important when comparing samples with similar correlation lengths. In the case of these samples, the nature of the surface is not known, and additionally there may well be large differences in the lateral correlation length between the samples caused by the deposition temperature changes. The high

degree of the conformality of the roughness cannot be assumed, and the diffuse scatter from the samples had to be simulated to obtain a more realistic picture of the correlations present in the samples.

Attempts by the author and collaborators to fit the diffuse scatter to a single set of parameters have not been successful. For sample *A3*, it was possible to fit the diffuse scatter to one covariance function. This was not the case for sample *A1* where two correlation lengths were required. One value of the correlation length accurately described the diffuse scatter away from the Bragg peak, but it was observed that a correlation length approximately 10 times this value was required to fit the diffuse scatter at the Bragg peak. Sample *A2* could be fitted with either model. These ideas at first sight seems strange as it should not be possible to have multiple fractal surfaces coexisting on a surface. During the high angle diffraction studies it was also observed that two length scales exist within the multilayer. The coexistence of two length scales is visually more apparent in the high angle results and so in the next section the high angle diffraction results will be presented. The modelling of the diffuse scatter obtained under grazing incidence conditions will be returned to in section 7.7 after the discussion of the high angle data.

7.6 HAXRD Measurements

The samples were initially characterised by double axis (large angular acceptance for the detector) diffraction by H. Laidler at the University of Leeds. In order to obtain detailed information about the sample the data obtained in grazing incidence experiments requires fitting. The same is true for data collected in high angle regimes. The high angle x-ray diffraction (HAXRD) scans from series *A* obtained in the University of Leeds laboratory are shown in figure 7.9:

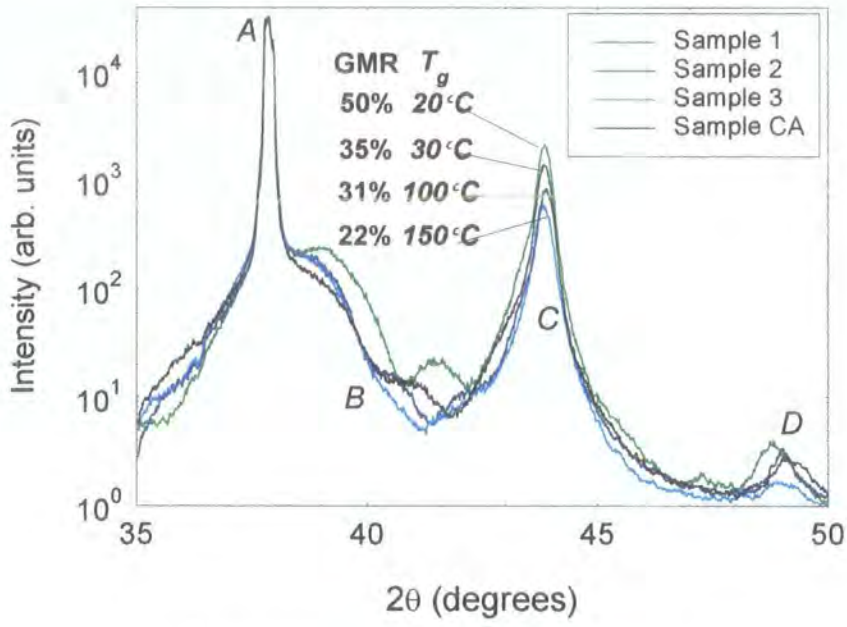

Figure 7.9: HAXRD scans originating from series *A*

The instrument resolution limited (110) sapphire substrate peak is clearly present in the scans and is marked as position *A* in figure 7.9. A strong Cu/Co (111) peak is observed at 2θ=43.8° (*C*) corresponding to the average *d*-spacing of Cu and Co. Information on the thickness and roughness of the Nb seed layer and capping layer can be found by fitting to the fringes observed between the substrate and the Cu/Co peaks, the region marked in figure 7.9 by *B*. A first order satellite (*D*) was observed in all samples. This peak arises from the effective lattice parameter of the bi-layer thickness of the multilayer and is the thus the same as the Bragg peaks observed in reflectivity studies. Immediately apparent in figure 7.9 is the changing height of the Co/Cu (111) peak. The intensity of the multilayer peak falls as a function of multilayer deposition temperature. This reduction in intensity is coupled with a slight increase in the width of the peak as the temperature increases. The changes observed in the zero order diffraction peak are matched by corresponding changes at the first order satellite peak.

A simulation programme was developed by H. Laidler [23] and modified by D. Dekadjevi [24]. The simulation programme is based on the SUPREX code developed by Fullerton et. al. [25] which inturn relies on the earlier work of Schuller

[26]. In this code, the diffraction of either multilayers or trilayers can be calculated. For the particular samples studied here, where a multilayer was deposited on a buffer and seed layers a modification was required to allow structural parameters on all the layers to be obtained. The seed, buffer and capping layers in these samples were modelled as a trilayer structure and the resulting simulation was added incoherently with the simulation resulting from the pure multilayer. For more details, the reader is referred to the *Ph. D.* thesis of Laidler [27] An example of a typical fit resulting from the procedure described above is shown in figure 7.10, where the HAXRD data has been simulated for sample *A1* by D. Dekadjevi, University of Leeds.

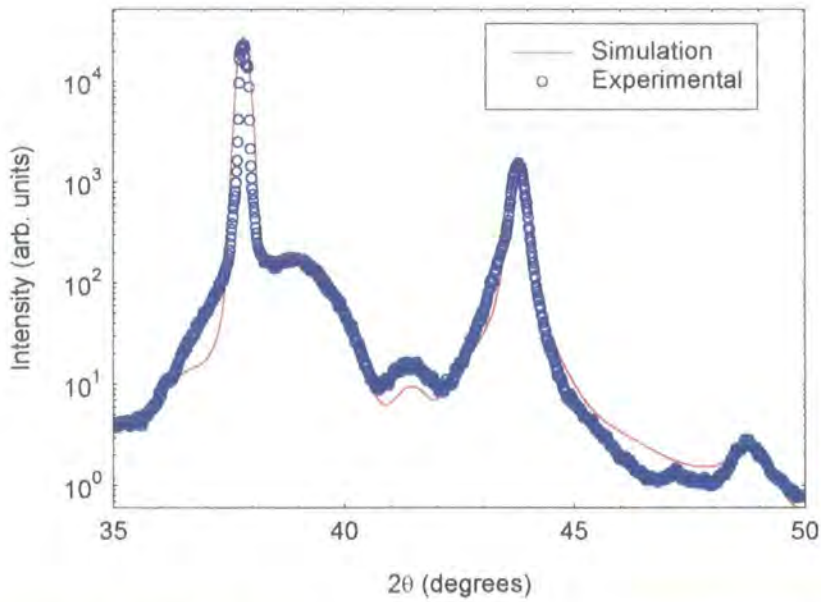

Figure 7.10: The HAXRD trace and corresponding best fit to sample *A1* [28]

The simulation program is able to calculate two different kinds of disorder in the multilayer [25]: discrete fluctuations on the bi-layer thickness and lattice parameter variations. Variations in the lattice parameter can either be modelled as an interdiffusion of the Co and Cu at the interface or as a "continuous roughness" which measures deviations of the lattice parameter away from the weighted average of the Co and Cu caused by increased strain at the interface. The simulations attribute the variation of the height of the Co/Cu (111) peak to changes in this continuous roughness (see table 7.5). The layer thickness fluctuation is not related to the crystalline order and therefore will have limited influence on the Co/Cu peak. Based

on the binary phase diagram of Co and Cu at these growth temperatures, the interdiffusion between them is expected to be negligible, and in these simulations this parameter has been set to zero.

The shape of the x-ray scan between the substrate and the main Co/Cu peak is due to scattering from the Nb and Cu buffer layers as well as from the gold cap. From the lattice spacings of Au and Nb, it is possible to model the shape of the shoulder on the right-hand side of the substrate peak. The maximum position of this shoulder will be strongly dependent on the exact composition of the cap. There is a displacement of this peak from one sample to the other which implies that the composition of the cap varies between layers. This can be explained by the formation of a Cu-Au alloy in the cap. The parameters obtained from the high angle fits are presented in table 7.5 below:

	Seed	**Buffer**	**Cu**		**Co**		**Cap**	
	t /Å ±5	*t /Å* ±5	*t /Å* ±0.4	σ_{CR} ±0.01	*t /Å* ±0.4	σ_{CR} ±0.01	*t /Å* ±5	*Alloy*
A1	52	28	7.9	0.04	10.6	0.04	53	$Cu_{20}Au_{80}$
A2	42	37	7.9	0.07	10.6	0.07	35	$Cu_{13}Au_{87}$
A3	42	35	7.9	0.08	9.8	0.08	41	$Cu_{13}Au_{87}$

Table 7.5: Parameters from the HAXRD experiments [28]

The results from the high angle data collected in the laboratory show similar trends to the grazing incidence reflectivity studies discussed previously. The continuous roughness which measures the change in lattice parameter due to strain at the interfaces is seen to increase as the deposition temperature rises. This continuous roughness is a measure of the interfacial roughness that was also observed to rise as the deposition temperature of the multilayer increased. The major differences between the data set collected at high angle, and that collected under grazing incidence is in the calculation of the composition of the cap. Grazing

incidence studies are highly sensitive to this term, whereas the calculation in the high angle scans relies on calculations of the lattice parameter according to Vegard's law. It has been shown experimentally [29] and theoretically [30] that CuAu alloys show deviations from this law, and as such the correct composition is more likely to be that determined from the low angle data presented in table 7.4.

The high angle diffraction work undertaken at Leeds was extended, and a high angle diffraction experiment was carried out by the author at Station 2.3, Daresbury SRS with an incident radiation of λ=1.38Å. Analyser slits immediately in front of the detector were set to 100μm, along with 100μm beam defining slits, giving a measured instrumental resolution of 39" which was far superior to that obtainable in the laboratory. Similar measurements were also undertaken by the author on BM16 at the ESRF where the wavelength was λ=0.6Å. The incident geometry on BM16 was the same as that on station 2.3, but as well as 100μm detector slits it was also possible to use a Ge(111) analyser crystal. [31]. With this increased resolution it is possible to obtain information on the lateral direction the x-rays have been scattered in both detector geometries. In this way it is possible to distinguish between lattice dilations ($\theta/2\theta$ scans) and tilt, or mosaic, distributions (θ scans) [32]. For the ultra high resolution double axis experiments (detector slits =100μm), the resolution in q_z and q_x is comparable to that obtained with a Ge analyser. In the experiments detailed here, the width of the slit was set to 4mm, resulting in poor resolution in q_y.

Figure 7.11 is an example of the high resolution HAXRD from the samples obtained at the synchrotron sources. Initially the samples were aligned with respect to the Sapphire $(11\bar{2}0)$ reflection. The position of the Co/Cu peak was then used to realign the sample and the $\theta/2\theta$ scan repeated. The large difference in intensity at both the Sapphire substrate peak and the Co/Cu peak indicate that the multilayer is misaligned to the substrate normal. This information was not accessible with the poor resolution of the laboratory experiment.

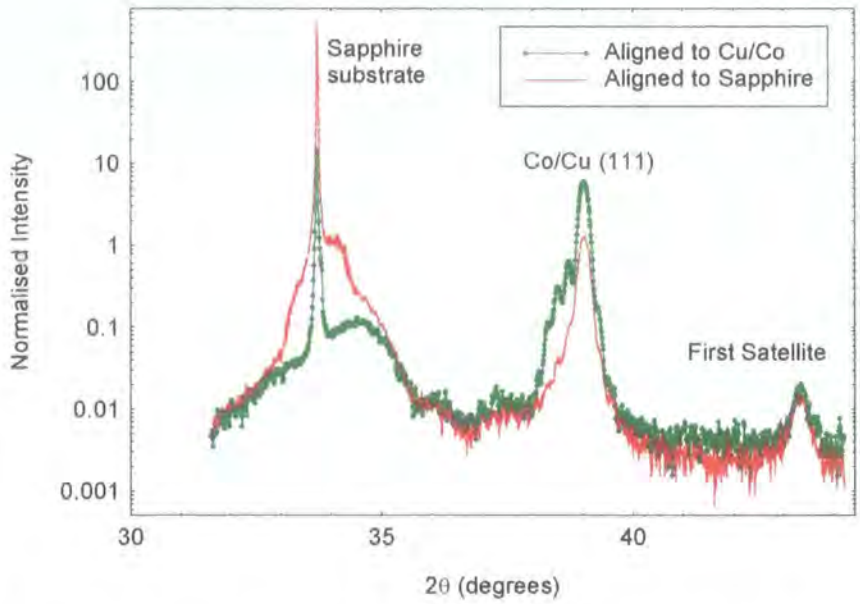

Figure 7.11: HAXRD data taken on station 2.3, SRS, obtained from sample *B2*

Information on the lateral structure of the sample can be obtained by investigating the scatter out of the specular condition. This scatter is usually measured by rocking the sample, whilst the detector angle remains fixed. In a single crystal the width of the Bragg reflection is defined, using dynamical diffraction theory, as the Darwin width [33]. The Darwin width defines the angular range over which the incident wave is reflected and as such is a measure of the separation of the dispersion surfaces. The Darwin width is very small, and the calculated FWHM for an incident wavelength of λ=1.54Å for Si 004 is 3.83" and Ge 111 16.69" [34]. In multilayer structures the width of the diffraction peak is much larger and kinematical theory can be used [35]. For surfaces with extended disorder, the rocking curve width is increased. The idea of a mosaic crystal is commonly employed to explain this observed broadening. A mosaic crystal can be considered to contain many smaller perfect crystals slightly misaligned with respect to one another. These mosaic blocks are large when compared to the coherence of the incident x-rays and thus the scattering from them does not interfere [36].

The effect of roughness and tilt, or mosaic distribution, can easily be separated by comparing the variation of the FWHM of these scans as a function of scattering vector. In general, if the broadening is caused by roughness, then the

FWHM of the peak will be constant in q_x. If, on the other hand, the width of the peak is caused by tilts, large in relation to the coherence length of the incident x-rays, the FWHM will be constant in angle. Holý et. al. has predicted that the interface roughness within a multilayer structure has no affect on the main multilayer diffraction peak (*C* in figure 7.9), and that the satellite peaks show a broadening which varies as the square of the satellite order [37]. This has been demonstrated in recent work on the Fe/Au system [38].

The initial work by the author on these samples investigated the mosaic nature of the samples by fitting the rocking curves to a Lorentzian line shape [39]. Within the error of the analysis there was no difference in the widths of the transverse scans taken through the zero order 111 Cu/Co multilayer peak and the first satellite due to the bi-layer. This suggests that the samples exhibit a mosaic character. In agreement with the earlier work carried out on these samples by Xu [3], the GMR increased as the mosaic spread reduced. The angular width of the transverse scans through the zero order Bragg peak ranged from $1.2 \pm 0.1°$ for the low GMR samples to $0.7 \pm 0.05°$ for the high GMR samples. A similar mosaic width was observed for epitaxial Co/Cu(001) multilayers deposited on sapphire substrates by Di Nunzio et. al.. Here the mosaic spread was found to be 0.7° [40]

Recently, work on metallic systems has shown that the broadening of the transverse scans can be caused by lateral correlations, or tilts which are small in comparison to the coherence of the x-rays. In this work, we have used the correlation function introduced by Gibaud et. al. [41]. This correlation function was used to explain the shape of rocking curves originating from a Nb layer deposited onto a Sapphire $(11\bar{2}0)$ substrate. The particular correlation function described in this work predicts a Lorentzian squared line shape for the transverse scan. The width of the peak in q_x is directly related to the inverse of the correlation length. A correlation length of approximately 76Å was found for the Nb layer under investigation. Similar work by Miceli et. al. showed that length scales of a similar order were found for thin films of ErAs and $In_{0.7}Ga_{0.3}P$ on GaAs.

Transverse diffuse scans through the zero and first order satellite high angle multilayer peaks were carried out at both station 2.3, Daresbury SRS and BM 16, ESRF. The transverse scans through the zero order diffraction peak from samples *A3* and *A1* are shown in figure 7.12 and 7.13 respectively.

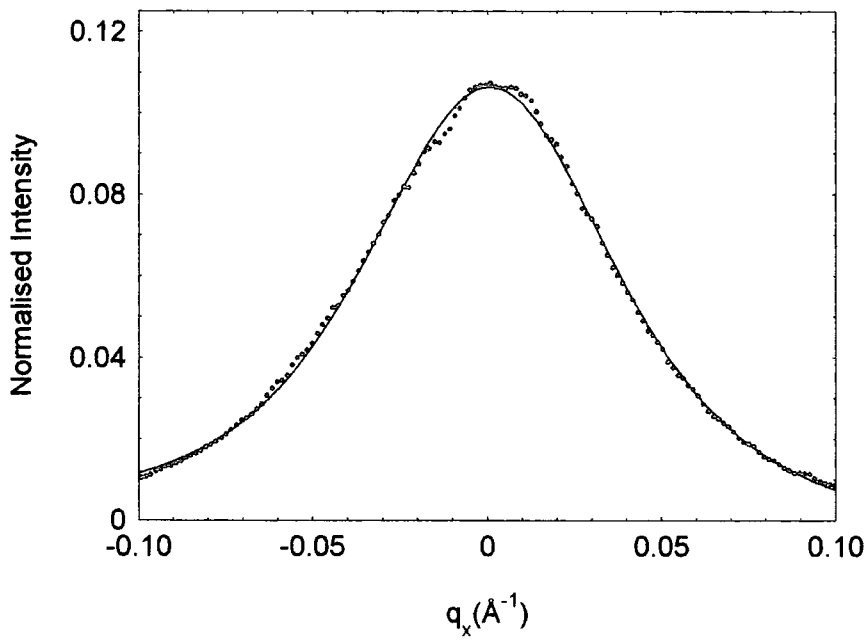

Figure 7.12: Transverse scan through the Cu/Co (111) peak for sample *A3*, taken at the ESRF using detector slits.
Experiment (points), fit to a Lorentzian squared line shape (line)

The rocking curves from all the samples could be fitted extremely well to the Lorentzian squared line shape introduced by Gibaud et. al. For the high temperature multilayers the rocking curves could be fitted to a single Lorentzian squared (as in figure 7.12) but, as the temperature of deposition decreased, a second peak was required to fit the line shape. This second peak, which could also be fitted to a Lorentzian squared line shape, was most pronounced in samples *A1* and *B1*. Figure 7.13 shows the rocking curve for sample *A1*, where a second, sharper peak is clearly visible.

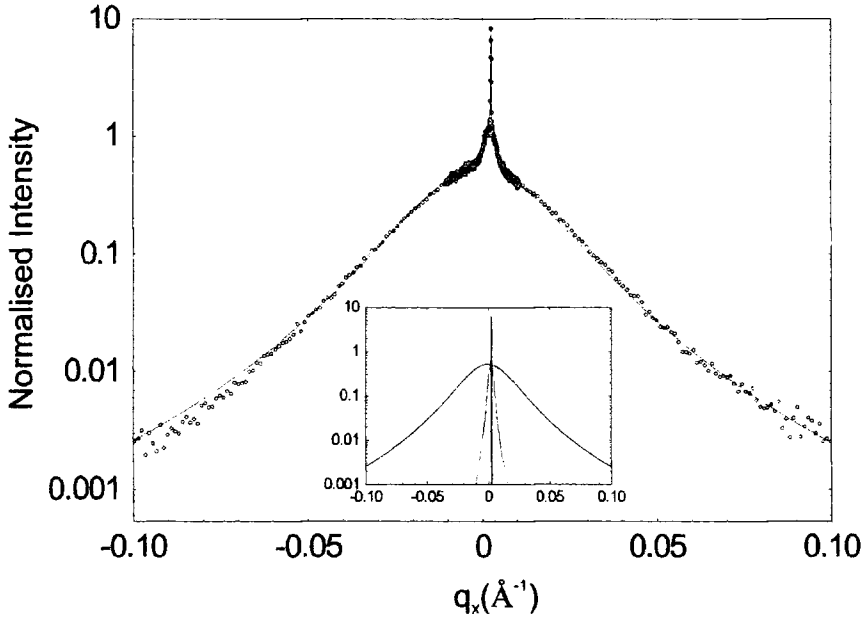

Figure 7.13: Transverse scan through the Cu/Co (111) peak for sample *A1*, taken on Station 2.3, Daresbury SRS using detector slits.
Experiment (points), fit to a convolution of Lorentzian squared line shapes (line)

Two component line shapes very similar to those shown in figure 7.13 have been observed for metal layers deposited on sapphire. Stierle et. al. evidence two component rocking curves for MBE grown Co films deposited on sapphire [42]. The widths and relative intensities of the two line shapes is very similar to that obtained above. A very similar result has also been observed in MBE deposited Cu/Co(111) multilayers deposited at 45°C by Bödeker et. al. [43].

Although this additional peak is required for an accurate fit, a comparison of the integrated intensities of the two peaks shown in figure 7.13 shows that the contribution from this second peak, corresponds to only 10% of the total integrated scatter for sample *A1*. For all samples, it is the broad line shape that dominates the rocking curve. Although the fit to the peaks is extremely good, a range of FWHM were found from each sample as the experiment was repeated at the different sources. The observed differences in the FWHM between experiments are related to the fact that the sample is not homogenous over its entire surface area and slightly different areas of the sample are probed whenever a new experiment is undertaken.

In some samples, a resolution limited spike was seen at $q_x \approx 0$. This sharp peak was only observed when narrow detector slits were used, and corresponds to a detector angle equal to that of the sapphire (113) reflection. Another possible explanation of this spike is that there are extremely long lateral correlations, of the order of 10,000Å present in these samples. However, correlations over this length scale seem unlikely. Additionally, if correlations of this length scale were present, a sharp spike should have been observed when a analyser crystal was used and this is conspicuously missing from all the experiments carried out with an analyser crystal. This feature probably arises only when slits are used, because of the very poor q_y resolution of the apparatus.

The correlation length in the model derived by Gibaud et. al. [41] is simply the inverse of the FWHM of the rocking curve in q_x. The correlation lengths calculated from the broad component of the rocking curves for all the samples are shown in figure 7.14. The error bars relate to the homogeneity of the samples and reflect the variation in observed FWHM, and are not related to the error on the fit itself which was always negligible. Series *A* and *B* follow the same linear dependence; as the GMR increases, so does the lateral correlation length.

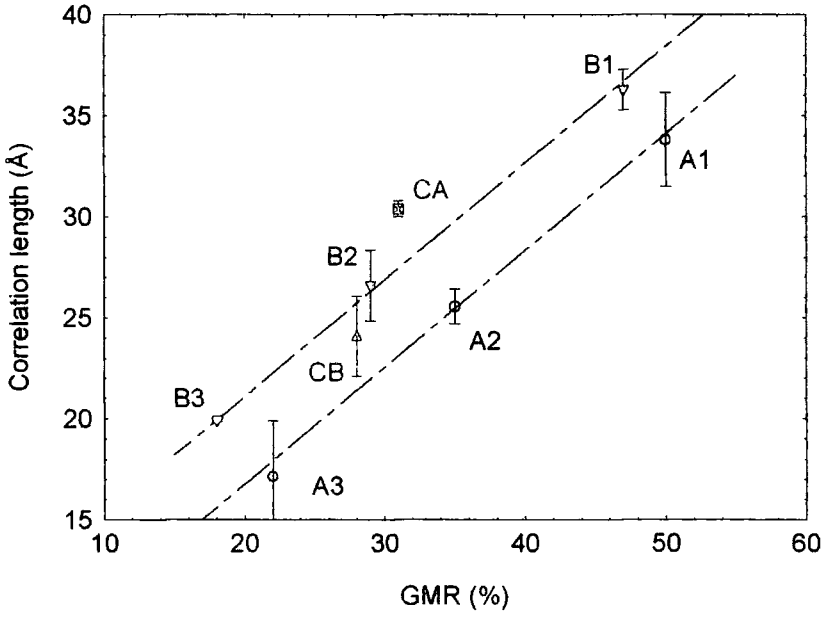

Figure 7.14: The correlation lengths calculated using the theory described in reference [41] as a function of GMR for series *A* and *B*

The correlation length relating to the second peak is much larger. For the samples where it is clearly defined, *A1* and *B1*, the calculated correlation lengths are 365 ± 20Å and 300 ± 30Å respectively. For the other samples, it was much more difficult to clearly define this second peak as it was convoluted with the broader one. For samples *A2*, *B2*, *CA* and *CB* this longer correlation length was found to be of the order of 110 ± 30Å. For these samples, the sharper peak was only responsible for 4% of the total integrated intensity in q_x, as opposed to 10% which was observed for samples *A1* and *B1*.

The short correlation length data shows that for a specific buffer layer temperatures, the correlation length follows a linear dependence on the multilayer deposition temperature. As this short correlation length scatter dominates the rocking curves, the multilayers can be considered to be primarily composed of structural domains with lateral correlations of the order of 20Å. The long correlation length also seems to follow the multilayer deposition temperature, but within statistical errors there is no dependence on the buffer layer temperature.

The results of the transverse scans show that a multilayer structure is very dependent on its growth temperature. Whether the observed structural changes are a direct result of the multilayer deposition, or the replication of sub-layer effects is unclear. The deposition of niobium onto sapphire has been shown to produce broad rocking curves, with correlation lengths of approximately 76Å [41,44]. These features could then be replicated through the copper buffer layer and be incorporated into the multilayer structure, although the dependence of the structure with multilayer deposition temperature then becomes unclear. The deposition of copper onto niobium has been studied by Batanouny et. al. who show that for layer thickness greater than 1.5 monolayers, the copper grows layer by layer [45].

The most likely place for the structural properties of the multilayer to be defined is at the buffer/multilayer interface. Whether the structure is determined by the cooling of the buffer layer or by the temperature of the cobalt deposition is unknown. The growth of cobalt onto single crystal copper has been investigated by

several authors using x-ray photoelectron scattering. In 1981 Gonzalez et. al. [46] demonstrated that the first monolayer of cobalt deposited onto copper forms two dimensional islands which subsequently coalesce. The cobalt layer then continued growth in a layer by layer manner. In a paper detailing the MBE growth of Fe and Co onto various copper crystals Kief and Egelhoff showed that due to the difference in the surface free energies of cobalt and copper, non-ideal film growth was the rule rather than exception [47]. Later studies [48,49,50,51,52] showed that cobalt does indeed form islands when deposited onto copper. These islands have been shown to extend to 5 monolayers in height, and STM images show their lateral size to be of the order of 100Å [53]. Li et. al. showed that by careful simulation of the reflectivity from Cu/Co multilayers that the surface between cobalt and copper was rougher than between copper and cobalt [54].

The results from the rocking curves do not match any of the lengths scales observed in the literature reviewed above. The fact that there are two length scales co-existing in some samples is unambiguous. It has not been possible to identify the origin of the two length scales, although several ideas have been presented based on growth arguments. The rocking curves which have been discussed above average over the same region of the sample as that in the grazing incidence scattering experiments, and so it is not surprising that the modelling of the diffuse scatter is so complicated.

7.7 Grazing Incidence Diffuse Scattering Revisited

Prior to the discussion of the HAXRD experiment it was suggested that the modelling of the diffuse scatter was extremely complicated. The quantitative analysis of the grazing incidence diffuse scatter was carried out by P.A. Ryan at the University of Leeds. Figure 7.15 shows the diffuse scans and fits at and away from the Bragg peak for samples *A1*, *A2* and *A3*. At the present time it has not been possible to fit the diffuse scatter from samples *CA*.

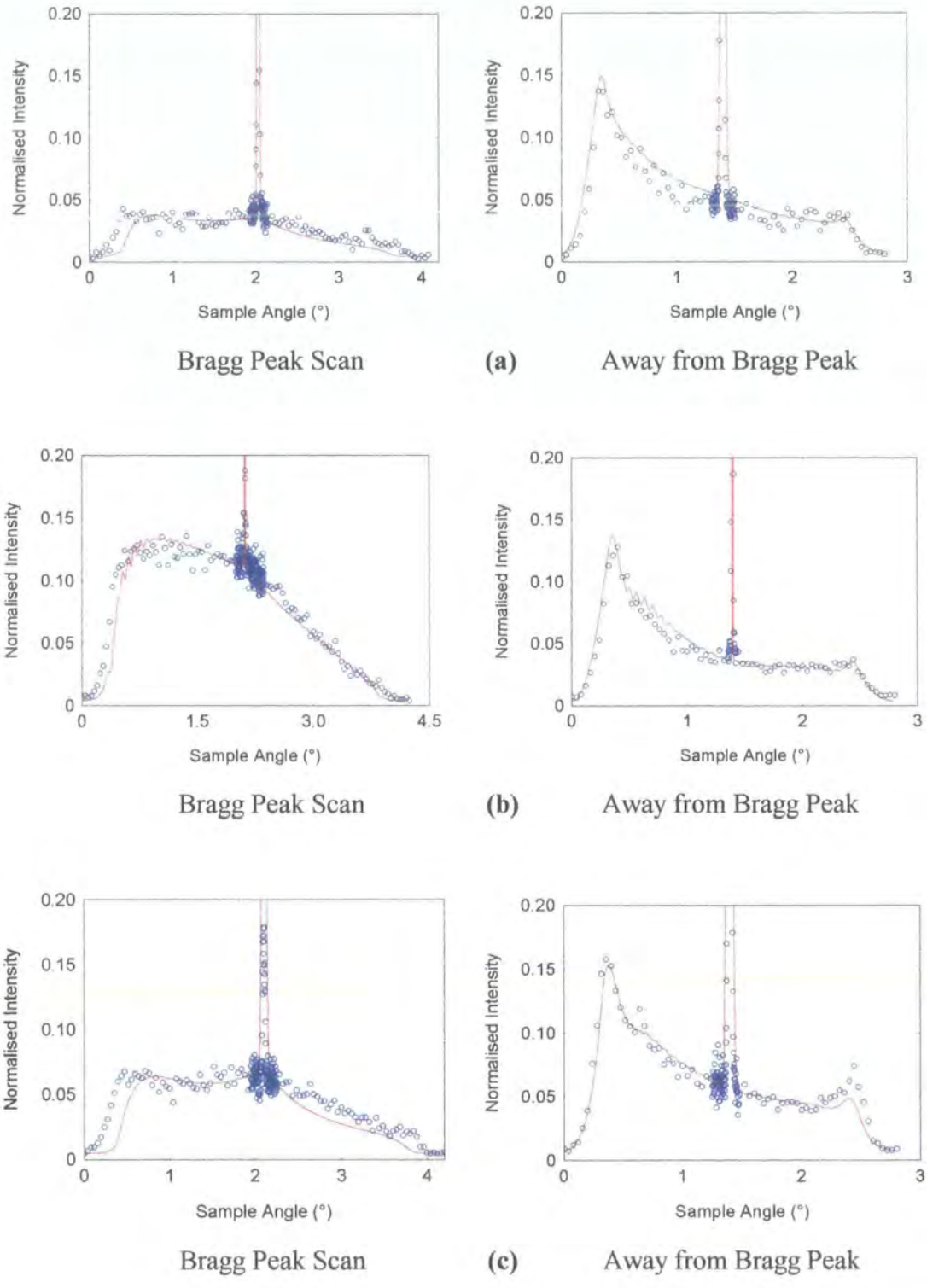

Figure 7.15: Transverse diffuse scans at and away from the Bragg peak for samples *A1(a)*, *A2(b)* and *A3(c)*

The parameters obtained from the fits outlined above are tabulated below in table 7.6:

	Copper ± 0.4 Å		Cobalt ± 0.4 Å		Average σ_c	Average σ_u		
	σ_c	σ_u	σ_c	σ_u			$\xi \pm 10$ /Å	h ± 0.05
1	3	2	4	5	3.5	3.7	370 & 45	0.25
2	5	1	6	3	5.5	2.2	40	0.35
3	4	4	9	5	7.0	4.5	42	0.25

Table 7.6: Main parameters obtained from the transverse diffuse simulations.

The fits to the diffuse scatter confirm the trend observed using the Born wave: the value of correlated roughness falls as the multilayer deposition temperature increases. The values of the fractal parameter are of the same order as that observed from other MBE deposited samples. Sample *A1* could only be fitted using two correlation lengths. The shorter of the two correlation lengths in all the samples is of the same order as that observed in the high angle scans.

Although the validity of the fractal model is questionable in these systems due to the presence of the two correlation lengths, it is interesting to note that the correlation lengths for the scans away from the Bragg peak are very similar to those obtained in the high angle scans. This is not surprising considering that the small correlation length dominates the scattering in both cases. The value of the lateral correlation length as deduced from the fits to the diffuse scatter is very similar to values recently obtained by other experimenters: Gu et. al. during an investigation of sputtered Cu/Co multilayers found a lateral correlation length of only 17Å [55]. A study by Smith et. al. of Cu/Co multilayers deposited on sapphire with a Pt buffer layer exhibited similar transverse widths to the high angle data, and also a lateral correlation length of 36Å [56].

7.8 Summary

The results analysed in this chapter arose from a comprehensive study of the x-ray scattering from Cu/Co multilayers deposited by MBE with differing substrate temperatures. Magneto-transport measurements show that the GMR of MBE deposited Cu/Co multilayers was dependent on the growth temperatures of both the multilayer and buffer layers. On the other hand, the saturation field was only dependent on the multilayer deposition temperature, and was not affected by the buffer layer deposition temperature.

The initial goal of this experiment was to separate the effects of crystalline order and interface roughness on the GMR. The results in this chapter show how difficult this is to achieve. The initial x-ray characterisations of the samples showed that the GMR was sensitive to the interface roughness. When the Born wave analysis was applied to the diffuse data it was shown that the smoothening of the interfaces was a direct result of the reduction in the correlated component of the interface roughness.

When the diffuse scatter was simulated, it was observed that it was not possible to simulate the data to a single set of parameters. The results obtained from a diffraction experiment were then presented. These results show that changing the deposition temperatures of the multilayer and buffer layer results in changes in the crystalline order. Initially these changes were attributed to a reduction in the mosaic spread of the crystallites. The application of a model which describes the crystalline disorder in terms of lateral correlations was then introduced. This model revealed that the multilayer was composed of domains with an average lateral size of approximately 30Å. For the high GMR samples, an additional length scale 10 times this was also observed. Thus far it has not been possible to identify the origin of this second length scale. Both of these length scales were subsequently observed in the diffuse scatter obtained at grazing incidence.

The results contained in this chapter relate to samples which show roughness confined to extremely short correlation length fractal surfaces. High angle diffraction studies suggest that these fractal areas are defined by crystallites of an extremely small dimension. When this is the case, it is conceptually difficult to separate interface roughness from crystalline disorder. In a recent study of sputtered Cu/Co systems, where the correlation length was significantly larger, the GMR was observed to depend on the amount of <111> texture in the samples [57].

The samples contained in this chapter have shown GMR's which range from 50% to 18%. The changes in the GMR are reflected in structural differences between the samples. Further experiments are required to separate the effects of the deposition of the buffer layer and the growth temperature of the multilayer itself. Varying the growth temperature of the layers has been observed to cause changes in the lateral domain size of the crystallites and lateral correlation length. In the case of the sample exhibiting high GMR, there is an additional length scale present in the sample. As yet, the presence and affect of this second length scale has not been explained satisfactorily.

References from Chapter 7

1 P. Bruno, C. Chappert, *Phys. Rev. Lett.*, **67**, *1602*, (1992)

2 A. Schreyer, K. Bröhl, J.F. Ankner, C.F. Majkzrak, Th. Zeidler, P. Bödeker, N. Metoki, H. Zabel, *Phys. Rev. B.*, **47** (22), *15334-15337*, (1993) [*and references therein]*

3 J. Xu, B.J. Hickey, M.A. Howson, D. Greig, M.J. Walker, N. Wiser, *J. Magn. Mag. Mat.*, **156** (1-3), *69-70*, (1996)

4 M.J. Hall, *Ph. D. Thesis,* University of Leeds (1993) and M.J. Flynn, *Ph. D. Thesis,* University of Leeds (1996)

5 K. Bröhl, P. Bödeker, N. Metoki, A. Stierle, H. Zabel, *J. Cryst. Growth*, **127**, *682-685*, (1993)

6 C.H. Marrows, Ph. D. Thesis, University of Leeds, (1997)

7 G.R. Harp, S.S.P. Parkin, R.F.C. Farrow, R.F. Marks, M.F. Toney, Q.H. Lam, T.A. Rabedeau, R.J. Savoy, *Phys. Rev. B.*, **47** (14), *8721-8733* (1993)

8 H. Laidler, I. Pape, C.I. Gregory, B.J. Hickey, B.K. Tanner, *J. Magn. Mag. Mat.*, **154** (2), *165-174,* (1996)

9 R. Clarke, D. Barlett, F. Tsui, B. Chen and C. Uher, *J. Appl. Phys.*, **75**, 6174 (1994).

10 H. Ueda, O. Litakami, Y. Shimada, Y. Goto, M. Yamamoto, *Jpn. J. Appl. Phys.*, **33**, *6173-1678* (1994)

11 J. Ben Youssef, K. Bouzaine, O. Koshkina, H. Le Gall, M. El. Harfouai, M. El. Yamani, J.M. Desvignes, A. Fert, *J. Magn. Mag. Mat.*, **165**, *288-291*, (1997)

12 T. Kingetsu, F. Yoshizaki, *Jpn. J. Appl. Phys.*, **33**, *6168-6172*, (1994)

13 E.E. Fullerton, D.M. Kelly, J. Guimpel, I.K. Schuller, *Phys. Rev. Lett.* **68**, *1996,* (1993)

14 K. Bouziane, J. Ben Youssef, M. El Harfaoui, O. Koshkina, H. Le Gall, J.M. Desvignes, M. El Yamani, A. Fert, *J. Magn. Mag. Mat.*, **165**, *284-287*, (1997)

15 K.P. Wellock, B.J. Hickey, D. Grieg, M.J. Walker, J. Xu, N. Wiser, *J. Appl. Phys.*, **75** (10) Pt 2B, *7055-7057*, (1994)

16 J. Barnas, Y. Bruynseraede, *Europhys. Lett.* **32**, *176*, (1995)

17 J. Barnas, Y. Bruynseraede, *Phys. Rev. B.*, **53**, *5449* (1996)

18 J. Barnas, G. Palsantzas, *J. Appl. Phys.*, **82** (8), *3950-3956*, (1997)

19 M. Safa, B.K. Tanner, *J. Magn. Mag. Mat.* **150**, *L290-L292* (1995)

20 P.A. Ryan, Ph. D. Thesis, University of Leeds, (1998)

21 Courtesy P.A. Ryan, University of Leeds

22 D.E. Savage, J. Kleiner, N. Schimke, Y.-H. Phang, T. Jankowski, J. Jacobs, R. Kariotis, M.G. Lagally, *J. Appl. Phys.*, **69** (3), *1411-1424*, (1991)

23 H. Laidler, *Ph. D. Thesis*, University of Leeds, (1997)

24 D. Dekadjevi, *Private communication,* University of Leeds

25 E.E. Fullerton, I.K. Schuller, H. Vanderstraeten, Y. Bruynseraede, *Phys. Rev. B.*, **45** (16), *9292-9310*, (1992)

26 I.K. Schuller, *Phys. Rev. Lett.*, **44** (24), *1597-1600,* (1980)

27 H. Laidler, *Ph. D. Thesis,* University of Leeds, (1997)

28 Courtesy of D. Dekadjevi, University of Leeds

29 P. Weinberger, V. Drchal, L. Szunyogh, J. Fritscher, B.I. Bennet, *Phys. Rev. B.*, **49**, *13366* (1994)

30 Lattice Spacings and Structures of Metals and Alloys, *W.B. Pearson,* **Pergamon**, (1958)

31 A.N. Fitch, *Materials Science Forum*, **228** (1&2) *219-221*, (1996)

32 C.D. Moore, I. Pape, B.K. Tanner, *Nuovo Cimento della Societa Italiana di Fisica D*, **19** (2-4), *205-212*, (1997)

33 Neutron and Synchrotron Radiation for Condensed Matter Studies Vol 1., *Eds. J. Baruchel, J.L. Hodeau, M.S. Lehmann, J.R. Regnard, C. Schlenker,* **Spring-Verlag**, (1993)

34 High Resolution X-ray Diffractometry and Topography, *D.K. Bowen and B.K. Tanner,* **Taylor and Francis**, (1998)

35 P.F. Fewster in, X-ray and Neutron Dynamical Diffraction: Theory and Applications NATO: Advanced Study Institute, *Eds. A. Authier, S. Lagomarsino, B.K. Tanner,* **Plenum Press**, (1996)

36 P.F. Miceli, C.J. Palmstrøm, *Phys. Rev. B.*, **51** (8), *5506-5509*, (1995)

37 V. Holý, J. Kubena, E. Abramof, A. Pesek, E. Koppensteiner, *J. Phys. D: Appl. Phys.*, **26**, *A146-A150*, (1993)

38 B.D. Fulthorpe, P. Ryan, T.P.A. Hase, B.J. Hickey , B.K. Tanner, *in prep.*

39 T.P.A. Hase, I. Pape, B.K. Tanner, H. Laidler, P. Ryan, B.J. Hickey, *J. Magn. Mag. Mat.*, **177-181**, *1164-1165*, (1998)

40 S. Di Nunzio, K. Theis-Bröhl, H. Zabel, *Thin Solid Films,* **279**, *180-188*, (1996)

41 A. Gibaud, R.A. Cowley, D.F. McMorrow, R.C.C. Ward, M.R. Wells, *Phys. Rev. B*, **48** (19),*14463-14471,* (1993)

42 A. Stierle, A. Abromeit, N. Metoki, H. Zabel, *J. Appl. Phys.*, **73** (10), *4808-4813*, (1993)

43 P. Bödeker, A. Abromeit, K. Bröhl, P. Sonntag, N. Metoki, H. Zabel, *Phys. Rev. B.*, **47** (4), *2353-2361*, (1993)

44 P.M. Reimer, H. Zabel, C.P. Flynn, J.A. Dura, *Phys. Rev. B*, **45** (19), *11426-11429,* (1992)

45 M. El.-Batanouny, M. Strongin, *Phys. Rev. B.*, **31** (8), *4798-4801*, (1985)

46 L. Gonzalez, R. Miranda, M. Salmerón, J.A. Vergés, F. Ynduráin, *Phys. Rev. B.*, **24** (6), *3245-3254*, (1981)

47 M.T. Kief, W.F. Egelhoff Jr., *Phys. Rev. B.*, **47** (16), *10785-10814,* (1993)

48 Th. Fauster, G. Rangelov, J. Stober, B. Eisenhut, *Phys. Rev. B.*, **48** (15), *11361-11366*, (1993)

49 M. Hochstrasser, M. Zurkirch, E. Wetli, D. Pescia, M. Erbudak, *Phys. Rev. B.*, **50** (23), *17705-17708*, (1994)

50 V. Scheuch, K. Potthast, B. Voigtländer, H.P. Bonzel, *Surface Science,* **318**, *115-128*, (1994)

51 K.Y. Kok, J.A. Leake, *Thin Solid Films,* **275**, *210-212*, (1996)

52 E. Jedryka, M. Wójcik, S. Nadolski, D.J. Kubinski, H. Holloway, *J. Magn. Mag. Mat.*, **165**, *292-296*, (1997)

53 J. de la Figuera, J.E. Prieto, C. Ocal, R. Miranda, *Phys. Rev. B.*, **47** (19), *13043-13046,* (1993)

54 B. Li, H. Shen, Y. Saitoh, T. Fujimoto, I. Kojima, *Thin Solid Films,* **315**, *104-110*, (1998)

55 T. Gu, A.I. Goldman, M. Mao, *Phys. Rev. B.*, **56** (11), *6474-6477*, (1997)

56 D.J. Smith, A.R. Modak, T.A. Rabedeau, S.S.P. Parkin, *Appl. Phys. Lett.*, **71** (11), *1480-1482*, (1997)

57 D.E. Joyce, C.A. Faunce, P.J. Grundy, B.D. Fulthorpe, T.P.A. Hase, I. Pape, B.K. Tanner, *Phys. Rev. B.*, **58** (9), *5594-5601*, (1998)

Chapter 8

X-ray Scattering from Gas Contaminated Cu/Co Multilayers

Chapter 8 deals exclusively with a series of Cu/Co multilayer samples deposited on silicon (100) substrates at the University of Leeds using sputtering techniques [1]. The work in this chapter has been undertaken in close collaboration with Dr. C.H. Marrows of the University of Leeds. The magnetometry results and conclusions about coupling deduced from them which are contained in the first two sections of this chapter (sections 8.1 and 8.2) and the initial part of section 8.3 are due to him.

This chapter falls into five main sections: In the first, the evidence that residual gas in the growth chamber can affect the magneto-transport properties, notably the magneto-resistance, is presented (section 8.1). The effects of residual gas on the coupling of the magnetic layers within the multilayer are investigated by placing contamination at selected points in a Cu/Co multilayer (section 8.2). Large changes are observed when the residual gas is placed in the middle of the copper spacer layer. In the third section, an x-ray characterisation of these samples is presented. These results include grazing incidence studies of the samples, as well as a detailed high angle diffraction experiment (section 8.3). The fourth section, section 8.4, presents the first experiments undertaken by UK researchers using soft x-rays on these types of samples. A specific advantage of using these soft x-rays in the vicinity of the L_3 edges is that x-ray scattering becomes sensitive to the magnetic moment in the samples. The results of these experiments are presented after a brief introduction to magnetic x-ray scattering (section 8.4.1). The diffusely scattered soft radiation is investigated in section 8.5, and the chapter is concluded with a summary, section 8.6.

8.1 The Effect of Residual gas on the Magneto-transport Properties of Cu/Co Multilayers

The effects of residual gas in Cu/Co multilayer structures was evidenced by the initial use of a Meissner trap on the sputtering machine. This trap consisted of a coil constructed of 0.25" copper pipe, through which liquid nitrogen was forced. A continuous flow of the liquid nitrogen is required during the deposition to reduce the residual gases remaining in the chamber. The largest single contaminant was found to be water vapour [2]. For multilayers deposited above a base pressure of $2*10^{-7}$ Torr the values of GMR were found to be extremely low. The use of a Meissner trap allows a final base pressure in the system of $2*10^{-8}$ Torr to be realised [3]. The importance of the Meissner trap is illustrated in figure 8.1 where the GMR and MOKE plots are compared between two samples deposited with (blue) and without (red) the Meissner trap operating. The samples were nominally identical and consisted of a 25 repeat bi-layer of Co(10Å)/Cu(10Å) deposited directly onto the silicon substrate.

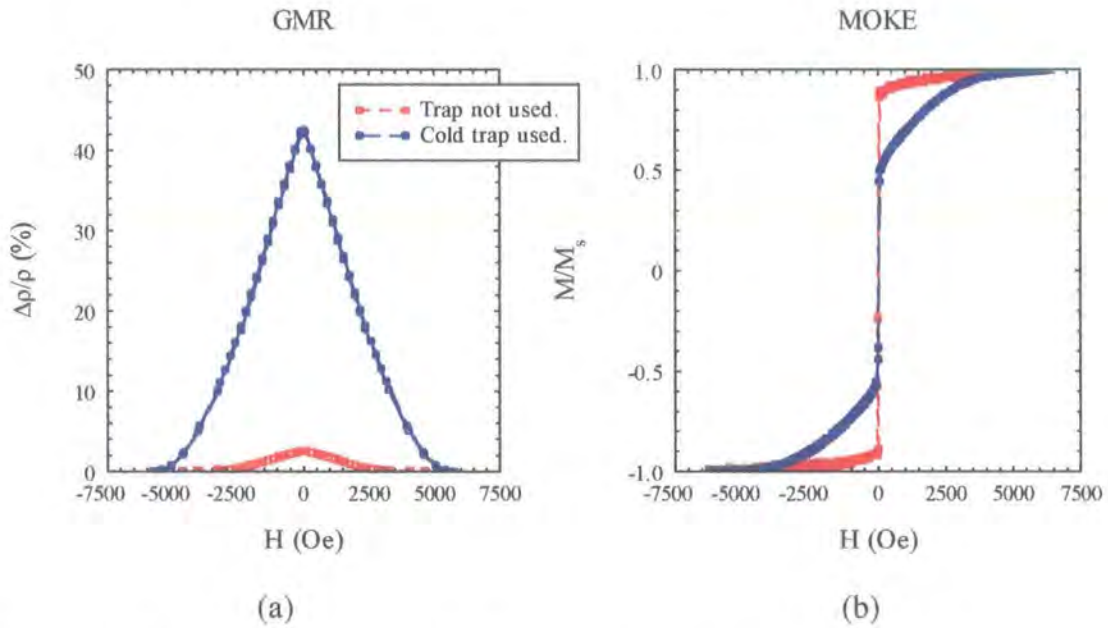

Figure 8.1: The room temperature GMR (a) and MOKE (b) curves for two nominally identical samples deposited under a good (blue) and poor vacuum (red) [4].

It can clearly be seen from figure 8.1 that deposition under non ideal conditions results in a multilayer which exhibits a strong ferromagnetic coupling behaviour (typified by the square magnetisation loop), and a low GMR (4% at room temperature). When liquid nitrogen was flowing through the Meissner trap, however, the sample shows a marked increase in anti-ferromagnetic interlayer coupling behaviour. The change in the relative remanence fraction between the samples is matched by a change in the GMR, rising to 40% when the vacuum is good. A similar result was obtained by Kagawa et. al. [5] who observed that the GMR changed from 60% to 4% when the base pressure of the sputtering machine was reduced from $4*10^{-6}$ Torr to $7*10^{-6}$ Torr. The changes in the magneto-resistance noted by Kagawa were accompanied by a squaring of the magnetisation loop for the low GMR sample, as was also observed in the samples studied above. Although the base pressure presented in the Kagawa experiment are higher that those in the experiment carried out be Marrows, the effects of oxygen contamination in the multilayer are clearly evidenced. Similar, but smaller effects were observed by Yoshizaki and Kingetsu [6]. In this reference, the magneto-transport properties of a series of Cu/Co multilayers deposited in base pressures of $2*10^{-8}$ and $2*10^{-4}$ Torr were compared. The changes in the GMR were most evident around the second AF coupling peak. It is not only oxygen and water that can effect the magneto-transport properties. Much smaller changes in the GMR were observed by Zhao et. al. [7] when metals such as Fe and Ni were placed in the copper spacer layer. Here the changes were typically a couple of percent on the addition of 4 at. % of contaminant in the copper spacer layer.

In an attempt to investigate what effect the residual gas might have on the structure of the multilayers, the samples were investigated using ^{59}Co NMR at 1.5K [8]. Although the NMR results showed that intermixing at the interfaces, resulting in magnetically dead CuCo alloys being formed in the interface regions had occurred, there were no major differences between the two samples. These results suggest that both samples have similar short range order.

With the failure of the NMR technique to yield structural differences between the samples, it was hoped that structural differences between the samples could be elucidated by the use of grazing incidence x-ray scattering techniques. The structural characterisation of the multilayers was undertaken on Station 2.3, at the SRS.

Figure 8.2 shows the differences in the specular scans between the two samples at λ=1.38 (the copper *K* absorption edge). In the low angle regime, both samples exhibit similar behaviour. Yoshizaki et. al. [6] also failed to notice any structural changes in their samples when they were characterised by cross-section TEM. The Bragg peaks in figure 8.2 are at a slightly different position due to fluctuations in the bi-layer repeat. The overall rate of fall off and the intensity of the Bragg peak are very similar for both samples. This means that although the samples were grown under different conditions, the roughness of the interfaces in the two samples are very similar. The only major difference is a high order fringe appearing in the sample deposited with the trap operating. This beat is from a layer of approximately 100Å, and given that there are no buffer or capping layers, is somewhat surprising.

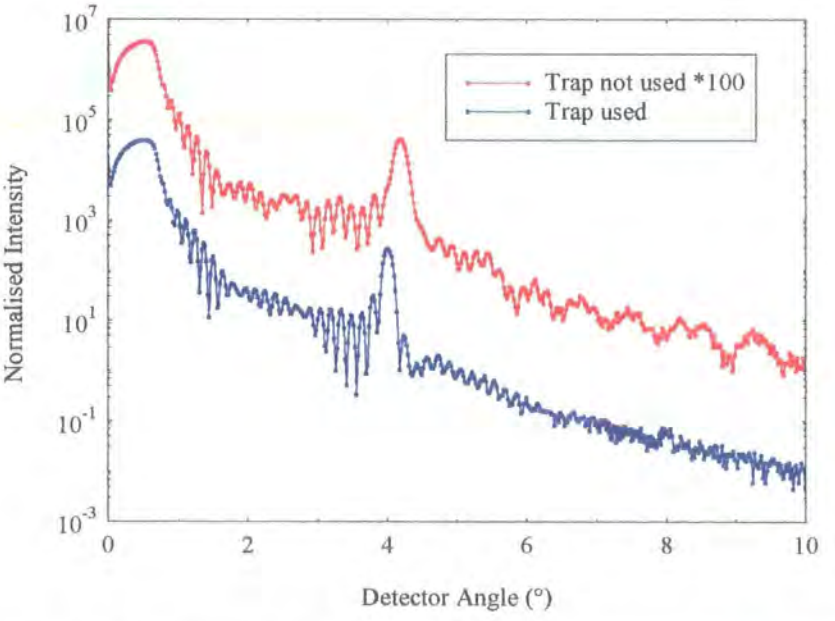

Figure 8.2: The specular reflectivity curves for two nominally identical samples deposited under a good vacuum (blue) and a poor vacuum (red).

The diffuse intensity was very low in these samples, and analysis of the off-specular scans shows that the majority of the roughness is correlated. Transverse scans were taken through the Bragg peak, and Born analysis was then carried out in order to quantify the amount of correlated roughness present. Transverse scans, recorded at and away from the copper absorption edge, through the Bragg peak of the sample, prepared in a poor vacuum are shown in figure 8.3.

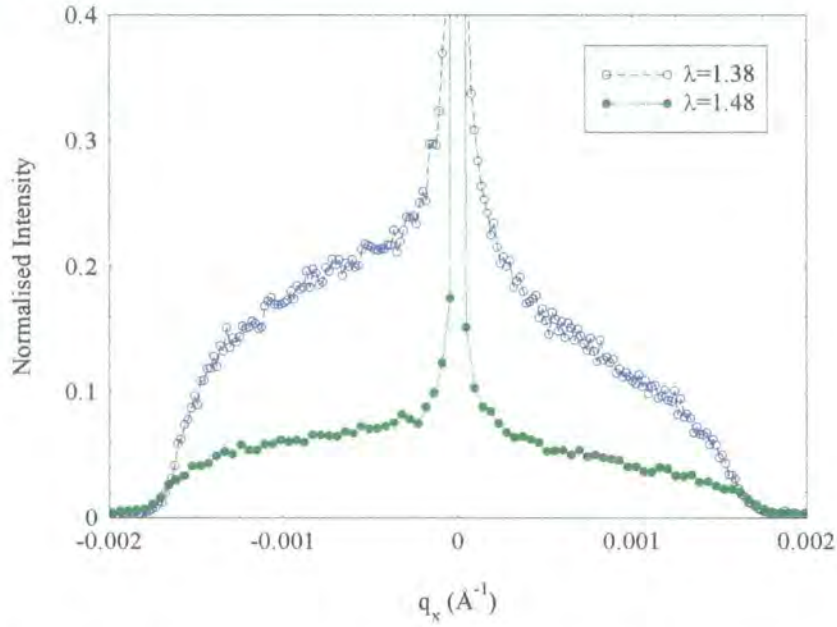

Figure 8.3 : Transverse diffuse scan taken through the Bragg Peak for the sample grown in a poor vacuum

A clear difference in intensity of the diffuse intensity at the Bragg peak is observed when the incident wavelength is tuned to the copper absorption edge. No such change is observed for scans through the Kiessig maxima. These changes in intensity with incident energy are consistent with a large amount of correlated roughness being present. The Born analysis revealed that the correlated roughness was 1.0 ± 0.5 Å. Similar results were obtained for the sample grown in a good vacuum, where the correlated roughness was also measured to be 1.0 ± 0.5 Å. These results confirm the very smooth nature of these samples, and the minute structural differences between them.

From the above discussion it is clear that although the two samples have very different magneto-transport properties, their structures are very similar. The roughness in both samples is extremely low, and what little roughness is present is highly correlated. Born analysis on the diffuse scatter at the Bragg peak for both samples yields the same value of correlated roughness. These results, along with the NMR results, suggest that the changes in the GMR are not being driven by changes at the interfacial regions in the samples. Figure 8.1 shows that the coupling is very different between the two samples, and the GMR is being influenced by this. In the next section, the coupling within gas contaminated Cu/Co multilayers will be investigated in more detail.

8.2 Studying the Effects of Contamination within the Multilayer

In the previous section, the use of the Meissner Trap was seen to be of vital importance in producing good GMR in Cu/Co multilayers. The structural effects of the contamination gas could not be observed by any of the characterisation techniques employed. In order to probe the multilayer structure selectively a series of Si(100)/{Co(10Å)/Cu(10Å)}*25 samples were prepared. The copper thickness was nominally at the peak of the first AF coupling peak. During the sample preparation, the deposition was halted for 10secs at selected points in the multilayer to allow contamination to occur. Three series of samples were grown, with the contamination occurring in the cobalt layer, in the copper layer and at the interfaces. A clean sample was also prepared and acted as a control sample. The 10sec delay time results in a contamination of approximately 0.1 monolayers of either O_2 or H_2O [9]

These samples were also investigated on Station 2.3 at the SRS. Again very little difference was observed between the samples. Figure 8.4 shows the specular scatter obtained from a clean sample, a sample where the contamination was confined to the copper spacer layer, and a sample where the contamination was at the interfaces. The best fit to the clean sample is also shown.

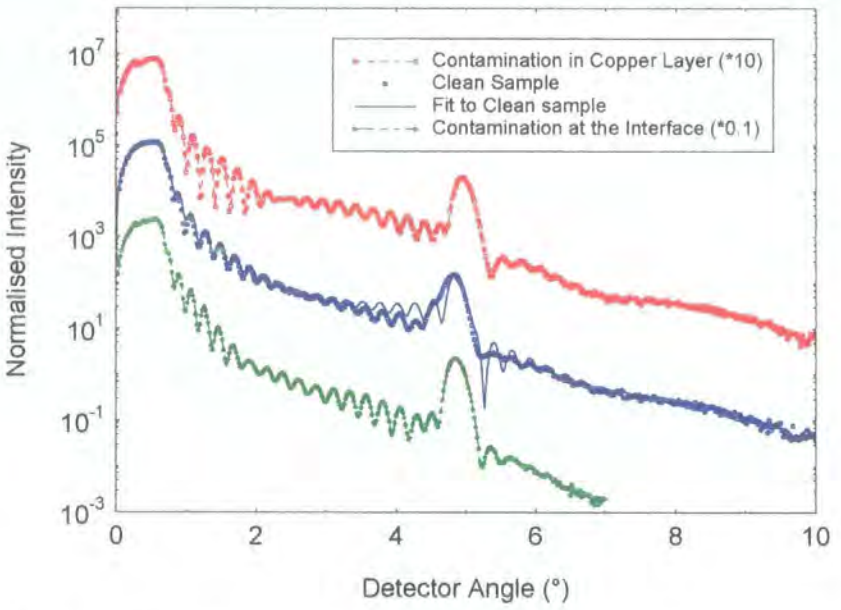

Figure 8.4: Specular reflectivity scans taken at the Copper absorption edge for samples with contamination at different points in the multilayer

The diffuse scatter from these samples was also investigated, and was found to be very similar to that originating from the initial samples (figure 8.3). The Born wave analysis again confirmed the smooth nature of the layers and suggested that the correlated component was 1.3 ± 0.5Å. The roughness as deduced from the best fits to the specular scatter indicate that the roughness of the multilayer interfaces was of the order of 4 ± 0.5Å. This value of roughness was consistent across the series of samples.

8.2.1 Magnetometry Results

The room temperature GMR (figure 8.5) was reduced on the inclusion of contamination into the multilayer structure. A slight reduction in the GMR was found for gas contamination confined to the interface region. The greatest GMR change, however, occurred when the contamination was allowed to occur in the middle of the spacer layer. When this was the case, the GMR fell from 47% to 25%. The inclusion of any contaminant caused a change in the shape and magnitude of the GMR curve.

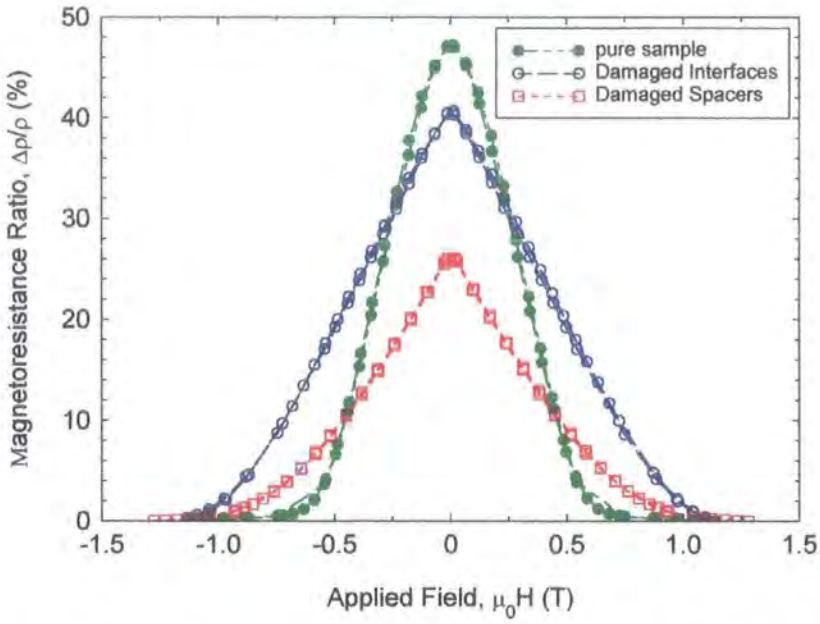

Figure 8.5: The room temperature GMR loops for Cu/Co multilayers with damaged introduced at the interface (blue) and spacer layer (red), compared to a pure sample (green)

A systematic change in the magnetisation loops investigated by MOKE was also observed. When contamination was introduced, the amount of AF coupling reduced, and the magnetisation loops exhibited a more ferromagnetic behaviour. These results are consistent with those presented in figure 8.1.

It is possible to determine the preferred magnetic state of a system by minimising its free energy. A phenomenological model can be used, whereby the sample is considered to be domain free and that magnetisation reversal is only performed by a coherent rotation of the magnetic moments [10,11]. Such a model approximates the free energy in the following form;

$$\varepsilon = -\mu_o t \sum_{i=1,2} \mathbf{m}_i \cdot \mathbf{H} - J_1\left(\hat{\mathbf{m}}_1 \cdot \hat{\mathbf{m}}_2\right) - J_2\left(\hat{\mathbf{m}}_1 \cdot \hat{\mathbf{m}}_2\right)^2 \qquad [8.1]$$

where t is the thickness of the layer, $\boldsymbol{m}$ is its saturation magnetisation, and $\boldsymbol{H}$ is the applied field. In this phenomenological model, the energy density is given by the Zeeman term plus a bi-linear term (defined by the coupling constant J_1) and a bi-

quadratic term with its associated coupling constant, J_2. In the normal convention, anti-parallel alignment of the spins results in a negative sign for the bi-linear coupling constant, and this is the convention used.

$J_1>0, J_2=0$ $J_1<0, J_2=0$ $J_1=0, J_2<0$

Figure 8.6: Magnetic coupling in Cu/Co multilayers

Figure 8.6 is a schematic representation of the possible spin alignment within a multilayer. The magnetic layers are bi-linearly coupled when $J_2=0$. When this is the case, the multilayer is either coupled Ferromagnetically (a), or Antiferromagnetically (b) depending on the sign of J_1. In a purely bi-quadratically coupled sample ($J_1=0$) the spins are still in the same plane as in the bi-linear case, but have rotated. For bi-linear coupling, the angle between spins in adjacent magnetic layers is either 0° (F) or 180° (AF). When the multilayer is bi-quadratically coupled, this angle is 90°.

For a sample which is totally bi-linearly coupled, the remanence of the magnetisation will be zero if $J_1<0$, or unity if $J_1>0$. As the remanence increases, the coupling becomes more bi-quadratic in nature and J_2 increases. A perfectly bi-quadratically coupled sample will have a remanent fraction of $\sqrt{2}/2$, and the GMR would be exactly half the value of a totally AF coupled sample [12].

Bi-quadratic coupling has been observed in Fe/Cr trilayers by the careful study of domain images [13]. The coupling was found to be bi-quadratic over a small range of chromium thickness. Like the Cu/Co system, the coupling is seen to oscillate from ferromagnetic to anti-ferromagnetic in this system. The bi-quadratic

coupling occurred for a thickness range between the ferromagnetic and anti-ferromagnetic coupling peaks. Bi-quadratic coupling has also been observed in Fe/Co trilayers [14] and in NiFe/Ag multilayers [11]

For thin film samples, where the magnetisation is forced into the plane due to the shape anisotropy, the only free parameter in equation 8.1 is the angle between the applied field and the magnetisation of the layer, θ_i. The magneto-resistance and MOKE expressions thus become:

$$\frac{M}{M_s} \propto \sum_{i=1,2} \cos\theta_i \quad \text{and} \quad \frac{\Delta\rho}{\rho} \propto -\cos(\theta_1 - \theta_2) \qquad [8.2]$$

Figure 8.7 shows Marrows' results of simultaneously minimising the MOKE and GMR loops obtained from the above samples. The deviations of the fits at high fields result in the model not including ordinary magneto-resistance.

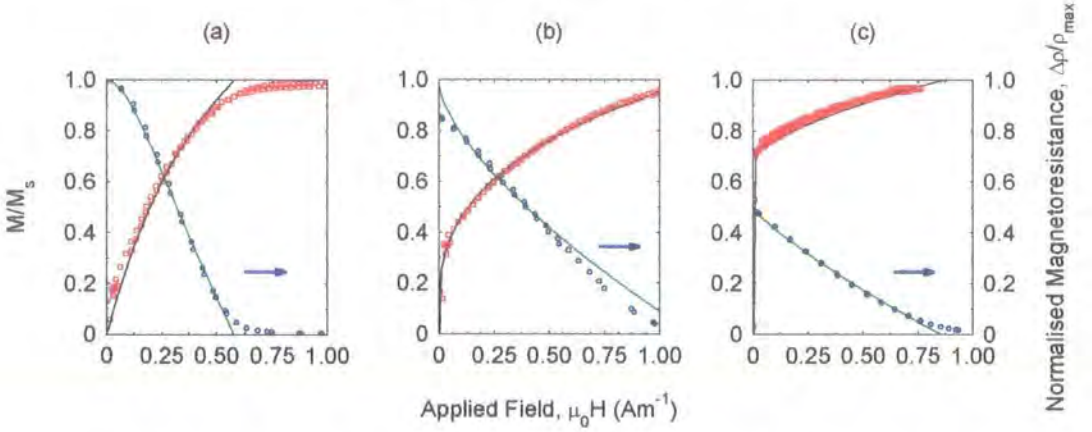

Figure 8.7: The MOKE (red) and GMR (blue) curves (points) and fits (line) for the clean sample (a), the interface damaged sample (b) and the copper spacer layer damaged sample (b) [8,15]

The results of these fits confirm that the clean sample is indeed predominantly AF coupled (J_1=-0.14mJm^{-2} and J_2=-0.02mJm^{-2}). For the interface damaged sample, the AF coupling is less perfect and $J_1 \approx 2J_2$. The largest differences are observed for the spacer layer damage. In this case, J_1=+0.01 mJm^{-2} and J_2=-0.15mJm^{-2} and the sample is clearly predominantly bi-quadratically coupled.

It is clear that the major effect on the coupling and hence on the GMR is due to the contamination within the copper spacer layer. It was decided to investigate this effect more fully by growing an additional series of samples. These samples were all prepared in a single batch and contained 50 repeats of Si(001)/Co(10Å)Cu(XÅ). The range of thickness for the copper layer was from 7 to 11Å in steps of 0.5Å. In one set of samples, the contamination was for 1 second and in another set of samples, the delay time was increased to 10 secs. The 10sec contaminated sample is equivalent to those studied above. The x-ray characterisation work in the following sections have been undertaken on these samples.

8.3 Gas Contamination in the Copper Layer

The samples which have been investigated have been labelled such that sample 1 corresponds to zero contamination, sample 2 has 1sec contamination and sample 3 has 10 secs. contamination in the spacer layer. Most of the data has been collected on the samples with the copper thickness corresponding to 9.5Å, which is close to the maximum of the first AF coupling peak.

The magnetic data for these samples was generally consistent with the earlier study by Marrows although a larger remanence in the magnetisation was found for the clean sample. It was still found that after 10secs of contamination the magneto-resistance was considerably reduced. The GMR of this series of samples was higher than that of the samples previously studied due to the larger number of bi-layers. Both the GMR and magnetisation loops for the clean sample and the sample with 1 sec contamination were very similar: Both showed a high degree of AF alignment (Figure 8.8 (b)) and a high GMR ~60% (figure 8.8(a)). For sample 3 (10 secs. contamination) a sharp drop in the GMR to ~30% and a corresponding squaring of the magnetisation loop were observed.

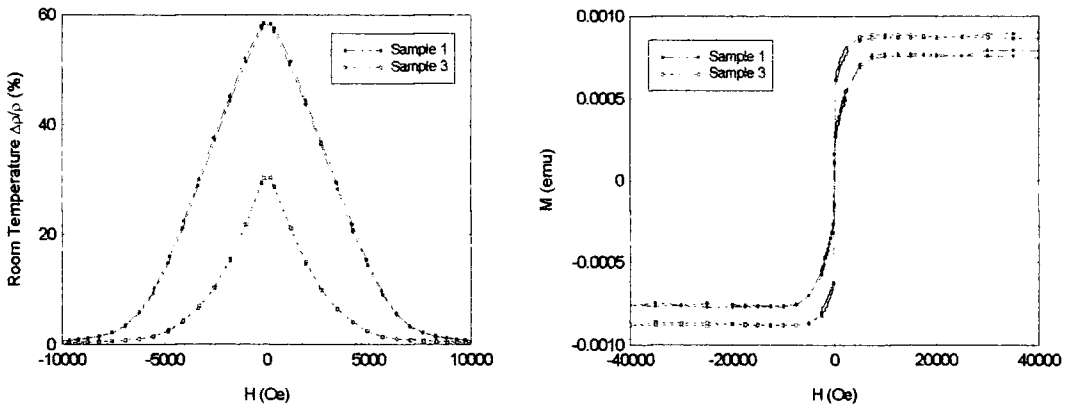

Figure 8.8: The GMR (a) and magnetisation loop for Samples 1 and 3 with the copper thickness, X=9Å [16]

These magnetisation and GMR loops were fitted to the same model that is described by equation 8.1 [8]. The results of the fit to these new samples show that the nominally clean sample along with sample *2* have a small bi-quadratic term. The fitted values for sample *2* give J_1=-0.16 ± 0.2 mJm^{-2} and J_2=-0.06mJm^{-2}. As $J_1 > 2J_2$, it can be concluded that this sample is still predominantly AF coupled. Sample *3* again shows strong bi-quadratic behaviour with J_1=+0.01 mJm^{-2} and J_2=-0.08 mJm^{-2}.

These samples were subsequently investigated on station 2.3 at the SRS. In the next section the results from a grazing incidence study are presented. The x-ray characterisation is continued in section 8.2.2 where the results from a HAXRD experiment are presented.

8.3.1 X-ray Characterisation of the Samples

Grazing incidence studies on the three samples once again shows that there is very little structural difference between the samples. Figure 8.9 shows the specular scans for all the samples away from any absorption edge, λ=1.48Å:

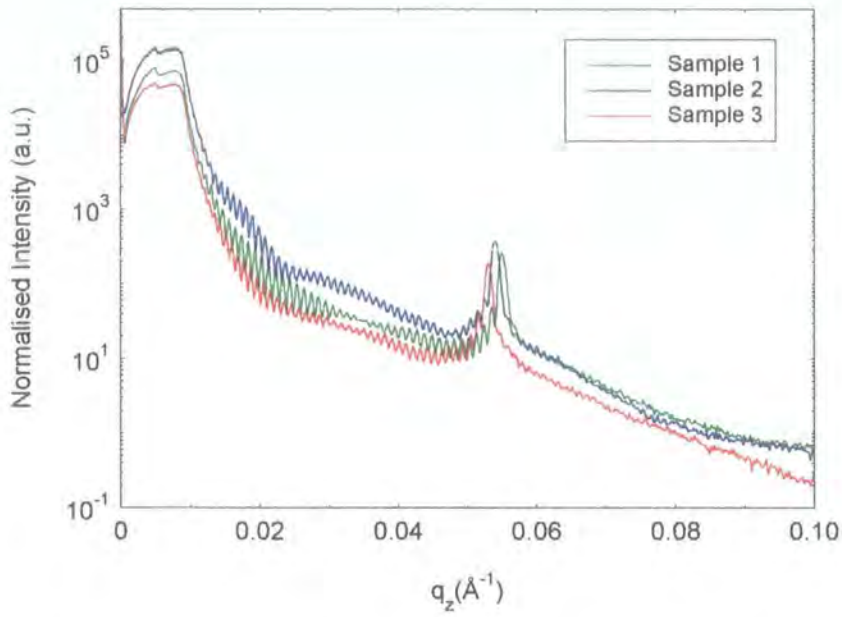

Figure 8.9: Specular $\theta/2\theta$ scans for the three samples taken at λ=1.48Å

From figure 8.9 there is a clear increase in the thickness of the bi-layers as the contamination time is increased. The bi-layer thickness deduced from the off-specular scans are listed in table 8.1:

Sample	Bi-layer thickness ± 0.2 (Å)
Sample 1	18.2
Sample 2	18.5
Sample 3	18.8

Table 8.1: Bi-layer thickness deduced from fits to the off-specular Bragg Peak position

Figure 8.10 compares sample 2 with the 20 period Cu/Co multilayer with similar contamination in the spacer layer (figure 8.4). As can be seen in figure 8.10, there is a degree of similarity between the two samples: Both samples exhibit smooth interfaces with a well defined Bragg Peak. The roughness in the two samples is highly correlated, but the vertical correlation length is less than the sample thickness in both cases, evidenced by the lack of Kiessig fringes in the off-specular scans.

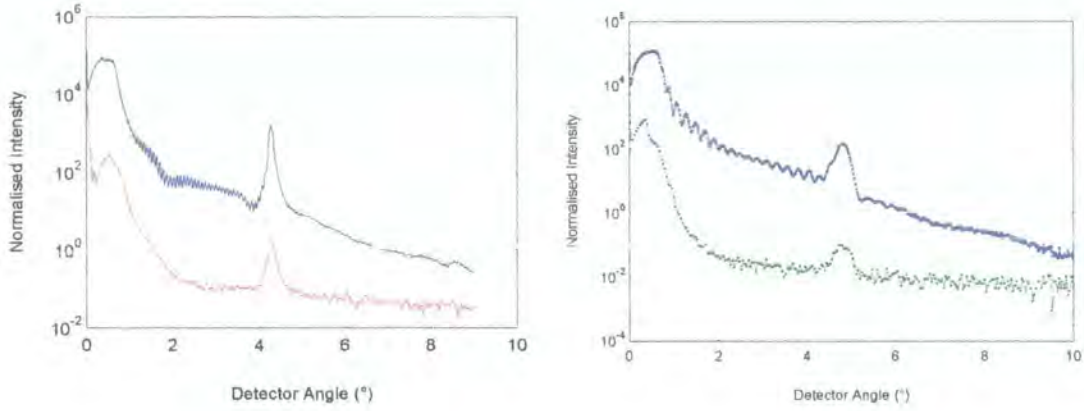

(a) (b)

Figure 8.10: Specular and off-specular scans at λ=1.38Å for Sample 2 (a) and the sample with 20 bi-layer repeats with the same level of contamination(b)

Transverse diffuse scans were taken at the two wavelengths used at a Kiessig Maximum and Minimum as well as through the Bragg peak. Figure 8.11 shows the transverse diffuse scans for sample 2. From figure 8.11 it is clear that tuning into the absorption edge causes much larger changes at the Bragg peak than at the Kiessig maximum. With the systems seemingly displaying a high degree of correlated roughness, the Born wave analysis was again performed on these samples.

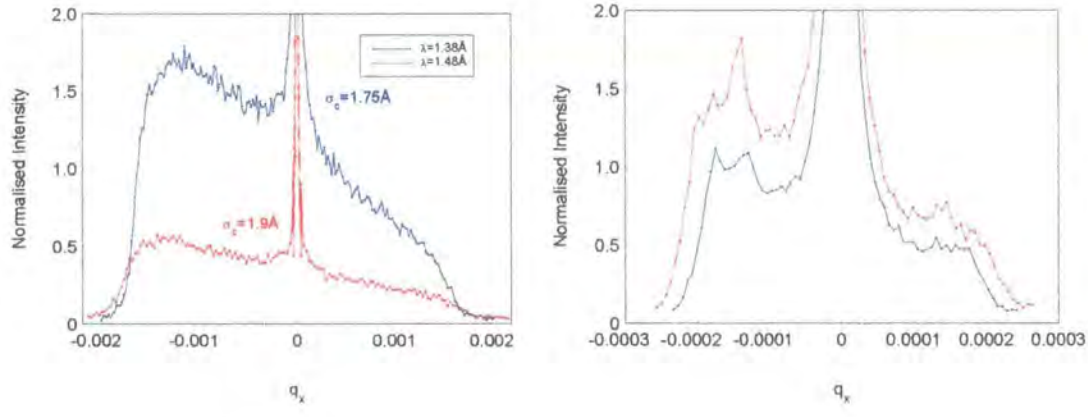

(a) (b)

Figure 8.11: Transverse diffuse scans through the Bragg Peak (a) and the Kiessig Maximum (b) for sample 2

Table 8.2 shows the results of this Born analysis on the samples:

Sample	σ_c (λ=1.38Å)	σ_c (λ=1.48Å)
Sample 1	1.62 ± 0.3 Å	1.80 ± 0.3 Å
Sample 2	1.75 ± 0.3 Å	1.90 ± 0.3 Å
Sample 3	1.24 ± 0.3 Å	1.47 ± 0.3 Å

Table 8.2: Correlated roughness deduced using the Born Wave for the three samples

Why there should be a systematic increase in the roughness when measured at λ=1.48Å is not totally clear, but we note that with the change in wavevector, more diffuse scatter will be detected. Within the Born approximation this would correspond to a larger measured roughness. However, both measurements show that the films are very smooth. It is interesting to note, that the sample which has the lowest GMR also has the lowest roughness.

8.3.2 HAXRD Characterisation

The high angle diffraction data from these three samples was also investigated. The 100μm detector slit used in the reflectometry studies was replaced by a set of Soller slits and the beam height was increased, from 100μm to 1mm. A $\theta/2\theta$ scan across the substrate reflection reveals the resolution in this geometry to be less than 0.01° which translates to a resolution in q_z of $<1.34*10^{-4}$ Å^{-1}. The resolution in q_x can be estimated by conducting a transverse scan through the same substrate reflection A Gaussian fit to this rocking curve revealed the resolution in q_x to be 0.015° or $8.3*10^{-5}$ Å^{-1}.

The three samples were initially aligned to the first allowed Si reflection, namely the 400. A $\theta/2\theta$ scan was then taken in the vicinity of the compromise Cu/Co 111 peak. Typical counting times were 30-40s per point with count-rates of approximately 100 counts per second at the maximum of the peak. Figure 8.12

shows the $\theta/2\theta$ scans in angular space. The compromise Cu/Co 111 peak was fitted to a Lorentzian so that the full width at half maximum (FWHM) could be more easily measured. In order to ensure a satisfactory fit, the stray substrate reflections that can be seen as isolated data points in figure 8.12 were removed prior to the fitting of the data.

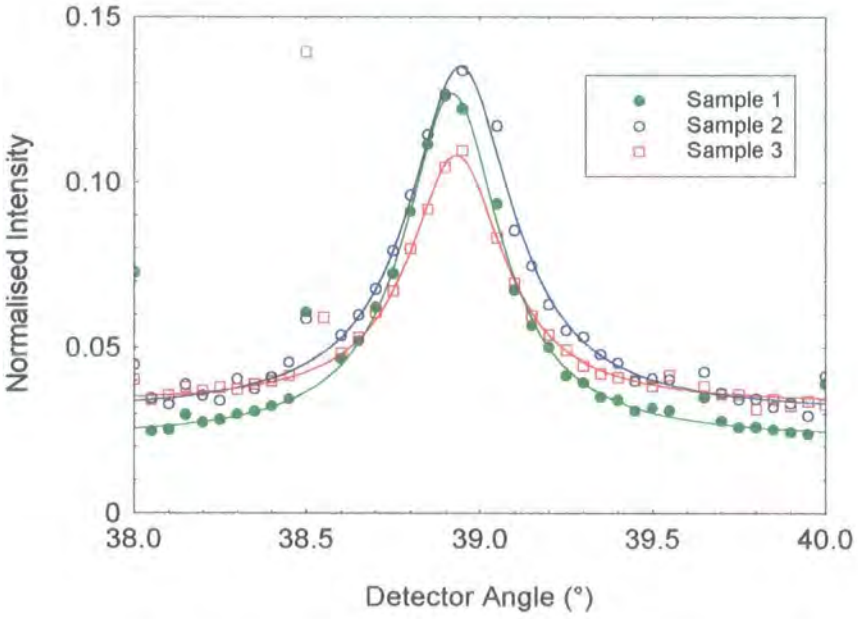

Figure 8.12: $\theta/2\theta$ scans for the three samples in the vicinity of the Cu/Co(111) peak for the three samples. λ=1.38Å.

The average grain size, L, can be obtained from the FWHM of the diffraction peak, by the application of the Scherrer equation [17]

$$L = \frac{0.94\lambda}{\Delta(2\theta)\cos(\theta_B)} \qquad [8.3]$$

where θ_B is the Bragg Angle and $\Delta(2\theta)$ is the width of the diffraction peak in radians. The results obtained from the fits to the diffraction peak are presented in table 8.3. All three samples have similar widths which correspond to grain sizes, using the Scherrer equation, of approximately 230Å.

Sample	Centre (Degrees) ± 0.006°	Lattice Parameter (Å) ± 0.001 Å	FWHM (Degrees) ± 0.01°	Minimum Grain Size (Å) ± 4Å
Sample 1	38.9202	3.5873	0.336	236
Sample 2	38.9438	3.5852	0.364	217
Sample 3	38.9317	3.5863	0.334	236

Table 8.3: Fit parameters from the HAXRD scans shown in Figure 8.13.

The lattice parameters for the three samples is close to the expected value of 3.581Å which corresponds to a 50:50 Co/Cu multilayer. Transverse scans were also taken through the compromise Cu/Co 111 peak. These are shown in figure 8.13. The experimental data was multiplied by sinθ in order to correct for the changing illumination area caused by the beam footprint.

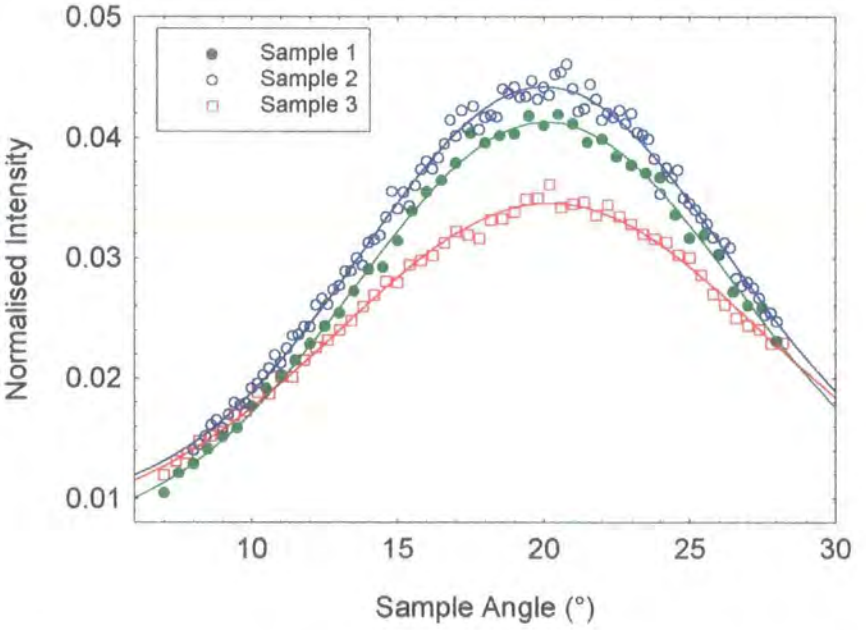

Figure 8.13: Transverse diffuse scans through the compromise Cu/Co 111 peak. Experimental data (points) and Gaussian fits (lines)

Unlike the Cu/Co multilayers deposited by MBE in the previous chapter these transverse peaks could be fitted well to a single Gaussian. The fit parameters are shown in table 8.4:

Sample	Centre (Degrees) ± 0.05°	FWHM (Degrees) ± 0.48°	FWHM ($Å^{-1}$) ± 0.005Å
Sample 1	20.08	15.34	0.129
Sample 2	20.02	14.74	0.124
Sample 3	20.21	16.98	0.144

Table 8.4: Fit parameters from the transverse scans through the Cu/Co 111 peak shown in Figure 8.13.

As can be seen from table 8.4, the FWHM of these samples is extremely large. This large FWHM of the transverse scans shows that the 111 grains are only aligned to within 8° of the surface normal. This explains the low intensity of the diffraction peak because at any one time, only a small proportion of the grains are diffracting.

The changes in the coupling accompanying the contamination are again not evidenced by the high angle data. All three samples show very similar data sets; the $\theta/2\theta$ scans reveal that all the samples have similar grain sizes (230Å) and that the composition of the multilayers is close to the expected 50:50 mixture of cobalt and copper. The transverse scans reveal an unusual structure, namely that the texture is quite widely distributed around the <111> direction.

All structural attempts to characterise these samples have failed to detect any differences between them. Indeed, the samples are all remarkably smooth and close to the desired structure. The high angle data shows an unusual texture, which is common to all the samples. NMR results on similar samples also fail to show any difference between the samples. However, the magneto-transport measurements clearly show that differences do exist between the samples.

With the failure of conventional techniques to characterise successfully the samples, a technique which is sensitive to both the magnetic moment and structure has to be employed. The standard method for such a characterisation is to utilise neutron reflectivity. Experiments are, in fact, being undertaken on these samples by Dr. S. Langridge [18]. However, these experiments suffer from a lack of flux for high momentum transfers. It is also difficult to analyse the diffuse scatter with neutron reflectivity.

Recently, however, it has been demonstrated that it is possible to utilise soft x-rays to probe the magnetic structure of materials. In the following section, an introduction to magnetic x-ray scattering will be presented as an introduction to the work undertaken on these samples using soft x-ray energies.

8.4 X-ray Characterisation using Soft X-rays

8.4.1 Theoretical Introduction to Magnetic X-ray Scattering

Since the 1840s it has been known that the interaction of light with a magnetic sample causes changes in the polarisation of that light. Initially, Faraday noted that the polarisation of the light changed when it had traversed through a magnetic material. In 1877, Kerr noted that a similar effect occurred when the light had been reflected from a polished iron mirror [19]. These effects are now routinely used in the characterisation of the magnetic properties originating from a wide range of materials. The incident light is now typically produced using lasers with energies in the range of 1-4eV. This energy range results in electronic transitions from filled to unfilled electronic valence states [20]. The Faraday and Kerr effects have also been recently evidenced using x-ray scattering from a Fe_3Pt sample[21].

Although the Faraday and Kerr effects originate from electronic excitations, the magnetic field associated with the incident x-rays can also interact with matter. Away from any resonance condition, these magnetic interactions alter the atomic scattering factor (equation 5.1) such that it now includes a magnetic term:

$$f = f_o + f^{mag} \qquad [8.4]$$

The normal Thomson scattering ($f = f_o$), of photons assumes no magnetic term and is approximately given by the product of the atomic number, Z, and the classical electron radius, r_o. The magnetic term in equation 8.4, f^{mag}, is proportional to the Fourier transforms of the orbital and spin magnetisation densities [22]. A pre-factor in the expression for this non-resonant magnetic term, given by $\left(\hbar\omega/mc^2\right)$, reduces the intensity of the magnetic scatter by a factor of $0.02r_0$ for 10keV radiation. For cobalt the difference in magnetic to charge scattering is therefore approximately 10^3. The magnetic scattering is further reduced because it is only the unpaired electrons in the *d* or *f* shells that can contribute. These two effects combine to cause the magnetic scattering to be seven or eight orders of magnitude lower than the charge scattering. In normal scattering experiments it is therefore not necessary to include this magnetic term.

The magnetic scattering arises from the direct interaction of the magnetic field vector ***B*** of the electromagnetic wave with both the spin and orbital moments. As has been demonstrated above, this interaction is weak, and so the corresponding magnetic scattering is difficult to observe. During an investigation of the magnetic spiral arrangement of holmium, Gibbs et. al. [23] observed a fiftyfold increase in the magnetic diffraction intensity as the x-rays were tuned through the holmium L_3 edge.

The resonance effects observed by Gibbs et. al. can be explained by resonance effects associated with electronic transitions. It has already been shown that at a resonance condition, the atomic scattering factor is altered to include a real and an imaginary part. The work described in chapter 5 has been extended by Hannon et. al. [24] to include the resonant 'magnetic' effects observed by Gibbs et. al. The atomic scattering factor can now be represented as:

$$f = f_o + f^{res} + f^{mag} = f_o + f' + if'' + f^{mag} \qquad [8.5]$$

where f^{res} is the resonant term and f^{mag} is the magnetic term introduced in equation 8.4. Following Hannon et. al. the resonant part of the atomic scattering factor for an L_3 transition can be written:

$$f^{res} = \frac{3\lambda}{8\pi}\left\{(\mathbf{e}_f \cdot \mathbf{e}_i)[F_{1\,1} + F_{1\,-1}] - i(\mathbf{e}_f \times \mathbf{e}_i)\cdot \mathbf{M}[F_{1\,1} - F_{1\,-1}]\right\} \qquad [8.6]$$

In equation 8.6, e_f and e_i are the polarisation vectors of the scattered and incident beams, and M is the direction of the magnetic moment. F_{LM} are complex numbers which contain matrix elements whose magnitude is related to the transmission probability between the ground state and the excited state. They are proportional to the L-polar (L=1 for dipolar transition) transition associated with a change of angular momentum (ΔM=0,$\pm$1 for dipolar transitions) along the axis defined by the magnetic moment [25]. A slightly different derivation is given by Altarelli [26], but the final results are the same.

If the excited state can be treated as atomic levels with an associated exchange splitting, Δ, between the lower energy orbitals, and the orbitals induced by the f electron shell, the atomic scattering factor can be simplified [24,27]:

$$f^{res} = F\left[(\mathbf{e}_f \cdot \mathbf{e}_i)n_h + i(\mathbf{e}_f \times \mathbf{e}_i)\cdot \mathbf{M}\,\frac{P}{4}\right] \qquad [8.7]$$

where

$$P = \left[n_e(\uparrow) - \left[\frac{\Delta}{\Gamma(x(\alpha,\eta) - i)}\right]n_h\right] \qquad [8.8]$$

In equation 8.7, F includes the radial part of the transmission probabilities, as well as, a resonant denominator. $n_e(\uparrow)$ is the number of up electrons, and n_h is the number of holes in the d band. The total width of the resonance is given by, Γ, and the deviation from the resonance condition, $(E_\eta - E_\alpha)$, is given by $x(\alpha,\eta)$ which is defined as:

$$x(\alpha,\eta)=\frac{2\left[\hbar\omega-\left(E_\eta-E_\alpha\right)\right]}{\Gamma} \qquad [8.9]$$

The first terms in equations 8.6 and 8.7 are independent of the direction of the magnetic moment and contain charge scattering information only. It is this term that gives rise to the resonance effects that were discussed in chapter 5. The second term, which is linear in the magnetic moment contains the resonant 'magnetic' scattering information. Equation 8.8 shows that the resonance condition is sensitive to the spin polarisation (n_e) in the conduction band and to the exchange splitting, Δ, in the core state induced by the *f* shell.

The splitting of the $L_{2,3}$ edges by the spin-orbit effect is large in *3d*-transition metals. This large exchange splitting results in a large 'magnetic' resonance at these edges. The derivation that resulted in equation 8.7 assumed that $\Delta \ll \Gamma$. With a large spin-orbit effect and the narrow *3d*-band (≈2eV) this would no longer be the case. Kao et. al. [27] observed large resonances in the scattering from a 35Å iron layer deposited on GaAs in the vicinity of the $L_{2,3}$ edges of iron. They extended the calculation of Hannon et. al. but found that no significant corrections to the model were required to fit then data taken at the $L_{2,3}$ edges of the *3d* transition metals.

From the discussion above, it is clear that the magnetic scattering intensity is proportional to the cross product of the incident and exit polarisation vectors dotted into the magnetic moment in the sample, $\left(\hat{e}_i \times \hat{e}_f\right)\cdot\vec{M}=\vec{P}\cdot\vec{M}$. For an incident beam polarised in the horizontal plane (σ polarisation), the magnetically scattered photons will have a polarisation vector in the vertical plane (π polarisation). This is schematically shown in figure 8.14

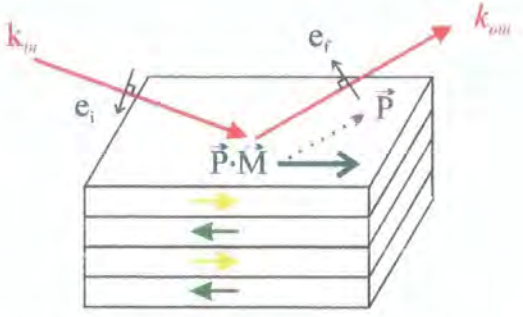

Figure 8.14: Magnetic Scattering Geometry

These resonance effects have been used to study a range of *3d* structures. In most cases, the incident x-rays are circularly polarised. To extract the magnetic scattering from the charge scattering it is necessary to conduct the experiments using both left- and right-handed circularly polarised light. In practice it is easier to use light of a single polarisation and reverse the magnetic moment direction rather than change the helicity of the light. By investigating the asymmetry in the reflectivity curves under the two scattering conditions it is possible to measure the magnetic properties of *3d* multilayers and spin valve structures [28,29,30,31].

In the next sections, soft x-ray magnetic x-ray scattering will be applied to a series of Cu/Co multilayers.

8.4.2 Characterisation of the Samples using Soft X-rays

This section continues the x-ray characterisation of the gas damaged samples, already investigated in section 8.3. The experiments in this section are the first soft x-ray magnetic reflectivity measurements undertaken at the Daresbury SRS [32]. The experiments in this section were undertaken on Station 1.1 [33] in collaboration with Dr. H.A. Dürr and Dr. E. Dudzik. Station 1.1 is a high vacuum beamline designed around a High Energy Spherical Grating Monochromator (HESGM) providing a high photon flux (~10^{10} photons/sec/100mA) and covers the energy range between 200 eV and 1400 eV (with a resolution of approximately 500 meV). A schematic of the beamline is shown in figure 8.15:

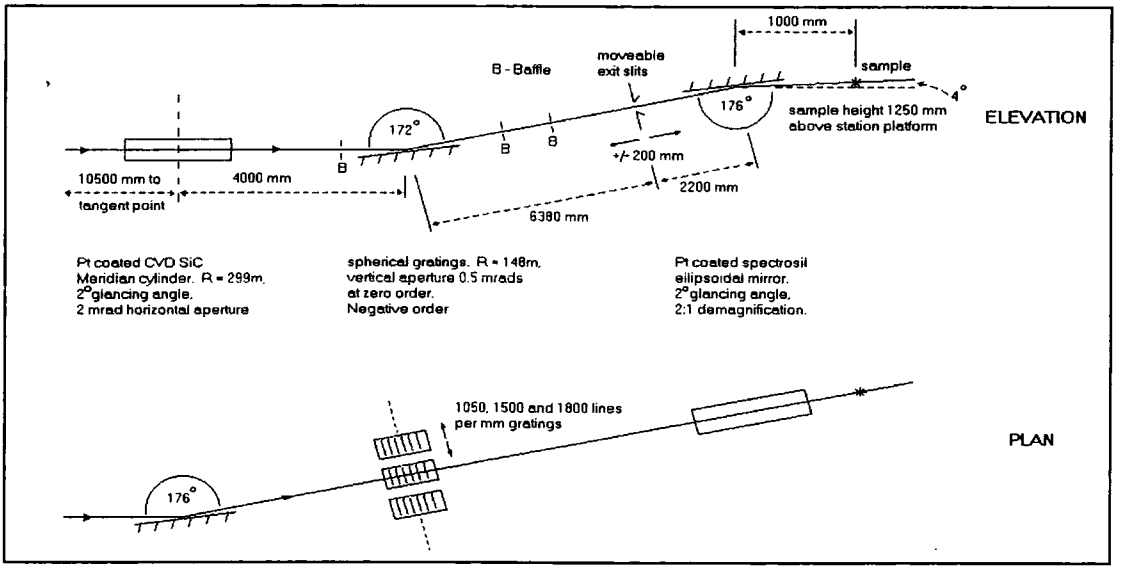

Figure 8.15: A schematic layout of Station 1.1 [33]

As there are no entrance slits defining the incident beam position impinging onto the grating, changes in the position of the synchrotron storage beam directly result in a change in a position on the grating, and thereby result in a shift in energy of the beam incident onto the sample. This means that the energy calibration must be checked after each beam-fill. The final beam position on the sample is defined by a second platinum coated focusing mirror.

For the experiments discussed in this section, a two circle diffractometer was placed at the end of the beam pipe. The diffractometer was then aligned to the beam by placing it at an angle of 4° to the horizontal. Plate 8.1 shows the diffractometer in position at the end of the beam pipe. The operating pressure of the diffractometer vessel was typically 10^{-5} Torr. This low pressure was required to reduce the effects of air scatter on the soft x-rays and in order to prevent damage to other elements in the beam line.

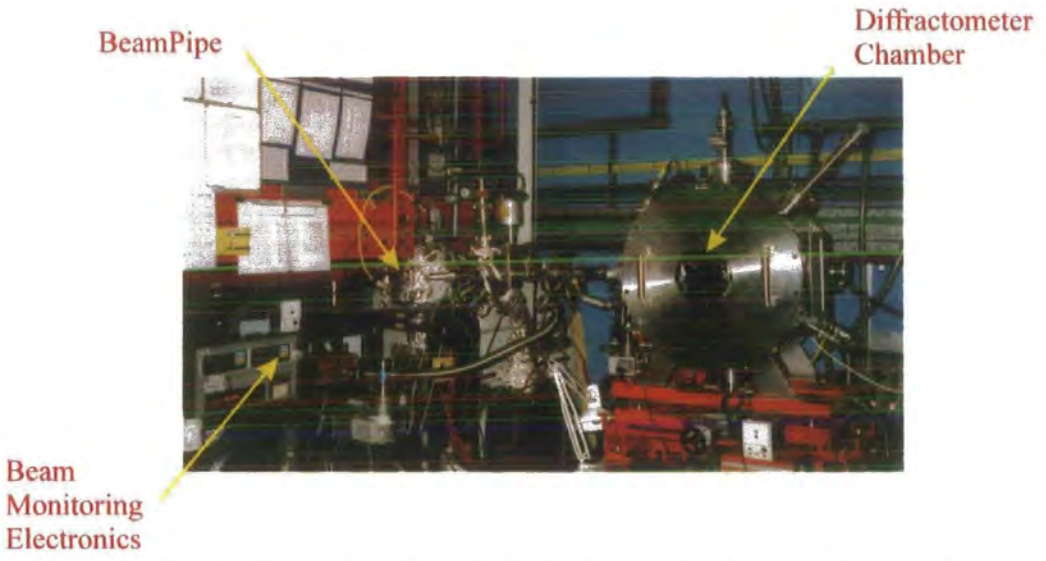

Plate 8.1: The diffractometer in position for the SoXMaS experiments

Plate 8.2 shows the interior of the diffractometer chamber. The incident beam was focused using the second Pt mirror onto the entrance slits of the diffractometer (far left of plate 8.2). A second set of slits helps to reduce the background scatter, and in plate 8.2 these two slits have been shielded with aluminium so as to reduce the background further. The sample was then placed between the pole pieces of an electromagnet.

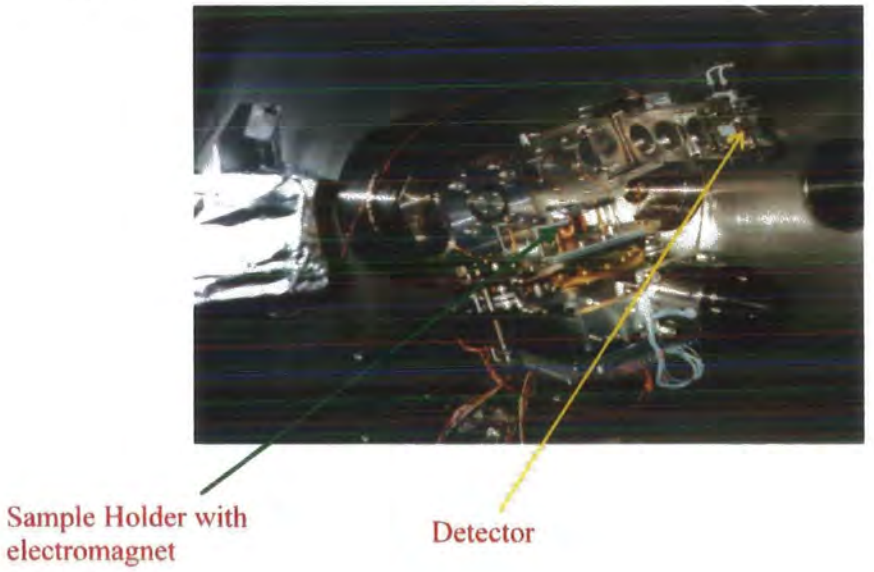

Plate 8.2: The interior of the diffractometer showing the sample environment and detector axis

8.4.3 Experimental Results Recorded using Soft x-rays

In order to investigate the feasibility of conducting experiments at soft x-ray wavelengths, the specular scatter was compared for scans recorded at λ=1.3926Å and λ=16.513Å. This comparison is shown in figure 8.16 where the intensity of the two scans was normalised to the structural Bragg peak.

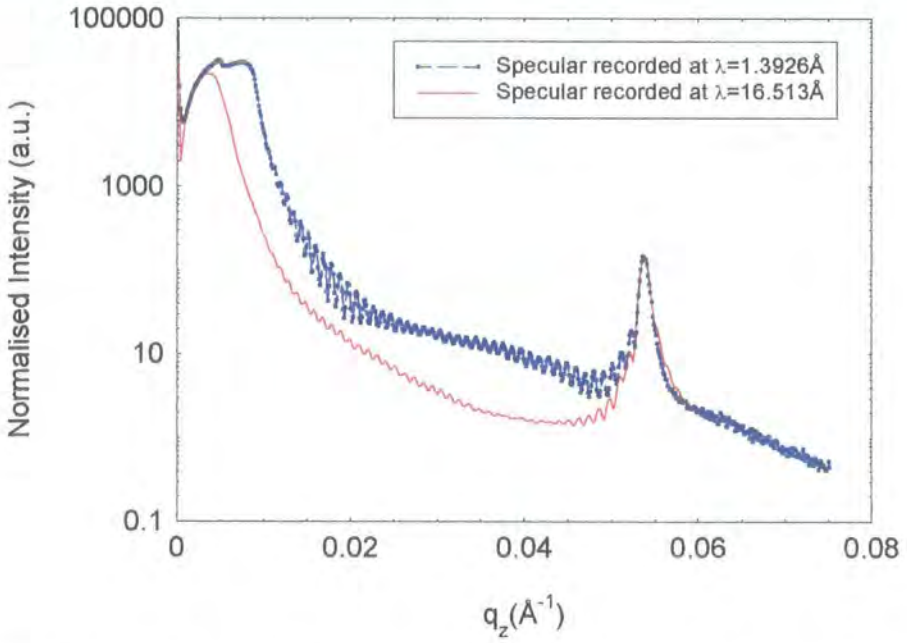

Figure 8.16: Comparison of the Reflectivity scans obtained from sample 2 using hard and soft x-rays. The intensity has been normalised to the structural Bragg Peak

An initial concern when working with such large wavelengths was that the penetration depth would be less that the total sample thickness. The penetration depth at the peak of the iron L_3 edge was found by Sacchi et. al. to be less than 275Å [31]. This is clearly not the case here because, as can be seen in figure 8.16, both scans clearly show Kiessig fringes of the same period suggesting that the x-rays at both wavelengths can penetrate the approximately 1000Å thick sample. The effects of the large absorption are evidenced in the soft x-rays by the blurring of the critical angle.

Figure 8.17 shows the specular reflectivity from sample 3 recorded at several incident energies.

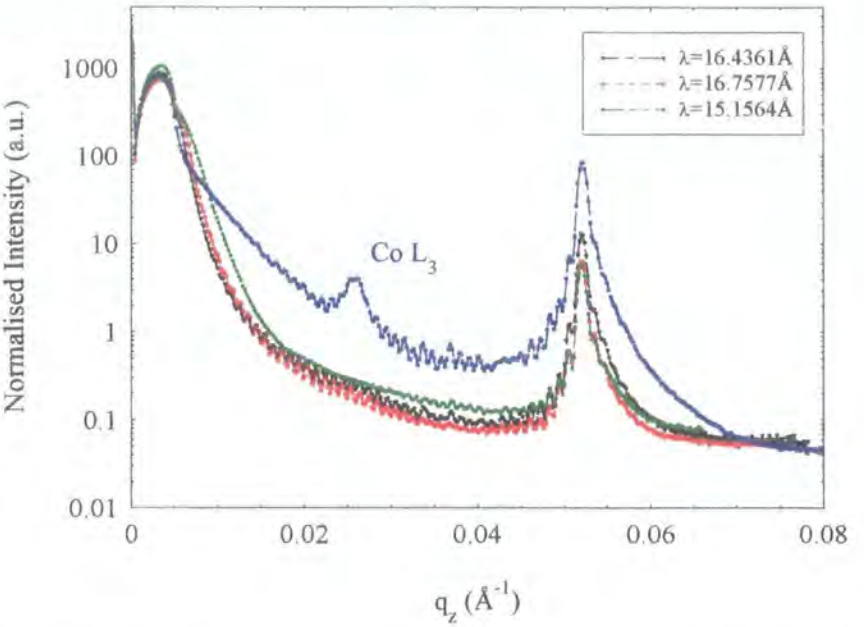

Figure 8.17: Specular scans as a function of incident energy for Sample 3

For incident energies away from the resonance condition, all the reflectivity scans show a similar behaviour, although the scan taken at λ=15.1564Å shows weaker Kiessig fringes. On the cobalt L_3 resonance, however, the shape of the reflectivity curve is very different. There is a peak at half the scattering vector of the structure peak. This corresponds to a *d*-spacing twice that of the structural periodicity. As this peak is not evidenced at the other energies it must result from the magnetic super-structure. The double *d*-spacing implies that the magnetic moment is either coupled anti-ferromagnetically or bi-quadratically. From the magnetometry results it is known that this sample should indeed be bi-quadratically coupled. The double *d*-spacing gives information of the direction of the spins in the cobalt layer: this will be discussed in more detail in later sections.

The change in the shape of the specular scatter at the cobalt L_3 edge could be due to the effects of magnetic roughness. However, a comparison between the scans taken at the Co and Cu L_3 edges (figure 8.18) shows that this is not the case.

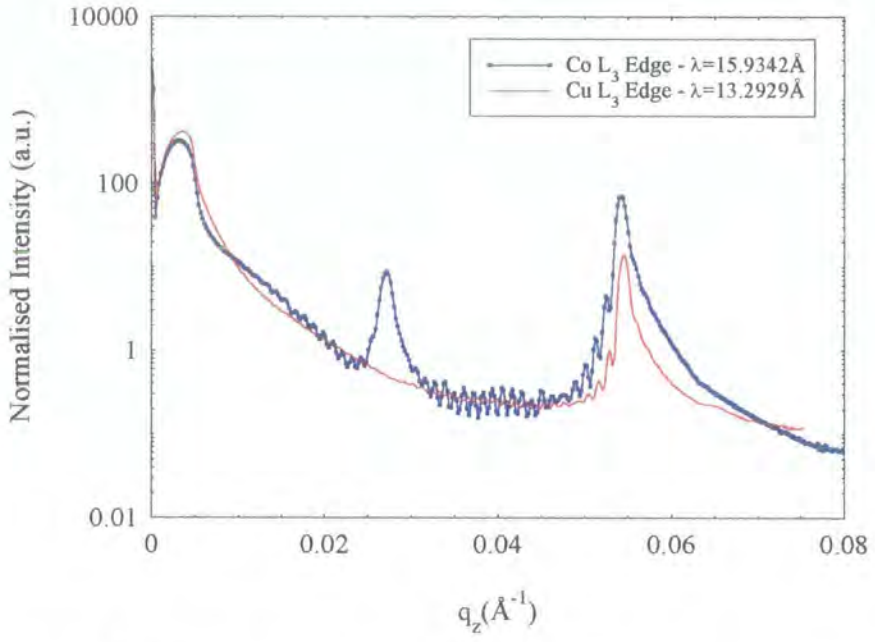

Figure 8.18: Specular scans recorded at the Cu and Co L_3 resonances

The rate of fall off is very similar in the two samples, however the intensity of the Kiessig fringes is very different at the two energies. There is no magnetic signal at the copper edge, showing that there is no magnetic moment associated with the copper spacer layer. There is a change in the intensity of the structure peak for the two wavelengths because at the copper resonance, the cobalt layers are absorbing strongly. This is analogous to the K edge data displayed in figure 5.5, although the effects are more pronounced at these energies. Thus the intensity changes observed in figure 8.17 must be due to anomalous dispersion corrections in the vicinity of the L_3 edges, rather than magnetic roughness.

Figure 8.17 shows that when the incident wavelength is tuned to the cobalt L_3 edge, a magnetic peak is observed. Figure 8.19 shows the variation of the intensity of this peak as a function of energy.

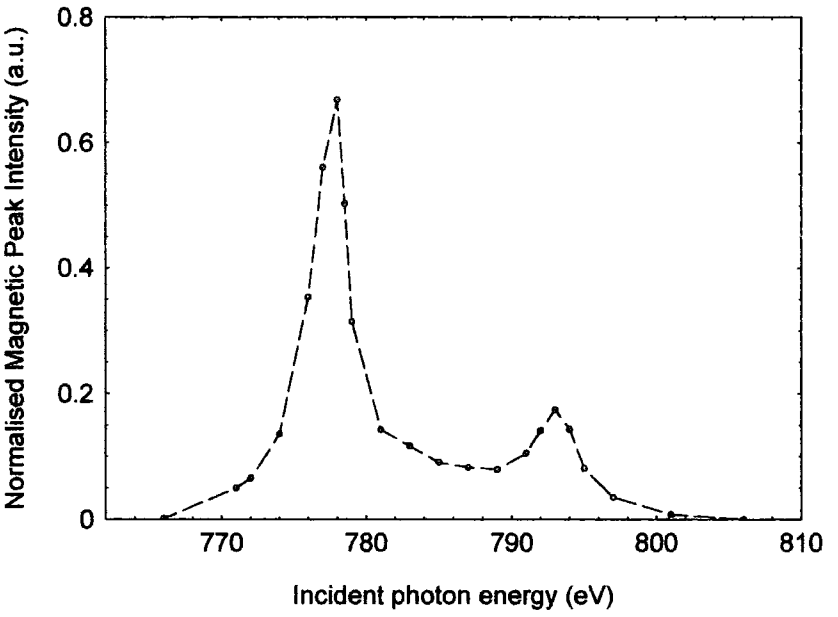

Figure 8.19: The intensity variation of the magnetic peak as a function of energy

A sharp increase in the magnetic peak intensity is observed just below the tabulated values of the Co L_3 edge. The wavelength calibration was carried out by conducting a series of specular scans over the magnetic peak in energy steps of 0.5eV around the cobalt L_3 edge. The energy which gave rise to the largest magnetic peak was then used, and is referred to as the on resonance scan.

Figures 8.17 and 8.18 show that the penetration depth of the soft x-rays is not always greater than the sample thickness. Specular scans taken over the magnetic and structure peaks show changes as the energy is tuned through the cobalt L_3 edge. These results are presented in figure 8.20. For energies below the cobalt L_3 edge, clear Kiessig fringes are observed in the vicinity of both peaks, but as the energy is tuned through the edge these fringes disappear showing that the penetration depth has reduced.

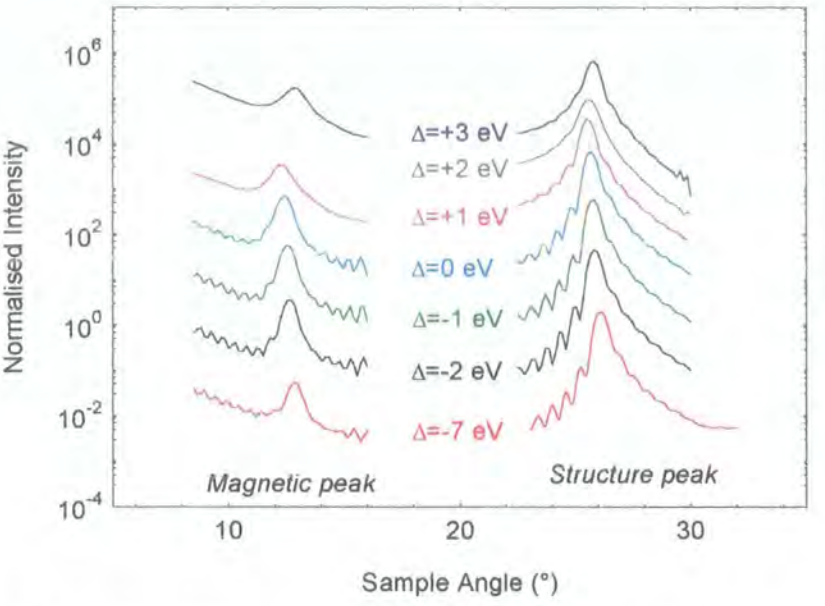

Figure 8.20: Specular scans across the magnetic and structural peaks of sample 1 as a function of energy.

The results displayed in figure 8.20, suggest that the penetration depth of the soft x-rays is reduced as the energy is tuned through the edge. If this were the case, the widths of the peaks should increase. This is because the FWHM of the two Bragg peaks is proportional to the total number of bi-layers being sampled. In the case of the magnetic peak this bi-layer repeat is twice that of the structure peak, due to the double periodicity of the magnetic moment induced by the coupling, and is approximately 40Å. The magnetic peak was fitted to a Voight function, and an exponential background was used to account for the fall off. Figure 8.21 (a) shows the variation of FWHM of the fitted peaks as a function of energy. Figure 8.21 (b) shows the inverse of the FWHM as a function of incident energy.

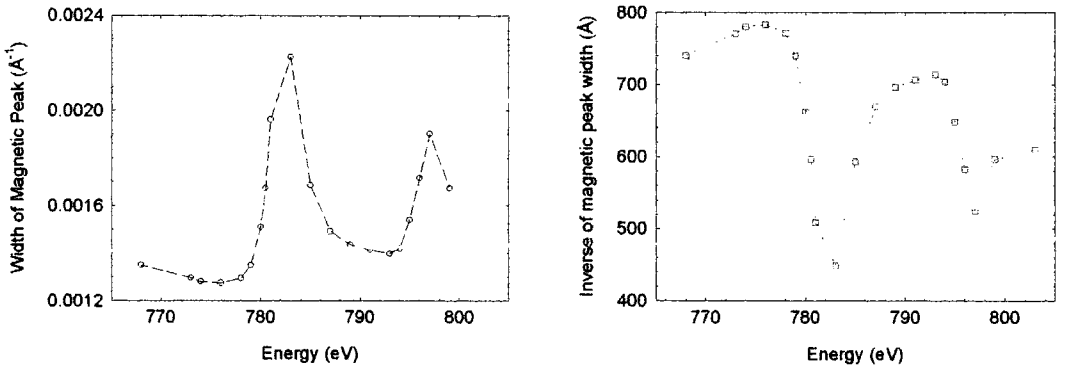

(a) (b)

Figure 8.21: The FWHM (a) and its inverse (b) of the magnetic peak from sample 1 as a function of energy through the Co L_3 and L_2 edges.

It is clear that there is a systematic increase in the width of the magnetic peak as the energy is tuned through the L_3 and L_2 edges. By inverting the FWHM, a measure of the thickness of the sample being probed in the experiment can be estimated. This is shown in figure 8.21 (b). The results from this simple approximation are encouraging. From the specular scatter we know that the x-rays sample the total stack thickness, which is approximately 1000Å. However, the inverse of the FWHM of the magnetic peak for energies below 780 eV, yield values less than this. The reasons for this is likely to be due to the cobalt layers nearest the substrate being coupled ferromagnetically. These agrees with the neutron experiments and the fact that GMR is only obtained after deposition of 4-5 bi-layers. The sample thickness that therefore contributes to the magnetic peak intensity would be less than the total sample thickness. However, figure 8.21(b) does shows a sharp reduction in the sample thickness that is probed at energies close to the two L edges caused by an increase of the absorption coefficient.

The importance of including anomalous dispersion terms in the atomic scattering factor have already been presented in chapter 5. The results contained therein show that for Cu/Co multilayers, a change in the wavelength only effects the Bragg peak intensity due to changes in the scattering factor difference between the two layers. These results can be modelled from theoretical arguments based on isolated electrons. The use of isolated electrons in calculating anomalous dispersion

effects limit the validity of the method to an energy range that only extends to 4keV. It is not possible to extend this theory to include these soft x-ray energies. Thus new methods are required to estimate the anomalous terms in the scattering factor. It has been demonstrated in figure 8.21, that a careful measure of the widths of the satellite peak in the reflectivity is a direct measure of the absorption coefficient. It should therefore be possible to calculate f' via the Kramers-Kronig relations. Such a method has been proposed by Tonnerre et. al. [34], but it has yet to be published.

It was noted above that the maximum magnetic peak intensity occurred just below the tabulated values of the Co L_3 edge. This is because on resonance, the scattered x-rays are absorbed strongly. Figure 8.22 shows the intensity and FWHM (absorption) of the magnetic peak on the same graph.

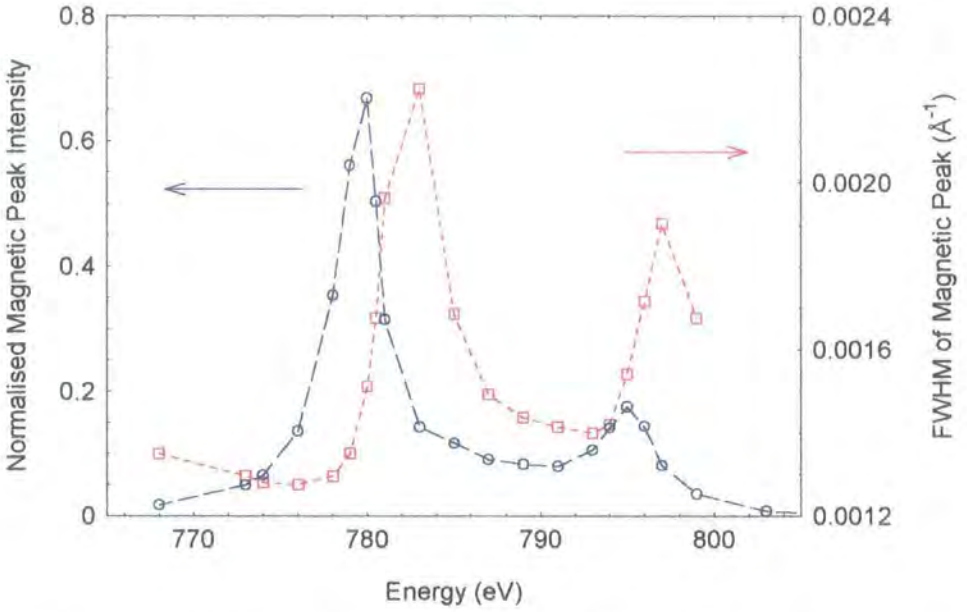

Figure 8.22: The intensity and FWHM of the magnetic peak observed from sample 1 as a function of energy

8.4.3.1 Field Dependence on the Magnetic Peak Intensity

From section 8.4.1 it is to be expected that the intensity of the magnetic peak should change as the direction of an external field is varied. This field dependence was investigated by initially applying a 730 Oe field parallel to the beam direction, using an external permanent magnet. A complete data set was then recorded with the sample magnetised in this direction. A field orthogonal to the x-ray beam could then be applied using the in-situ electromagnet which is shown in plate 8.2. A schematic of the field directions is shown in figure 8.23.

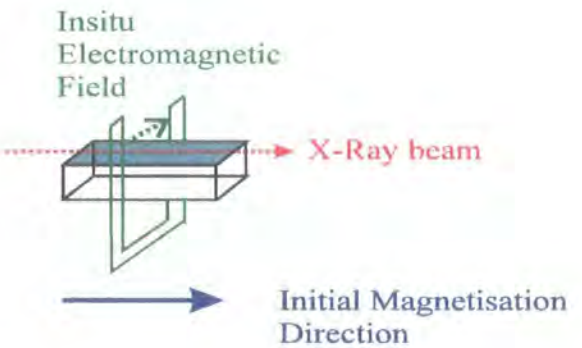

Figure 8.23: A schematic of the field orientations used in the soft x-ray experiments

The field produced by the electromagnet was calibrated at atmospheric pressure using a hand-held Gauss meter. The calibration is shown below in figure 8.24.

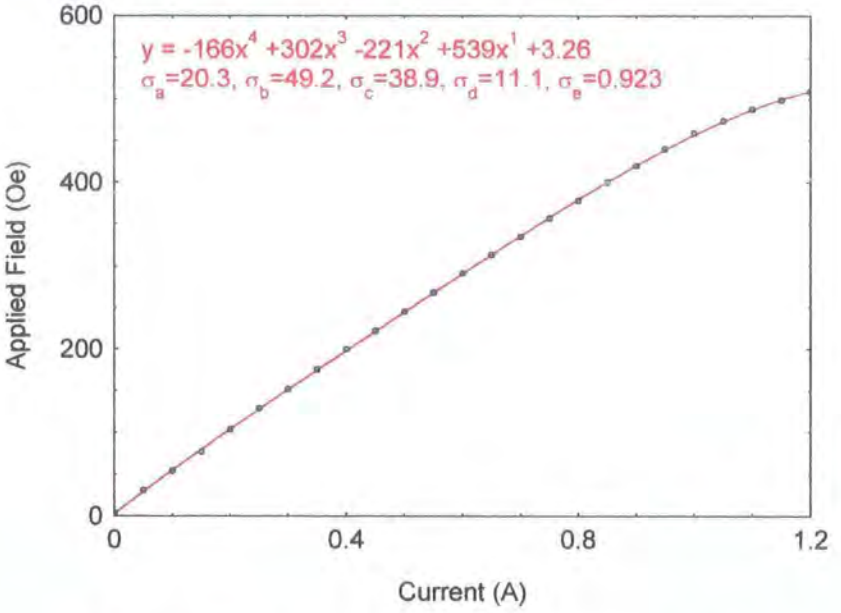

Figure 8.24: The calibration of the electromagnet

The gap between the pole pieces of the electromagnet was of the order of 1 cm. In order to increase the field at the sample position, the sample was mounted next to two thin iron shims. The gap between the iron shims and the sample was 1mm, and the gap between the electromagnet and the iron shims was of the same order. The use of the iron shims enabled the field applied at the sample to be increased from approximately 300 Oe to 500 Oe. All the data contained in this section was obtained with the samples in this geometry

The non-linearity observed for high currents in figure 8.24 is due to Ohmic heating in the electromagnet coils. This effect is more pronounced when the current is applied in a low pressure environment where it is harder to dissipate the heat generated in the coils. It was not possible to conduct a calibration in-situ due to the design of the diffractometer. In order to maintain a constant temperature at the sample, high currents could only be passed for a few seconds. This in practice limited the time that large fields could be applied to a few tens of seconds. After application of this orthogonal field, another complete data set was recorded, in zero field. Thus the differences between the two data sets can only result from a change in

the magnetic state of the samples. Figure 8.25 shows the effect of changing the magnetisation on the specular scatter from sample 2.

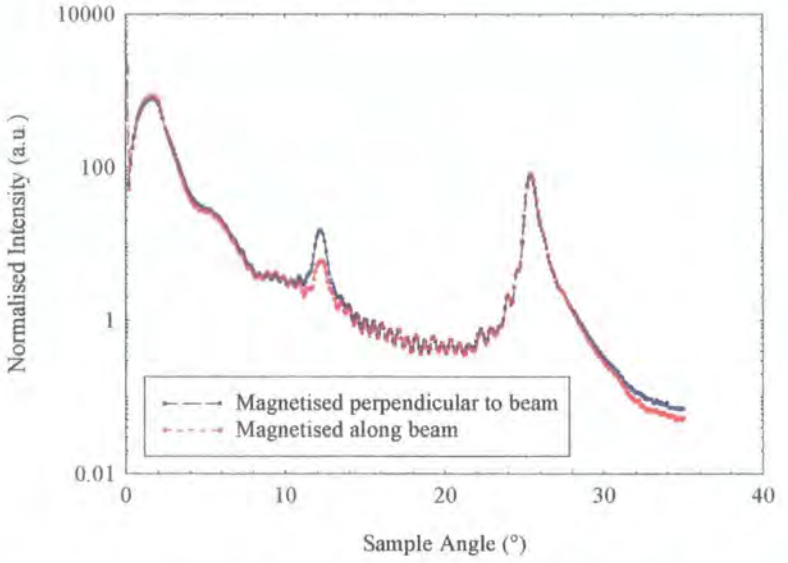

Figure 8.25: Specular reflectivity for sample 2 in zero field after the sample had been magnetised along the beam direction (red) and orthogonal to it (blue)

It is clear that the only effect of changing the magnetisation direction is on the intensity of the magnetic peak. An increase in the magnetic peak intensity is observed when the field is applied perpendicular to the x-ray beam. A similar change in intensity was observed for sample 1 which was also bi-linearly coupled. The changes in intensity of the magnetic peak with applied field for the bi-linear samples is shown, on a linear scale, in figure 8.26.

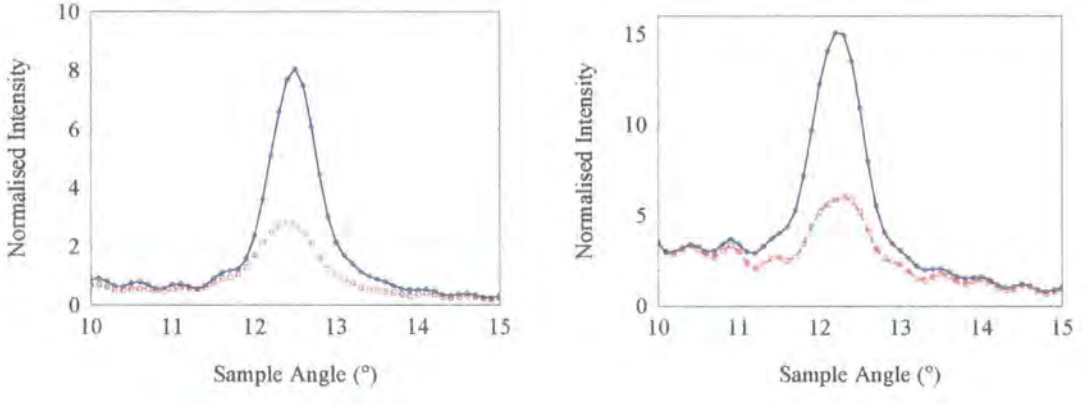

Figure 8.26: The magnetic peak intensity with the field applied along (red) and perpendicular (blue) to the beam for sample 1 (a), sample 2 (b)

When the field is applied along the beam direction for a purely AF coupled sample the intensity of the magnetic peak should be zero. This is because above a critical field the spins in the magnetic layers should spin-flop resulting in a zero net moment pointing along the x-ray beam [35]. When the field is applied perpendicular to the beam, this effect is reversed and the intensity of the magnetic peak should increase as the spins return to their initial positions. This effect is shown schematically in figure 8.27.

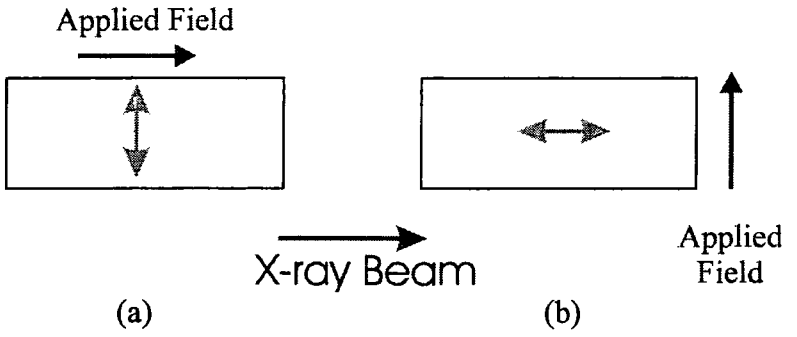

Figure 8.27: Spin-flop alignments for a pure AF coupled sample on application of an external field parallel to the beam direction (a) $\vec{\mathbf{P}} \cdot \vec{\mathbf{M}} = 0$, and perpendicular (b) $\vec{\mathbf{P}} \cdot \vec{\mathbf{M}} \neq 0$

It is, however, clear from figure 8.26 that after a field had been applied along the beam direction that there was still a significant magnetic peak. Thus there must still be a net moment pointing along the beam direction. This moment could result from either ferromagnetic or bi-quadratic domains being present in the sample. Another possibility is that the angle between the spins in adjacent cobalt layers is not exactly 180°, resulting in a small net moment which can resist a spin-flop alignment.

If the angle between the spins in alternate cobalt layers is 90°, then bi-quadratic samples can exist in two orientations. The moment produced by the spin alignment in the two orthogonal directions (along the beam, and orthogonal to it) would be the same: (figure 8.28).

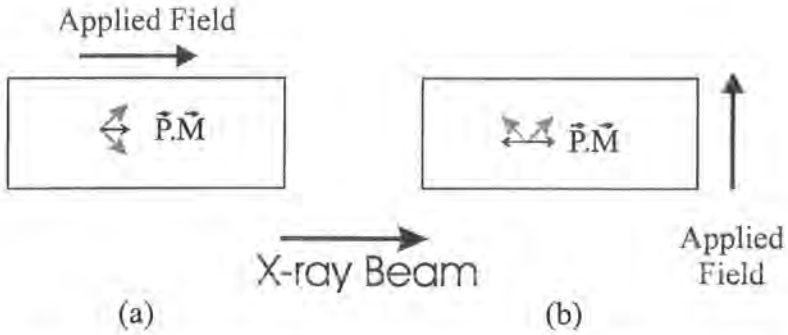

Figure 8.28: The two possible orientations for the spins in a bi-quadratically coupled sample

It is possible to distinguish between these two configurations by conducting soft x-ray scattering experiments. If the coupled layers are in configuration shown in figure 8.28 (a) the magnetic superstructure is no longer at a *d*-spacing twice that of the structure peak, and the magnetic scattering would be surperimposed under the structural Bragg peak. This is schematically represented in figure 8.29.

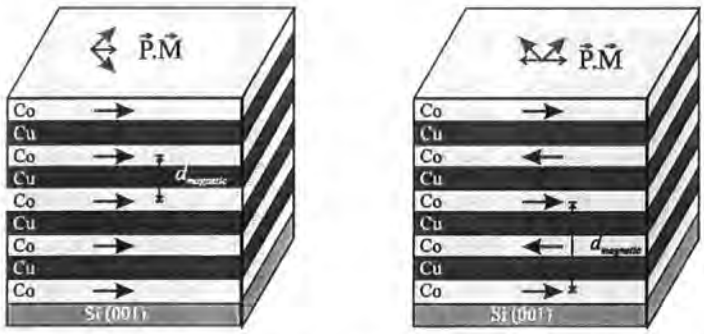

Figure 8.29: The magnetic super-structure for the two cases depicted in figure 8.28

The bi-quadratically coupled, sample 3, showed a magnetic peak at the same momentum transfer as the bi-linearly coupled sample, showing that the spin configuration was that shown in figure 8.28 (b). However, the dependence of this magnetic peak on the magnetic field direction was very different from the other bi-linear samples. Figure 8.30 shows the specular scans, on a linear scale, across the magnetic peak for the two magnetisation directions.

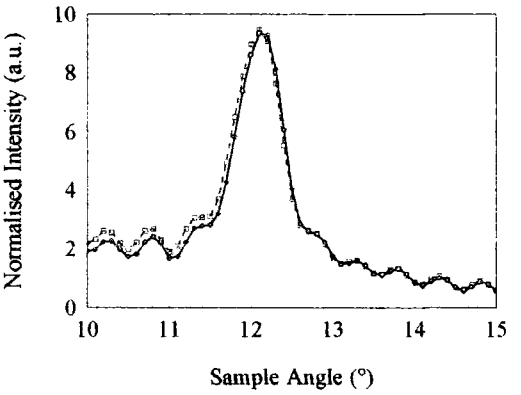

Figure 8.30: The magnetic peak intensity with the field applied along (red) and perpendicular (blue) to the beam for sample 3

There was no observed change in zero field of the intensity of the magnetic peak with applied field in this sample. Thus the configuration of the spins in the bi-quadratic samples must remain the same for both magnetisation directions. Additionally it was observed that there was also no change in the intensity of the structural peak for the two field directions, suggesting that there are no ferromagnetic domains.

The magnetisation studies so far undertaken show that there are significant differences between the bi-linear and bi-quadratic samples, and that their behaviour cannot be explained in very simple terms. It was decided to investigate the magnetic peak intensity as a function of applied field in greater detail. The samples were initially subjected to the same external field of 730 Oe applied along the beam direction and the intensity of the magnetic peak was then recorded for a series of applied orthogonal fields. After the field was applied for 5 seconds the magnetic peak intensity was recorded, the field was removed, and the zero-field intensity was recorded. Figure 8.31 shows the variation of the magnetic peak as a function of applied field for sample 2. Both bi-linear samples exhibited similar behaviour. The blue data points correspond to data taken with the field on, and the red data points are the zero-field data.

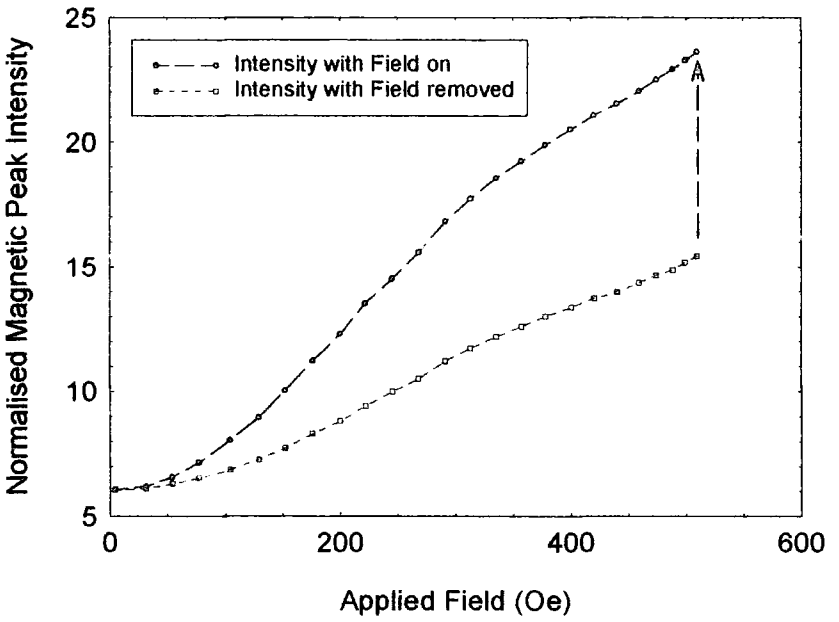

Figure 8.31: Magnetic peak intensity as a function of applied field for Sample 2. Data recorded with the field on (blue), and zero-field data (red)

Little change in the magnetic peak intensity is observed for fields below 100 Oe. Thereafter, a steady increase in both the with field and without field data is observed. It is interesting to note that the magnetic peak intensity has not saturated, even for an applied field in excess of 500 Oe. After this orthogonal field had been applied, the magnetic peak intensity in zero-field had increased by a factor of just under 3, in agreement with figure 8.26. These results are somewhat surprising considering that the coercive field of these samples is of the order of 20 Oe. It would be expected that the greatest changes in intensity of the magnetic peak would occur for applied fields of this order.

The with-field data shown in figure 8.31 shows that it is possible to increase the intensity of the magnetic peak still further on the application of an orthogonal field. For this increase in the magnetic peak intensity to occur, the net magnetic moment aligned to the beam must increase when this field is applied. When the field is removed, this net moment must rotate out of the beam direction. The dependence of this rotation angle with applied field was investigated by following the green arrow in figure 8.31. The results of the experiment are shown in figure 8.32:

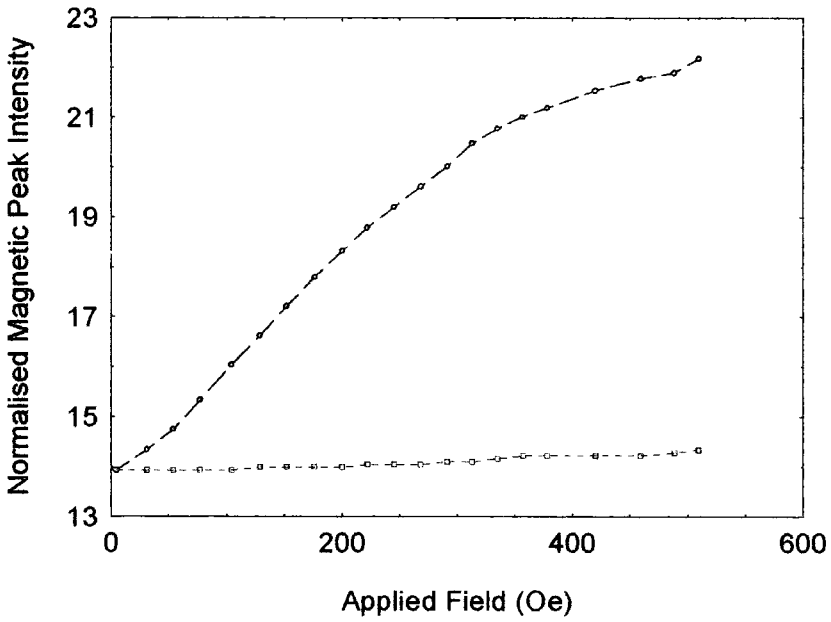

Figure 8.32: The field dependence on the rotation of the magnetic moment with the blue points corresponding to the peak intensity with field and red the intensity at zero field.

The intensity of the magnetic peak again increases steadily as the orthogonal field is applied. As expected the magnetic peak intensity in zero-field does not change significantly. On removal of the field, the magnetic peak intensity fell sharply, a slow decay to the initial value being then observed. This decay was of the order of minutes. The data displayed in figure 8.32 were recorded thirty seconds after the field had been removed.

The magnetisation behaviour of the bi-linear samples is surprising considering the very low values of the coercive field, and the correspondingly large fields applied here. The same experiment was undertaken on the bi-quadratically coupled sample. This sample showed a very different behaviour to that of the bi-linear samples. It was shown in figure 8.28 that there was no change in the magnetic peak intensity (in zero field) for the two orthogonal field directions. This was in sharp contrast to the behaviour of the bi-linear samples.

The analogous experiment that gave rise to figure 8.31 was undertaken on sample 3. The results are presented in figure 8.33:

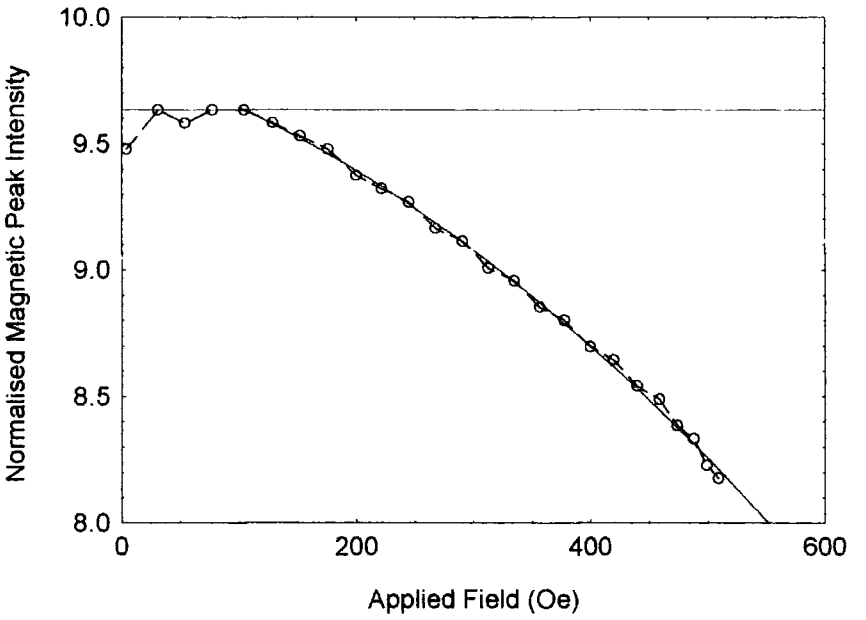

Figure 8.33 Magnetic peak intensity as a function of applied field for Sample 3. Data recorded with the field on (blue), and zero-field data (red).
A parabolic fit to the with field data is shown in green.

Again, the behaviour of the magnetic peak intensity with applied field is very different for this bi-quadratically coupled sample. In contrast to the bi-linear samples, the with field magnetic peak intensity falls on the application of an orthogonal field. A slight increase in the peak intensity is observed for low fields, but for fields above approximately 100 Oe, the peak intensity follows a parabolic dependence on the field strength. As was observed earlier, the zero-field intensity always returned to the initial value.

The magnetisation experiments show that even when fields as large as 500 Oe are applied, the magnetic peak intensity has still not saturated. These fields are considerably larger than the coercive field which is approximately 20 Oe. In order to understand the magnetisation experiments, it is useful to consider some TEM and Lorentz electron microscopy results on a similar series of samples. This work was undertaken by Prof. J. Chapman's group at the University of Glasgow [36].

The physical microstructure of the samples was investigated by Chapman and the average grain size was found to be approximately 200 Å, in excellent agreement with the results deduced from our high angle x-ray data presented in section 8.3.2. The magnetic microstructure was investigated by the use of the Fresnel mode of operation. Images of the magnetisation were taken as a function of applied field, after the sample had been saturated by a 6 kOe field. The magnetisation sequence was conducted along a nominally hard and easy axis.

The Chapman TEM studies show that whilst there was a clear signal from the bi-quadratic samples suggesting ferromagnetic or bi-quadratic coupling the nominally anti-ferromagnetically coupled sample had extremely low contrast. For a purely AF coupled sample there should be no contrast. The contrast in the AF coupled samples suggest that the angles between the spins in adjacent cobalt layers is slightly less than 180°, and that there is a small net moment associated with the coupling between the cobalt layers.

For both samples, the Chapman TEM images suggest that the samples are single domain, and that major changes to the magnetisation do not occur above the coercive field. This is in agreement with the MOKE data. All the samples show a degree of magnetic ripple which are local variations in the mean direction of the magnetisation. These ripples run perpendicular to the direction of the magnetisation. The magnetic ripple is more pronounced along the hard axis, and in low fields.

The TEM and MOKE data both agree that the magnetisation in the samples does not change significantly in fields greater than 40 Oe. However, this is still in contradiction to the results obtained from the x-rays. It should be noted that the techniques of TEM and MOKE are measuring very different aspects of the magnetisation to the soft x-rays. In the MOKE and TEM studies, it is the net, resultant, moment that is being measured. The x-rays are only sensitive to the anti-ferromagnetically coupled component of the magnetisation in the direction of the x-ray beam.

8.4.3.2 Explanations of the Magnetisation Results obtained using Soft X-rays

In the deposition chamber, a small field is present. This field, of approximately 100 Oe, is used to align magnetic layers in spin valve structures, and in the case of these samples has the effect of aligning the spins within the cobalt layers. In the geometry of the current experiment, this field is at right angles to the beam direction. This growth field defines the nominal easy axis in the samples.

When the spins align at 90° to each other, a large net moment associated with the coupling is present (light arrows in figure 8.34). This moment will align along the growth field, and form a strong easy axis, which was observed in the Chapman TEM micrographs. The 'as grown' state is shown schematically in figure 8.34. Although the TEM suggests that the sample is a single domain state, there may be a some small demagnetising domains.

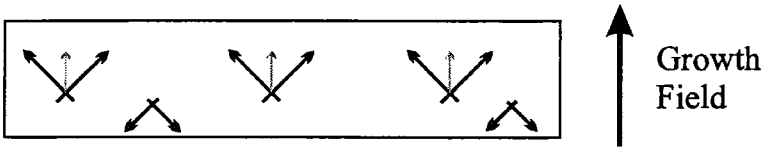

Figure 8.34: The as grown magnetic state of the bi-quadratic sample

When an external field is applied, these moments will rotate to align to it. When this field is applied along the beam direction, these moments are pulled out of the easy axis towards a harder magnetic state. The layers will always remain coupled because the exchange coupling is so strong (the saturation magnetisation is of the order of 1T, figure 8.8). The alignment of the moments in a field along the beam direction is shown in figure 8.35

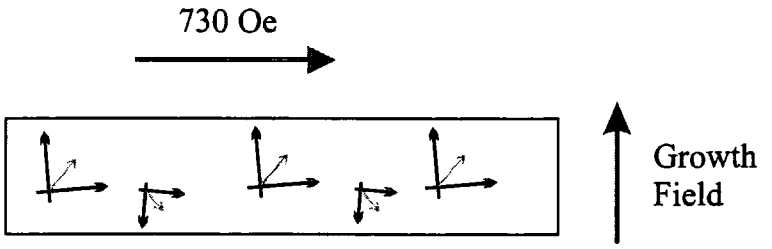

Figure 8.35: The bi-quadratic sample, with a field applied along the beam direction

When the field is removed, the moments associated with the coupling will rotate back towards the easy axis, and return to their original positions, figure 8.34. If an external field is now applied along the easy axis, i.e. orthogonal to the beam, the sample forms a single domain state. This process may explain the slight increase in the magnetic peak intensity observed at low fields in figure 8.33. When the orthogonal field is increased still further, the angle between the spins in adjacent layers reduces. This reduction in angle corresponds to a reduction in the component along the beam, and therefore a reduction in the magnetic peak intensity. This phenomenon is schematically shown in figure 8.36:

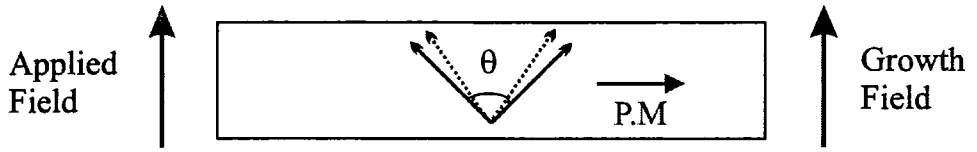

Figure 8.36: The bi-quadratic sample on the application of a large field along the easy axis

The TEM results are required to explain the bi-linearly coupled samples. It was noted above, that in a purely AF coupled sample, there should be no magnetic peak intensity when the sample is magnetised along the beam direction. The fact that there was a substantial magnetic peak implies the sample had either bi-quadratic domains, or that the antiferromagnetic alignment was not perfect. The TEM results confirm that the AF alignment is not perfect, and that the sample is in a single domain state. As the coupling is not 100% AF, there will be a small moment which can align with the growth field. The as-grown state will therefore have the spins lying along the beam direction, with the small moment associated with the coupling pointing along the growth field, figure 8.37:

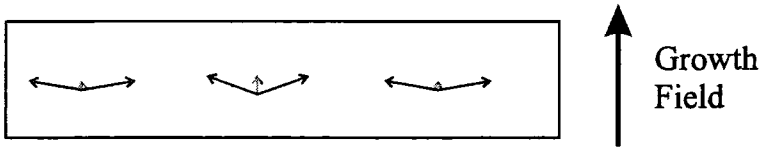

Figure 8.37: The as grown magnetic state of the bi-linear samples.

As this moment is very low it is difficult to ascribe an easy or hard direction to the sample. The TEM results suggest that the differences in energy between the two orthogonal directions are very small. In a similar way to the bi-quadratic sample, when an external field is applied along the beam direction, the moments will rotate towards it. However, unlike the bi-quadratic sample, the spins will not necessarily rotate back to the easy axis defined by the growth field, on removal of the external field. They will become pinned along an intermediate axis which is a result of a complex energy surface. There are many local minima in which the moments can become trapped due to the extremely small moment, and the large magnetic ripple which is seen to exist in these low field regimes is evidence of these fluctuations in the energy state. A schematic of the magnetic structure on removal of the external field is shown in figure 8.38:

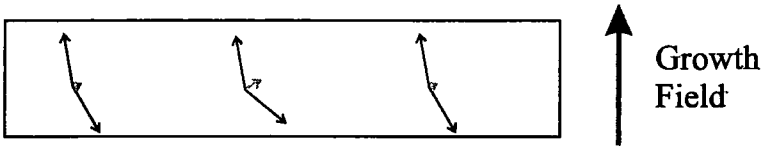

Figure 8.38: The magnetic structure of the bi-linear samples, on removal of the external field applied along the beam direction

When an orthogonal field is applied, these moments start to rotate back towards the growth field direction. However, unlike the MOKE and TEM measurements, the sample has not been saturated, and the sample is always returned to a zero-field state after each field has been applied. This motion of the moments is restricted by the energy surface, and it requires relatively large fields to rotate the moments back towards the nominal easy axis. This behaviour is seen in figure 8.31. The variation of the magnetic peak intensity with applied field, is a measure of the degree of this rotation. The with-field data is therefore a measure of the maximum rotation. However, when the field is removed, some of the moments rotate away from the growth field direction towards a local easier axis, and the magnetic peak intensity is seen to reduce. Figure 8.31, is a measure of the 'shape' of the weak, global energy minima, and figure 8.32 maps the shape of the local energy minima. If it had been possible to apply a large field, the intensity of the magnetic peak in the bi-linear

samples should saturate, and then start to reduce in intensity for the same reasons as in the bi-quadratic sample.

The magnetic scattering from the soft x-rays has yielded a large amount of information about the magnetic state of the samples. The explanations of the magnetic data agree with the results obtained from the Chapman TEM study, although the very different field ranges have yet to be explained fully. The discrepancies are likely to be due to the fact that the two techniques are sensitive to different components of the magnetisation.

Thus far, it has only been the specular scatter that has been studied. With the high flux of station 1.1, it has, however, also been possible to investigate the diffuse scatter from these samples. There are several advantages of using soft x-rays to investigate the diffuse scatter from metallic multilayers and these will be presented in the next section.

8.5 Diffuse Scatter Measurements at Soft X-ray Energies

There have been very few cases in the literature where the diffuse scatter has been investigated using soft x-rays. The diffuse scatter from polished silicon substrates [37], as well as from W/C multilayers [38] has been studied. These samples were investigated away from any resonance condition and the theory developed by Sinha et. al., (see chapter 3 above) was employed to give values of the roughness, lateral correlation length and fractal parameter. The values deduced were in good agreement with similar measurements carried out at harder x-ray energies, and through AFM studies.

In this section, the results obtained by analysing the diffuse scatter will be presented. The flux from station 1.1 is high, and the diffuse intensity was easily observed. The background was high, and in future runs this needs to be corrected. Figure 8.39 shows the specular and off-specular scans from sample 1.

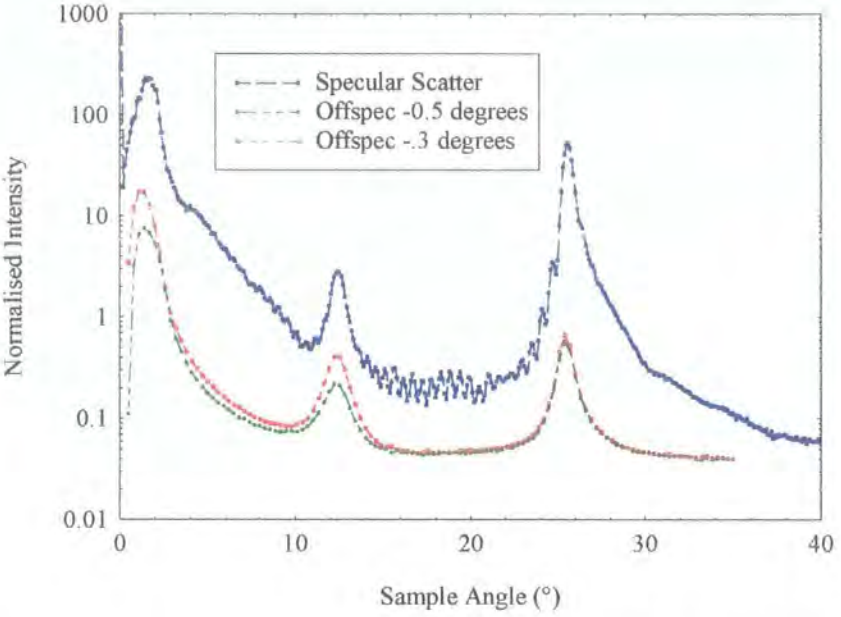

Figure 8.39: Specular and off-specular scans from sample 1 taken at the Co L_3 edge

The off-specular scans shown in figure 8.39 confirm the results from the hard x-rays - namely that the roughness in the system is highly correlated. The diffuse scatter is also peaked at the momentum transfer corresponding to the magnetic super-lattice. The high levels of intensity enabled transverse diffuse scans to be successfully undertaken and these will now be discussed.

One particular advantage of studying the diffuse scatter with soft x-rays is that the range of reciprocal space that can be probed is vastly increased over what is observable by hard x-rays. If the transforms between real and reciprocal space are recalled;

$$q_z = \left(\frac{2}{\lambda}\right)\sin\left(\frac{\phi}{2}\right)\cos(\delta) \text{ and } q_x = \left(\frac{2}{\lambda}\right)\sin\left(\frac{\phi}{2}\right)\sin(\delta) \qquad [8.10]$$

it is clear that the range in q_x that can be explored is directly proportional to δ, the angular difference between the incident angle and the specular condition. The limits of δ are defined by the critical angles of the incident and scattered radiation. For the multilayers that we are considering in this chapter, the Bragg peak occurs at a detector angle $2\theta \approx 5°$ (figure 8.10) at a wavelength of 1.38Å. Thus the maximum

value of δ is 2.5°, and the minimum length scale that can be probed is of the order of 500Å. As sputtered multilayers have lateral correlations typically a lot shorter than this, much of the diffuse scatter is not observed and the correlation length can only be deduced by an observed lack of intensity in the transverse diffuse scatter.

When soft x-rays are used, the Bragg peak occurs at a sample angle approaching 30°. The angular difference, δ, is now 15°, and lateral length scales down to a few tens of Angstroms can now be directly probed. Thus, in the soft x-ray regime, correlation length scales commonly observed in these sputtered systems are easily accessed.

Figure 8.40 shows scans through the structural Bragg peak taken at hard and soft energies. The difference in the range of q_x that is probed is immediately apparent.

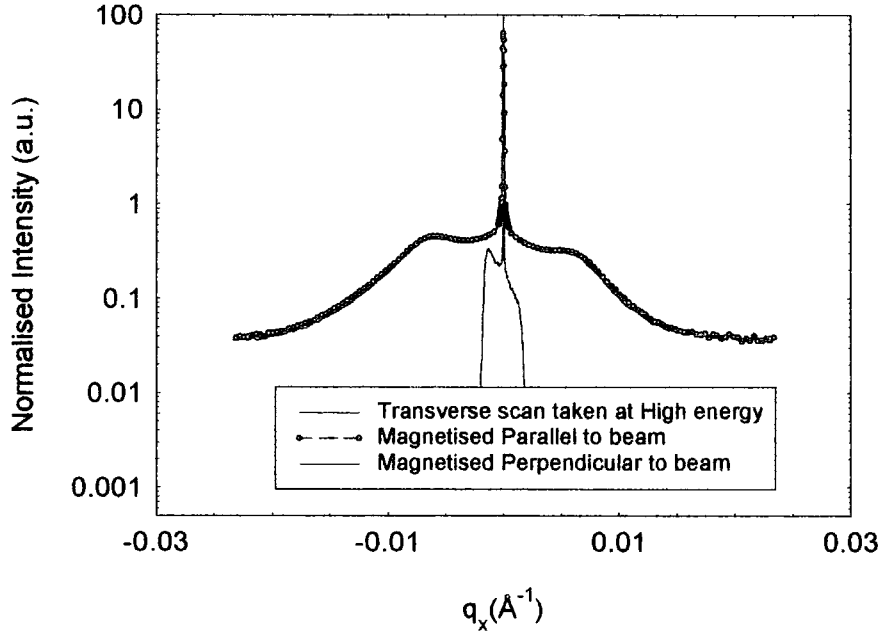

Figure 8.40: Transverse diffuse scans through the structural Bragg peak for hard x-ray energies (green) and soft x-ray energies (red and blue)

It is interesting to note that there is no dependence on the magnetic peak intensity on the direction of the magnetic moment, confirming that there is no ferromagnetic component in these samples. Figure 8.40 also shows that the diffuse scatter observed

by the soft x-rays is peaked either side of the specular condition. This occurs at length scales of the same order as the assumed lateral correlation length (approximately the grain size). This feature was present in all the samples studied. In the standard 2 circle diffractometer geometry these features can never be probed using hard x-rays. A series of scans was carried out over the structure peak and a full reciprocal space map (FRSM) was produced to investigate these features more fully.

The FRSM of the structure peak is shown in figure 8.41. The data is not symmetric due to a high level of noise present in the scans at high sample angles, which resulted in the useable data being truncated. This noise was later identified as a wiring problem and was corrected by the time the scan in figure 8.40 was taken. There was, however, insufficient beam time available to repeat the reciprocal space map.

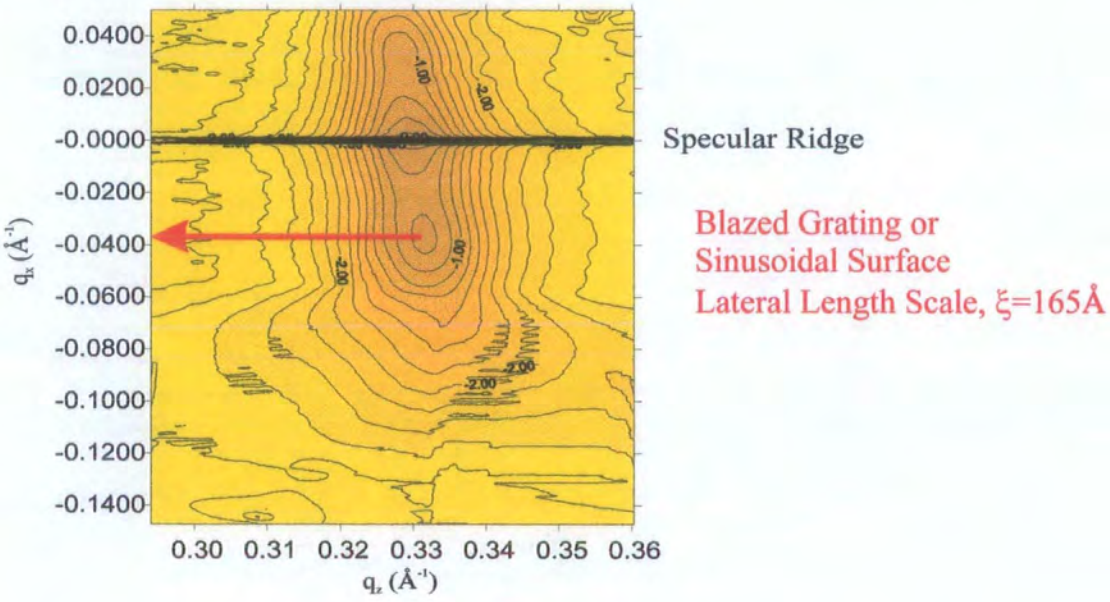

Figure 8.41: A full reciprocal space map across the structural Bragg peak form sample 2

From the FRSM it is clear that the enhancement of the diffuse scatter is peaked not only in q_x, but also in q_z. The fact that the feature is peaked at the same q_z value as the structure peak means that it is a feature that is replicated from layer to layer, i.e. it is correlated. Enhancements of the diffuse scatter either side of the specular ridge originate from either a Blazed grating, or a sinusoidal interface.

A sinusoidal interface is similar to a surface with a long length scale roughness which is what is commonly measured as the lateral correlation length. It could be that we are directly measuring the lateral correlation length here. Indeed, a blazed grating effect originating from the substrate could define the length scale over which the surface can be defined as being fractal, and in a highly correlated system this feature would be present over many bi-layer repeats. Figure 8.41, also shows that the roughness is correlated over all length scales up to this point. This is evidenced by an almost constant intensity of the diffuse scatter as a function of q_x.

It was also possible to measure the magnetic roughness. The fact that there was such a strong diffuse peak in the off-specular scatter (figure 8.40) at the magnetic peak position suggests that the magnetic roughness is also highly correlated. Magnetic roughness has been evidenced in other systems [39,40], but this is the first direct evidence of correlated, magnetic roughness. A careful inspection of figure 8.40 also shows that the extension in q_x, is different for the magnetic and structural correlated roughness. This is further evidenced by a comparison of the full reciprocal space maps of the magnetic and structural diffuse scatter around their respective Bragg peaks. Figure 8.42 compares the magnetic and structural FRSMs over the same q_x range.

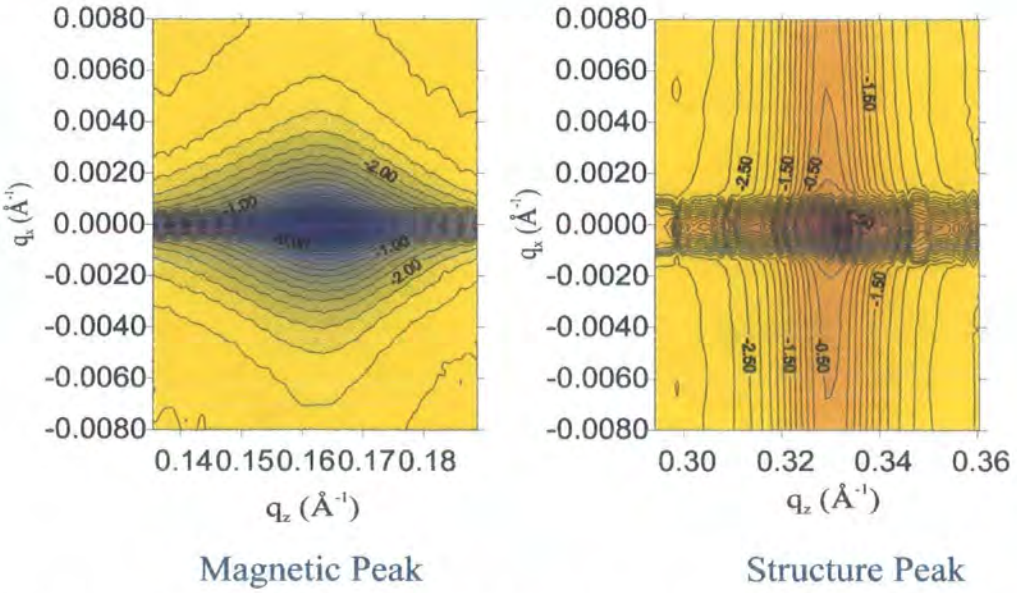

Figure 8.42: The FRSM of the diffuse scatter around the magnetic and structural Bragg peaks in sample 2, magnetised parallel to the beam.

It is immediately obvious that whilst the structural roughness is correlated over all the length scales probed, the magnetic roughness is only correlated over long length scales. Slight differences were observed between the structural and magnetic roughness length scales in references 39 and 40, but they were small compared with the present findings.

When the sample was magnetised orthogonally to the x-ray beam, the intensity of the magnetic peak increased. A FRSM was also taken when the sample was magnetised in this configuration. Figure 8.43 shows a comparison of the two FRSMs with the same intensity scale.

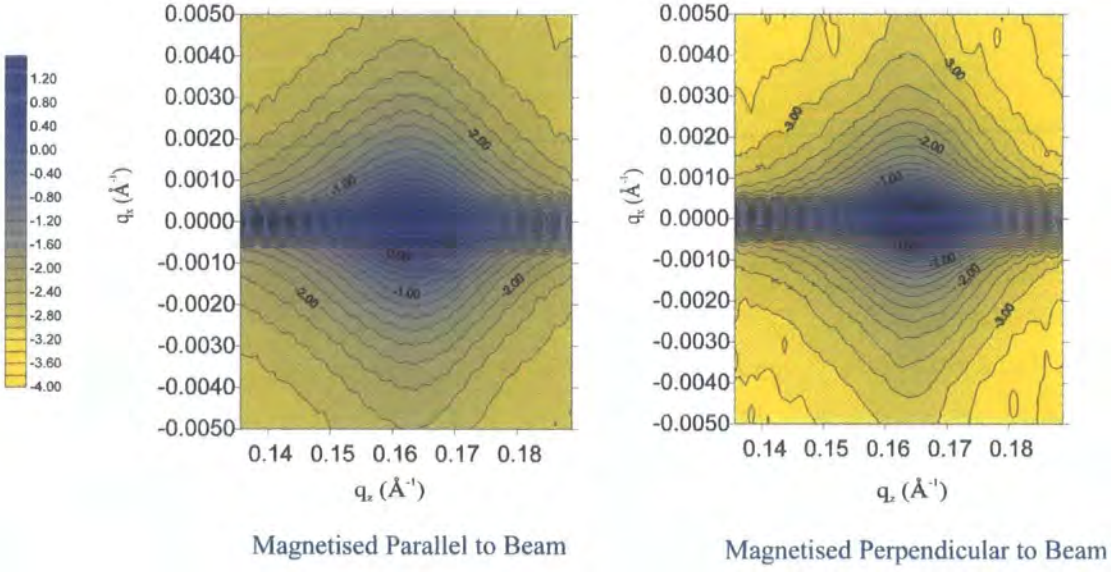

Figure 8.43: A comparison of the zero-field magnetic FRSM for the two orthogonal magnetisation directions.

It is clear that the increase in magnetic peak intensity is accompanied by a sharpening of the magnetic peak in q_x. This corresponds to correlations only being present over longer length scales. The same effect was observed for sample 1, and figure 8.44 shows the transverse scan taken through the magnetic Bragg peak, under the two orthogonal magnetisation directions.

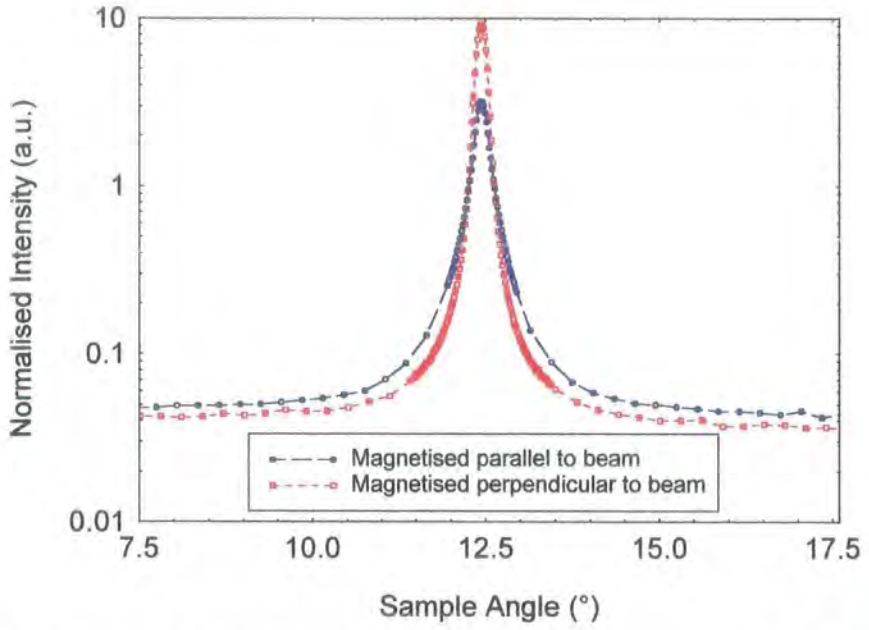

Figure 8.44:Zero field transverse scans through the magnetic peak for Sample 1

A measure of the magnetic correlation length can be made by fitting the curves in figure 8.44. The line shape should consist of two components, a central peak which is the instrument resolved specular ridge, and a broader diffuse component. The correlation length is then the inverse of the FWHM of the diffuse component. Due to the large lateral correlation length, and the poor resolution of the instrument, it has not been possible to deconvolve the two curves totally successfully. The current best fits give a magnetic correlation length of the order of 11,000 ± 3000Å when the sample is magnetised along the beam direction, and 14,000 ± 3000Å after the field was applied orthogonally to the x-ray beam.

Although it was not possible to pass large currents through the electromagnet for long periods of time, it was possible to conduct experiments whilst a small field was applied. Figure 8.45 shows the transverse diffuse scans taken through the magnetic peak whilst a field was being applied orthogonally to the x-ray beam for samples 1 and 2. In agreement with the magnetisation studies, a slight change in the intensity of the magnetic peak is observed. The peaks are also seen to become sharper in the tails of the diffuse peak

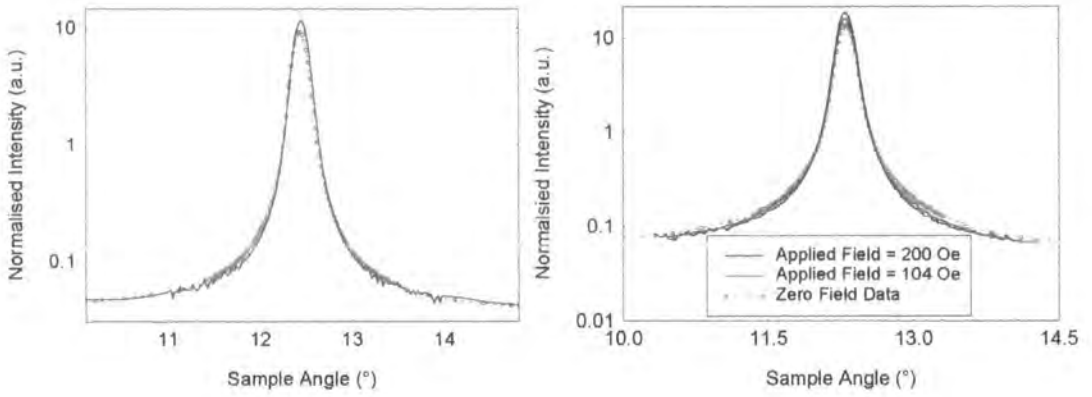

(a) (b)

Figure 8.45: Transverse scans taken through the magnetic peak with a field applied orthogonal to the x-ray beam. For sample 1 (a) and Sample 2 (b)

The lateral magnetic correlation length was seen to be of the order of 1μm. This is the length scale which corresponds to the magnetic ripple length scale that was observed in the TEM. Figure 8.46 is a reproduction of the TEM micrograph corresponding to zero applied field.

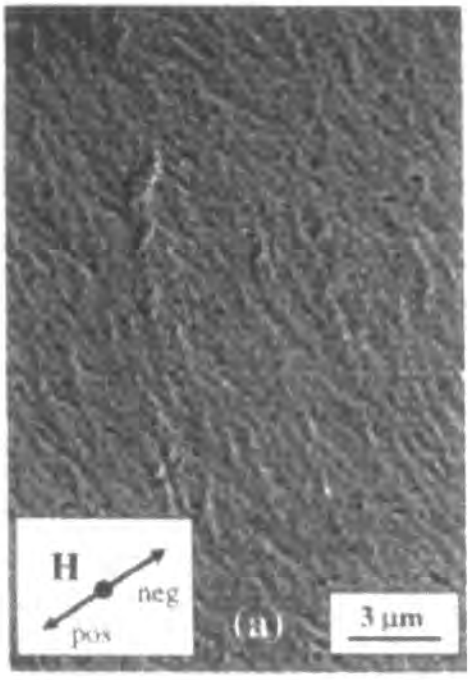

Figure 8.46: TEM micrograph taken in zero field, along the magnetisation sequence taken along the nominally easy axis [36].

Although the magnetic ripple is weak, it can be seen that its length scale is approximately the same as that observed by the x-rays.

8.6 Summary

The effects of gas contamination have been seen to be particularly important in obtaining good GMR. The largest effect on the magneto-transport measurements was to induce bi-quadratic coupling when the contamination was placed in the copper spacer layer. Structural characterisations were attempted on the samples, and although they showed the samples to be of a good quality no differences between them could be observed.

The samples were then studied using soft x-ray reflectivity and the structural and magnetic super-structure were investigated. It was shown how it was possible to conduct structural characterisations using soft x-rays. Although these again failed to show significant differences between the samples, large enhancements of the diffuse scatter were observed for length scales similar to the grain size.

The magnetic super-structure has been evidenced by the use of linearly polarised x-rays. The energy and field dependence of the magnetic peak have been investigated. The energy dependence of the peaks is as expected from the theory. A theory for the magnetic dependence of the peak has been put forward based on results from a TEM investigation. It has also been possible to investigate the structural/charge and magnetic roughness correlations. It has been observed that the two types of roughness are correlated over very different length scales. The structural roughness is correlated over all the length scales probed, whilst the magnetic roughness is only correlated over distances of approximately 1μm. These results are in marked contrast to previously reported findings, but the presence of a magnetic ripple was not reported in these works.

References from Chapter 8

1 Samples courtesy of Dr. C.H. Marrows, University of Leeds

2 C.H. Marrows, *Ph. D. Thesis*, University of Leeds, (1997)

3 C.H. Marrows, R. Loloee, B.J. Hickey, *J. Magn. Mag. Mat.*, **184**, *137-144*, (1998)

4 Reproduced from C.H. Marrows, *Ph. D. Thesis*, University of Leeds, (1997)

5 K. Kagawa, H. Kano, A. Okabe, A. Suzuki, K. Hayashi, *J. Appl. Phys.* , **75** (10), *6540-6542*, (1994)

6 F. Yoshizaki, T. Kingetsu, *Thin Solid Films,* **239**, *229-239*, (1994)

7 J.G. Zhao, K. Takanashi, Y. Obi, H. Fujimori, *Materials Transactions, JIM*, **36** (6), *712-718,* (1995)

8 C.H. Marrows, B.J. Hickey, M. Malinowska, C. Mény, *IEEE Trans. Mag.,* **33** (5:2), *3673-3675*, (1997)

9 C.H. Marrows, *Ph. D. Thesis*, University of Leeds, (1997)

10 C.H. Marrows, B.J. Hickey, Submitted to Phys. Rev. B.

11 S. Young, B. Dieny, B. Rodmacq, J. Mouchot, M.H. Vaudaine, *J. Mag. Magn. Mat*, **162**, *38-42*, (1996)

12 C.H. Marrows, *Ph. D. Thesis,* University of Leeds, (1997)

13 M. Rührig, R. Schäfer, A. Hubert, R. Mosler, J.A. Wolf, S. Demokritov, P. Grünberg, *Phys. Stat. Sol. A*, **125**, *635-656*, (1991)

14 V. Chakarian, Y.U. Idzerda, H.-J. Lin, C. Gutierrez, G.A. Prinz, G. Meigs, C.T. Chen, *Phys. Rev. B.*, **53** (17), *11313-11316*

15 Reproduced from C.H. Marrows, *Ph. D. Thesis,* University of Leeds, (1997)

16 Data recorded using the SQUID system at Michigan State University by C.H. Marrows

17 X-Ray Diffraction in Crystals: Imperfect Crystals and Amorphous Bodies, *A. Guinier*, **Dover Publications Ltd. (New York)** (1994)

18 *Private communication*, ISIS Facility, Rutherford Appleton Laboratory

19 J. Kerr, *Phil. Mag.*, **Series 5, 3** (19), *321-343*, (1877)

20 X-ray Magnetic Circular Dichroism: Basic Concepts and Theory for 3D Transition Metals, Proceedings NATO Advanced Study Institute - "New Directions

in Research with 3rd Generation Soft X-Ray Synchrotron Radiation Sources", *J. Stöhr, Y. Wu*, **Kluwer Academic Publishers (NL)**

21 S.P. Collins, *Data presented at X-rays in Magnetism Workshop*, Daresbury Laboratory, (1998). Paper under review

22 C. Vettier, *J. Magn. Mag. Mat.*, **129**, *59-65*, (1994)

23 D. Gibbs, D.R. Harshman, E.D. Isaacs, D.B. McWhan, D. Mills, C. Vettier, *Phys. Rev. Lett.*, **61**, *1241*, (1988)

24 J.P. Hannon, G.T. Trammell, M. Blume, D. Gibbs, *Phys. Rev. Lett.*, **61**, *1245*, (1988) AND *Phys. Rev. Lett.* **62** *2644(E)* (1989)

25 F. de Bergevin, M. Brunel, R.M. Galéra, C. Vettier, E. Elkaïm, M. Bessière, S. Lefèbvre, *Phys. Rev. B.*, **46** (17), *10772-10776*, (1992)

26 Neutron and Synchrotron Radiation for Condensed Matter Studies Vol. 1, *Eds. J. Baruchel, J.-L. Hodeau, M.S. Lehmann, J.-R. Regnard, C. Schlenker*, **Springer-Verlag**, *261-269*, (1993)

27 C. Kao, J.B. Hastings, E.D. Johnson, D.P. Siddons, G.C. Smith, G.A. Prinz, *Phys. Rev. Lett.*, **65** (3), *373-376* (1990)

28 C.-C. Kao, C.T. Chen, E.D. Johnson, J.B. Hastings, H.J. Lin, G.H. Ho, G. Meigs, J.-M. Brot, S.L. Hilbert, Y.U. Idzerda, C. Vettier, *Phys. Rev. B.*, **50** (13), *9599-9606*, (1994)

29 V. Chakarian, Y.U. Idzerda, C.-C. Kao, C.T. Chen, *J. Mag. Magn. Mat.*, **165**, *52-55* (1997)

30 J. W. Freeland, V. Chakarain, Y.U. Idzerda, S. Doherty, J.G. Zhu, J.-H. Park, C.-C. Kao, *Appl. Phys. Lett.*, **71** (2), *276-278*, (1997)

31 M. Sacchi, C.F. Hague, E.M. Gullikson, J.H. Underwood, *Phys. Rev. B*, **57** (1), *108-111*, (1998)

32 *http://www.dl.ac.uk/SRS/SXR/highlights/SoXMaS/*

33*http:// www.dl.ac.uk/SRS/SXR/1-1hp/1-1hp.html*

34 J.M. Tonnerre, L. Sève, D. Raoux, G. Soullié, B. Romacq, P. Wolfers, *Phys. Rev. Lett.*, **75** (4), *740-743*, (1995)

35 The Physical Principles of Magnetism, *A.H. Morrish*, **John Wiley & Sons, Inc. (New York)** (1965)

36 C.H. Marrows, B.J. Hickey, M. Herrman, S. McVitie, J.N. Chapman, *In Press*

37 C. Teihcet, J.F. MacKay, D.E. Savage, M.G. Lagally, W. Brohl, P. Wagner, *Appl. Phys. Lett.*, **66** (18), *2346-2348*, (1995)

38 D.E. Savage, Y.-H. Phang, J.J. Rownd, J.F. MacKay, M.G. Legally, *J. Appl. Phys.*, **74** (10), *6158-6164*, (1993)

39 J.F. MacKay, C. Teichert, D.E. Savage, M.G. Lagally, Phys. Rev. Lett., 77 (18), 3925-3927

40 G. Srajer, C. Nelson, C. Venkataraman, J. Lang, H. Hasizume, N. Ishimatsu, O. Sakata, T. Iizuka, N. Hosoito, K. Namikawa, T. Iwazumi, S. Sinha, *Data presented at X-rays in Magnetism workshop*, Daresbury Laboratory, (1998) and H. Hashizume, N. Ishimatsu, O. Sakata, T. Iizuka, N. Hosoito, K. Namikawa, T. Iwazumi, G. Srajer, C.T. Venkataraman, J.C. Lang, C.S. Nelson, L.E. Berman, *Physica B*, **248**, *133-139*, (1998)

Chapter 9

X-ray Scattering Studies from Spin Valve Structures

9.1 Introduction

In this chapter, the results of an experiment designed to elucidate the thickness of the non-magnetic layer in a spin valve will be presented. These results have been obtained using hard x-rays. The structure of the chapter is such that an introduction to spin valves and their coupling is presented in section 9.2. The samples are introduced in section 9.3, prior to an investigation using grazing incidence x-ray reflectivity. An introduction on x-ray fluorescence is given in section 9.4. This leads onto a discussion about grazing incidence fluorescence (section 9.5). Grazing incidence x-ray fluorescence is discussed in section 3.6. A structural analysis of the samples using grazing incidence fluorescence is then presented in section 9.7, and the chapter is concluded in section 9.8.

9.2 An Introduction to Spin Valves

Spin valves form a subset of the much wider group of layered systems which exhibit giant magneto-resistance (GMR). Where they differ from the samples previously studied in this thesis is that they are made up of two uncoupled ferromagnetic layers, separated by a non-magnetic spacer layer. The criteria for the layer thicknesses are the same as for the more conventional Cu/Co or Fe/Cr multilayers; namely that the thickness of the layers must be smaller than, or of the same order as the mean free path of the electron. Additionally spin valves require that the thickness of the non-magnetic layer is such that the ferromagnetic layers are decoupled (although this criterion is rarely realised in full for most systems). We have already seen that one of the basic requirements for the GMR effect is an anti-parallel alignment of the spins in the ferromagnetic layers. All spin valves realise this

anti-parallel alignment by the exchange biasing of one of the ferromagnetic layers. This is achieved by bringing one of the ferromagnetic layers into contact with an anti-ferromagnet and cooling the system below the Néel temperature of the antiferromagnet, or by growing the sample in an external field whose strength is enough to saturate the ferromagnetic layer, typically a few tens of Oersted.

The preferred method to achieve anti-ferromagnetic biasing in spin valves is to grow them in an external field using a sputtering system. This induces a unidirectional anisotropy for the pinned layer, H_{EB}, along the external field direction which can be described by a real energy density term, J_{EB} [1] or in terms of an anisotropy constant, K_p [2]. This anisotropy results in a shift of the magnetisation loop of the pinned ferromagnetic layer to a higher field.

The antiferromagnetic coupling here is assumed to be caused by a surface interaction between the ferro and anti-ferromagnetic layers. Recent work by Gökemeijer et. al. [3] suggested that this interaction might extend over much larger distances. However, repeat experiments performed by C.H. Marrows [4] whereby a non-magnetic material is deposited at the interface between the ferro and antiferromagnetic layers suggests that the interaction distance is extremely small and confined to the interface region. Although the biasing is predominantly caused by interface interaction, experimental evidence [5] shows that there is a dependence on the biasing energy with the thickness of the antiferromagnetic layer. The exact value of antiferromagnetic layer thickness for which the biasing energy saturates is dependent on the material used for the AF layer, although it is typically tens of Ångstroms.

The magnetisation loops for a spin valve structure, taken along the anisotropy direction, will therefore show a stepped arrangement. The magnetisation of the unpinned ferromagnetic layer will switch direction on application of a field greater than the coercive field of the free layer. The pinned layer will only switch when a field greater than the biasing field is applied. The resistance will also change in the same way. For samples which are initially ferromagnetically coupled through the

spacer layer, a sharp increase in resistance will occur when the spins become anti-parallel. The resistance will then reduce to its original value once the pinned layer flips, and the spins return to a parallel alignment. For a commercial device, the magnitude of the coercive field is of as much importance as the resistance change. An experimental room temperature MR loop [6] for a typical spin valve is shown in figure 9.1. A sharp increase in resistance is observed when the spins become anti-parallel after a field greater than the coercive field is applied. The original parallel alignment returns after the biasing field is applied, and the MR returns to its original value.

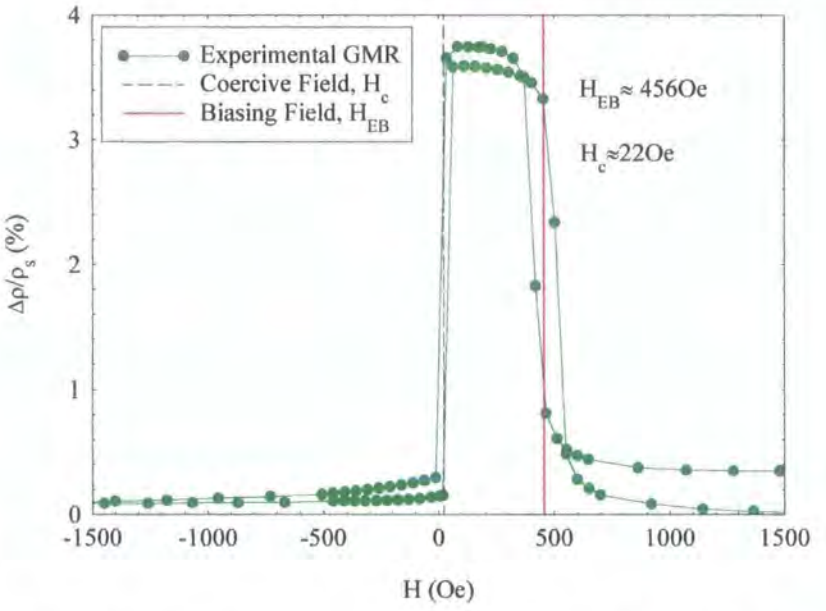

Fig 9.1 Magnetisation loops from a typical spin valve [6]

The typical structure of a spin valve is therefore, substrate/Ferro/Non-magnetic/Ferro/Anti-Ferro. Although these structures do not give as high GMRs as Cu/Co multilayers, their resistance changes are much higher than materials that are currently used in magneto-resistive recording. Typical values for the GMR in spin valve samples are 4-6% [1,7]. The basic structure outlined above was the first spin valve developed by Dieny et. al. [6], and is defined as a top spin valve. Due to the large number of possible materials that can be used in manufacturing spin valves, it is sometimes advantageous to grow the spin valve in reverse, i.e. with the anti-

ferromagnetic layer deposited on the substrate, a bottom spin valve. The more basic spin valve layouts are shown in figure 9.2:

Figure 9.2: The basic spin valve structures; (a) Top spin valve, (b) Bottom spin valve and (c) Interface engineered spin valve

The most common material used for the ferromagnetic layer is permalloy, $Ni_{80}Fe_{20}$. This is favoured because of its soft magnetic behaviour and ability, therefore, to switch the unpinned layer at extremely low fields. The other material that is commonly used for high GMR structures is cobalt. The choice of the non-magnetic spacer layer is determined by matching the conduction bands of the ferromagnetic layer with those in the spacer layer. As in the case of the GMR multilayers this restricts the choice to the noble metals; Cu, Ag and Au. Copper is the preferred spacer material due to the close lattice parameter matching between copper and the permalloy layer. The original choice for the anti-ferromagnetic layer was the gamma phase of FeMn - $Fe_{50}Mn_{50}$. Again an additional benefit of FeMn is its close epitaxial relationships with the Cu and NiFe layers below (γ-FeMn: a_0=3.63Å, Cu: a_0=3.61Å and NiFe a_0=3.57Å). The normal growth mode for $Fe_{50}Mn_{50}$ is the alpha phase, but it is possible to stabilise the gamma phase up to a few tens of nanometres if the crystallinity is good [1]. Typically this is achieved by depositing the spin valve on a buffer layer. Tantalum is the most widely used material, and for thicknesses in the range 75 to 100Å produces strongly (111) textured films [8]. Other crystalline texture can be induced by changing the substrate or buffer layers. In order to protect the surface of the spin valve from oxidation or other damage, a thin surface layer of the same material as the buffer layer is typically used. Work has also been carried out with nickel oxide as the antiferromagnet, but elevated temperatures are required for its growth and so it is usually the first layer to be deposited and hence a bottom spin valve results

An important factor in spin valve structures is the relative layer thicknesses. The value of the MR that is found in spin valve systems generally varies with the thickness of the various layers and most importantly that of the non-magnetic spacer layer. The minimum thickness of the non-magnetic layer is typically between 20Å for copper and 50Å for silver [9]. In layers thinner than this, a large number of pin-holes inevitably develop through the spacer layer causing the ferromagnetic layers to couple strongly. The magneto-resistance falls as the layer thickness increases. This is due to two factors. Firstly, as the non-magnetic layer thickness increases there is an increase in the scattering of the conduction electrons. Secondly, more of the current is shunted through this layer [9]. Dieny [9] introduced a phenomenological law to describe the MR as a function of the non-magnetic layer thickness

$$\frac{\Delta\rho}{\rho}(t) = A\frac{\exp\left(-t/l\right)}{1+\left(t/t_o\right)} \qquad [9.1]$$

where A is a constant proportional to the ferro and non-magnetic materials used, l is proportional to the mean free path of the electrons within the spacer layer, t_o is an effective thickness related to the shunting in the other layers in the structure and t is the thickness of the spacer layer. Thus to maximise the GMR, the spacer layer should be as thin as possible, but greater than the minimum thickness required for decoupling the ferromagnetic layers.

However, the coupling strength is not only defined in terms of the non-magnetic spacer layer, there is an additional term relating to the structure of the interfaces. Scanning Tunnelling Microscopy (STM) images from a spin valve of the type NiFe/Co/Cu/Co/NiFe/FeMn deposited on glass show that the layers have a tendency to form wavy humps, with wavelengths of approximately 10nm [10]. Atomic force microscopy studies on Si/NiFe/NiO [11] also reported a similar

behaviour. This wavy surface is an ideal candidate for Néel's orange peel coupling. Orange peel coupling is also supported by Egelhoff et. al. [12], who show that by using lead, gold or indium as a surfactant at the interfaces reduces these humps. As a direct result of this reduction in the wavy nature of the interface, the coupling reduces by a factor of 3. Thus, there is an additional term relating the coupling, and hence the coercivity, of spin valve systems to Néel's orange peel coupling. This orange peel coupling does not effect the magnitude of the GMR, but reduces the field at which the alignment of the ferromagentic layers change.

In previous chapters we have tried to relate the structural and interface morphology to the GMR of the materials under examination. The coupling mechanisms behind spin valve structures are now well understood and easily measured. It is also relatively easy to engineer different interface morphologies, either by varying the sputtering pressure or by the addition of a new ferromagnetic material. No additional steps in the magnetisation loops of a spin valve result from the addition of an additional ferromagnetic layer such as cobalt as in an interface engineered spin valve (figure 9.2), because the coupling between the two adjacent ferromagnetic layers is so large that they always flip together. Parkin [13] showed that the addition of a few monolayers of Co at the interface between the NiFe and Cu in a top spin valve biased with FeMn increased the GMR of the spin valve by a factor of 2. This suggests that the MR is proportional to spin scattering from magnetic states confined to a region of 1.5-3Å from the interface between the ferromagnetic and non-magnetic layers. An alternative explanation is that the addition of cobalt at the interfaces reduces the amount of interdiffusion between the copper and permalloy layers, and thereby increases the effective thickness of the spacer layer.

The magneto-resistance of bottom spin valves made with NiO and Co and exposed to O_2 show significant increases in GMR up to 17% [14]. This large increase in GMR is offset by an increase in the coercivity of the free layer from 35 Oe to 54 Oe. Although the coercivity is large, (common for spin valves with NiO as the

antiferromagnetic layer) this example shows the large range of MR values that can be achieved by the use of different materials and growth environments.

The development and improvement of spin valves has been driven by commercial applications, and, as a result, most of the analysis of these materials done to date has been limited to consideration of the magneto-transport or coupling energy factors. There have been very few reported attempts at structural analysis in the literature, apart from direct methods of altering the interface as described above. Much of the structural analysis has been undertaken using STMs [1,15] or AFMs [10]. Attempts have been made to characterise spin valves using x-ray methods, notably by grazing incidence x-ray reflectivity [16,17].

The rest of this chapter is devoted to a structural investigation of two spin valves using grazing incidence x-ray techniques. The use of reflectivity as a possible method of structural characterisation is examined. The use of grazing incidence x-ray fluorescence (GIXF) is explored and in conjunction with the reflectivity results a structural model is proposed for two spin valve samples.

9.3 Structural Investigation of Spin Valve Systems: The Samples

The samples used in the experiments detailed in this chapter were of a basic top spin valve structure, namely NiFe/Cu/NiFe/FeMn. The samples were all prepared in the same vacuum cycle in a fully automated sputtering machine at the University of Leeds by C.H. Marrows. The base pressure of the system was ~$2.3*10^{-8}$ Torr, and the Ar pressure during deposition was 5.0 mTorr. The targets were not calibrated, but the growth rate for all the materials was of the order of 4Å/s and the deposition times were controlled to produce samples which were nominally:

Si/Ta(120Å)/$Ni_{0.8}Fe_{0.2}$(40Å)/Cu(X)/$Ni_{0.8}Fe_{0.2}$(30Å)/$Fe_{0.5}Mn_{0.5}$ (40Å)/Ta(20Å)

with X of 20 and 60Å. The sample with X=20Å was designated sample 1 and sample 2 corresponds to X=60Å.

An increase in the thickness of the non-magnetic spacer layer should lead directly to a reduction in the GMR, as described above in equation 9.1. To investigate this, the magneto-transport measurements were undertaken at room temperature [18] and the GMR fell from 3.7% for sample 1 to 2.2% for sample 2. The exchange fields were measured by examining the shift in the magnetisation loop of the pinned layer as detailed above. They where similarly high for both samples: 460 Oe for sample 1 and 450 Oe for sample 2. The experimental GMR trace is shown in figure 9.1.

An attempt to characterise the structure of the samples was then attempted to confirm that the observed changes in the MR were as a direct result of a change in the thickness of the non-magnetic spacer layer.

9.4 Structural Investigation of Spin Valve Systems: X-ray Reflectivity

Like the Cu/Co multilayers investigated in previous chapters, the scattering factor difference in spin valve systems between the NiFe and Cu layers, as well as, between the FeMn and NiFe layers is extremely small. Whereas it is possible to separate and enhance the scatter from a Cu/Co multilayer by the use of anomalous dispersion (chapter 5), this is not possible in a spin valve structure because of the low number of interfaces. If roughness is correlated through a multilayer then, due to coherent scatter from all the interfaces in the multilayer stack, off specular Bragg peaks are formed and anomalous dispersion can then be used to good effect. In the case of spin valves, there is no regime where constructive interference can occur, and the effects of anomalous dispersion are negligible. Thus, as the scattering factor varies monotonically across the Periodic Table, the scattering factor difference between the *3d* elements is very low and the *3d* elements appear as a single 'block' in reflectivity experiments. This is clearly shown in figure 9.3 where, in a simulated structure, all the *3d* elements in the spin valve block are replaced by a single copper

layer of the same thickness. The simulations are compared at and away from the Cu absorption edge to highlight the negligible effect of anomalous dispersion.

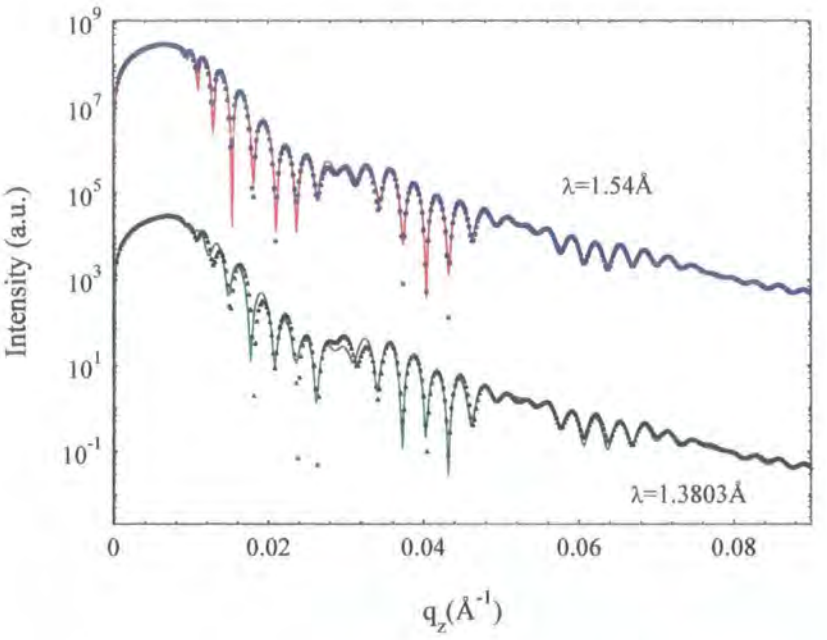

Figure 9.3: Simulated reflectivity profiles from a spin valve structure Si:Ta(50Å)/NiFe(75Å)/Cu(20.4Å)/NiFe(47Å)/FeMn(99Å)/Ta(38.8Å)/Ta_2O_5(26.4Å) Upper curves at λ=1.54Å and lower curves correspond to the Cu absorption edge (λ=1.3803Å). Lines correspond to replacement of all the *3d* elements by Cu

The structure in figure 9.3 is the same as that simulated in reference [16]. In this reference, the reflectivity profile from a spin valve was fitted using an least-squares approach, with an added parameter for the diffuse scatter. From the resulting excellent fit, parameters for all the *3d* layers were deduced, but as is clear from figure 9.3 there is a considerable degree of doubt over the validity of a model which claims to readily distinguish between the *3d* layers on the basis of the fit alone, and the conclusion in reference [16] is clearly wrong.

It is not only in x-ray reflectivity that difficulties arise when trying to separate the *3d* layers in spin valve structures. In HR-XTEM it is also impossible to distinguish between the *3d* layers [1]. Additional complications arise when the binary phase diagrams of the constituent materials are considered. It is well known that Cu readily diffuses into NiFe layers. This should cause a reduction in the GMR,

which is temperature dependent, due to an increase in the scattering of electrons from the paramagnetic NiFeCu alloy that is formed at the interface [19]. There is also, however, no direct measurement possible using HR-TEM of the Ta/NiFe interface. The phase diagrams of TaNi and TaFe are reproduced below:

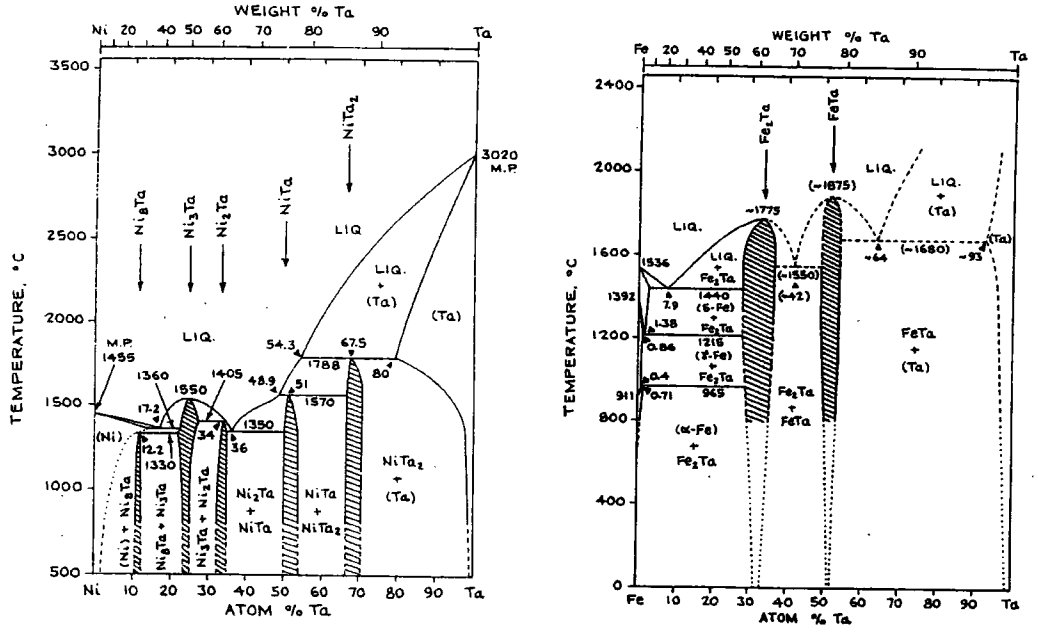

(a) (b)

Figure 9.4: The binary phase diagrams of Ta/Ni (a) and Ta/Fe (b) [20]

It is clear that there are many possible alloys that can form at the interfaces not only of Ta/NiFe but also NiFe/Cu. The alloying of the Ta with its adjacent *3d* layers, is not only of concern at the buffer interface, but also at the capping layer interface between the FeMn and the Ta.

We have already seen that reflectivity measurements are insensitive to the NiFe/Cu interface, so much so that if the NiFe layer were to form a completely paramagnetic alloy we would be unable to distinguish it from the indented structure. In the samples studied however, the magneto-transport measurements indicate that diffusion across this NiFe/Cu interface is small and, as such, only a limited amount of the paramagnetic alloy has formed. This example serves to illustrate the difficulties involved in structural refinement from reflectivity data alone.

Furthermore, the magneto-transport measurements are not sensitive to the Ta/NiFe interface, and yet interdiffusion across this interface must be distinguished from the reflectivity if the latter is be an effective tool. Alloying at the Ta/NiFe interface will result in an increase in the apparent roughness of the interface due to an increase in the interface width. As discussed in chapter 5 the reflectivity is only sensitive to the interface width, and in all models this interface width is assumed to be an error function perpendicular to the sample surface.

Reflectivity measurements on samples 1 and 2 were undertaken at Station 2.3 at the SRS. Although the effects of anomalous dispersion are negligible, the wavelength was still tuned to the Cu absorption edge (λ=1.38Å). The reflectivity scans are shown in figure 9.5:

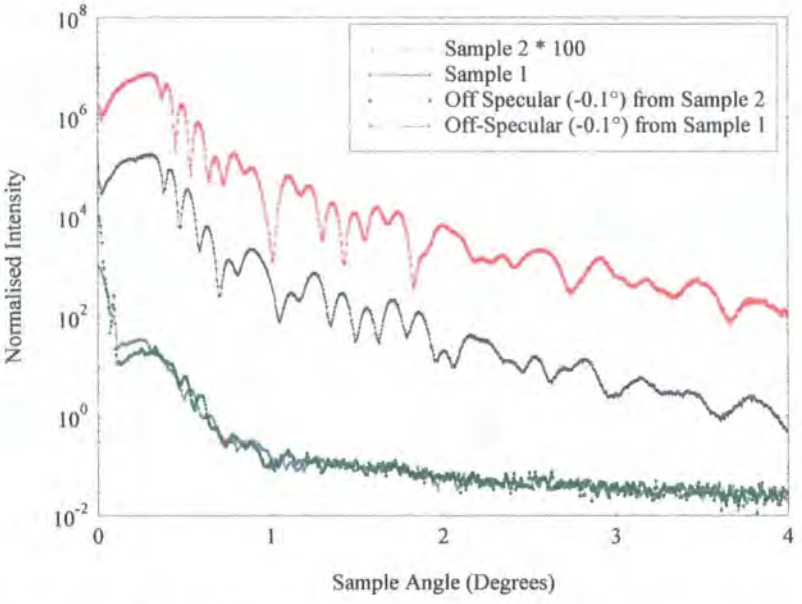

Figure 9.5: Specular and Off-Specular (-0.1°) from samples 1 and 2

From figure 9.5, it is clear that there are similarities between the two samples but, there is no clear difference which can specifically be attributed to a change in the copper layer thickness. There is certainly a change in the Kiessig fringe period, indicating that the total film thickness has increased in sample 2. A modulation

occurs in both curves around a sample angle of 1 degree which is probably due to a beat coming from the oxidised Ta capping layer. A longer frequency period towards higher sample angles is an indication of the thickness of the buffer layer. The fall-off of the reflectivity curve is low, suggesting that the interfaces are smooth. This low roughness can also be inferred from the diffuse scatter. The off-specular scans from the spin valves are also shown in figure 9.5. Apart from the very low intensity, clear fringes are observed at low scattering angles suggesting that the roughness in spin valves is correlated from the substrate surface.

As it proved impossible to separate the *3d* elements, an attempt at fitting the specular reflectivity using a tri-layer structure of Ta/$Fe_{0.5}Mn_{0.5}$/Ta. FeMn was used. Following the work of Huang [16,17], it was decided to allow the Ta to oxidise to the form Ta_2O_5. Unfortunately, it was not possible to fit the specular scatter. As it has proved impossible to obtain detailed information on the *3d* elemental layers in a spin valve system with reflectivity, a new technique was required. In the next section, an introduction to fluorescence techniques and theory is presented with a view to it being used in structural characterisations of spin valves.

9.5 X-ray Fluorescence

Since absorption can only occur when the energy quantum is greater than the energy associated with a transition probability, the absorption as a function of energy shows discontinuous jumps. As the energy is increased, a threshold is reached for a particular transition, and a new channel for absorption opens up, resulting in the discontinuities observed. In between the discontinuities the variation of absorption with wavelength is approximately cubic. This behaviour is illustrated in figure 9.6, where the mass absorption coefficient has been calculated as a function of wavelength for Ta [21]:

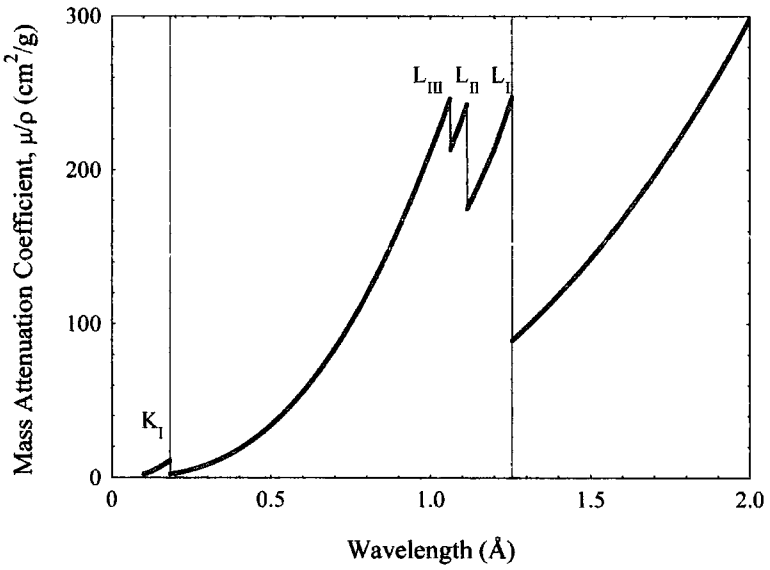

Figure 9.6: The mass attenuation coefficient as a function of wavelength for Ta. The red lines at λ=0.184Å and λ=1.255Å correspond to the K and L absorption edges respectively, as quoted in the International Tables [22]

In an absorption process, the incident energy of the photon, *E*, is transferred to an electron in a particular shell. The electron is then excited into the continuum with an energy $E\text{-}E_{Shell}$ leaving the atom in an excited state with a hole in the shell. The atom has two distinct decay routes; non-radiative decay namely, Auger Emission, and radiative decay, i.e. Fluorescence. A schematic of the absorption process and fluorescence recombination is shown in figure 9.7:

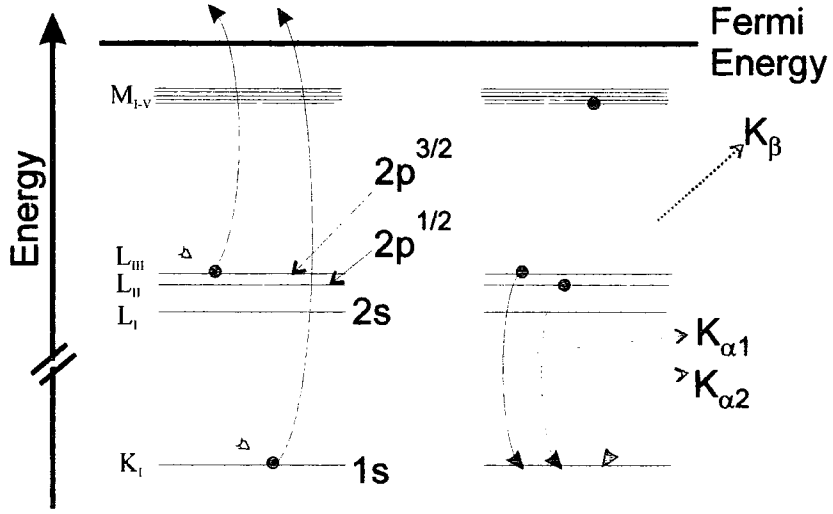

Figure 9.7: The schematic diagram of the absorption process and the fluorescence decay channels.

In the Auger process two electrons are involved; as one electron recombines with a hole in the *1s* state, the resulting energy is used to excite an electron from another *s* shell into the continuum. In contrast to this, in fluorescence the energy released by the recombination of the exciton is emitted as a photon with a characteristic energy. The rate of Auger emission is a constant, α, whereas the emission of fluorescence photons is proportional to the atomic number to the fourth power. The fluorescence rate, ω_k - ratio of the fluorescence yield to the total yield, can therefore be defined as [23]:

$$\omega_k = \frac{\text{Fluorescence Yield}}{\text{Total Yield}} = \frac{Z^4}{Z^4 + \alpha} \qquad [9.2]$$

For the *K* shell, the Auger constant is $1.12*10^6$. The variation of the fluorescence yield with atomic number is shown in Figure 9.8:

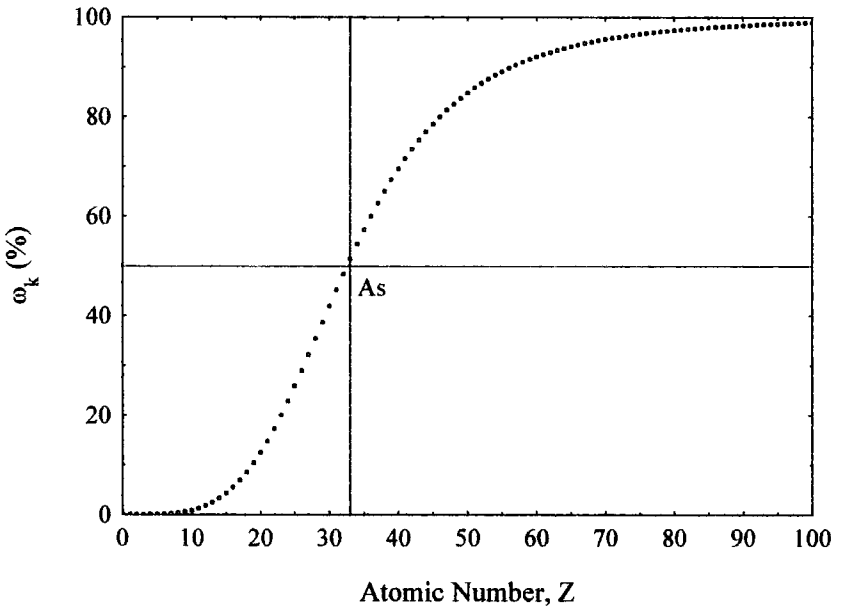

Figure 9.8: Fluorescence yield as a function of Atomic Number, *Z*

For a core hole in the 1s level, the selection rules, $\Delta l = \pm 1$ and $\Delta j = 0, \pm 1$, determine that fluorescence recombination can only occur from *p* shells. The highest transition probability involves the *2p* levels. The *2p* level is split into the *2p½* which has a two-fold degeneracy and the *2p3/2* which has four-fold degeneracy. From figure 9.7, it is clear that the $K\alpha_1$ originates from the *2p3/2* level and the $K\alpha_2$ comes from the *2p½* shell. From these arguments, it may be expected that the ratio of the $K\alpha_1$ to

the $K\alpha_2$ should be 2. Tabulated values of the radiative transition probabilities [24] give the ratio for Fe and Ni to be 1.976 and 1.969 respectively. For the heavier elements, this simple model breaks down and the ratio reduces to 1.616 for Uranium. The ratio of the $K\alpha$ to $K\beta$ is harder to describe in simple terms, but the tabulated ratio between the two for Fe is 7.46 and for Ni is 7.41.

One of the most common uses of x-ray fluorescence in structural measurements on condensed matter systems is in EDAX. Here high energy electrons are bombarded onto the surface to be investigated, and the structural parameters are deduced from the resulting x-ray emissions. The sensitivity in this technique is proportional to the signal to noise ratio. In the geometry of the experiment, the electrons are incident at high angles, so for thin samples there is always a large substrate contribution to the signal. A method to improve the sensitivity both to depth and concentration is to use x-rays as the exciting energy source. Additionally, a geometry is used whereby the x-rays are incident at grazing angles. This is the process known as total reflection x-ray fluorescence, TXRF.

9.5.1 Total Reflection XRF

In TXRF a small amount of material (typically 100 mg) is deposited in the form of a thin sample, or droplet, onto a quartz substrate. If the incident x-ray beam is kept below the critical angle, only the evanescent wave can excite the material and fluorescence from the substrate is substantially lowered. Another advantage of this method is that both the incident and reflected beam can stimulate fluorescence. Unlike EDAX results, the effects of absorption and secondary fluorescence can be ignored due to the thin nature of the sample.

This technique has been used to measure impurities in semiconductors and liquids. Typical relative detection limits are in the ppm range for a few micrograms of material [25]. The fluorescence yield is proportional to the volume sampled, therefore as the penetration depth increases with incident angle, a degree of depth

sensitivity is inherent in TXRF. This angle dependent TXRF can be used to measure the impurity profile at a semiconductor surface [26].

9.6 Grazing Incidence Fluorescence, or Angle Dependent TXRF

Like reflectivity, when the sample becomes more complex with the addition of layers, a more detailed theory is required to predict the fluorescence yield as a function of sample angle. In principle the features in GIXF can be described in similar terms to those found in reflectivity. As the fluorescence yield is proportional to the intensity of the incident wave at any point in the sample, a dependence on the electric field may be expected. If one considers a single layer, the Kiessig fringes in the specular scatter are the direct result of interference between the incident and exit beams. This interference produces so called x-ray standing waves both above and within the sample. Changing the incidence angle causes the nodes and anti-nodes of the standing wave to move through the sample. As reflectivity is primarily concerned with interfaces between media, reflectivity maxima occur when the anti-nodes of the standing wave are incident onto an interface. Information on the layer itself is best studied when the maxima of the x-ray standing wave is in the middle of the layer. Thus, for simple systems, there is a π phase shift between the reflectivity and fluorescence maxima. This is shown in figure 9.9 where the reflectivity and the fluorescence have been calculated for a 200Å layer of Au on Si. The incident wavelength was 1Å, and the Au $L\alpha_1$ line is the fluorescence line that is excited:

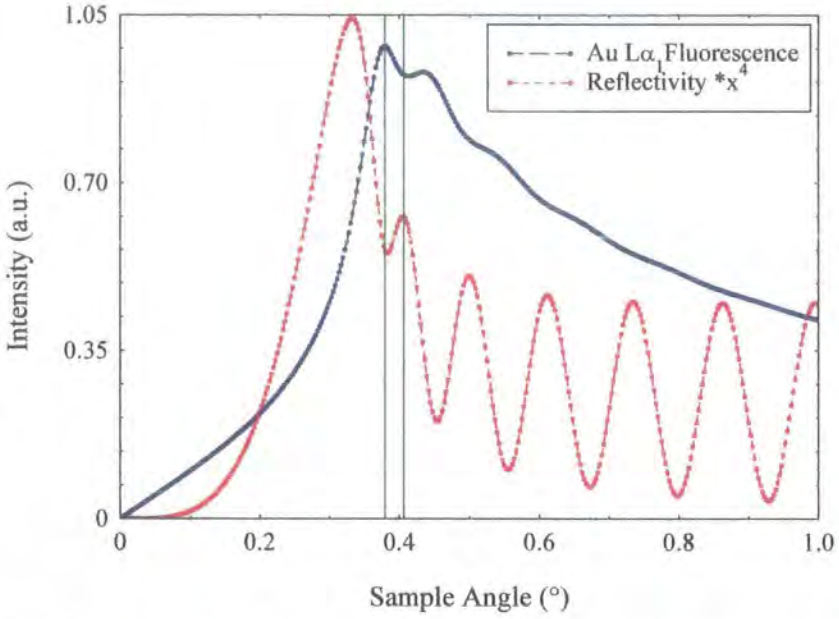

Figure 9.9: Specular reflectivity and the Au $L\alpha_1$ fluorescence calculated for a 200Å Au film grown on Si. The incident wavelength was 1Å.

The intensity of an elemental emission line, can be calculated if the electric field is known throughout the sample. A method for calculating the electric field and hence the fluorescence yield has been developed by de Boer [27,28]. In the thin film limit the intensity of an elemental emission is approximated by:

$$I_{aj} \approx I_o C_{aj} \rho_{aj} \tau_{a\lambda} J_{a\lambda} \omega_a g_a S_1 \exp\left[-\sum \frac{\mu_{na} d_n}{\sin \psi_d}\right] \frac{\left|E_j^t + E_j^r\right|^2}{\left|E_o\right|^2} d_j \qquad [9.3]$$

where I_o is the intensity of the incident radiation, C_{aj} is the mass fraction of element a in layer j, ρ_j is the density of layer j, $\tau_{a\lambda}$ is the photoelectric absorption coefficient for element a at wavelength λ and S_1 is the illuminated area. $J_{a\lambda}$ is the absorption jump factor which is related to the ease of hole creation for a particular incident energy. ω_a is the fluorescence yield as described above in equation 9.2, and g_a is the relative emission rate for the particular fluorescence line considered in preference to other emission lines which could originate from the same hole state. The terms in the exponential refer to the absorption of the created XRF line when leaving the sample: μ_{an} is the linear absorption coefficient for element a in layers n. ψ_d is the angle of exit of the radiation, considered to be well above the critical angle. In most cases, the

detector is positioned vertically above the sample so this angle is $\pi/2$. d is the thickness of the layer/s and E is the amplitude of the plane waves; E^t for the transmitted, E^r for the reflected and E_o for the incident wave. The fluorescence intensity is therefore, not unsurprisingly proportional to $C_{aj}\rho_j d_j$ - the amount of element a in layer j, modulated by the x-ray standing wave.

As in the case for the Yoneda scatter in transverse diffuse scans, the electric field intensity at the critical angle is 4 times that of the incident intensity, and so the fluorescence signal will be peaked at the critical angle, and decay as the angle is increased and the effects of absorption become appreciable. Special cases can occur when a thin film of a low density is grown on top of a high density substrate, such as Si grown on Au [24] or C on Rh [29]. In cases such as these, the maximum of the electric field can be as high as 15 times the incident intensity due to waveguiding through the layer.

With the addition of more layers, the modulations in the fluorescence data caused by the electric field become more complex. The maxima of the fluorescence data for specific elemental lines no longer occur at the critical angle of the sample, but occur when the anti-node of the x-ray standing wave passes through the layer in question. The predominant modulations in electric field are caused by interference resulting from the total stack thickness. As a result of this, when considering buried layers, there are modulations observed that correspond to the total thickness of the sample and not the layer under consideration. It is observed that these modulations in the fluorescence signal are quickly damped, so much so that by a sample angle of 1°, there are usually no oscillations and the intensity is only proportional to the amount of material that is fluorescing. The angular dependence of the fluorescence signal is then proportional to the absorption of the incident and fluoresced radiation.

To demonstrate the usefulness of the technique and to highlight some of features found in GIXF, the Cu $K\alpha$ fluorescence from the structure in reference [16] was simulated, but instead of changing all the *3d* elements to Cu, 10Å from each of

the NiFe layers was removed and added to the Cu layer. The results are shown in figure 9.10:

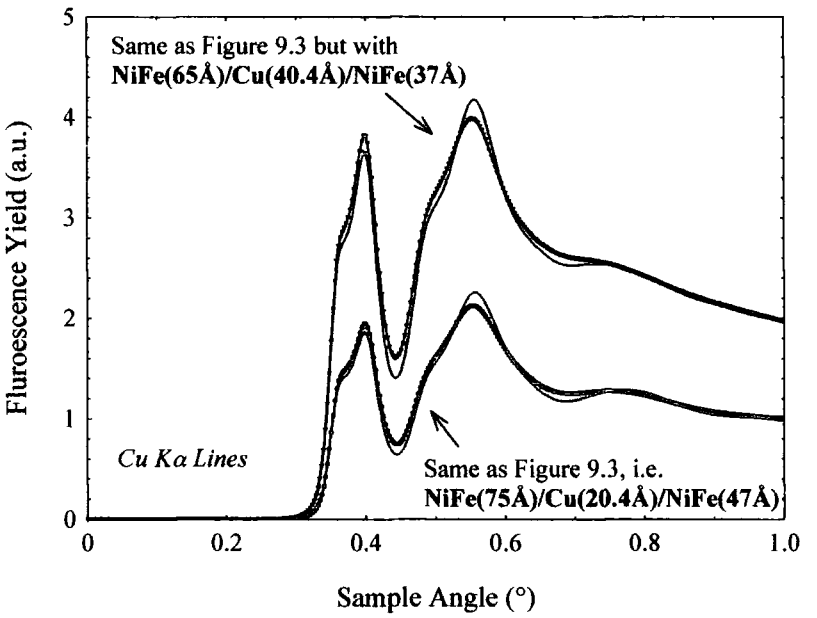

Figure 9.10: Simulation of the structure in Ref. 16. Points correspond to a sample with no roughness at the interfaces, and the lines correspond to a roughness of 10Å per interface.

Immediately apparent is the change in intensity of the Cu $K\alpha$ emission line, showing the sensitivity of the technique to changes in the thickness of one of the *3d* layers. Similar results are obtained if any of the other *3d* elements are considered. The technique, however, is rather insensitive to the roughness of the layers, again demonstrated above. As the copper layer is sufficiently buried below the surface, the evanescent wave cannot excite the Cu fluorescence. Thus the fluorescence yield at low angles is zero and the rise in intensity is sharp as the anti-node moves quickly through the sample as the incident angle is changed.

In order to obtain more detailed information about the samples detailed in section 9.2, and to improve the x-ray reflectivity analysis, grazing incidence fluorescence techniques were employed. This proved to be a far more satisfactory tool in obtaining information about the *3d* elemental layers within the samples.

9.7 Structural Investigation of Spin Valve Systems: Grazing Incidence X-ray Fluorescence

Fluorescence experiments were conducted on station 2.3 at the SRS, with an incident wavelength of 1.3Å, close to the peak flux of the station. The detector was situated above the sample as the reflectivity measurement was made and an additional set of data was recorded. The integrated intensity under the specific peaks from individual layers was then plotted as a function of the incident x-ray beam angle. The code for simulating the grazing incidence fluorescence is already contained in the Bede Scientific GIXS software which we use for simulation of the specular and diffuse scatter.

The elemental emission lines were taken from the International Tables [19]. With the solid state detector it is not possible to separate the $K\alpha_1$ and $K\alpha_2$ and the ratio between them was assumed to be 2:1 and it is thus the weighted average that is recorded in the detector. The weighted averages are tabulated in table 9.1:

Element	Kα	Kβ
Fe	6.399883	7.058447
Ni	7.472856	8.265032
Mn	5.895402	6.490786
Co	6.925674	7.649776
Cr	5.411974	5.947033
Cu	8.041591	8.905791

Table 9.1: Weighted Average of the α and β peaks (keV) for selected Elements

The detector was initially calibrated using an Fe^{55} source, but this calibration was not saved with the text file and another calibration was required prior to fitting. In order to calibrate the detector, the channel number of 'clean' peaks - i.e. peaks

with no other peaks convoluted with them - were recorded for several incident angles and averaged and then plotted against their weighted average energy. The peaks used were Mn $K\alpha$, Fe $K\beta$, Ni $K\alpha$, Cu $K\beta$ from the spin valves and Cr $K\alpha$,Co $K\alpha$ and Co $K\beta$ from a Co-Cr trilayer. A least squared fit was then made on the data, enabling calibrations into keV to be made. The calibration curve is shown below in figure 9.11:

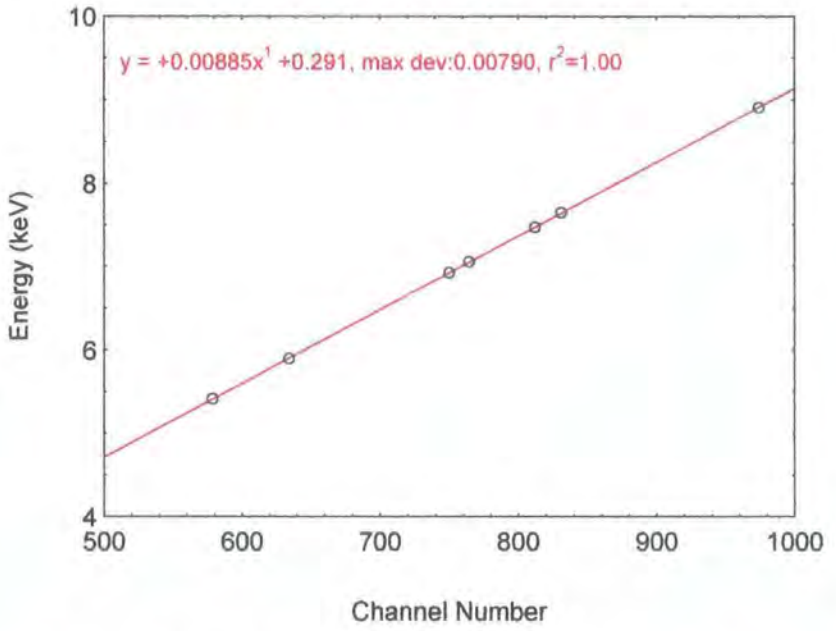

Figure 9.11: Calibration curve for the Solid State Detector

As can be seen in figure 9.12, it is relatively easy to separate out the elemental emission lines from elements adjacent in the periodic table. Prior to fitting, the fluorescence spectra were normalised for counting time and synchrotron beam current. The spectra were fitted by fixing the position of the peak to the values tabulated above and the full width at half maxima (FWHM) for the fitted Gaussians was kept the same for all emission peaks. The inherent low noise of the detector removed the need to include a background in the fits:

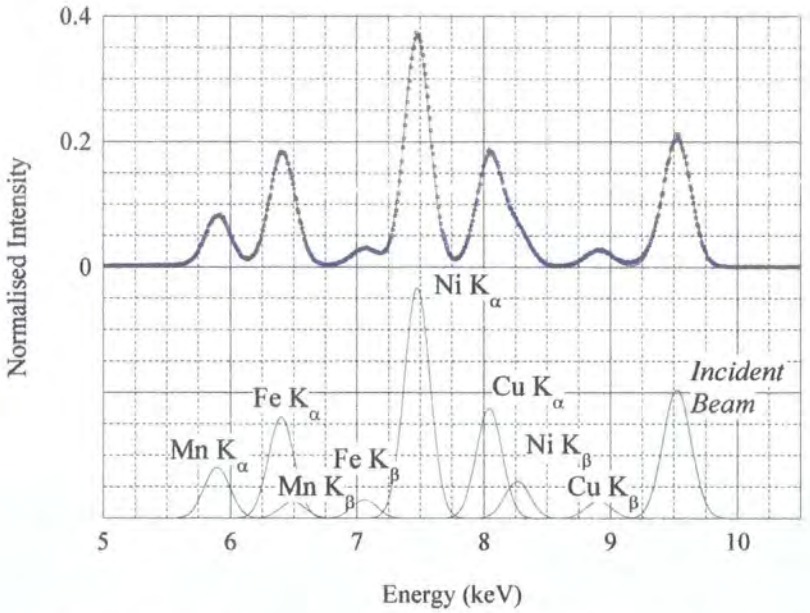

Figure 9.12: Fluorescence spectrum from sample 1 with the sample set to angle of 0.38° and wavelength 1.3Å

There is no contribution from the Ta cap and buffer layer because the *L* absorption edge is at 1.25511Å, and therefore an incident wavelength of 1.3Å does not have sufficient energy to excite the *L* lines of Ta. The spectra at each reflectivity point were fitted as detailed above, and the integrated intensity under each emission line was then plotted as a function of angle as in figure 9.13:

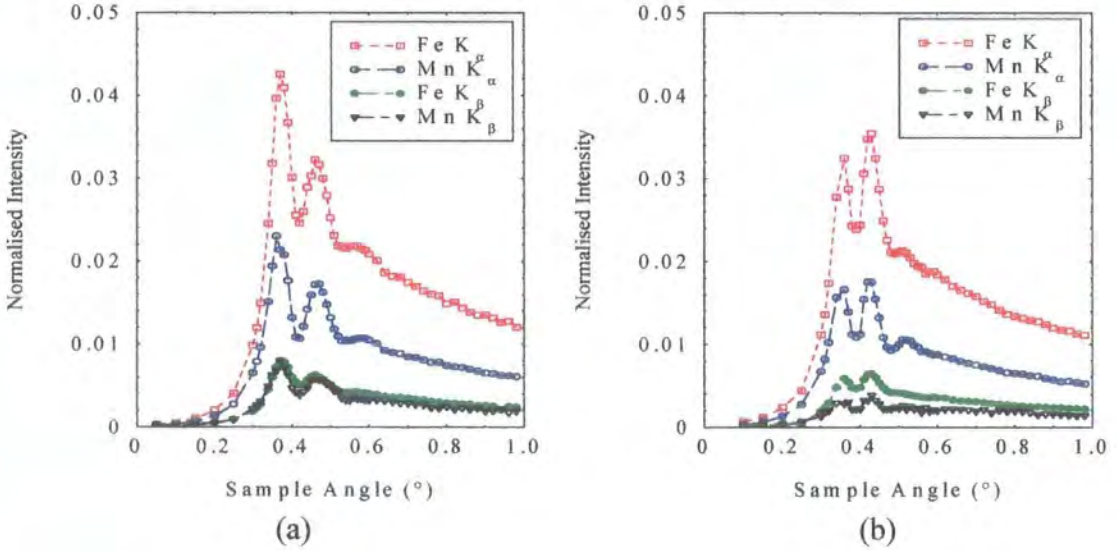

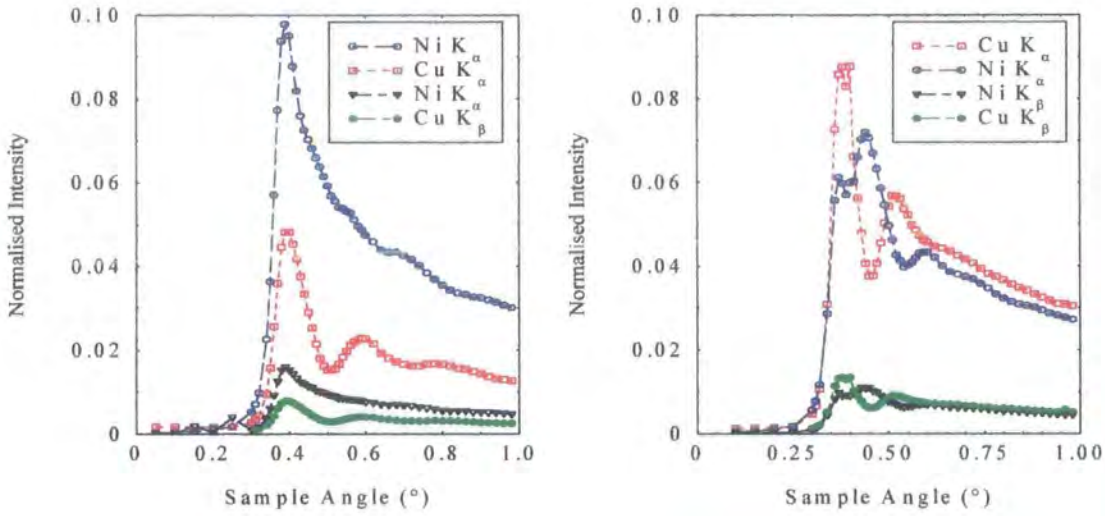

Figure 9.13: The integrated intensity under the elemental lines plotted as a function of angle for Sample 1 (a) and Sample 2 (b)

In order to make comparisons between the two samples easier, the $K\alpha$ lines of the elements Fe and Mn are plotted in figure 9.14 and Ni and Cu are compared in 9.15:

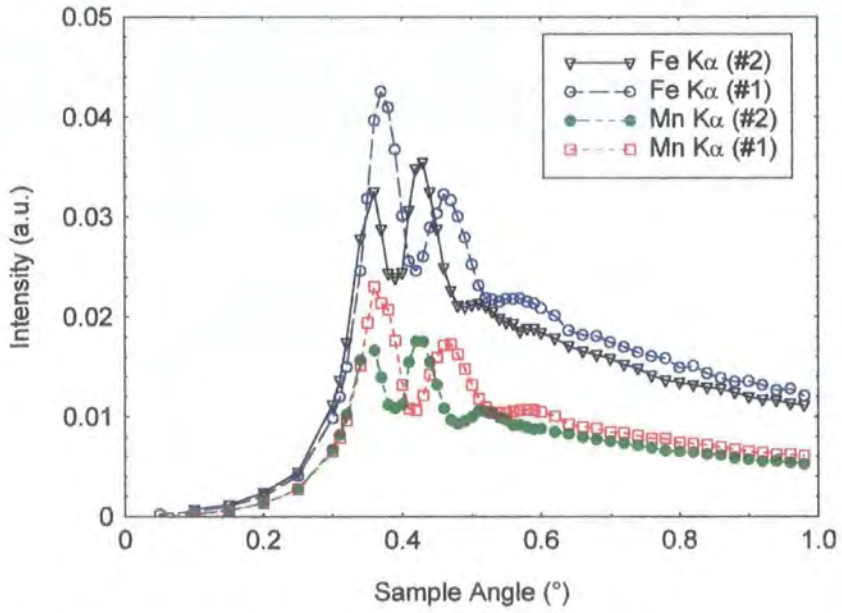

Figure 9.14: The Fe and Mn $K\alpha$ lines from Sample 1 and Sample 2

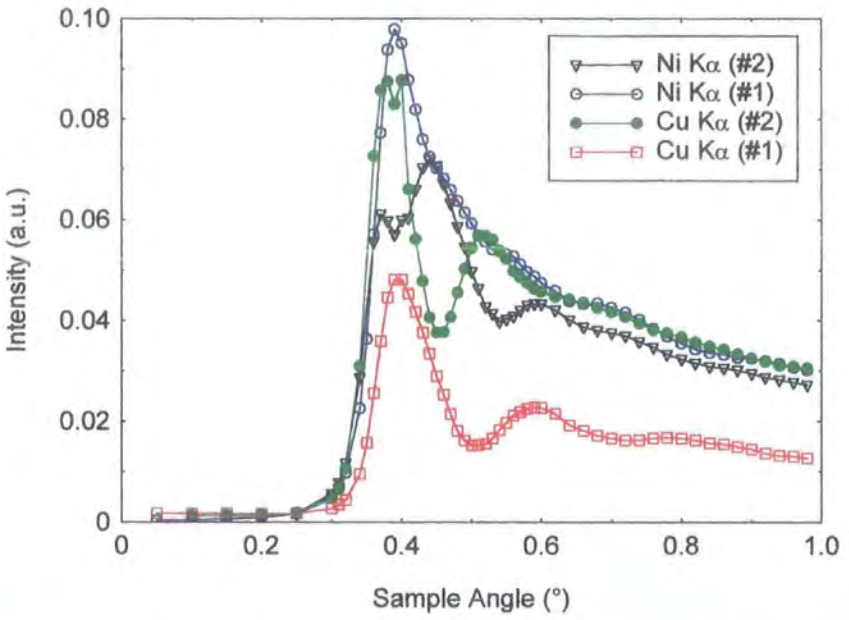

Figure 9.15: The Cu and Ni $K\alpha$ lines from Sample 1 and Sample 2

From figure 9.14 it is clear that the 'Kiessig' period is larger for sample 2 than sample 1. This is due to the different film thickness. In the high angle regime, both the iron and manganese curves for sample 2 are lower than sample 1. In order to quantify this difference the fluorescence yields from the an incident angle of 0.98° were compared. These results suggest that there is 10% less Fe and Mn in sample 2 than in sample 1. A similar analysis was conducted for the Ni and Cu $K\alpha$ lines, shown in figure 9.15. This confirmed that the NiFe layers were reduced by 10% in sample 2. Figure 9.15 shows that there was approximately 2.5 times more copper in sample 2 than in sample 1. This is shown graphically in figure 9.16:

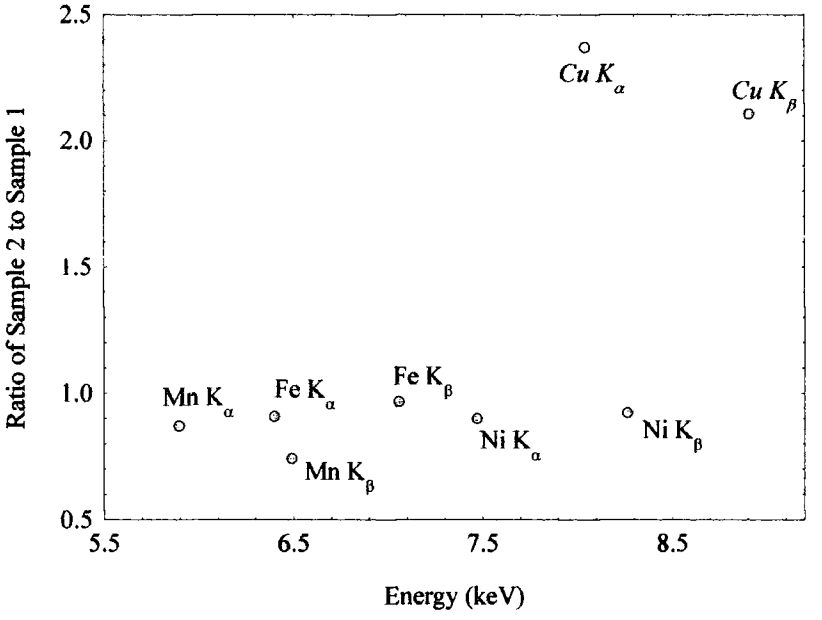

Figure 9.16: Graphical representation of the changes in layer thickness between the two samples

The percentage composition of the *3d* elemental block was calculated, again using the fluorescence yield at an angle of about one degree. As the iron signal is coming both from the NiFe and FeMn layers, the composition of the layers was assumed to be as- grown - i.e. $Ni_{80}Fe_{20}$ and $Fe_{50}Mn_{50}$. The result of these calculations is tabulated in table 9.2:

	Sample 1	Sample 2
$Fe_{0.5}Mn_{0.5}$	19.4 ± 1%	14.2 ± 1%
$Ni_{0.8}Fe_{0.2}$	60.3 ± 1%	45.4 ± 1%
Cu	20.3 ± 1%	40.4 ± 1%

Table 9.2: Compositions of the *3d* layer

The fluorescence yield for the Cu and Ni was simulated using the best fit structure as deduced from the reflectivity, and the compositional parameters calculated above. This simulation should be compared with figure 9.15.

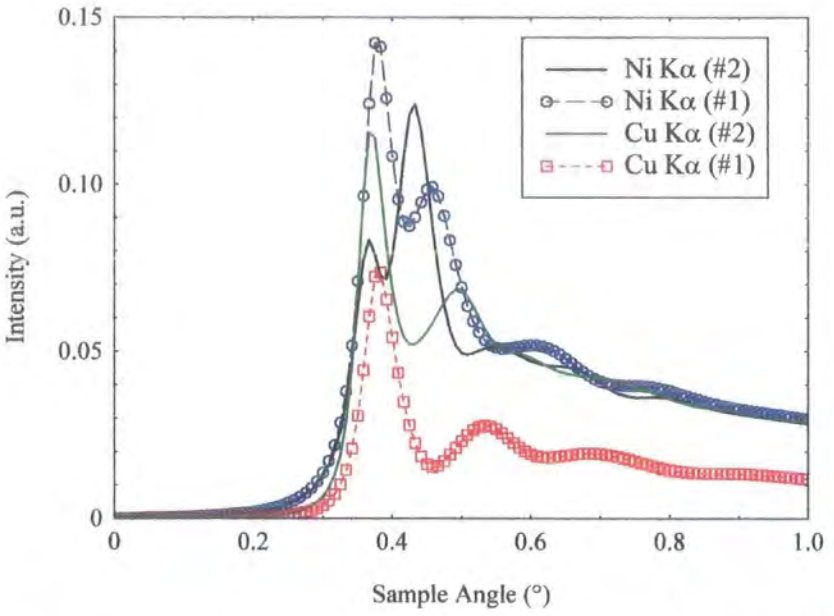

Figure 9.17: Simulation of the integrated intensity under the Cu and Ni Kα lines, for the best fit to samples 1 and 2.

The best fit of the reflectivity from sample 1, estimates the thickness of the total *3d* elemental layer to be 130 ± 30Å; this implies that the NiFe layer is 10% thicker than the nominal structure in sample 1. It also shows that the FeMn layer is much thinner than expected (reference 5) for both samples (25Å for sample 1 and 22.5Å for sample 2). The high biasing fields suggested a much thicker FeMn layer than was measured for the thickness of the pinned NiFe layer, but this is not the case here. No evidence of alloying was proved, although the evidence suggesting that alloying may have occurred at the Ta/NiFe interface is strong from the distorted high angle fringes in the reflectivity data.

9.8 Conclusion

Reflectivity experiments have been used to try and elucidate the structure of two spin valves. However, it has been shown that it is only possible to fit a crude tri-layer model to the system. Contrary to the claims of Huang et al (reference 16), no knowledge of the *3d* elements can be obtained by this method alone, but by combining the reflectivity results with simple fluorescence analysis, information on the *3d* elemental layers has been obtained [30]. The change in thickness between the samples has been shown not only to be due to the copper layer increasing, but also that both the NiFe and FeMn layers have reduced by 10%.

Both methods have disadvantages; the reflectivity is insensitive to the *3d* layers, whilst fluorescence is insensitive to interface roughness. A combination of the two methods, should lead to a better understanding of the samples under investigation. Although neither set of data has been fitted exactly, there is no reason why for a sample grown with sharper interfaces, quantitative fits should not be obtained.

This technique can be extended to investigate structures where the interface between the ferromagnetic and non-magnetic layers has been changed with the addition of cobalt. Although the inclusion of cobalt would complicate the fluorescence spectra, there may be advantages in looking at these systems and trying to include in the discussion the relation between structure and coupling from the diffuse scatter from such an interface. Cobalt could also be added at the Ta/NiFe interface to reduce the interdiffusion across this interface in the same way that it does at the NiFe/Cu interface.

References from Chapter 9

1 J.C.S. Kools, *IEEE Trans. Mag.*, **32** (4), *3165-3184*, (1996)

2 M.R. Parker, H. Fujiwara, S. Hossain, W.E. Webb, *IEEE Trans. Mag.*, **31** (6), *2618-2620*, (1995)

3 N.J. Gökemeijer, T. Ambrose, C.L. Chien, *Phys. Rev. Lett.*, **79** (21), *4270-4273*, (1997)

4 Private Communication

5 T.Lin, C. Tsang, R.E. Fontana, J.K. Howard, *IEEE Trans. Mag.*, **31** (6), *2585-2590*, (1995)

6 Courtesy of C.H. Marrows, University of Leeds

7 B. Dieny, V.S. Speriosu, S.S. Parkin, B.A. Gurney, D.R. Wilhoit, D. Mauri, *Phys. Rev. B*, **43** (1), *1297-1300*, (1991)

8 K. Nishioka, S. Gangopadhyay, H. Fujiwara, M. Parker, *IEEE Trans. Mag.*, **31** (6), *3949-3951*, (1995)

9 B. Dieny *J. Magn. Mag. Mat.*, **136,** *335-359*, (1994)

10 R.D.K. Misra, T. Ham, Y. Kadmon, C.J. Powell, M.D. Stiles, R.D. McMichael, W.F. Egelhoff Jr., *Mat. Res. Soc. Proc.*, **384,** *373-383*, (1995)

11 D.-H. Han, J.-G. Zhu, J.H. Judy, *J. Appl. Phys.*, **81** (8), *4996-4998*, (1997)

12 W.F. Egelhoff Jr., P.J. Chen, C.J. Powell, M.D. Stiles, R.D. McMichael, C.-L. Lin, J.M. Sivertsen, J.H. Judy, T.Takano, A.E. Berkowitz, *J. Appl. Phys.*, **80** (9), *5183-5191*, (1996)

13 S.S.P. Parkin, *Phys. Rev. Lett.*, **71** (10), *1641-1644*, (1993)

14 W.F. Egelhoff Jr., P.J. Chen, C.J. Powell, M.D. Stiles, R.D. McMichael, C.-L. Lin, J.M. Sivertsen, J.H. Judy, T.Takano, A.E. Berkowitz, T.C. Anthony, J.A. Brug, *J. Appl. Phys.*, **79** (8 pt. 2A), *5277-5281*, (1996)

15 N.J. Gökemeijer, T. Ambrose, C.L. Chien, N. Wang, K.K. Fung, *J. Appl. Phys.*, **81** (8), *4999-5001*, (1997)

16 T.C. Huang, J.P. Nozieres, V.S. Speriosu, H. Kekakis, B.A. Guerny, *Appl. Phys. Lett.*, **60,** *1573-1575*, (1992)

17 T.C. Huang, J.P. Nozieres, V.S. Speriosu, B.A. Guerny, H. Lefakis, *Appl. Phys. Lett.*, **62** (13), *1478-1480,* (1993)

18 Courtesy of C.H. Marrows, University of Leeds

19 B. Dieny, P. Humbert, V.S. Speriosu, B.A. Gurney, P, Baumgart, H. Lefakis, *Phys. Rev. B,* **45,** *806-813* (1992)

20 Reproduced from The Handbook of Binary Phase Diagrams Vols. 1-5, *W.G. Moffat,* **Genium Publishing Corporation**, (1987)

21 GIXS Software, BEDE Scientific

22 International Tables for X-ray Crystallography Vol. III, *Gen. Ed. K. Lonsdale,* **D. Reidel Publishing Company,** (1985)

23 X-ray Science and Technology, *Eds. A.G. Michette and C.J. Buckley,* **IOP Publishing**, (1993)

24 CRC Handbook of Chemistry and Physics 73rd Edition, *Ed. D.R. Lide,* **Chemical Rubber Publishing Company,** (1992-93)

25 U. Kramar, *J. Geochemical Exploration,* **58,** *73-80,* (1997)

26 M. Brunel, B. Gilles, *J. Phys. (Paris) Colloq.,* **50,** *C785-C796,* (1989)

27 D.K.G. de Boer, *Phys. Rev. B,* **44** (2), *498-511,* (1991)

28 D.K.G. de Boer, A.J.G. Leenaers, W.W. van den Hoogenhof, *X-Ray Spectrometry,* **24,** *91-102,* (1995)

29 S.I. Zheludeva, M.V. Kovalchuk, N.N. Novikova, A.N. Sosphenov, *Adv. in X-ray Chem. Anal. JAPAN,* **26,** *181-186,* (1995)

30 T.P.A. Hase, B.K. Tanner, P. Ryan, C.H. Marrows, B.J. Hickey, *IEEE Trans. Mag.*, **34** (4 Pt. 1), *831-833*, (1998)

Chapter 10

In Summary

This chapter summarises and reviews the theoretical and experimental results presented in this thesis. This leads directly onto a discussion as to how the results contained herein can be developed and used in the future.

The aim of this study was to relate magnetic coupling to structural models of the interface of certain multilayers. In so doing, it was observed experimentally that the theory could not describe grading or interdiffusion at an interface. The theoretical models of x-ray diffuse scattering were modified to include grading at an interface by M. Wormington (Bede Scientific Inc., USA), and this amended theory was then tested on a range of metallic systems. Although it has not been possible to link roughness or crystallinity with the giant magneto-resistance (GMR) effect, the study shows how x-ray scattering can be used to elucidate structural changes which can, and do, modify the coupling character of the samples.

The work contained in chapter 6 is a good example of how the structure was found to be directly related to the coupling. Anomalous coupling was found to be a direct result of structural imperfections within the samples. Chapters 5 and 6 detail how the development of the theory of x-ray diffuse scattering has been modified to include interdiffusion or grading at an interface. The results in chapter 6 confirm that the distorted wave Born approximation can be used to model highly graded systems with multiple layers. These results are an extension of earlier work where the scattering from a single surface was investigated. A comparison of the interface models derived from x-ray diffuse scattering and high resolution transmission electron microscopy show that the interface model deduced by the x-rays is accurate. An important result from this study was the observation that the lateral correlation length was of the same order as the crystal grain size. A similar result was obtained in chapter 8 where the grain size and lateral correlation lengths were also similar.

This is an important result as it highlights the inherent difficulty in separating the effects of crystallinity and roughness when relating structural changes to macroscopic phenomena.

Chapter 7 contains the results of an in-depth investigation of a series of molecular beam epitaxy samples. The GMR of the samples was seen to vary as a function of deposition temperature of both the multilayer and the buffer layer. The x-ray scattering from both low and high angles revealed structural changes were taking place within the samples as the temperature of deposition varied. It was, however, not possible to identify exactly where or what these changes were, but it was observed that two length scales were present on the surface. These two length scales were observed in both the low angle experiments and in the high angle rocking curves.

The samples studied in chapter 8 were a series of Cu/Co multilayers prepared by sputtering techniques. By varying the amount of time contamination was allowed to occur within the spacer layer, it was observed that the coupling between the magnetic layers changed from bi-linear (anti-ferromagnetic) to a bi-quadratic type of coupling. No structural changes were observed between samples which exhibited these very different couplings when standard x-ray scattering techniques were used. In a novel experiment soft x-rays tuned to the cobalt L_3 resonance condition were used. X-rays of these wavelengths are sensitive to the magnetic moment within the sample via low order electric dipole transitions. An in-depth study of the magnetic super-structure revealed that the bi-linearly coupled samples behaved in a very different way from the bi-quadratic samples. The motion of the net anti-ferromagnetic moment was measured as a function of applied field, and the resulting M-H type measurement was found to show a very different variation than was evidenced by either magnetometry studies or Lorentz Force Microscopy. For the first time, it was possible to measure unambiguously the magnetic roughness of the samples. This was found to be highly correlated both in and out of plane. Unlike previously reported experimental results, the in plane correlation length of the magnetic roughness was approximately 1000 times greater than that of the structural roughness. In addition, the in plane magnetic correlation length was observed to

depend on the direction of the applied magnetic field. Analysis of the Lorentz Force Microscopy images suggests that the x-rays are sensitive to the magnetic ripple, and that this ripple is correlated through each of the magnetic layers within the sample.

The experimental work in this thesis was concluded by a fluorescence experiment designed to elucidate the thickness of buried layers in spin valve structures. Unlike multilayers, which have a well defined Bragg peak, it is non trivial to measure the thickness of buried *3d* layers in spin valves using grazing incidence reflectivity or diffuse measurements. The fluorescence technique provides a powerful alternative measurement tool to calculate the parameters of buried layers. Although it was not possible to simulate accurately the fluorescence yield as a function of angle for the two samples under investigation, the power of the technique was evidenced in the approximate determination of the thickness of a copper layer in a spin valve sample.

It has been shown through the experimental work contained within this study that x-ray scattering can provide much detailed information on the structure of magnetic metallic multilayers. In turn this information can be used to explain macroscopic effects such as coupling in magnetic metallic multilayers.

The data collected in chapter 7 is still not satisfactorily explained. Another series of experiments is required to explain more fully the results so far obtained. A systematic study of the effects of buffer layer deposition on the structure of the multilayer film is required. A parallel study utilising high resolution transmission electron microscopy would also be beneficial in identifying the areas where the imperfections in the structure exist. With the knowledge thus deduced, the effect of the deposition temperature of the multilayer on the structure of the film, and hence the coupling could be attempted.

In the future, it is hoped that the fluorescence technique can be used simultaneously with grazing incidence x-ray reflectivity studies. Development of the technique will have industrial uses in the manufacture and control processes of hard disk components.

In parallel with the development of grazing incidence fluorescence techniques as an analytical tool, it is hoped that more experiments can be undertaken using soft x-rays. In the last experimental run conducted on station 1.1, Daresbury SRS, an Fe/Au multilayer was investigated using soft x-rays in the vicinity of the Fe L_3 edge. No magnetic resonance was detected, and it is envisaged that a repeat experiment on this beamline will occur in the near future. It is also hoped that larger magnetic fields can be applied in-situ. This will enable the magnetisation experiments conducted with x-rays to be compared with those obtained by more normal magnetometers. This technique could be used as a highly sensitive magnetometry device, specifically sensitive to anti-ferromagnetically coupled magnetisation behaviour in multilayers.

Appendix A

This appendix gives details of a Pascal programme written to correct data for the dead-time inherent in scintillator detectors. It is based on a Newton-Raphson technique which solves the equation:

$$R_{Meas} = R_{Real}\exp\left(-R_{Real}\tau\right) \quad \text{where } \tau \text{ is the dead-time of the detector}$$

```
Program Detector_corrections;

{By Tom Hase      3rd May 1996}

Uses dos,crt;

Var
 Func_Measured_counts,Deriv_Measured_counts,dead_time,
 maximum_iterations,error_variable,beam_monitor          : extended;
 ome,time,Chan2,Chan3                                    : real;
 x_n                                                     : Array [1..100] of real;
 Measured_counts,Real_counts,Position                    : Array [1..1900] of real;
 Angle                                                   : Array [1..1900] of String[14];
 File_header                                             : String [100];
 File_extension,file_type                                : String [5];
 ext                                                     : string [2];
 i,x,code,nodp                                           : integer;
 Filnam                                                  : string[60];
 Data_input,Data_Output                                  : string [60];
 f                                                       : text;
 test,stop                                               : Boolean;
 change                                                  : Char;
 Posx,Posy                                               : Byte;


 Begin
  clrscr;
  textcolor(3);
  writeln('------------------------------------------------------------------');
  writeln('                    DETECTOR CORRECTIONS');
  writeln('------------------------------------------------------------------');
  writeln('');
  writeln(' Corrects count rates for detector dead times by solving the equation:');
  writeln('   Measured Counts = Real Counts * Exp(-(Real Counts * Dead-time))');
  writeln(' using a Newton-Raphson iteration technique');
  File_type:='Dares';           {Daresbury file - default input}
  error_variable:=1e-6;         {Stop accuracy between the nth and n+1 points in iteration}
  maximum_iterations:=100;      {maximum number of iterations in loop}
  writeln(' ');
  textcolor(5);
  writeln('These are the current parameters being used:');
  writeln('');
  writeln('File type: ',file_type);
  writeln('Iteration stop accuracy: ',error_variable);
  writeln('Maximum number of Iterations: ',maximum_iterations);
  writeln('Would you like to change any of these? (y) ');
  Readln(Change);
  If change='y' then
   begin
    Writeln('File type (Dares or Ascii) ');
    Readln(File_type);
    Writeln('Iteration stop accuracy');
    readln(error_variable);
    Writeln('Maximum number of Iterations');
    Readln(Maximum_iterations);
   end;
```

```
textcolor(2);
Writeln('');
Writeln('Name of data file to be ammended (inc. extenstion):');
Readln(Data_Input);
If file_type='Dares' then
 begin
  i:=0;
  repeat
   i:=i+1;
   Filnam:=copy(Data_Input,i,1);
   If i=100 then filnam:='.';
  until filnam='.';
  filnam:=copy(Data_Input,1,i);
  ext:=copy(Data_Input,i+2,2);
  Assign(f,data_input);                          {** Reads File **}
  Reset(f);
  For i:=1 to 19 do
   readln(f,file_header);
  nodp:=0;
  beam_monitor:=0.0;
  Repeat
   stop:=true;
   nodp:=nodp+1;
   readln(f,Angle[nodp],ome,time,Chan2,Measured_Counts[nodp]);
   Measured_counts[nodp]:=Measured_counts[nodp]/(time+1e-7);
   beam_monitor:=Beam_monitor+Chan2;
   If angle[nodp]=' END OF DATA' then stop:=false;
   If angle[nodp]=' SCAN ABORTED' then stop:=false;
  until stop=false;
  close(f);
  nodp:=nodp-1;
  beam_monitor:=Beam_monitor/nodp;
  For i:=1 to nodp do
   begin
    angle[i]:=copy(angle[i],5,6);
    Val(angle[i],position[i],code);
   end;
 end;

If File_type='Ascii' then              {ASCII file type - two data strings}
 begin
  i:=0;
  repeat
   i:=i+1;
   Filnam:=copy(Data_Input,i,1);
  until filnam='.';
  filnam:=copy(Data_Input,1,i);
  Assign(f,data_input);                          {** Reads File **}
  Reset(f);
  Writeln('Input the number of data points');
  Readln(nodp);
  For i:=1 to nodp do
   readln(f,position[i],measured_counts[i]);
  Close(f);
 end;

Writeln('');
Writeln('Input the Dead time for the detetor (in nanoseconds)');
readln(dead_time);
dead_time:=dead_time*1e-9;             {Dead time of Detector}

For x:=1 to nodp do
 begin
  x_n[1]:=Measured_counts[x];
  i:=0;
  repeat
   test:=false;
   i:=i+1;
   Func_Measured_counts:=((x_n[i]*exp(-(x_n[i]*dead_time)))-Measured_counts[x]);
   Deriv_Measured_counts:=exp(-(x_n[i]*dead_time))*(1-(x_n[i]*dead_time));
   If Deriv_Measured_counts=0 then
    Begin
     Real_counts[x]:=x_n[i];
     test:=true;
    end;
   x_n[i+1]:=x_n[i]-(Func_Measured_counts/Deriv_Measured_counts);
   If Abs(x_n[i+1]-x_n[i])<Error_Variable then
```

```
        begin
         Real_counts[x]:=x_n[i+1];
         test:=true;
        end;
       If i=maximum_iterations then
        Begin
         Real_counts[x]:=x_n[i+1];
         test:=true
        end;
     until test=true;
    end;

  If file_type='Dares' then
    Data_Output:=Filnam + 'cor';
  If file_type='Ascii' then
   Data_Output:=Filnam + 'cor';
  Assign(f,data_output);
  rewrite(f);
  If file_type='Dares' then
   begin
    for i:=1 to nodp do
     Real_counts[i]:=Real_counts[i]/Beam_monitor;
   end;
  For i:=1 to nodp do
   writeln(f,Position[i],'     ',Real_counts[i]);
  writeln(f,'');
  writeln(f,'Data corrected using a dead time of: ',dead_time);
  close(f);
  textcolor(4);
  writeln('');
  writeln('Your corrected file has been saved in: ',data_output);
  textcolor(7);
  writeln('');
end.
```